GEO-3900

MASTER'S THESIS IN

GEOLOGY/GEOPHYSICS

Geological Fluid Flow Systems at Nyegga of the Mid-Norwegian Margin

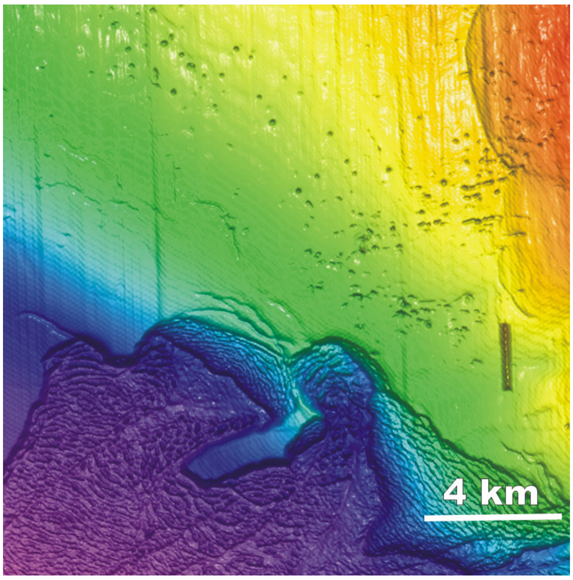

Wiktor W. Weibull

November, 2007

FACULTY OF SCIENCE
Department of Geology
University of Tromsø

GEO-3900

MASTER'S THESIS IN

GEOLOGY/GEOPHYSICS

Geological Fluid Flow Systems at Nyegga of the Mid-Norwegian Margin

Wiktor W. Weibull

November, 2007

Foreword

When I first came to Tromsø in august 2005, I came to meet Professor Jürgen Mienert and ask him if he would accept to supervise me for a Master Thesis. I should mention that I was very nervous and could not say anything that made sense. But yet he gave me a chance and in 2006 I became a part of the Group of Geophysics. As a part of this group I had the opportunity to participate in two scientific cruises and experience the challenges and difficulties which are involved in doing geophysical research in the ocean. This was truly a remarkable experience for me. I wish to express my gratitude to Jürgen Mienert for giving me these opportunities and also for helping me during the course of this master thesis project. I would also like to thank all other scientists and students of this very successful group, in special my co-supervisor Stefan Bünz who also helped me a lot with the thesis. I need to thank Steinar Hustoft and Andreia Plaza for sharing and discussing their works with me. These discussions added a lot to the result of this paper.

I would like to thank all students who I had the pleasure to meet during the course of these two years. In special, Jon, Sten, Leif, Gustav. Aamir, Iver, Mats, Heike, Christina, Hilde, Rune and Tine.

Last but not least, I would like to thank Carla, my wife, who took extra time taking care of our son so that I could stay longer in the university during the last months. This thesis is just as important for them as it is for me. I also wish to thank my parents in Brazil for their encouragement and support during these years in Tromsø.

Tromsø, 15 November 2008

Wiktor W. Weibull

Abstract

The Nyegga area is located at the north-eastern escarpment of the large Storegga Slide on the south of the Vøring plateau. The region has long been a natural laboratory for shallow fluid flow investigations, mainly due to the large number of fluid flow expressions found on the bathymetric and seismic data, and the possibility to investigate the relationship between fluid flow, gas hydrate formation and slope stability. The seafloor at Nyegga is marked by hundreds of small depressions and mounds. These are in turn the upper termination of semi-circular zones of low amplitude, upbended or downbended reflections called acoustic chimneys or pipes. These chimneys terminate also at different stratigraphic horizons below the seafloor and have been interpreted as episodic fluid flow expulsion features. Underlying Eocene-Oligocene polygonal fault systems are suspected of being a long term source of fluids to the shallow subsurface sediments, while Tertiary domes are suspected to be possible leakage areas for thermogenic fluids. The area is characterized by the presence of free gas trapped beneath a seal of gas hydrates as indicated by a bottom simulating reflector (BSR).

In this study 287 pockmarks, 23 mounds and 441 acoustic chimneys were investigated using high resolution swath bathymetry and 3D seismic data. The data allowed mapping and quantification of several parameters of seabed and subseabed expressions of fluid flow. The results showed that the pockmarks and mounds at Nyegga are not directly related to the polygonal fault system, but instead are product of blowout events originating from two locally overpressured shallow reservoirs overlying the polygonal fault system. Indications of fluid migration starting from the base of the polygonal faults system were found, but these fluids are most likely being distributed by the shallow reservoirs. The blowout events are the result of hydraulic fracturing starting mainly from structural crests or updip pinchouts within free gas-accumulation zones beneath the base of the gas hydrate stability zone or from traps beneath glacigenic debris flow deposits. Quantification of the pockmarks, mounds and acoustic chimneys showed that the largest pockmarks and mounds are found overlying structural closures and traps with presumably highest overpressure within the free gas zones, indicating a relationship between their size and the degree of overpressure. Pockmarks, mounds and acoustic chimneys are mainly elongated features and in some areas their orientation was found to be parallel to the free gas trapping structures in the subsurface. This is an indication that the orientation of pockmarks and mounds in these areas is inherited from the acoustic chimneys and hence from the axis of hydraulic fracturing.

Summary

Foreword i
Abstract ii
Summary iii
1. Geological Fluid Flow 1
1.1 Introduction 1
1.1.1. Study area 6
1. 2. Nature and origin of fluid flow 8
1.2.1. Importance of sediment compaction and transformation for fluids 9
1.2.2. Fluid migration pathways 11
1.2.3. Fluid Flow dynamics 11
1.2.4. Modes of fluid migration and accumulation 13
2. Geology of the Nyegga study area 17
2.1. Regional geology 17
2.1.1. Tectonic evolution 17
2.1.2. Stratigraphy and sedimentary processes 19
2.2. Gas Hydrates 25
2.3. Regional Oceanography 26
3. Material and Methods 29
3.1. Data description 29
3.1.1. Multibeam survey at Nyegga (July 2006) 29
3.1.2. 3D Seismic cube ST0408 from StatoilHydro 33
3.2. Data interpretation methods 34
3.2.1. Swath bathymetry interpretation 34
3.2.2. 3D seismic interpretation 34
3.3. Mapping and quantification of fluid flow expressions 37
3.3.1. Pockmarks and mounds 37
3.3.2. Acoustic chimneys 41
3.4. Statistical analysis methods 42
4. Results 45
4.1. Interpretation of the high resolution swath bathymetry 45
4.1.1. Mapping of seabed expressions of fluid flow 46

4.1.2. Multivariate statistical analysis of pockmarks and mounds..53
4.2. 3D Seismic Interpretation and subsurface distribution of acoustic chimneys 57
4.2.1. Description of stratigraphy within the area..58
4.2.2. The Polygonal faults 62
4.2.3. Geometry of shallow reservoirs 64
4.2.4. Mapping and quantification of acoustic chimneys 68
4.2.5. Multivariate statistical analysis of the acoustic chimneys 76
5. Discussion 83
5.1. Spatial distribution of geophysically inferred free gas and fluid flow expressions................83
5.1.1. Distribution and migration of fluids in the subsurface 83
5.1.2. Origin and distribution of acoustic chimneys, pockmarks and mounds 85
5.2. Origin of fluids to the seabed pockmarks and mounds...98
5.3. Suggestions for the timing and duration of seafloor seepage 100
6. Conclusion 103
References...105
Appendix...113

1. Geological Fluid Flow

1.1 Introduction

Fluid flow expressions onshore such as mud volcanoes are well known features, and have been studied for more than 150 years (Dimitrov, 2002; Kopf, 2002, and references therein; Planke et al., 2003). But offshore, these features were not recognized until about 40 years ago (King and MacLean, 1970). This time lag can be explained by the lack of technology. There was simply no way to image the sea floors at a high enough spatial resolution. Even with the development of single beam echo sounders in the early 1930s, scientists could only acquire a coarse grid of lines of the seafloor, this way missing the smaller targets of seafloor expressions related to focused fluid flow.

Development of areal mapping in the 1960s came to revolutionize the way morphological studies of the seafloor were carried out, and led to the discovery of a wide range of previously unknown morphologies at the seafloor. King and McLean (1970) described one such feature, which they called **pockmark** and defined as *"A concave crater-like depression of the type that occurs in profusion on mud bottoms across the Scotian Shelf* ". Although they had no convincing proof as to what process had shaped these negative relief features, they interpreted them as being formed by upward-migrating gas bubbles lifting the sediments and putting them into suspension, or in their own words "gas-turbation". Similar features were soon recognized in the North Sea and in many other areas around the world, not only in mud, but also in sandy seabeds (e.g. Hovland, 1981; Hovland and Judd, 1988; Gay et al., 2006b) (figure 1). They were soon confirmed to be expressions of former or present fluid migration and seepage through the seabed connected to chimneys in the subseabed (Hovland et al., 1985). Contemporary studies of pockmarks show that they are generally found on the continental margins overlying deep and/or shallow hydrocarbon reservoirs. And that they normally span in diameter from less than 1 m to more than 250 m, and range in depth from less than 1m to more than 40 m (Judd and Hovland, 2007). Accounts of single pockmarks with diameters of up to 1500 m and depths of up to 150m have been also reported (Pilcher and Argent, 2007).

Other less common features were found, sometimes associated with pockmarks, these are positive relief features often called **mud volcanoes**, **mud mounds**, and **carbonate mounds**. Mud volcanoes are known from onshore areas where fluid migrating from subsurface entrains fine grained particles leading to the extrusion of mud flows. Mud Volcanoes are also largely associated with petroleum migration (Hjelstuen et al., 1997; Dimitrov, 2002; Kopf, 2002; Planke et al., 2003; Hansen et al., 2005).

Isolated mud and carbonate mounds were previously unknown and have been the subject of intense studies. Many theories have been used to explain their formation, including structural deformation due to density inversion, subsurface authigenic carbonate precipitation derived from methane oxidation (Naeth et al., 2005; Hovland and Svensen, 2006; He et al., 2007; Paull et al., 2008a), and cold water coral growth (e.g. *Lophelia* sp) stimulated by high current speeds and food supply (Wheeler et al., 2007). Review of mounds literature revealed that they vary in size and shape from small, ovoid low relief features a few meters tall and with tens of meters across to giant mounds hundreds of meters tall and a few kilometers wide (Dimitrov, 2002; Kopf, 2002; Wheeler et al., 2007, and references therein).

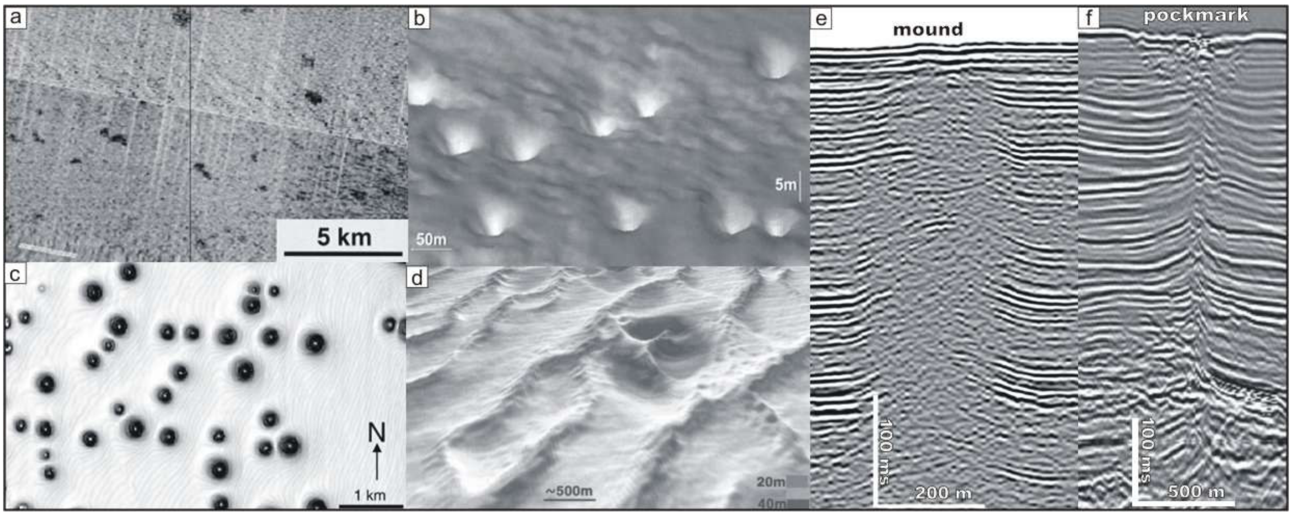

Figure 1 – Examples of geologic fluid flow expressions; (a) Pockmarks and mounds are seen as high backscatter patches in sidescan sonar data from Nyegga (Bouriak et al., 2000); (b) Swath bathymetry shaded relief image of pockmarked mud seabed of Norwegian North Sea (Hovland, 2003); (c) Dip map of seabed reflection in 3D seimsic survey taken over mega pockmarks in turbiditic sands offshore Gabon, West Africa (Pilcher and Argent, 2007); (d) Swath bathymetry shaded relief map showing pockmarks formed at the base of a sand wave in southern North Sea (Hovland, 2003); (e) High resolution seismic data showing an acoustic chimney underlying a mound in Nyegga (Westbrook et al., 2008); (f) Multichannel seismic data showing an acoustic pipe underlying a giant pockmark in Lower Congo Basin (Gay, 2006).

In addition to areal mapping, 2D seismic has also been a major geophysical tool used by scientists studying fluid flow expressions (Judd and Hovland, 2007). Seismic profiles provide an image of the subsurface which can be used to understand the development of fluid flow, including the possibility of visualizing the source and migration pathways of the fluids which are seeping through the seafloor. But scientists using seismic data were facing two big problems. One problem was related to the spatial sampling capability of 2D seismic acquisition which only allowed the imaging of a reduced number of targets. Another problem was that seismic sections crossing fluid venting systems usually showed localized amplitude attenuation and disrupted reflections, the so called **seismic blanking zones**, **acoustic chimneys or blow-out pipes** (figure 1e-f). These "acoustically turbid" zones were suspected to be linked to the migration of fluids through sediments, but several possible theories may apply. Examples of these theories include signal starvation due to high reflective material at or close to the seabed (e.g. gas hydrates, carbonate concretions), amplitude blanking due to reduced acoustic impedance contrast within gas hydrated sediment (Lee and Dillon, 2001); destruction of sediment layering by minor folding and fracturing associated with flowing of fluids out of overpressure areas (e.g. Hustoft et al., 2007); over pressured pore water reducing the shear modulus of the sediments and their ability to reflect acoustic energy; and acoustic scattering by the presence of gas in sediments (Wood et al., 2002). Many studies have confirmed the presence of gas in the sediments within the blanking zones, and the lateral change in acoustic impedance due to gas can then be used to explain the diffractions and the acoustic attenuation observed (e.g. Jones et al., 1986; Yuan et al., 1992). The acoustic image of the seismic chimneys dramatically differs between seismic lines that are shot with different seismic sources and also between single- and multi-channel seismic, indicating that the blanking effect may also be frequency and offset dependent (e.g. Vanneste et al., 2001; Riedel et al., 2002; Schmitz and Jokat, 2007).

The introduction of 3D seismic surveying in the 1970s allowed for high resolution images in depth and lateral space, but the high costs restricted its application only to the most prospective petroleum provinces. This has changed, now 3D seismic surveying has become a common tool in hydrocarbon exploration, and this technology is increasingly being transferred to academia for their research. Together with swath bathymetry it has become a popular geophysical tool for fluid flow studies (e.g. Heggland, 1997; Heggland, 1998; Bünz et al., 2005; Cartwright and Huuse, 2005; Davies and Posamentier, 2005; Hansen et al., 2005; Hustoft et al., 2007; Westbrook et al., 2008), and has also been increasingly used for seismic morphology studies (e.g. Andreassen et al., 2008; Rafaelsen et al., 2008). It allows mapping migration pathways of fluids and gases and the fluid flow expressions both on the subsurface and through the seabed with unprecedented detail (figure 2). But as with all remote sensing tools, ground truthing needs to be added to confirm the results.

Fluid flow in continental margins shows diverse sources at different depths ranging from the crust and petroleum reservoirs to the upper sediment column. There is a general acceptance that, where thermo-baric conditions favor hydrate stability, fluid flow is responsible for localized gas hydrate accumulations in the close subsurface (e.g. Ginsburg and Soloviev, 1997; Booth et al., 1998; Ivanov et al., 2007) (figure 3). And at the sea floor the fluid flow seeps are frequently characterized by the presence of chemosynthetic communities (e.g. Hovland et al., 2005; Hovland and Svensen, 2006) and methane-derived authigenic carbonate deposits (e.g. Hovland et al., 1985; Hovland et al., 2005; Mazzini et al., 2005) (figure 4). The worldwide distribution of fluid flow expressions has led the scientific community to recognize their relevance for marine geo- hazards, marine ecology and global climate (e.g. MacDonald et al., 2002; Judd and Hovland, 2007).

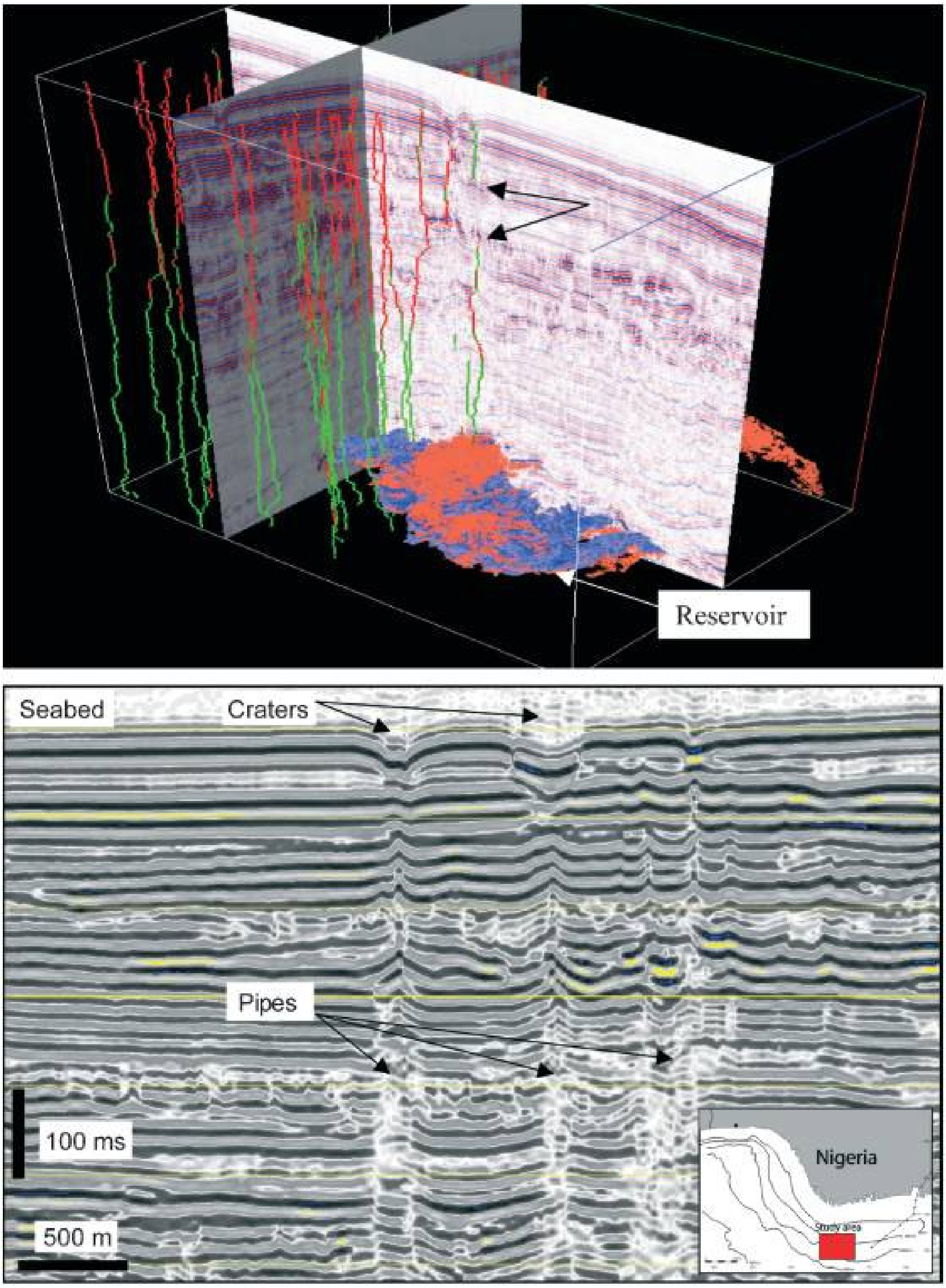

Figure 2 – The spatial geometry and extent of acoustic chimneys caused by gas escape from a buried reservoir through sealing mudstones was first clearly imaged by this high-quality 3D seismic data from the South Niger Delta (from Løseth et al., 2001).

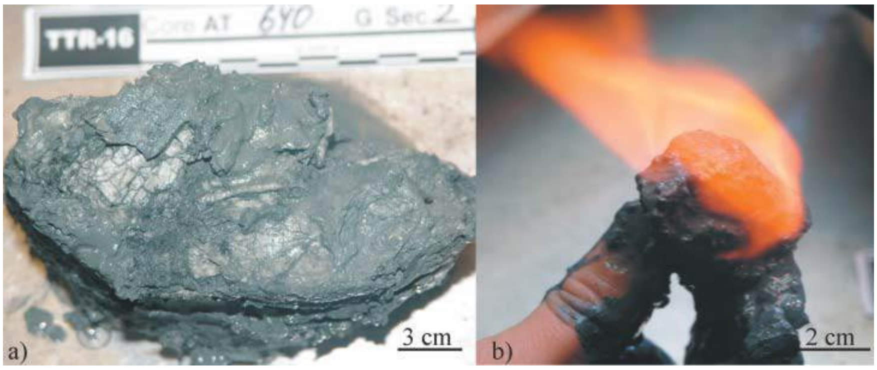

Figure 3 - Photos of gas hydrate. (a) A very thin kind of 'stratification' exhibited by hydrate cementation. (b) A burning piece of core with hydrate in it (from Ivanov et al., 2007).

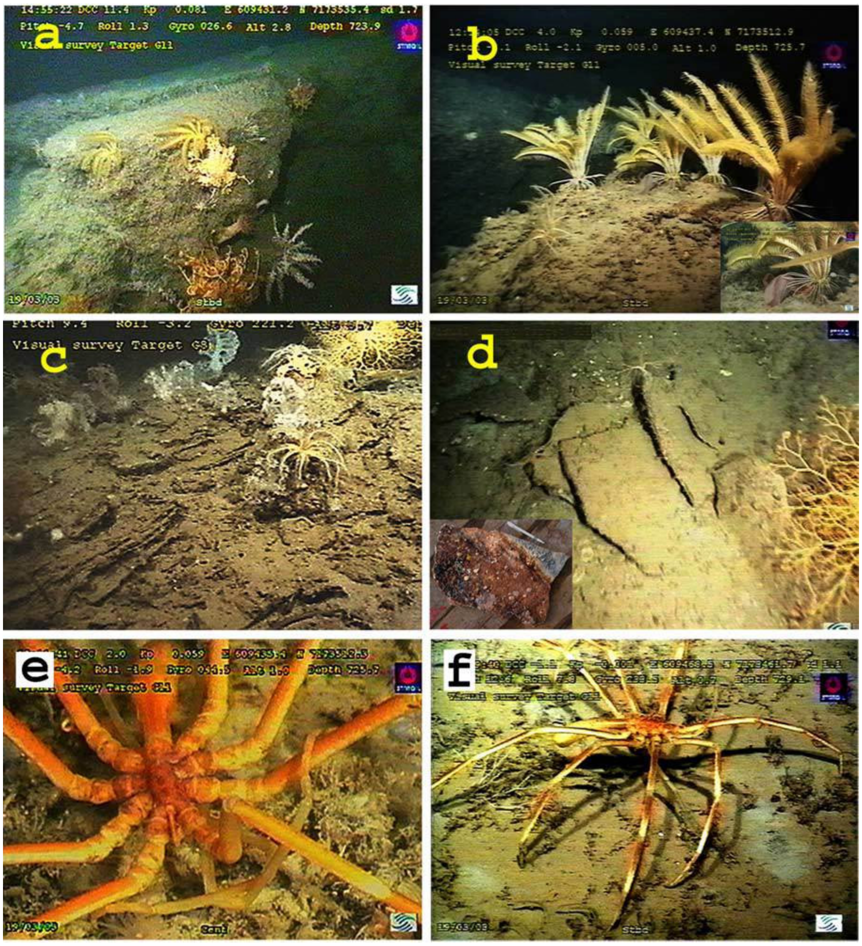

Figure 4 - Underwater colour images grabbed from the ROV-acquired video footage from a pockmark in Nyegga. a) Up to 24 m^3 large carbonate slabs occur inside the pockmark. Notice that most of these macrofaunal organisms are perched on the lower side of the carbonate rock. b) Five stalked crinoids perched on top of an adjacent slab to that shown in a). Note the fish (eel pout?) resting next to one of the crinoids (inset detail). c) Layered and friable (crisp and fragile) exposed sediment structure is suspected to represent carbonate-cemented sediments. The organisms include basket stars, crinoids, and unidentified macro-fauna. d) Five exposed thin wafer-like carbonate rocks found in the deepest portion of the pockmark. e) A sea spider (pycnogonid suspected to be a Collossendeis sp.) located on one of the large slabs near that shown in a). f) A pycnogonid, measuring about 15 cm across (between tips of legs) (from Hovland et al., 2005).

1.1.1. Study area

The study area for the present Master Thesis is the Nyegga area. This area comprises the northern escarpment of the large Storegga Slide on the south of the Vøring Plateau, between the hydrocarbon prone Vøring and Møre basins (figure 5). The region has long been a natural laboratory for shallow fluid flow investigations, mainly due to the large number of fluid flow expressions found on the bathymetric and seismic data and the possibility to investigate the relationship between fluid flow and slope stability (e.g. Bugge et al., 1987; Mienert et al., 1998b; Bouriak et al., 2000; Berndt et al., 2003; Buenz et al., 2003; Gravdal et al., 2003; Hovland et al., 2005; Hovland and Svensen, 2006; Mazzini et al., 2006; Hustoft et al., 2007; Westbrook et al., 2008).

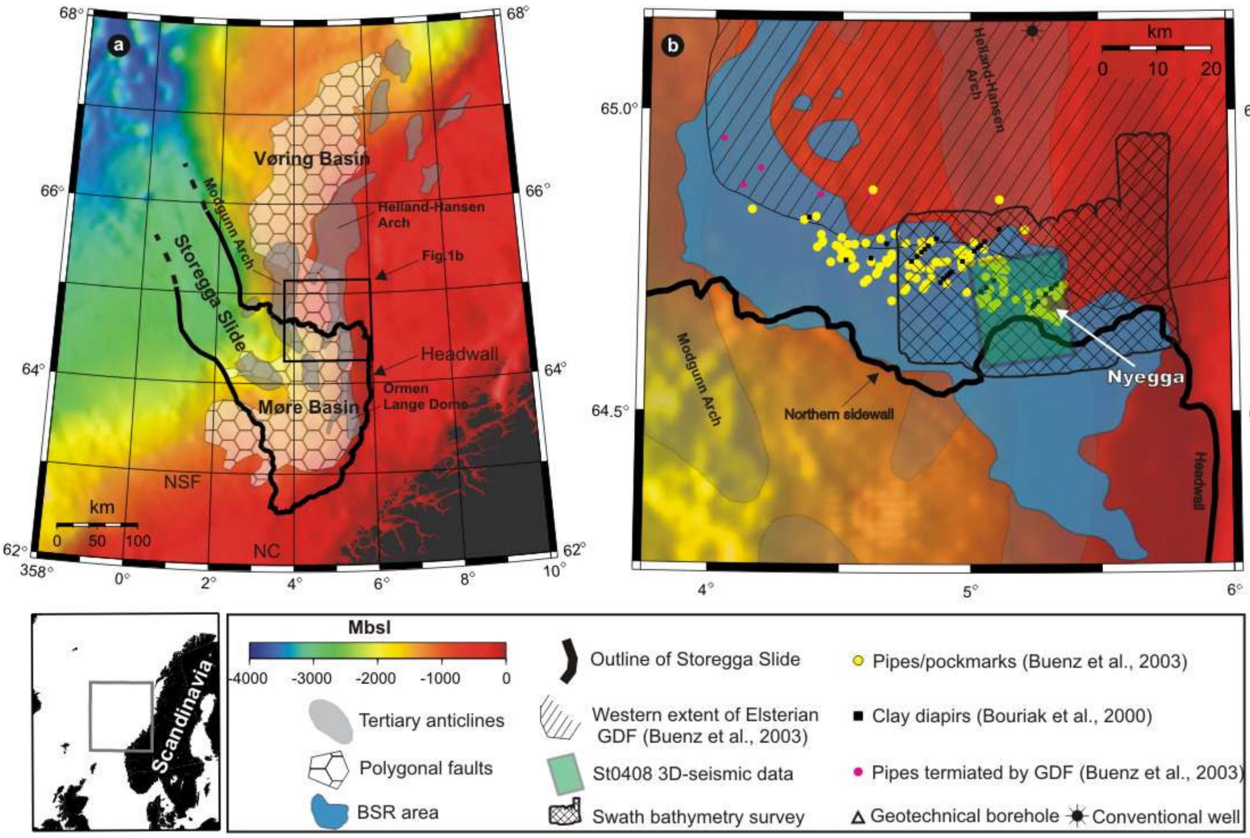

Figure 5– Location map of the study area relative to (A) Mid-Norwegian margin (Wessel and Smith, 1991; Smith and Sandwell, 1997) and (B) the Storegga Slide (modified from Hustoft et al., 2007).

The fluid flow expressions in the Nyegga area were first documented from 2D seismic records by Bugge et al., (1987). They were recognized as local topographic anomalies associated with a bottom simulating reflector (BSR). At first these anomalies were interpreted as possible mud diapirs. And later, based on side scan sonar and high-resolution seismic records, Mienert et al., (1998) and Bouriak et al., (2000) identified them as pockmarks, mud diapirs, and mud volcanoes.

Mud volcanism was soon dismissed by Gravdal et al., (2003), which used Tobi Side-scan sonar and higher resolution seismic to show that there was no evidence of mobilized mud in these features. Meanwhile Berndt et al. (2003), found evidence that pockmarks and other fluid flow features at Nyegga are at least partly associated to vertical migration of fluids through focused fluid flow pipes. The presence of widespread polygonal faulted oozes at depth was speculated as a possible long term source for the fluids. In a more regional study, Buenz et al., (2003), using a dense grid of regional seismic lines, mapped the extents of the BSR in part of the Mid-Norwegian Margin and found that many fluid flow features were associated with its distribution, which he interpreted to be geologically controlled.

Most of the subsequent studies carried out on Nyegga, have aimed to access the stability of the margin for the safe development of the Ormen Lange field located to the south (e.g. Solheim et al., 2005b). Other number of studies has focused in investigating in detail some of the fluid flow seeps in the seafloor. In one of these studies, Hovland et al., (2005) investigated a set of complex pockmarks consisting of a mixture of craters and carbonate ridges. Using Remote operated vehicles (ROVs) equipped with seismic, bathymetric and sampling capabilities, they were able to make detailed mapping and collect samples of the seafloor at these vent sites. Their results showed the presence of a distinct fauna with, for example, local bacterial mats and small tubeworms, giving evidence of active fluid flow. The sediment samples had light hydrocarbon gases (C1-C5) with carbon isotopic delta values ($\delta^{13}C$) ranging from -54 ‰ to 69 ‰ PDB (Vienna Pedee Belemnite), suggesting the presence of both bacterial and thermogenic gases. While carbonate samples had $\delta^{13}C$ between -52 ‰ to -58 ‰ PDB which suggests precipitation within the sediments of methane derived carbonate. During the study only micro-seepage was observed, that means no visual fluid flow could be seen. But to account for the scattered distribution of carbonate slabs and debris inside the pockmarks, the authors concluded that the formation of the pockmarks was through one catastrophic event, after which only micro-seepage occurred. In a different study Mazzini et al., (2005) sampled carbonate crusts, nodules and chemoherms from different pockmarks and mounds in Nyegga. The results obtained from the petrographical and geochemical studies of the samples showed similar results as those of Hovland et al., (2005) with distinct depletion in δ^{13} (-31,6 ‰ < δ^{13} < -52 ‰) suggesting methane as a primary source for the carbonate carbon. In the complex pockmark named G11 (Hovland et al., 2005; Hovland and Svensen, 2006; Mazzini et al., 2006), the existence of gas hydrates within near surface sediments has been proven by sediment core sampling (Ivanov et al., 2007).

Petroleum industry acquired 3D seismic surveys of the Nyegga became available to the University of Tromsø for their research at the Department of Geology. At the same time, new cost effective 3D seismic survey methods were being developed by IFREMER in France (e.g. Thomas et al., 2004), and by a joint effort of the University of Tromsø, VBPR and Fugro (Oslo), and National Oceanographic Centre (Southampton,UK). In the first joint academia 3D seismic investigation concentrated on Nyegga, Hustoft et al. (2007) used the IFREMER acquired very high resolution (6x6m bins and 80Hz dominant frequency) data to study hydrofracturing and fluid flow processes.. They identified clusters of acoustic chimneys that originate at potentially over pressured sediment layers. Another study concentrating on p- and s-wave acoustic tomography of chimneys G11 and CNO3 in Nyegga is presently carried out in cooperation with IFREMER, National Oceanographic Centre and University of Birmingham (Plaza-Faverola et al., 2008; Westbrook et al., 2008). The data aquired uses a surface-towed seismic source and seabed recorders consisting of 4 component ocean bottom seismometers (OBS) arrays.

The history of studies in Nyegga demonstrates that there is a large interest in elucidating the development of fluid flow and its expressions. But despite the interest and the shown scientific advances, the complexities inherent of studying fluid flow in the marine environments are still unsolved, and many questions about the development of the fluid flow in Nyegga remain unanswered. It would be interesting to know, for example, what is differentiating pockmarks and mounds besides the trivial topographical difference. What is controlling their location at the sea floor? And are the fluids produced within the area or are they coming from the neighboring basins?

In the present master theses I will try to answer these questions using 3D seismic and swath bathymetry data. The methods applied are first mapping pockmarks as well as mounds from the swath bathymetry, and second quantifying their shape. In a next step, 3D seismic will be used to map and quantify acoustic chimneys and interpret the subsurface structure and stratigraphy. Finally, the data are used for carrying out a spatial and statistical analysis, from which the origin and migration pathways for fluids are inferred.

1. 2. Nature and origin of fluid flow

Fluid flow is a long-term and complex geological process. It is part of a system where fluid generation, migration, accumulation and seabed seepage all may occur at different times. Therefore, to understand fluid flow processes in the sea bed, it is important to determine and to understand the coupling of the various parts in the geological fluid flow system.

1.2.1. Importance of sediment compaction and transformation for fluids

Fluids are an inherent part of sediments and rocks. They are generally present in the sediments from their deposition to their very deepest burial depth, though being gradually reduced by compaction processes.

Compaction is the most important cause of fluid expulsion in sediments. It is an irreversible process which starts early after burial and continues through the burial history of the sediments. The main fluid produced by compaction is interstitial water, but hydrocarbons can also be expelled. Highly permeable coarse grained sediments are normally easily compacted, while thick fine grained deposits like muds and oozes are particularly susceptible to under-compaction (Bjørlykke, 2006). In these cases interstitial water cannot escape regularly as burial continues, giving rise to abnormally high porosities and internal pressures. These high pressures seem to develop very early after burial (< 1km) (Cartwright and Dewhurst, 1998). The resultant over-pressured shale formations are sometimes deformed by a series of faults and folds, called polygonal fault systems (Cartwright and Dewhurst, 1998; Cartwright et al., 2003). And in some cases the high pressured shales can deform into diapirs, and also migrate vertically to produce mud volcanoes at the surface. The latter process has been documented in the Vøring basin (Hansen et al., 2005). A late stage compaction occurs when temperatures are between 60 and 150^{o}C. At these temperatures, the sediments are generally in an advanced degree of compaction where the bulk of the insterstitial water has already been mechanically expelled (~ 88% at 500m and ~ 98% at 2500m) (Perrodon, 1983). Compaction then continues through the temperature induced chemical transformation of certain minerals, like smectite, kaolinite, and silica/quartz (Bjørkum and Nadeau, 1998). The two former minerals are transformed into illite which has a fibrous pervasive growth habit in the pores (Nadeau et al., 2005). This implies in the division of the pore spaces and reduction of the permeability, which in turn lends the rock prone to overpressure and fluid expulsion through hydraulic fracturing. While the dissolution of silica followed by diffusion of the dissolved products and precipitation in the pore spaces, leads to a strong porosity reduction, and therefore also fluid expulsion.

Fluids in sediments can also be genetically related to transformation of organic matter, where sediments contain appreciable amounts of it. Organic material is result of biologic production and is deposited together with the sediments. The organic matter is gradually transformed as the sediments are buried, and in this process part of it is released as fluids in the sediments. This transformation is subject to biological, chemical and thermal changes, and can be simplistically described in the following way (Perrodon, 1983; Selley, 1998) (figure 6). The first stage of transformation is called diagenesis and occurs in low temperature (below 50 ^{o}C). Here where oxygen is present, bacterial oxidation of the organic matter is fast and effective, leading to remineralization of the organic matter and production of CO_2 and H_2O. Eventually the oxygen which is coming from the seawater is depleted, and organic matter is remineralized by sulphate reducing bacteria and when sulphate is depleted, methanogenesis (methane production) by anaerobic archaea bacteria takes place. Above the threshold of 50 ^oC, the remaining unoxidized organic matter is subject to a process called catagenesis, in which the organic matter is thermo-chemically broken into smaller constituents. The result of this process is dependent on the nature of the organic matter, and could be oil, wet gas (ethane, propane, butane and pentane), dry gas (methane) or coal. The continued burial of these products to depths where temperatures are over 200 ^oC will lead to metagenesis, which means they are transformed into methane and anthracite. The depths at which these processes take place are highly variable since they depend on the geothermal gradient of the depositional basin.

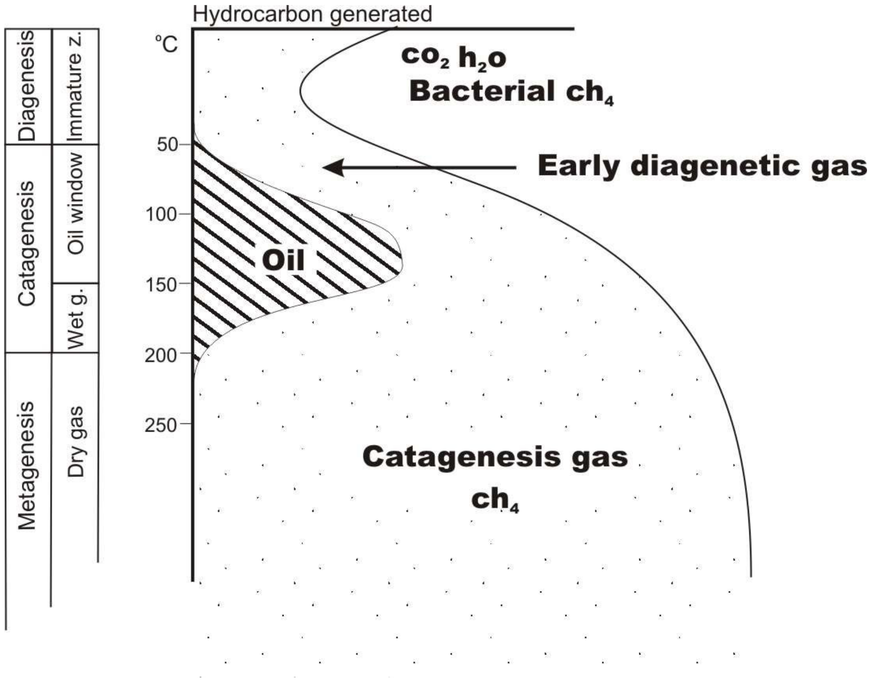

Figure 6 – General scheme for hydrocarbon generation versus temperature.

Fluids are also present in volcanic rocks. The presence of gas in magma is evidenced by gas bubbles and vesicules in cooled and solidified magma. The most common gases in magma are in order of abundance: CO_2, H_2O, CO, SO_2, S_2 and H_2S. Other less common are nitrogen and methane. These gases are expelled to the surface along volcanic margins and spreading ridges. And where magma intrude in sedimentary basins, these fluids can contribute, together with the heated sediments porewater, to hydrothermal activity leading to fluid venting at the seafloor (Svensen et al., 2003). Records of such processes are described by Svensen et al., (2003) for the Vøring Basin during the late Paleocene/early Eocene thermal maximum.

Except for upper oxic and sulphate rich sediments, all other above mentioned processes show methane as a byproduct. It turns out that methane gas is the most common hydrocarbon in marine sediments. This has been proven by numerous examples of geochemical surveys and Ocean Drilling project (ODP) results (Judd and Hovland, 2007). Since most of the fluid flow seeps on the seafloor are expelling mainly methane rich fluids, and the fact that methane can be produced at almost any stage makes the nature and origin of the fluids difficult to trace. Discriminating between sources is not always possible, but there are some measurements, which can help to decipher the methane source. The most popular tool used for this discrimination is the stable isotope analysis (Stahl et al., 1981). The carbon isotopic composition of bacterial methane ranges from -55 to -85 ‰. Methane in thermogenic gases has isotope values heavier (i.e., more positive) than -55 ‰; oil-associated gases have methane carbon isotopic values of -55 to -40 ‰, while methane in catagenesis and metagenesis dry gas tends to have values in the -30's ‰.

1.2.2. Fluid migration pathways

The fluids that end up in the effective porosity of sediments and rocks are relatively free to migrate. Two stages of migration are defined in petroleum geology. The migration of the fluids out of the sediments where they are generated is called primary migration. The primary migration occurs concomitantly with fluid generation and involves hydrofracturing and vertical migration (Bjørkum and Nadeau, 1998; Aydin, 2000). The secondary migration is the process by which fluids accumulate and migrate along porous and permeable pathways. Both migration stages obey essentially to the same physical dynamics. That is, in order to migrate fluids need a driving mechanism. The driving mechanism is generally a combination of buoyancy and hydrodynamism (Perrodon, 1983; Selley, 1998; Judd and Hovland, 2007). The migration pathway is usually classified as lateral if the fluids migrate along the stratigraphy and vertical if the fluids migrate across it. The former involves the presence of continuous permeable beds overlain by low permeability sealing sediments (Hindle, 1997). While the latter involves high capillary entry pressures or some sort of seal bypass system (SBS), such as for example, faults and fractures (Cartwright et al., 2007).

1.2.3. Fluid Flow dynamics

Fluids in sediments can be present in liquid and/or gaseous phases. Within the liquids we can find both oil and water which are immiscible, while the natural gases can be dissolved in the liquids or present in gaseous phase. Oil and gas can migrate relatively independent of the aquifer due to their buoyancy, since they are less dense than water. The buoyancy increases with increasing density difference between the fluids, which makes buoyancy stronger for natural gas in the gaseous phase than for oil, due to the higher density contrast between water and gas.

It is widely accepted that fluids flow from higher pressure zones toward lower pressure zones. Migration of oil and gas is thus also conditioned by hydrodynamics, which controls the slow movement of the aquifer. The hydrodynamic gradient facilitates or works against seepage, according to whether they oppose or enhance buoyancy. Hydrodynamics is more important for fluids which have densities in the same order as water, and less important for gas migration. On the other hand, dissolution in water is particularly important factor in methane migration, as the solubility of methane rises rapidly with increase in pressure. At great depths, large quantities of gaseous hydrocarbons may accumulate in aquifers (Perrodon, 1983). Part of this gas may be released if the aquifer undergoes rapid pressure drop. At shallow depths (< 1500 m) methane could also migrate easily in solution in the water and could be released at the seabed (Berndt, 2005).

Buoyancy and hydrodynamics are in turn opposed by capillary forces. This force, which is the essential feature of the impermeability of fine-grained rocks, is the resistance, due to the interfacial tension, of a fluid droplet to the deformation that is necessary for it to be able to pass through the pore throats of sediments. The smaller the throat the stronger this force is. Variations in the capillary resistance along and across strata thus control the permeability of the fluid flow pathways.

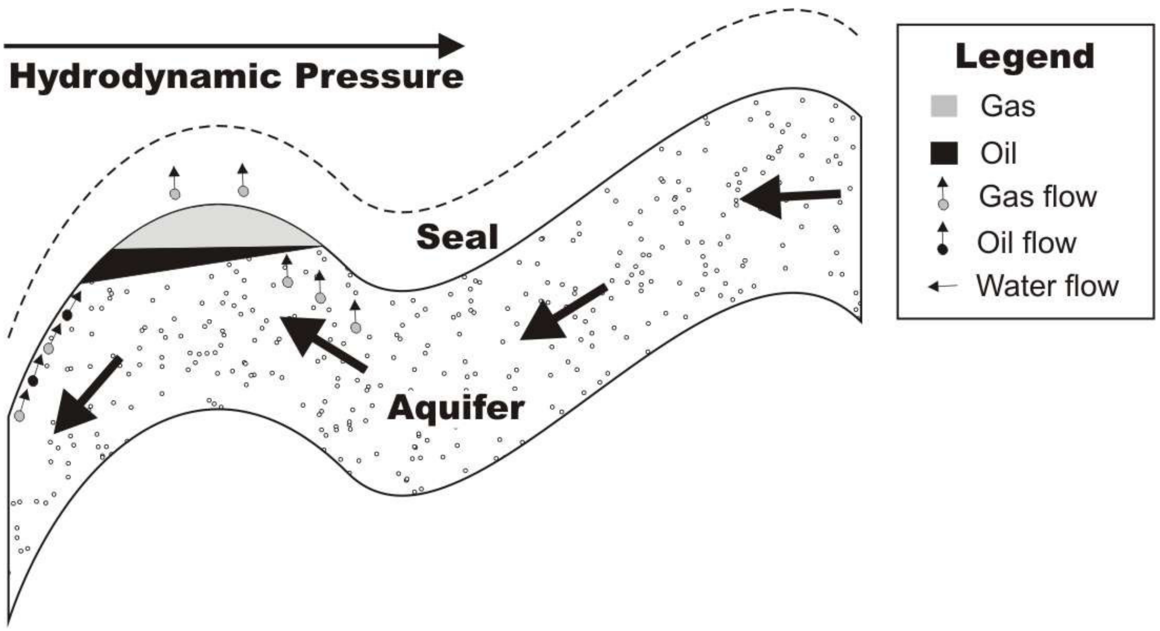

Figure 7 – Conceptual illustration of fluid flow dynamics, aquifer movement is controlled by the pressure potential field, while buoyancy pushes oil and gas updip.

1.2.4. Modes of fluid migration and accumulation

Fluids may laterally flow at the top of continuous permeable beds, in contact with the impermeable seals. These carrier beds and the lateral migrations they allow are important for the concentrations of fluids, especially hydrocarbons, at the top or on the flanks of high regional zones. In stable margins, lateral migrations are able to continue over long distances, ranging from 10 to >100 km. Hydrocarbon migration pathways within carrier beds are determined by the three-dimensional geometry of the top boundary of bed, along which fluids migrate by taking the structurally most advantageous routes (Hindle, 1997). For buoyancy driven hydrocarbons, that means migrating updip along directions perpendicular to the strike of the top boundary (England et al., 1987). Discontinuities such as sealing faults or pinch-outs may create a permeability barrier, in which case hydrocarbons might accumulate and be trapped downdip of this seal. Otherwise hydrocarbons will accumulate at structural crest traps, and if the sourcing of hydrocarbons continues at a rate that surpasses any eventual leakeage, fluids will eventually fill the trap. Excessive fluids could then spill and continue migrating updip by taking other paths within the carrier bed until arriving at other traps.

Vertical migration called seepage occurs across stratified sediments, including very low permeability sealing sediments (figure 8). Given the high capillary resistance of sealing sediments, this migration mode is restricted to areas where fluids have built high capillary entry pressure, or to where heterogeneities on the sealing sediments make for more permeable pathways for fluid migration. Typical areas of focused overpressure are at structural crests and at updip limits of aquifers, at these parts fluids are trapped and may be susceptible to pressure build up. Lithological and structural heterogeneities in the sealing sediments are also important in the context of vertical migration, since it is natural for fluids to be drained through the most permeable part of the seal.

A different scenario for vertical migration is when large scale geological features promote bypass of the pore network. Some of these features have only recently been described with the advent of 3D seismic data. Cartwright et al. (2007) based on 3D seismic interpretation, recognizes three main groups of seal bypass systems: (1) fault related, (2) intrusion related, (3) pipe related.

Faults are known to have an ambiguous role when it comes to fluid flow, since they can be both sealing and trap defining or focused vertical fluid migration pathway (Aydin, 2000). A difficulty then appears when trying to identify which faults are acting as a seal and which faults act as fluid flow pathways. There is also the possibility of faults being transient fluid flow pathways, that is, the role of fluid flow pathway is restricted to periods of active fault slip. As one major example of fault related vertical fluid migration, polygonal fault systems have been indirectly linked as the main conduits to gas leakage in many parts of the Mid Norwegian margin (e.g. Berndt et al., 2003; Hustoft et al., 2007), while at the same time the ultra low permeability sediments which host these faults overlie many prolific reservoirs in the same area (Stuevold et al., 2003). Another way fluids migrate vertically is by creating their own permeability through hydrofracturing the sealing sequence (Hustoft et al., 2007). Hydraulic fractures develop when pore pressures are sufficiently high to cause mechanical fracture of the sealing sediments. This fracturing opens a permeable pathway through the sealing sequence, allowing fluid migration.

Intrusive structures allow fluids to flow through by breaching the integrity of the sealing sequence. Within intrusive bypass structures we find sandstone intrusions, igneous intrusions, mud diapirs and diatremes, and salt diapirs.

Sandstone instrusions are newly recognized geological phenomena, by which high pressured sandstones are liquefied and emplaced as sills and dikes in low permeability sequences (Huuse and Mickelson, 2004). Sandstone intrusions affect fluid flow through inserting several meters wide permeable conduits through a sequence with low permeability (Cartwright et al., 2007). Igneous intrusions, in contrast, have generally lower permeability than the seals they intrude, but in turn cause intense fracturing associated with their forceful intrusion, hydrothermal linked metamorphism and subsequent thermal contraction (Cartwright et al., 2007). These fractures provide permeability for fluid flow around the intrusion, potentially allowing the bypass of the sealing sequence (e.g. Svensen et al., 2003).

Mud diapirs and diatremes and associated mud volcanoes, are characterized by episodic mud intrusions and extrusions and are known to cross impermeable sediments. Mud volcanoes in the Vøring basin, are found to cross 1 km of otherwise intact sealing sequences (Hansen et al., 2005). Mud diapirs or mud volcano conduits which pierce hydrocarbon accumulations are normally associated with leakage of hydrocarbons at the surface, above or surrounding the mud intrusion (e.g. Planke et al., 2003).

Salt diapirs influence fluid flow through the development of fractures and faults associated with the piercement of sealing sequences by the episodic salt movement. These faults and fractures develop mainly at the crest of the diaper and are often associated with amplitude anomalies around them and presence of fluid flow expressions on the seabed above them (e.g. Egeberg, 2000; Chand et al., 2008).

Cartwright et al., (2007) described pipes that appear in seismic data as vertical or near vertical columnar zones of disturbed reflections, sometimes associated with stacked amplitude anomalies (e.g. Berndt, 2005). These characteristics make them very similar to seismic artifacts, such as migration anomalies and lateral velocity anomalies. "*True pipes are known to emanate from* *crestal regions, tilted fault block crests, fold crests, or crests of sand bodies with positive topography, or any other focusing element at depth*" (Cartwright et al., 2007). The detailed geologic structure of the pipes is poorly understood, and could be highly variable (Cartwright et al., 2007). Some pipes appear to consist of stacked pockmarks or stacked amplitude anomalies related to gas accumulation, while other pipes appear to consist of near circular zones of sediments deformed by minor folding and fracturing. By analogy to published descriptions of breccia pipes discovered in outcrops or in mines, pipes seen on seismic are likely to consist of brecciated seal facies with zones of intense fracturing and intruded by material transported along the conduit (e.g. Gernon et al., 2007). According to Cartwright et al., (2007), there are four families of pipes: Dissolution pipes, which are associated to dissolution of salt at depth and concomitant collapse of sediments above; Hydrothermal pipes, associated with igneous intrusions; Blowout pipes, associated with overpressured reservoirs at depth and which terminate in seafloor fluid expulsion; and Seepage pipes, which are similar to blowout pipes but are not associated with seafloor fluid flow expressions. Of particular relevance to this study are the blowout pipes and seepage pipes, both of which have been observed and described from seismic data in the study area by many authors (Mienert et al., 1998b; Bouriak et al., 2000; Buenz et al., 2003; Berndt, 2005; Hustoft et al., 2007).

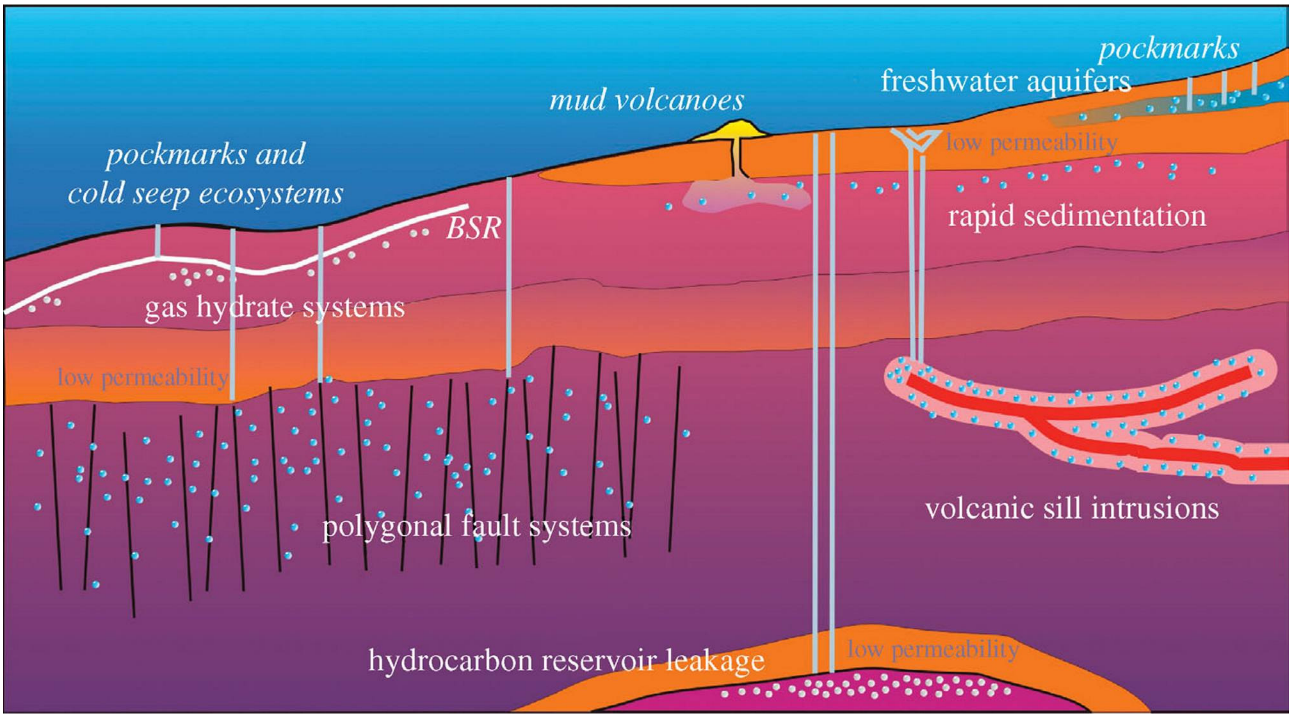

Figure 8 - Sketch showing different fluid flow systems discussed in the text (from Berndt, 2005).

2. Geology of the Nyegga study area

2.1. Regional geology

The Nyegga area is located at the Mid-Norwegian margin, which comprises the stretch between 62°N and 68°N of the Norwegian continental margin. The Mid-Norwegian margin is characterized by the NE-SW-trending Vøring and Møre basins. The flanks of the basins are the Vøring and Møre marginal highs to the west and the Trøndelag Platform/Norwegian mainland to the east (figure 9; figure 10). The Jan Mayen Fracture Zone and its landward continuation, the Jan Mayen Lineament, separate the Vøring and Møre margins. The present structure of the margin reflects the effect of a multiphase rifting event that controlled the basin development, where also large scale volcanism, uplift and inversion doming events took place.

2.1.1. Tectonic evolution

Three major rifting events occurred: the Permian/Triassic, Late Jurassic/Early Cretaceous and Late Cretaceous/early Tertiary and the locus of rifting migrated westward with time (Bukovics and Ziegler, 1985; Brekke, 2000). During the first major rifting phase, horsts and grabens were formed in the area where now lies the Trøndelag Platform. These major faults, which were also active through much of the Triassic, gave rise to several en echelons NE-SW trending basins filled with Triassic and Upper Paleozoic sediments, one example of such basins is the Froan basin (Figure 9). More to the west, the Late Jurassic rifting is characterized by the rotated blocks of the Halten Terrace and the development of small basins over listric normal faults, in the Møre and Vøring basins. During the Cretaceous maximum subsidence occurred in the NE-SW trending Vøring and Møre Basins (Brekke, 2000). Late Cretaceous arrival of the Iceland mantle plume culminated in the continental break-up in latest Paleocene–earliest Eocene time (Skogseid et al., 2000), where volcanism accompanied continental break-up. An elevated, sub-aerial spreading axis that existed in late Paleocene time (Skogseid et al., 2000) extruded extensive flood basalts in the early Eocene as break-up occurred (Eldholm et al., 1989). These lavas built the Vøring and Møre marginal highs, and spilled over into the basins to the east. Following break-up, the Vøring and Møre margins underwent rapid thermal subsidence (Bukovics and Ziegler, 1985).

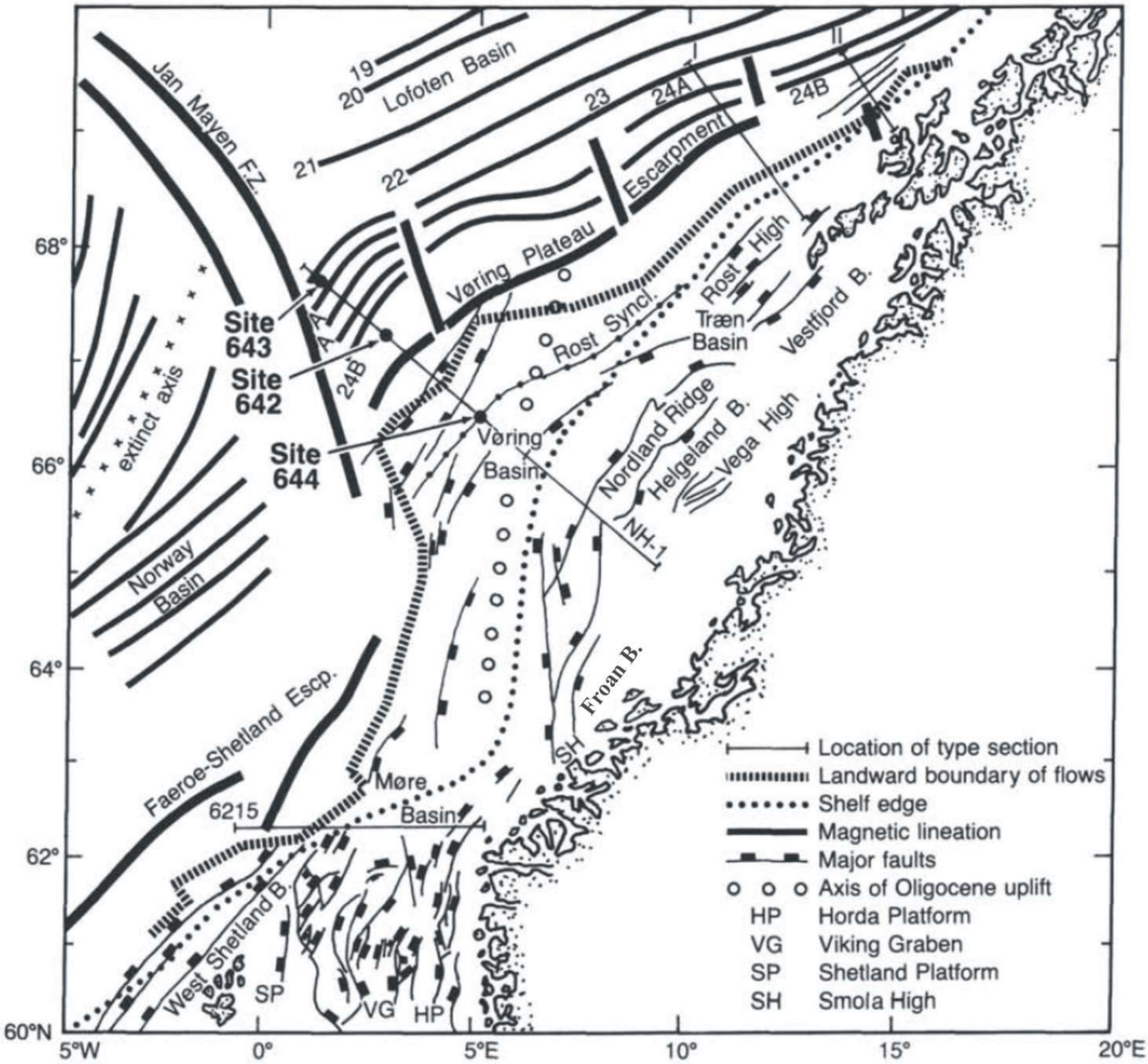

Figure 9 - Main regional features of the Mid-Norwegian continental margin (from Eldholm et al., 1989).

N-S trending inversion domes and arches such as the Ormen Lange dome and the Helland Hansen arch developed in the Mid-Norwegian margin (Doré and Lundin, 1996; Vågnes et al., 1998; Lundin and Doré, 2002). Different explanations about their origin exist. For example, Doré and Lundin (2002) suggest that a change in plate motion during the Eocene-Oligocene boundary which led to Greenland moving to the W-NW of Norway triggered the doming, while Kjeldstad, et al. (2003) show results suggesting that the formation of the Helland Hansen arch is genetically linked to differential sedimentary loading and thermal subsidence which occurred during the last 3 to 2 million years. These domes constitute potential structural traps for hydrocarbons in proven petroleum plays on the Mid-Norwegian margin, as for example the Ormen Lange gas reservoir (Doré and Lundin, 1996; Brekke, 2000; Kjeldstad et al., 2003).

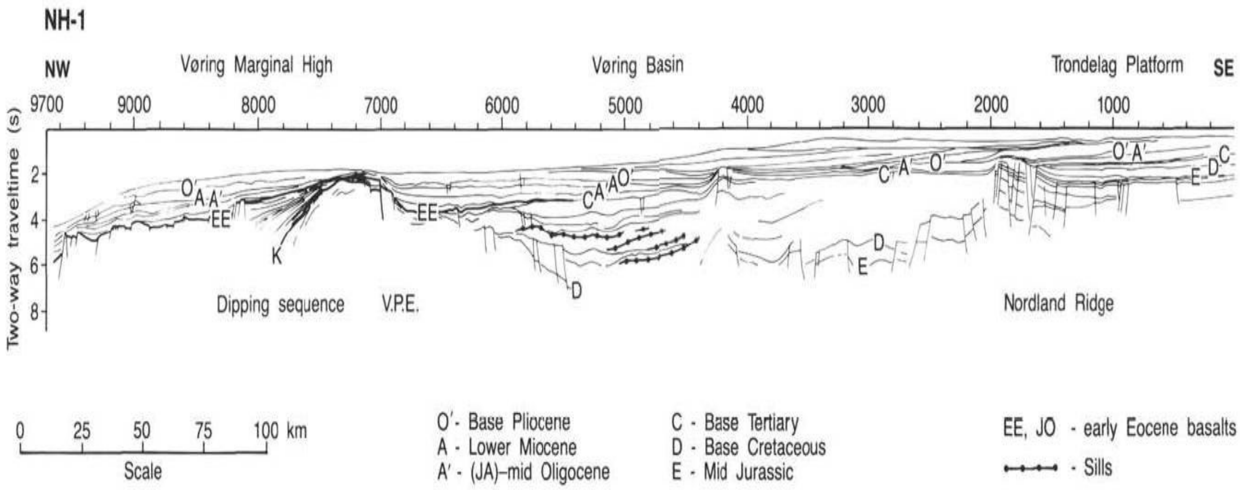

Figure 10 - Interpreted seismic section across the Vøring margin, showing the main geological provinces and structural elements (Eldholm et al., 1989). See figure 9 for location.

2.1.2. Stratigraphy and sedimentary processes

During the Cretaceous sedimentation was restricted to the subsiding Møre and Vøring basin, where approximately 9-13 km thick sequences were deposited (Brekke, 2000; Skogseid et al., 2000). Exploration wells in the Vøring margin show mainly clay and silt with sand sheets (Hjelstuen et al., 1999), with sediments coming from the west and east (Brekke, 2000). In the Møre basin, the upper Cretaceous sediments consist of bioturbated mudstones and sandy turbidites (Gjelberg et al., 2001). During the Paleocene, the erosion of the exposed Vøring Marginal High and Intra basinal fault blocks led to deposition of a thick prograding fan of muddy and sandy mass flow deposits (Hjelstuen et al., 1999). These sediments thin out to the east and appear to be absent over highs (Figure 10). The Møre basin shows Paleogene sediments that are thickest at its eastern flank (Brekke, 2000; Gjelberg et al., 2001). Overlying the Cretaceous and Paleocene mega sequences are the Eocene-Oligocene mega sequences that are part of the Brygge Formation (Dalland et al., 1988). In the Vøring basin these deposits are fine grained sediments throughout the whole Eocene, consisting mainly of clay. However, in the Møre basin sandstones are present (Gjelberg et al., 2001). The absence of Eocene sediments over domes and ridges indicates that these features remained important source areas, in addition to the marginal highs. The Oligocene sediments are thickest south of the Helland-Hansen Arch, and along the SW edge of the Vøring Basin, but are also thin or absent over structural highs (Hjelstuen et al., 1999). During earliest Oligocene, sea level fall, tectonic uplift and subsequent erosion, led to formation of deltas and shelf margin progradation (Henriksen and Vorren, 1996; Hjelstuen et al., 1999; Gjelberg et al., 2001). The Norwegian mainland and present inner continental shelf were important source areas, as evidenced by the deltaic pebbly sands preserved on the Trøndelag Platform (Henriksen and Vorren, 1996).

The Neogene stratigraphy in the Mid-Norwegian margin consist of two unconformity bounded units, the Miocene to Lower Pliocene Kai Formation and the Late Pliocene to recent Naust Formation (Dalland et al., 1988). The Kai formation, also named lower Neogene series, is characterized during the middle and lower Miocene by deepwater hemipelagic siliceous mud and ooze and during the upper Miocene–lower/upper Pliocene by siliceous/nannofossil mud and siliceous and calcareous ooze (Eldholm et al., 1987). Data from ODP site 643, over the Vøring Marginal High suggest that the Miocene–middle Pliocene succession in the area is characterized by shifts between intervals of high biogenic opal and carbonate deposition (Eldholm et al., 1987). Samples of the Kai formation sediments south of the Vøring Plateau show very high water content (70-80%) and low unit weight (14-15 kN/m^3) (Bryn et al., 2005b).

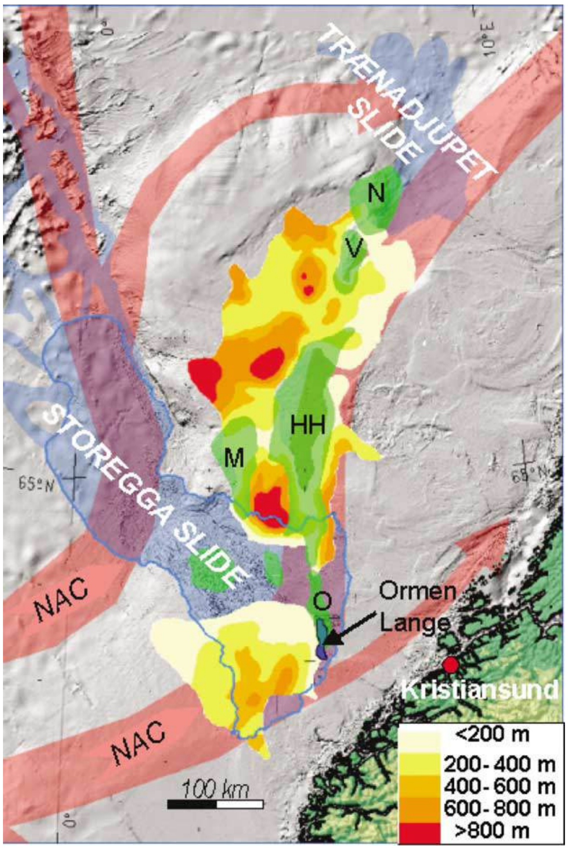

Figure 11 - Thickness map of the Kai Formation showing the contouritic drift depocenters. In the Vøring Plateau the drifts are found along the western slopes of the main domes (green) indicating that these topgraphic highs influenced the current path. NAC, Norwegian Atlantic Current (from Bryn et al., 2005b). N, Naglfar Dome; V, Vema Dome; HH, Helland Hansen Arch; M, Modgunn Arch; O, Ormen Lange.

The sedimentation and distribution of the Kai formation is partly controlled by deepwater hemipelagic deposition, erosion and reworking by contour currents (Figure 11). This resulted in large thickness variability and in discrete depocenters, which reflect the influence of the interaction between the bathymetry and the oceanic currents, and sediment availability. From the Base Kai Unconformity (BKU) up to the Mid-Miocene the Kai formation developed mainly in the form of deepwater hemipelagic deposition of biogenic sediments. Increased oceanic circulation after the Mid-Miocene marks the onset of the contour currents and the rework of the sedimentation. In seismic sections this change of sedimentation style is marked by the Intra-Miocene unconformity (figure 12). The first large contourite drifts formed during this period, and were deposited preferentially west of the Tertiary domes where they formed more than 600 m thick deposits (Evans et al., 2002; Bryn et al., 2005b; Stoker et al., 2005a; Stoker et al., 2005b) (figure 11; figure 12). This alongslope sedimentation continued throughout the late Miocene and early Pliocene. For the aim of the thesis is the sediment of the Brygge and Kai formation of special importance since they are the host of numerous networks of polygonal faults (Hjelstuen et al., 1997; Berndt et al., 2003). These faults are inferred to have been developed early after burial, and to be associated with long term episodic fluid expulsion and contraction of the hemipelagic sediments (Berndt et al., 2003; Gay et al., 2006a; Hustoft et al., 2007). During early late Neogene (late early Pliocene) a regional erosional unconformity, named Base Naust Unconformity (BNU), developed in the Mid Norwegian Margin. The BNU has been inferred to reflect the combination of the tectonic modification of the bathymetry and the increased velocity of the southward moving bottom currents due to the strengthening of the Norwegian Sea Deep Water (NSDW) formation. These events led to the redistribution of the bottom currents paths along the margin, causing a shift in the areas of submarine erosion and deposition associated with them (Laberg et al., 2005).

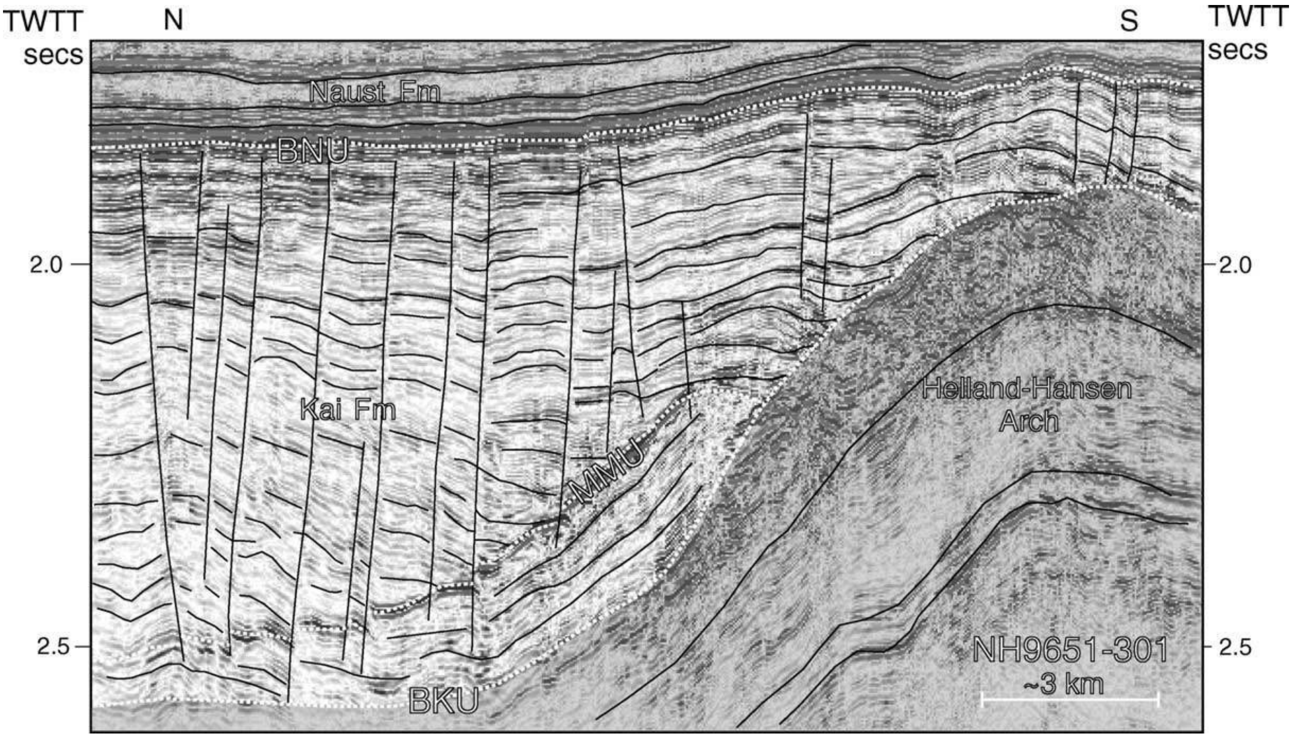

Figure 12 - Seismic profile across the Helland-Hansen Arch, Mid-Norwegian margin, showing its relationship to the Base Kai (BKU) (base of the Neogene) and Mid-Miocene (MMU) (intra-Miocene) unconformities, and associated Miocene sedimentary units (from Stoker et al., 2005a). BNU, Base Naust (intra-early Pliocene) unconformity.

After the depositional break marked by the BNU, the margin started building out in the form of westward advancing prograding wedges. This change in the sedimentation style from along slope deposition to downslope deposition is caused by two major events, the uplift of the margin at early Pliocene (ca. 5.3-3.6 Ma BP) (Poole and Vorren, 1993; Henriksen and Vorren, 1996; Japsen and Chalmers, 2000) and the initiation of the Plio-Pleistocene Northern Atlantic glaciations at the late Pliocene (ca. 2.5 Ma BP) (Berg et al., 2005; Bryn et al., 2005b; Rise et al., 2005; Solheim et al., 2005a). The Naust Formation has been divided into a number of sequences, named Naust W, U, S, R and O in ascending stratigraphic order (figure 13) (Berg et al., 2005). The sediments are mostly of glacial origin, intercalated with glaciomarine, hemipelagic and contouritic deposits.

Horizon	Unit	Sub-unit	Age (Ma)
Seafloor			
	Naust O	O1	0.024-0
INO1			
		O2	
INO2			
		O3	0.13-0.024
INO3			
		O4	0.2-0.13
INO4			
		O5	
INO5			
		O6	
INO6			
		O7	
INO7			
	Naust R	R1	0.38-0.2
INR1			
		R2	
INR2			
		R3	
TNS			
	Naust S	S1	0.7-0.38
INS1			
		S2	
INS2			
		S3	
INS3			
		S4	1.1-0.7
INS4			
		S5	
INS5			
		S6	
TNU			
	Naust U	U1	>1.1
INU1			
		U2	
TNW			
	Naust W		2.6-1.7
BNAUST			
	Kai	E.Mio.-L.Plio.	
BKAI			
	Brygge	Eoc- E.Mioc.	
BBRYGGE			

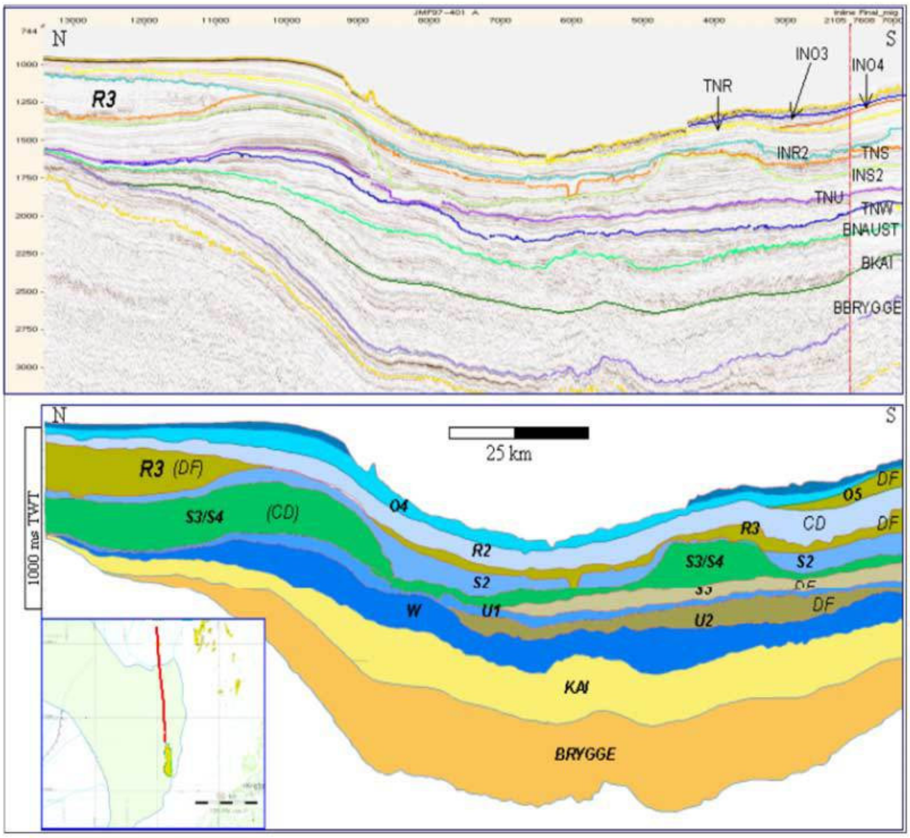

Figure 13 – Left: Seismic stratigraphy of the Mid-Norwegian margin; Top right: Seismic profile over the Nyegga and Storegga areas; Bottom right: Interpretation of seismic profile above (from Berg et al., 2005). CD, contourite drift; DF, debris flow deposit.

Although the initiation of Northern Atlantic glaciations dates to about 2.75 Ma, the first glaciers did not reach the shelf in the Mid-Norwegian margin before 1.1 Ma. Starting at 500 ka the whole margin experienced repeated glacial advance to the shelf at a periodicity of 100 kyrs. During these periods fast flowing ice streams would transfer thick till deposits to the shelf. These till units would build up at the shelf edge eventually being released in the form of debris flows and turbidity currents. The intercalaction of the downslope processes during glacial maximums with along slope sedimentation during interglacial and interstadial periods resulted locally in repeated slope instabilities (Hjelstuen et al., 2004a; Hjelstuen et al., 2004b; Hjelstuen et al., 2005; Mienert et al., 2005b; Solheim et al., 2005a), as exemplified by the recent Storegga (Bugge et al., 1987; Bryn et al., 2005a) and Traenadjupet slides (Laberg et al., 2002) (Figure 11; Figure 13; Figure 14). The Storegga slide is the last of a series of slides that affected the Nyegga region during the last 500 ka years. It is considered the largest exposed submarine slide in the world, having affected an area of 95000 km^2 and displaced 2400-3200 km^3 of sediments (Haflidason et al., 2004; Haflidason et al., 2005) (Figure 5).

The thickest accumulations of the Naust formation in the Mid-Norwegian margin are close to the margin in the Vøring Plateau and in the North Sea Fan, where it reaches thicknesses inferred by seismic in excess of 1600ms TWTT (Figure 14). The thicknesses decrease to the west of the Vøring Plateau and are thinnest over the Vøring Marginal High. This is verified by several wells. In well 6607/5-1, close to the shelf-margin depocentre, the thickness is 1654m, and westward, towards the base of the slope, the distal part of the wedge shows a thickness > 253m in ODP Site 644 (base of unit not reached at this site), decreasing to 65–71m at ODP Sites 642 and 643 on the Vøring Plateau (Eldholm et al., 1989). In the North Sea Fan region, a thickness range from 718m in well 34/8-3A to 1089m in well 34/2-4 (Eidvin and Rundberg, 2001).

The sedimentation history of Nyegga during Oligo-Pliocene has been markedly influenced by the interaction of the bottom currents with the Vøring Plateau, and after the Oligocene doming, with the Helland Hansen arch. During the Plio-Pleistocene, two geologically contrasting provinces formed. In northeast of the area, over and northwest of the Helland Hansen dome, it was sparsely affected by Plio–Pleistocene downslope sedimentation and the drift growth which initiated during the Miocene persisted into the Plio–Pleistocene, such that Naust Formation drifts are built upon Kai Formation drifts. These sheeted drifts are not associated with mass wasting processes. In contrast, North, east and Southeast of the Helland Hansen arch the sedimentation is characterized by intercalation of deposited glacigenic debris flow deposits and sheeted and infilling contourites, being affected by several episodes of slumping and sliding. The presence of glacigenic sediments could be of special relevance to the fluid flow investigation. Buenz et al., (2003), have published results that show that glacigenic till deposits in Nyegga can act as a barrier to upward fluid migration. Contourites are also important in the sense that, due to their homogeneity, continuity and high water content, they could act as shallow fluid reservoirs in the area.

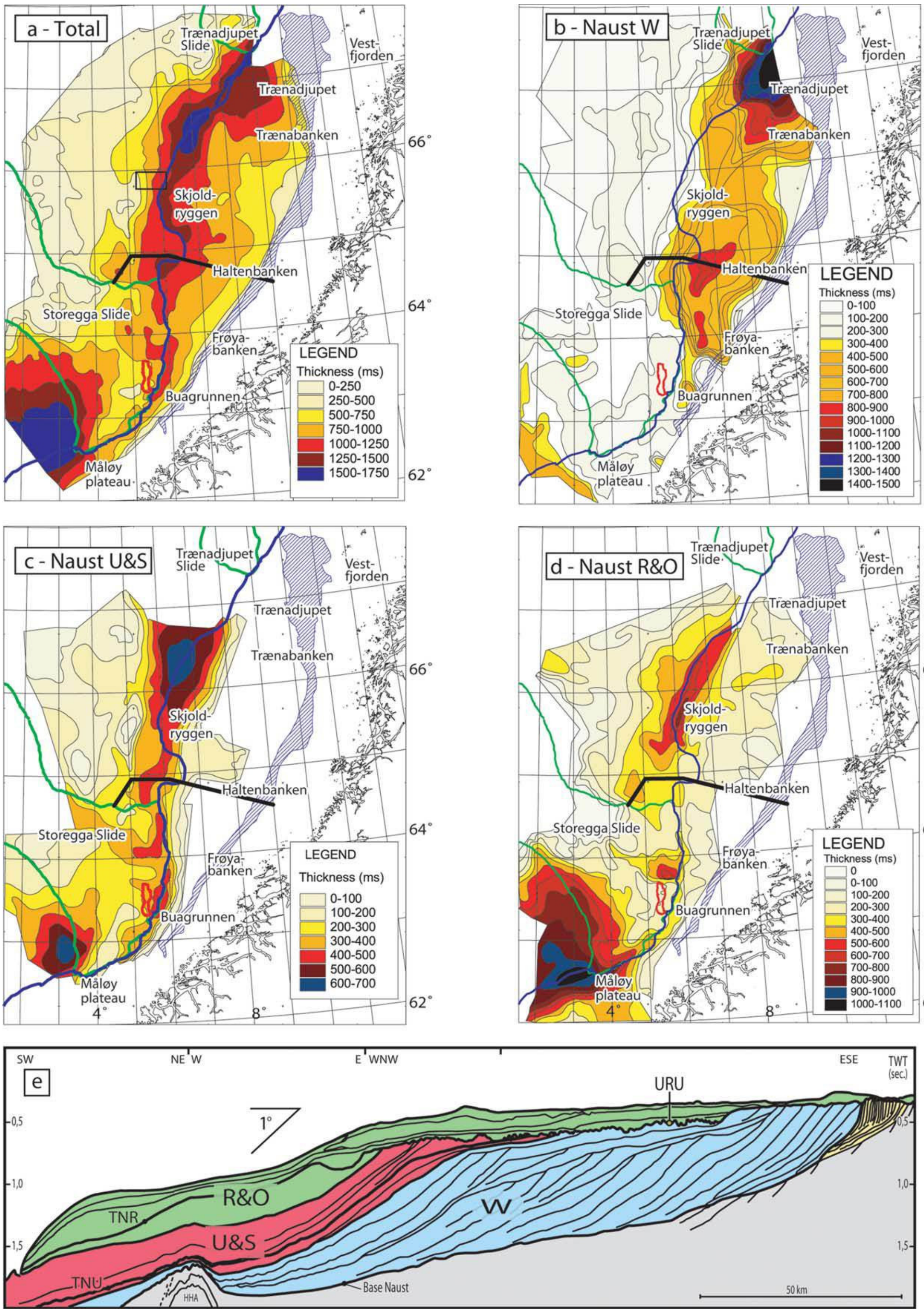

Figure 14 - Time thickness maps (two way travel time; twt) of: (a) Naust Formation; (b) Naust W; (c) Naust U and S; (d) Naust R and O. Note that the sediment thicknesses in the southern area increase towards younger ages. The blue line shows the present-day shelf break. The interpreted seismic line (e) illustrates the shelf to slope development through Naust time, west of the Molo Formation (yellow). URU; Upper regional unconformity (From Rise et al., 2005).

2.2. Gas Hydrates

North of the Storegga slide area the sea floor is very smooth having a mean slope close to 1^o. The average water depth of about 750m together with bottom water temperatures of less than 0^oC (Mienert et al., 2005b) puts the uppermost few hundred meters of sediments in the area within the Gas Hydrate Stability Zone (Kvenholden, 1998). This zone is a thermo dynamic equilibrium zone within which natural gases are expected to be "frozen" in cages formed by molecules of water. These cages are generally named clathrates or in the specific case of water, hydrates, and for this reason the resultant crystals are called gas hydrates (Sloan, 1998). This has important implications for the characteristics of the sediments with respect to their ability to allow shallow migration of hydrocarbon rich fluids. Once formed, gas hydrates have a crystalline non-flowing nature, such that their presence in the pore spaces of sediments decreases the permeability of the last ones to gases and liquids (Kvenholden, 1998). Furthermore, those fluids that eventually penetrate the gas hydrate stability zone are themselves susceptible of freezing into gas hydrates.

Gas hydrates have been, until recently, inferred to exist within the area mainly through the widespread presence of Bottom Simulating Reflections (BSR), which are related to the acoustic impedance contrast between hydrated and non hydrated sediments. The BSR is also sometimes accompanied by enhanced reflections shown to be associated to the trapping of free gas below the impermeable GHSZ (e.g. Bünz et al., 2003; Berndt et al., 2004; Bünz and Mienert, 2004; Mienert et al., 2005a). It renders its name from the observation that it often mimics the seafloor reflection. This is due to the fact that the GHSZ is primarily temperature controlled, with its lower limit depth being determined by the geothermal gradient which is generally constant over small to medium areas.

Large efforts have been made to study the distribution of the BSR in the area (Mienert et al., 1998a; Bouriak et al., 2000; Buenz et al., 2003; Bünz and Mienert, 2004). Bouriak et al., (2000) observed the presence of the BSR within the slide scar deposits, indicating that the GHSZ is in equilibrium with the present seafloor. Bunz et al., (2003) mapped the extent of the BSR in part of the Mid-Norwegian margin, the regional distribution of which is shown in figure 15. These authors observed that the BSR is distally bounded by its intersection with sediments of the Kai formation which they conclude to be devoid of hydrates. To the north it is bounded by the presence of glaciogenic till deposits which inhibit fluid flow to the GHSZ, while to the east, temperatures along the shelf are too high for hydrates to be stable. More recently shallow gas hydrate samples were recovered in cores retrieved within the study area (Ivanov et al., 2007), giving the necessary ground truth that was lacking from the BSR inference of gas hydrates.

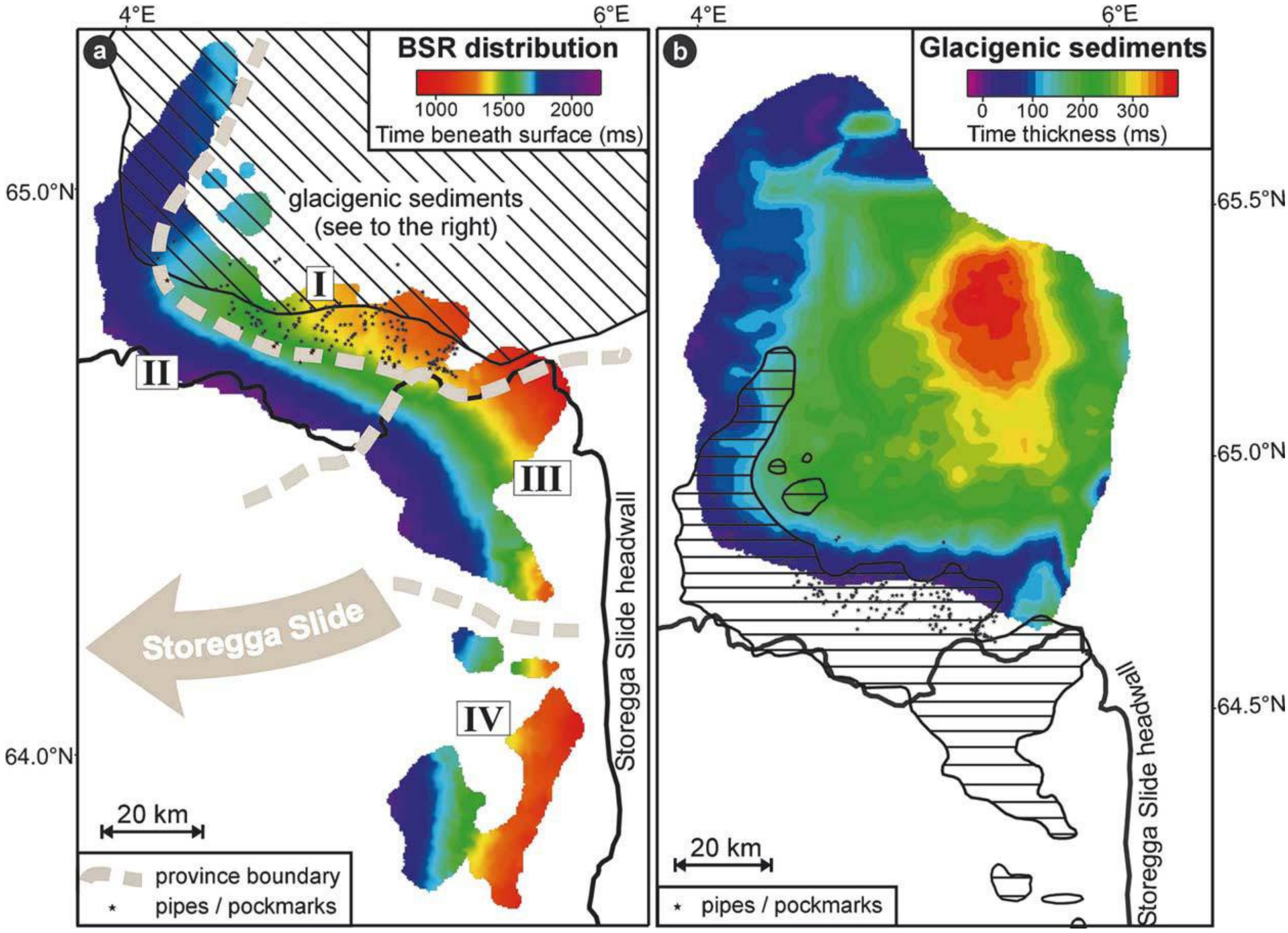

Figure 15 – (a) Distribution of the BSR on the mid-Norwegian margin and (b) time thickness map of the glacigenic debris flow deposits.

2.3. Regional Oceanography

Prior to the Cenozoic, the Norwegian margin was part of an epicontinental sea between Eurasia and Greenland (Myhre et al., 1992). The opening of the Norwegian-Greenland Sea created a potential gateway for the exchange of surface and deep waters between the Arctic and NE Atlantic oceans. In the earliest Eocene, surface-water interaction in the Norwegian-Greenland Sea was restricted to small basins due to widespread extrusion of lavas and syn-rift uplift. Mid- to late Eocene subsidence transformed the region into a deeper ocean basin. During this time regional surface-water interaction may have existed, but deep-water exchange was minimal (Eldholm and Thomas, 1993). It was probably not until the mid-Miocene that a pervasive, interconnected, Arctic–North Atlantic thermohaline circulation system became fully established through both the Northern (Fram Strait) and Southern (Faroe Conduit) Oceanic gateways (Eldholm and Thomas, 1993; Stoker et al., 2005b).

Presently, this surface circulation system consists of warm and saline Atlantic water moving northwards as the Norwegian Atlantic Current (NAC), which cools to the north and sinks to form Norwegian Sea Deep Water (NSDW). The southerly return flow of NSDW is exported into the Atlantic Ocean via deep-water passageways, such as the Denmark Strait and the Faroe-Shetland channel (Faroe Conduit) (Bryn et al., 2005b; Laberg et al., 2005). Adjacent to the Mid-Norwegian margin, the NAC is made of two northward-flowing branches (Orvik and Niiler, 2002; Bryn et al., 2005b) (figure 16a). The eastern branch passes through the Faroe–Shetland region and over the upper part of the Storegga Slide area, continuing northwards over the Vøring plateau. The western branch is across the Greenland Scotland Ridge, between Iceland and the Faroe Islands, and follows the continental slope north of the Faroe Islands into the Storegga area, above the lower escarpments of the Storegga Slide, continuing northwards along the outer part of the Vøring Plateau. The NAC dominates the upper water column down to the strong thermocline which fluctuates between a water depth of 500–700 m, where the water temperature drops from 5–6 to less than 0 ^{o}C (Mienert et al., 2005b). The thermocline represents the transition to the water mass known as Norwegian Sea Arctic Intermediate Water (NSAIW). The NAC is subject to significant variability due to atmospheric forcing. This is reflected in a wider range including a higher maximum value (above 1 m/s) of the current speed as well as less directional stability than the underlying NSAIW. The flow direction of the NSAIW is aligned with the large-scale bottom topography and the average current speed is measured to 0.5–0.6 m/s (Figure 16b). The seabed topography strongly affects the local current pattern as current speed intensifies with an increase in steepness of the slope as well as where the seabed topography is rough. This may lead to local strong bottom currents, capable of entraining sand sized particles (Viana et al., 2007). But the ‘normal’ is of slope and basin settings with low- to medium-intensity currents, capable of transporting fine-grained sediment population (Laberg et al., 2005; Stoker et al., 2005b).

Temperature variations in the NAC related to the inflow of warmer water during interglacial and interstadial periods and colder water during glacial periods have implications for the stability of gas hydrates Nyegga, and may have affected fluid flow in the area (Mienert et al., 2005b). These authors use modeling of the GHSZ to show that during inflow of warmer waters (up to 5 ^{o}C warmer at the end of Younger Dryas – ~11.5 ka) there is a concomitant shoaling of the base of GHSZ in the upper 1000m of sediments in the Storegga area. Dissociation of hydrates produces water and gas, and this sudden increase in fluids could lead to localized overpressure and fluid migration (Mienert et al., 2005b).

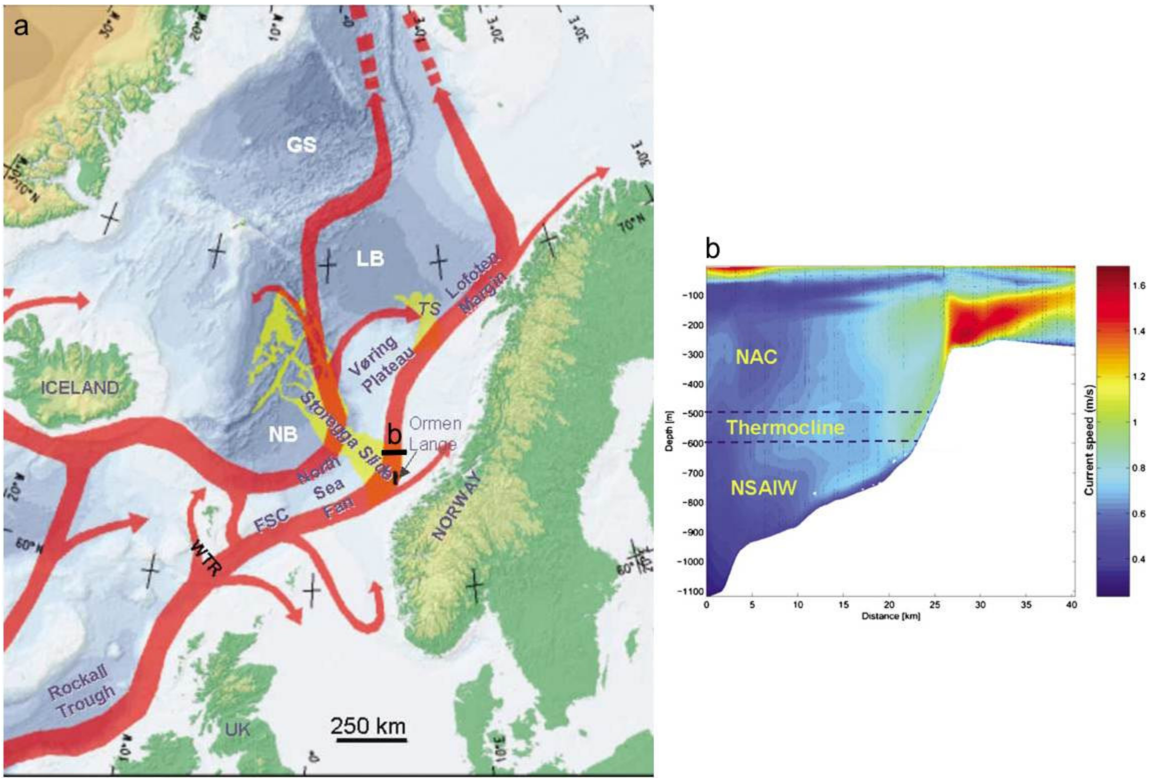

Figure 16 – a) The Norwegian Atlantic current (red colour) along the margin. WTR, Wyllie Thomson Ridge; FSC, Faroe–Shetland Channel; S, Trænadjupet Slide; NB, Norwegian Basin; LB, Lofofoten Basin (from Bryn et al., 2005b). The two large Holocene submarine slides offshore Norway, the Storegga Slide (8.2 ka) and the Trænadjupet Slide (4 ka) are shown in yellow; b) Results from a numerical ocean model showing increase in current velocities around the shelf break (from Bryn et al., 2005b). The colour bar shows current velocity in m/s. NAC, Norwegian Atlantic Current; NSAIW, Norwegian Sea Arctic Intermediate Water.

3. Material and Methods

3.1. Data description

3.1.1. Multibeam survey at Nyegga (July 2006)

Approximately 1650 km^2 of swath bathymetry data were acquired in the Nyegga region in water depths from 300 to 1300 m as part of a NFR and Statoil funded PETROMAKS “Fluid Flow” project. Multibeam data were collected using a Kongsberg-Simrad EM300 Multibeam sonar system, hull-mounted aboard the R/V Jan Mayen operated by University of Tromsø (Mienert et al., 2006).

During this survey, the swath bathymetry data were recorded using WGS-84 datum. Prior to the start of the survey, we ensured optimal positioning resolution of the system. This required a calibration using a sound velocity profile measured at CTD station 279 (table 1). Two additional (CTD station 280 and 281) sound velocity profile were measured for this survey (table 1). The angular sector was chosen to be 126 degrees with equidistant beam spacing. The maximum swath width was set to 10000 m, but was never reached. Though the Multibeam (MB) system was kept online for most part of the cruise collecting overlapping data, the oceanographic conditions of the area are such, that exact positioning resolution is limited and most of the data encounter ray bending problems. Ray bending occurs due to refraction in the water column in response to water mass boundaries and spatial sound velocity variations. The most abundant and consistent errors encountered were those resulting from inappropriate refraction corrections due to inaccurate water column velocity models (figure 17; figure 18).

Table 1 - CTD station list and water depth.

Date	Station type	UTC-time	Identification	Latitude	Longitude	Depth (m)
14.7	CTD Start	07:56	279	64 40.560’ N	05 00.712’ E	823
14.7	CTD Stop	08:23	279	64 40.774’ N	05 00.889’ E	812
15.7	CTD Start	19:47	280	64 36.441’ N	05 48.916’ E	372
15.7	CTD Stop	20:06	280	64 42.310’ N	05 48.916’ E	370
15.7	CTD Start	22:01	281	64 42.953’ N	05 26.460’ E	624
15.7	CTD Stop	22:24	281	64 44.643’ N	05 25.719’ E	620

Post processing of the data took place at the Department of Geology of the University of Tromsø. We used the Neptune software from Kongsberg maritime that allowed a post-processing of bathymetric data collected from single beams of the multi-beam. The processing consists in cleaning and filtering of positioning data, analysis and correction of depth data, tidal height adjustments, automated data cleaning based on statistical rules or manual editing, controlled data thinning, and export of final soundings for further data processing. All the above steps were applied to the main survey lines and the result was a xyz data set using a 30 meter grid cell size. Figure 1 shows the positioning of the survey lines as well as a gridded (100m x 100m grid cell size) version of the swath bathymetry.

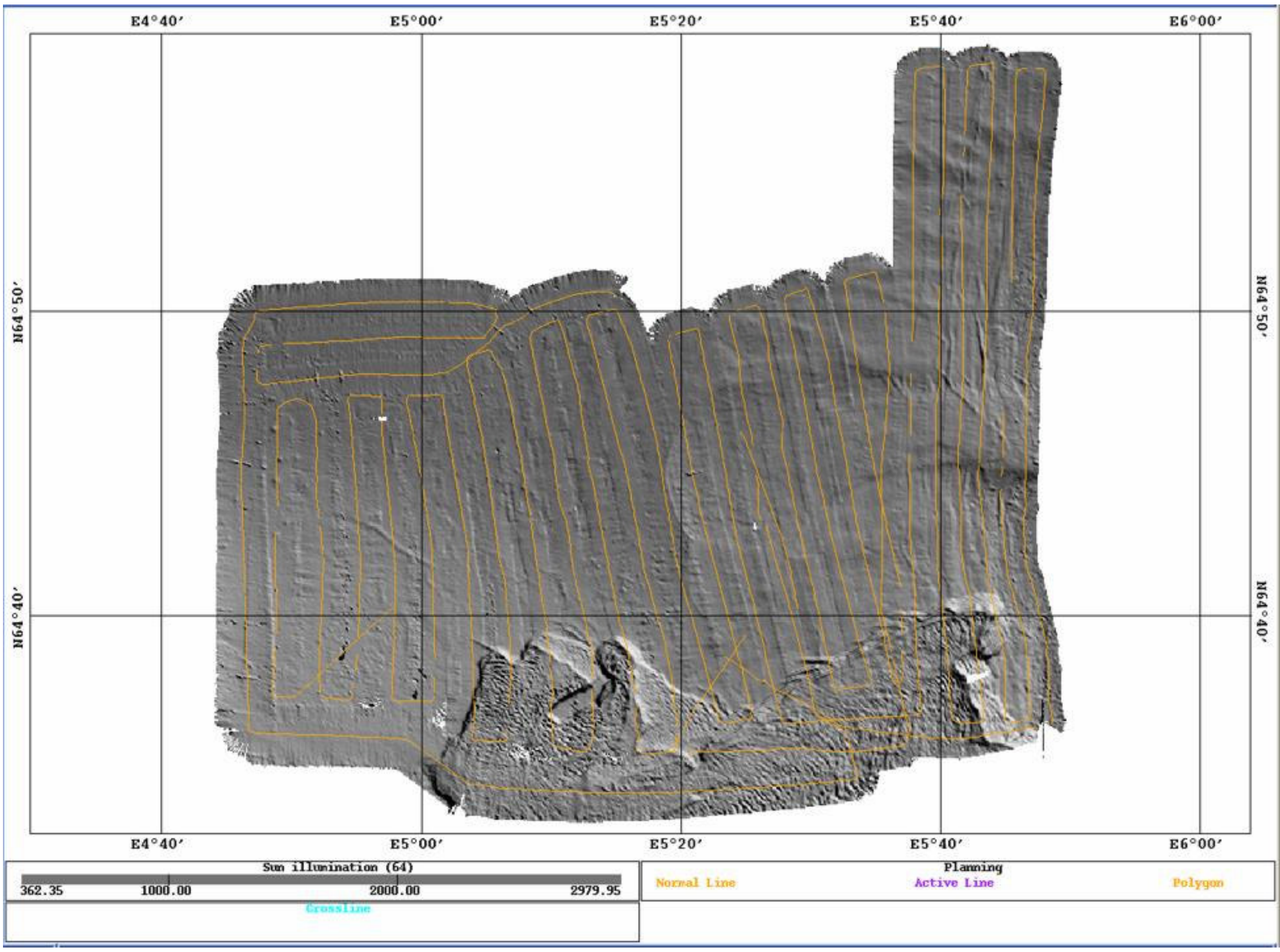

Figure 17 – This figure shows a windows from Neptune. The orange line is the ship track indicating the survey lines, the illuminated gray shaded image is the bathymetry, illumination if from the SW.

Figure 18 – The figure shows overlapping soundings from adjacent swaths. The fact that the outer beam soundings of the orange swath are below the green indicates inaccurate refraction correction to these outer beams (Mosher et al., 2006).

Spatial and horizontal resolution of multibeam sonar method is governed by several separate but dependent parameters. Sonar or acoustic resolution is a function of the area of ensonification which is dependent on (Clarke et al., 1998; Mosher et al., 2006):

1. the beam width along the two axes of the acoustic signal
2. the method of bottom detection within the beam footprint (amplitude or phase bottom detection)
3. spatial sampling density (samples per area)
4. positioning resolution, which is function of precision and accuracy of locating the sounding of on the seafloor

The latter factor is dependent on the vessel's navigation system and the ability to measure and integrate all components of vessel motion, water column structure, and sounding information, including correct bottom detection.

The beam width along the two axes will determine the area of ensonification. The area of ensonification of an acoustic beam is the area of an ellipse ($\pi \times r_1 \times r_2$). For the vertical beam, its area is a function of the water depth (z) and the angle width of the beams in the along-track (φ) and cross-track (θ) directions (figure 19). For the beams off vertical, the area is additionally a function of the beam emission angle (α, from vertical) and the seabed grazing angle (β, from the seabed surface).

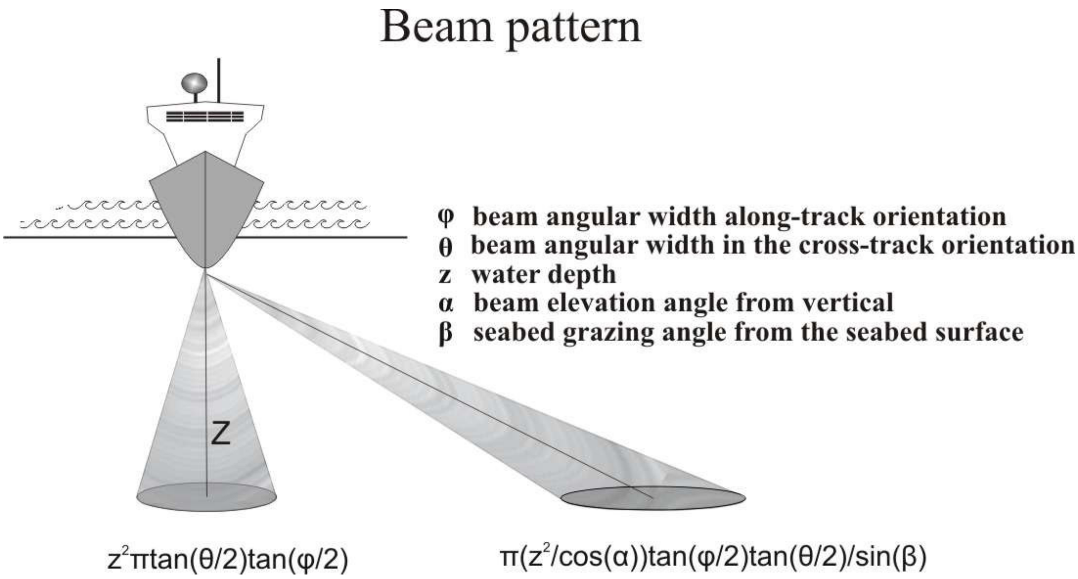

Figure 19 – Schematic of multibeam sonar beam angle considerations for calculations of area of ensonification (modified from Mosher et al., 2006).

From figure 19 we can see that the area of ensonification grows as depth increases and also as the beam becomes more oblique, resulting into a poorer spatial resolution. Although the obliquity of the beam angle increases the ensonification area, at a certain critical angle, the system transforms from amplitude bottom detection to a phase detection algorithm. This later greatly enhances the precision of the depth sounding but is still representative of the larger elliptic area. Field results have proved that with phase detection it is possible to image features smaller than the beam footprint, while the same is not true for amplitude detection (Clarke et al., 1998). This implies that reducing the beam spacing will increase the sounding density, but the resolution of features smaller than the area of ensonification will still depend on the bottom detection algorithm. Values for the area of ensonification for different water depths and different beam angles are shown on table 2.

Table 2 – Theoretical area of ensonification of multibeam data ($2^0/1^0$ beam angular width in along/cross-track):

Water depth(m)	Area of ensonification (m^2) (0^0 incidence)	Area of ensonification (m^2) (15^o beam)	Area of ensonification (m^2) (30^o beam)	Area of ensonification (m^2) (45^o beam)	Area of ensonification (m^2) (63^o beam)
300	43	46	57	86	209
500	120	128	160	239	580
‖700	234	251	313	469	1138
900	388	415	517	775	1881
1100	579	621	772	1158	2809
1300	809	867	1078	1618	3924

Factors affecting the density of soundings of the seafloor can be divided in the two axes. In the along ship direction the density is a function of ping rate and vessel motion. While across, it is a function of beam spacing, orientation (speed, heave, pitch, roll and yaw) and the amount of overlap between swaths on successive lines. The beam spacing is usually less than 1^o (it varies depending on the angular sector employed and whether beams are equidistant or equiangular). Water depth and obliquity of the beam determine the ping rate, in that the ping period must be greater than the time taken for the sound to travel to and from the most distant target, so wider angular sectors imply smaller ping frequencies. Vessel speed determines the physical distance between two successive pings.

3.1.2. 3D Seismic cube ST0408 from StatoilHydro

The 3D seismic survey used in this thesis is the ST0408 seismic cube provided by StatoilHydro (Stavanger) This seismic volume covers a surface area of 350 km^2 and has an available recording length of 3.1 s. It has a bin spacing of 25m and therefore a relatively good spatial resolution. The highest frequency present in the data is 40 Hz. The survey is processed to a zerophase waveform and is recorded with SEG (Society of Exploration Geophysicists) standard reverse polarity. That means positive reflections representing increase in acoustic impedance are recorded by a negative number. In this thesis, the colorscale is set to display the positive reflections (negative numbers) as peeks.

The spatial resolution limit of the 3D seismic data is often quoted as equal to the bin spacing (range typically 12.5-37.5m) of the 3D data set, but it can be more than that. For a fixed acquisition geometry, the spatial resolution of migrated 3D seismic data is directly proportional to the distance between the source and the reflection point (point scatterer), and inversely proportional to the dominant frequency of the seismic wavelet (GMT; Chen and Schuster, 1999). This way we can expect to have a decrease in resolution with depth, since we both experience an increase in distance from the source and a decrease in the frequency as we move down to deeper stratigraphic levels. This causes the resolution to range from the bin spacing up to 200m, depending on the target depth.

The potential vertical or temporal frequency is dependent on the highest frequency content of the seismic signal and the velocity of the medium. It can be approximated by the Rayleigh criterion, which dictates one-quarter of the wavelength (λ/4) of the seismic wavelet. As shown in the following equation:

$$\Delta R_z \approx \frac{\upsilon}{4 f_{max} \cos(i)}$$

Where:
v = velocity;
f_{max} = maximum frequency;
i = angle of incidence;

For normal incidence paths, cos(i) ≈ 1. The likely limits for the temporal resolution of the ST0408 data used in this study are in the range between 11-20m, considering p-wave velocities in the range of ~ 1800 to ~ 3000 m/s.

3.2. Data interpretation methods

3.2.1. Swath bathymetry interpretation

Interpretation and visualization of the bathymetry was done using maps produced by Generic Mapping Tools (GMT; Wessel and Smith, 1998) and interactively in Saga GIS.

Trend surface analysis (Davis, 1986; Rock, 1988) was sometimes used to separate local anomalies from regional trends. This method, which constitutes a segment of the statistical field of regression analysis, consists of fitting a plane (trend) to a surface, such that the squared deviations of the surface from the plane are minimized. The resultant plane is the regional trend. The regional component expresses the large scale effects or trend influencing the entire map area (i.e. mean slope). The residual component is the difference between the observed and regional values and expresses local effects or anomalies which influence only parts of the map. What is regional and what are anomalies is highly arbitrary and depend on the scale of the surface to be analyzed. As one example, pockmarks and mounds which are 300 m in diameter lying on top of a 10 km wide debris flow lobe are anomalies within a 2x2 kilometer area, while the debris flow lobes may become the anomalies when considering a surface of 30x30 kilometers.

3.2.2. 3D seismic interpretation

For visualization and interpretation of the 3D seismic data I used Charisma seismic interpretation software from Schlumberger. The Automatic Seismic Area Picker (ASAP) is the software's tool for tracking horizons. It uses the interpretation done within one or more inlines or crosslines as a "seed" and tracks across the surface as we "paint brush" it. Parameters have to be chosen for the ASAP in accordance with part of the seismic wavelet to be tracked along the horizon, that is to follow maximum or minimum amplitude, or upper or lower zero crossing (figure 20). The quality of the interpretation is very important here, as you interpret quickly through large areas, so it is imperative to specify correct parameters for the quality control of the ASAP, this is done in a set of tabs on the ASAP tool including dip/trace, track technique and quality, correlation, and snap range. Choosing too strict quality control will lead to many areas being left uninterpreted, while choosing too loose parameters will lead to a lot of "miss-picks".

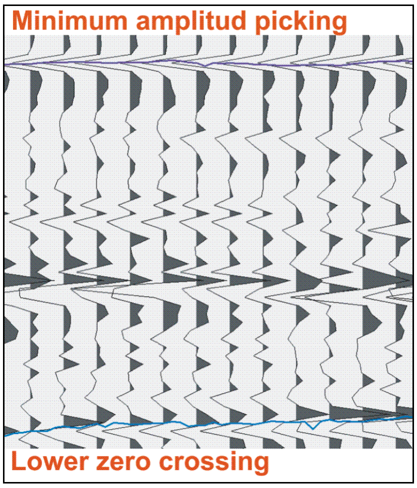

Figure 20 - Seismic wiggle traces and the ASAP picks.

In case a surface changes seismic polarity from one region to the other, ASAP will be incapable of continuing picking through the same surface. In this case if I wanted to map the surface it had to be through creating another horizon and using a different parameter for ASAP to pick the rest of the area and then merge the two horizons into one surface.

Seismic interpretation included analysis of seismic attribute maps. Seismic attributes are measurements derived from seismic data. These are very useful in making geologic interpretation and analysis from seismic data. Countless seismic attributes exist. The most popular attributes and their potential geologic significance are presented in table 3.

Table 3 – List of popular seismic attributes and their potential geologic interpretation:

Geologic significance of Seismic Attributes	
Amplitude	Lithological contrasts Bedding continuity Bed spacing Gross porosity Fluid content
Instantaneous Frequency	Bed thickness Lithological contrasts Fluid content
Reflection strength	Lithological contrasts Bedding continuity Bed spacing

	Gross porosity
Instantaneous phase	Bedding continuity
Polarity	Seismic polarity Lithological contrasts

In charisma, seismic attributes can be extracted along interpreted surfaces or over volumes, which can be defined between interpreted surfaces or time windows. The extracted attributes are then displayed as attribute maps. It is also possible to display the seismic attributes along profiles.

For analysis of lateral fluid flow pathways along potential interpreted free gas zones I created directional gradient maps. The gradients were calculated from 30x30 m gridded versions of exported interpreted time surfaces. The grdmath tool of GMT was used to extract the directional derivatives in X and Y direction. These were filtered by a median filter using a 270 meter radius circle around each grid cell. The results are then presented as a map where the filtered directions were plotted as vectors in equal spaced points 540/540 meters apart. Major fluid flow pathways are then interpreted with the help of Saga GIS's hydrological modeling of catchment area module. This is justified by the fact that the processes of secondary migration of hydrocarbons in subsurface strata are similar to the surface water flow in that both of them are fluid flow processes controlled by gradient of the surface or the boundary along which flow processes occurred. The main differences of secondary hydrocarbon migration from water flow lie in the mechanisms and flow directions: water flow on earth surface is driven by gravity force, while secondary hydrocarbon migration is mainly driven by the differences of buoyancy and capillary pressure (Liu et al., 2008). In addition, water flows downwards, while oil and gas migrates upwards, meaning that the digital elevation model needs to be inverted (multiplied by -1).

Assumptions have to be made regarding the directional gradients of time surfaces as to roughly reflect the major directions of buoyant (free gas?) fluid flow pathways. This is due to the fact that surfaces used in the seismic interpretation represent the time domain in two way travel time, and distortions may exists due to lateral seismic velocity changes in the overburden. Changes in velocity may be found due to lateral changes in lithology, as for example from contourite to glacigenic debris flow depsosits. Also permeability may vary along sediment formations due to lateral changes in the capillary resistance, to which fluids naturally respond by taking the paths of least resistance. But in the absence of depth converted surfaces and fluid potential data, directional gradients of the time surfaces are the best approximation to the directions of buoyant fluid flow (Hindle, 1997; Liu et al., 2008).

3.3. Mapping and quantification of fluid flow expressions

3.3.1. Pockmarks and mounds

A total of 9 parameters were collected for the pockmarks and mounds at the seafloor. The parameters collected include size parameters (area, perimeter, long axis length, and short axis length), depth or elevation parameters (mean and variance), slope parameters (mean and variance) and orientation of the long axis. These parameters are summarized in Table 4.

In the first attempts to collect information from the pockmarks and mounds, I noticed that it was sometimes very difficult to measure them precisely by using only eye judgments. For example, it was sometimes very time costly and imprecise to determine which was the long axis and short axis of the features. Also the depth and elevation, as well as slope varied very much within the objects. It would be interesting to get a measure of this variation instead of only collecting a maximum value. Also, in order to distinguish the pockmarks and mounds by statistical methods it was important that the error of the measurements did not surpass the differences between the observations. For the above stated reasons, an experimental method for collecting the parameters was developed. The purpose of it was then to minimizing the measurement errors and get the most possible information of the pockmarks and mounds.

The method consisted in a series of steps. The first was to block the data. That means I divided the data into several 2 by 2 km blocks (figure 21), leaving out the slide scar, where the blocks of debris make it too difficult to detect any fluid flow feature. The bathymetric data came from two sources, a file with the accepted depths after processing the Multibeam bathymetry with Neptune, and where the 3D Seismic data was available, the picked seafloor horizon was converted to depth using a sound velocity of 1480 m/s and also separated using the same blocks. The advantage of having two independent data sets in the same area is to isolate acquisition or processing artifacts from both surveys (figure 23a-b). The data blocks were then transformed in a grid using 10/10 meters grid cells with a near neighbor algorithm. The resultant grid blocks had a very high resolution bathymetry, but in order to extract information from the pockmarks and mounds additional steps were needed (figure 22).

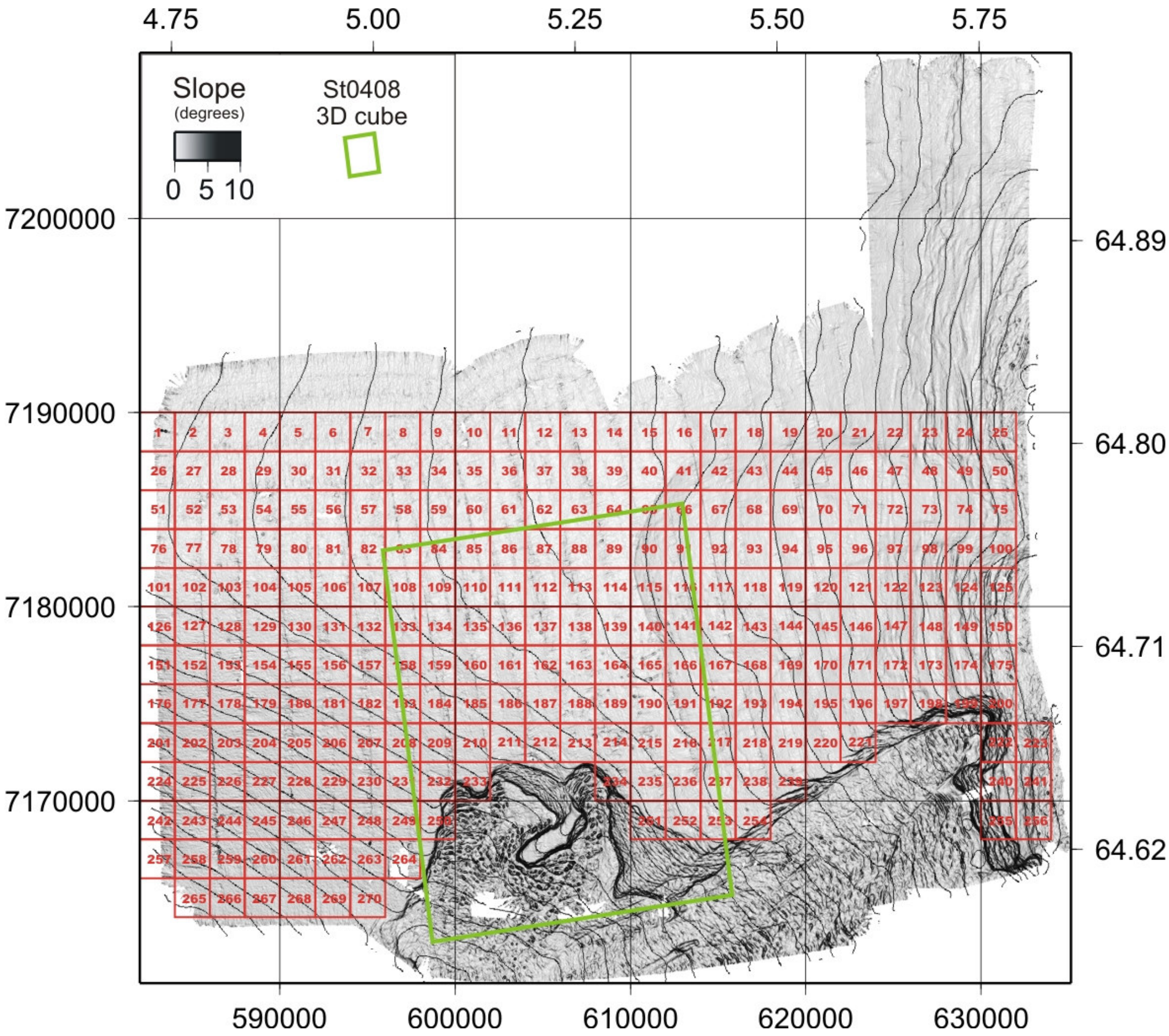

Figure 21 – Slope map derived from the swath bathymetry data of the study area, showing the 2x2 blocks used to map and acquire the input parameters from the pockmarks and mounds. It also shows the location of the ST0408 3D seismic survey indicating for which blocks this data was available.

The gridded blocks were further processed with the GMT tool ”*trend2d*”, which is a *surface trend analysis* tool. The results are deviations of the depths from the least squares best fitting plane over the data block. In the case the seafloor is planar, the residuals give the depth of the pockmarks, or in the case of mound their height. But sometimes the seafloor is not planar, as in the case of places where there are debris flow fans and also due to the ”smile” and ”frown” artifacts caused by the inappropriate refraction corrections of the outer beams of the multibeam swaths. For this reason, I applied a method called residual analysis (Davis, 1986). This method consists in filtering the surface by a running average filter, such that all pockmarks and mounds are averaged out, and then subtracting the filtered surface from the non filtered surface. The resultant *residuals* are then giving the pockmarks and mounds depths and elevations (figure 23c).

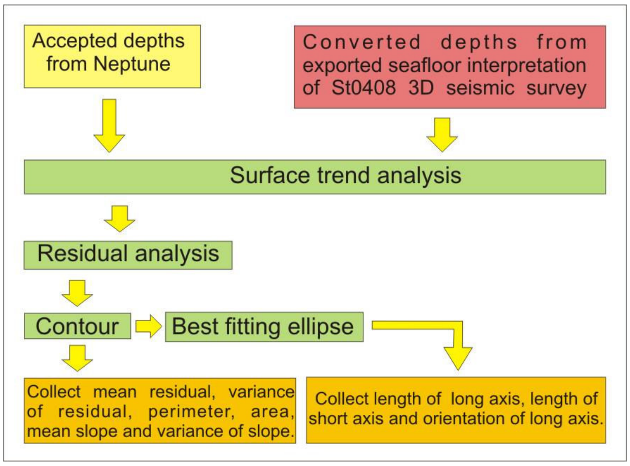

Figure 22 – Pockmark's and mound's parameter acquisition workflow.

With the results of the residual analysis I could then contour the pockmarks and mounds, and get the statistics from the grid inside the contour. The mean residual (depth or elevation) and variance of the residual were calculated from the grid cell values falling inside the contour. The mean slope angles and variance of slope angles were calculated from the grid along the contour. Also the contour was used to get perimeter and area. Orientation, short axis and long axis length are collected through fitting an ellipse to the contour (Mulchrone and Choudhury, 2004) (figure 23c). One important point is that the fluid flow expressions are contoured using a base level of 2 residual. This is because the Multibeam bathymetry is not sufficiently smooth. The many small variations due to the inaccuracy of the multibeam method contribute to make the contours open. Also the 2 contour runs through the slope of the feature giving information of the slope angle much better than the actual rim would give. Sometimes the residual is not large enough to get the 2 contour, then in these cases the 1 contour is taken. But the result is the depths, lengths, area and perimeters are not comparable. In some areas there was large difference between the 3D seismic seabed horizon and the multibeam data. For example, fluid flow expressions identifiable in the 3D seismic data were sometimes affected by artifacts or in some cases not present at all in the Multibeam data. In these exceptional cases, I used the seismic data as the source for the parameters.

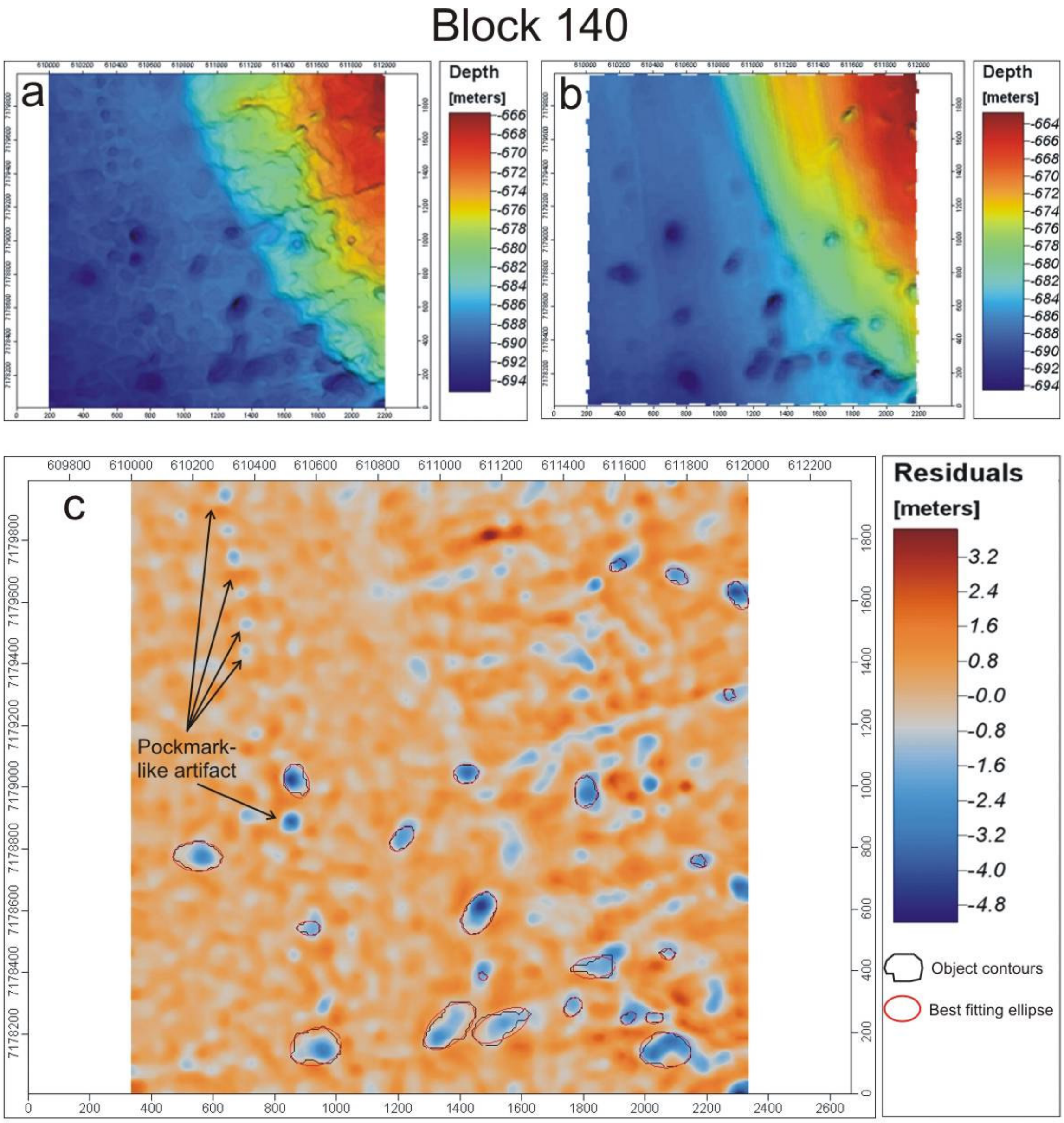

Figure 23 – Figure illustrating the acquisition of parameters from the pockmarks and mounds in block 140. In (a) we see the depths from the swath bathymetry while in (b) we see the depths from the depth conversion of the 3D seismic pick of the seafloor horizon; In (c) we see the results from the residual analysis, the contour used for getting information from the grid (depth, perimeter, area, slope angle) and the best fitting ellipse used to calculate the lengths of the long and short axis as well as the azimuth of the long axis. In the swath bathymetry figure (a) we can also see some artifacts along the ships track which are resultant of poor correction of ships heave.

Table 4 - Parameters collected from the fluid flow expressions in the bathymetric data.

Parameters	Description
Perimeter	Calculated from the contour
Area	Calculated from the contour
Mean residual	Average of all samples inside the contour
Variance of residual	Variance about the mean residual
Mean Slope	Average of all samples along the contour
Variance of Slope	Variance about the mean slope
Long axis	Long axis of the best fitting ellipse
Short axis	Short axis of the best fitting ellipse
Orientation (degrees azimuth)	Orientation of the Long axis of the best fitting ellipse

3.3.2. Acoustic chimneys

The acoustic chimneys were quantified in the Petrel seismic interpretation software from Schlumberger. The parameters collected and a short description are shown in the Table 5. The collected parameters are also shown in figure 24.

Table 5 – Parameters collected from the fluid flow expressions in the 3D seismic data.

Parameters	Description
Height (ms)	Bottom (ms) – Top (ms)
Top horizon	Horizon at top termination
Bottom horizon	Horizon at bottom termination
Maximum pull up (ms)	Maximum up bending of the reflection
Maximum push down (ms)	Maximum down bending of the reflection
Swap level of Pull up to Push down	Horizon at which Pull up turns to Push down, in the case both occur.
Horizon of Maximum pull up	Horizon at which the up bending is maximum.
Horizon of Maximum push down	Horizon at which the down bending is maximum.
Length of short axis (m)	A
Length of long axis (m)	B
Orientation of Long axis (degrees azimuth)	
Area of the ellipse defined by the two axis (m^2)	Area = π x A x B

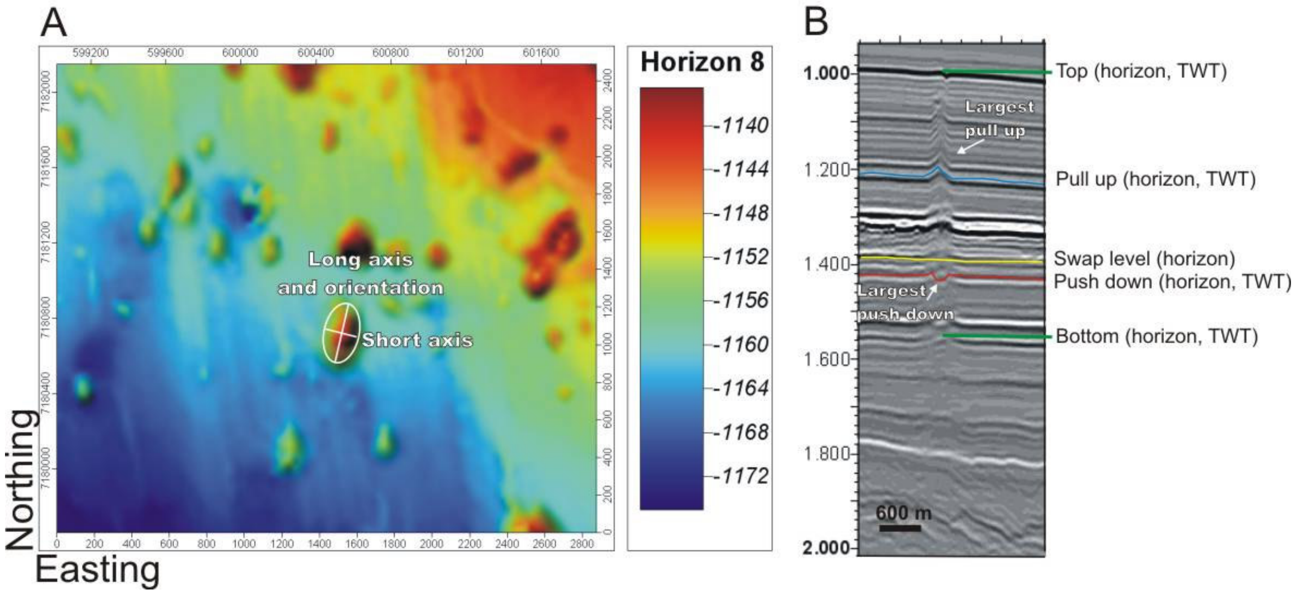

Figure 24 – Collected parameters for the acoustic chimneys in: (A) Map view; (B) Cropped seismic profile.

3.4. Statistical analysis methods

The collected parameters were analyzed by series of graphical and numerical methods. The graphical methods included frequency histograms, boxplots and scatter plots. The numerical methods included Multidimensional scaling (Davis, 1986; Rock, 1988) and K-means cluster analysis (Davis, 1986; Rock, 1988).

Multidimensional scaling is an ordination technique (Davis, 1986). It essentially aims to reduce the dimensionality of data, that is, to allow relationships between multivariate objects to be displayed as accurately as possible in as few dimensions as possible (ideally in 2D). Relationships and possible groupings can then be sought using the remarkable natural abilities of the human eye. The method uses a matrix of dissimilarities (e.g. Euclidean distances), and generates coordinates for a set of points in 2D or 3D space. The solution (i.e. final configuration), consists of an arrangement of points in the chosen number of dimensions, located such that the distance between the points matches the dissimilarities between the objects as closely as possible. This way the method offers a good alternative to the classical scatter plots. The measure of the quality of fit between the scaled solution and the input matrix is done via a factor called stress. In a mathematical standpoint, non-zero values of stress are the result of insufficient dimensionality. That is, reducing the dimension of the input data produces some degree of distortion. Stress can be informally interpreted according to the following guidelines (Johnson and Wichern, 2002) (table 6):

Table 6 – Stress interpretation guidelines

Stress	*Goodness of fit*
20%	Poor
10%	Fair
5%	Good
2.5%	Excellent
0%	Perfect

The multidimensional scaling was carried out in MATLAB® using the *mdscale* function. The values of (1 – spearman's rank correlation) were used as input dissimilarities for the R-mode (based on the correlation matrix) solutions, and the Euclidean distances for the Q-mode (based on the matrix containing the distance between each pair of observations) solutions. I used Kruskal's formula 1 (3.1) for calculating the stress.

$$\text{Stress} = \sqrt{\frac{\sum\sum\left(x_{ij} - d_{ij}\right)^2}{\sum\sum d_{ij}^{\ 2}}} \tag{3.1}$$

Cluster analysis is the name given to a set of techniques designed to perform classification by assigning observations to groups so each groups is relatively homogeneous and distinct from other groups (Davis, 1986). The great advantages of these methods is that they provide a relatively simple and direct way to classify objects, and the results are presented in a manner that is both familiar and easy to understand. In K-Means cluster analysis (Davis, 1986), a predetermined number of clusters (K) are chosen, into which the data set is to be divided. The technique usually starts by taking the first K points in the data-set as the initial estimates of the future cluster means. The remaining objects are then assigned to the nearest of these clusters. For example, if K=2, the first two objects initially represent the 2 clusters, and the 3rd object is assigned to cluster 1 if it's mean is the nearer. The mean of cluster one is recalculated as the mean of objects 1 and 3, and object 4 is then assigned to the (recalculated) cluster 1 or to cluster 2, whichever mean is nearer. Once all objects have been assigned to the continually evolving clusters, the process is repeated iteratively with the entire data-set, each object being reassigned as necessary, wherever this will increase the ratio of within clusters dispersion (ANOVA is used as a criteria). Many passes through the data-set may be necessary for the results to stabilize.

Cluster analysis was carried out in MATLAB® through the function *kmeans*. The input to the function is a matrix of dissimilarities and the number of clusters (K) in which the algorithm is going to classify the observations. The datasets were first standardized to zero mean and variance of 1, and then the dissimilarities were calculated using the Euclidean distance.

4. Results

The results chapter is divided into two major parts, the first part shows the results of the mapping and quantification of the pockmarks and mounds observed in the seafloor. This was done mainly using the swath bathymetry supported by the depth converted ST0408 seafloor horizon map. Since the area covered by the swath bathymetry is larger than that of the ST0408 seismic survey, part of it lacks seismic data which hinder us from analysing the subsea bed influencing the distribution of fluid flow features. However, the second part shows results of the interpretation of the ST0408 seismic data concerning subseabed chimneys connected to the pockmarks and mounds at the seabed. Some parameters within the vertical acoustic chimneys are quantified (table in appendix). A comparison between the parameters of the chimneys and the overlying pockmarks or mounds is shown at the end of this chapter where possible relationships are investigated and discussed.

4.1. Interpretation of the high resolution swath bathymetry

Before presenting the mapping results of fluid flow expressions at the sea floor, it is necessary to give an overall description of the regional seabed morphology. Therefore, the most prominent elements of the sea floor are described based on the high resolution multibeam survey (figure 25).

In the south, the Storegga slide escarpment is the most remarkable feature, showing the steepest slope (>20 degrees). Inside the slide scar, many small blocks of debris and an apparently undisturbed sediment block exist. The eastern part of the bathymetric map shows iceberg plough marks, and moraine ridges on the shelf (figure 25). From the shelf westwards to the upper continental slope large debris flows can be found, representing sediment transfer in front of glaciers that reached the shelf during the last glaciation of the Weichselian age (Rise et al., 2005). Some of these glacigenic debris flow (GDF) lobes terminate at the slide scar to the south, indicating that they were probably swept away by the Storegga slide event at 8.2 ka (Haflidason et al., 2004). The western part of the bathymetric map shows a very smooth seafloor, and the most prominent feature is an elongated crest running roughly east-west. Surface trend analysis of the bathymetry clearly reveals this slight positive feature (figure 26). This crest represents an important element with respect to the fluid flow expressions as will be shown in subchapter 4.1.1.

4.1.1. Mapping of seabed expressions of fluid flow

A total of 310 seabed expressions that indicate focused fluid flow have been mapped, of which 287 (92.5%) have a predominant concave relief and are classified as pockmarks (see examples in figure 27). The other 23 (7.5%) fluid flow expressions were classified as mounds because they had either a predominant convex relief or they show a positive relief structure inside the pockmarks that were large enough to be distinguished and mapped. Examples of these both types of mounds are shown in figure 28. Fluid flow features were found between water depths of 600 and 900 m of water depth. Conservative estimates based on the lateral resolution of the multibeam method for these depths fall between 172 and 800 m^2 for the shallowest depths (600 m) and between 388 and 1881 m^2 for the deeper sites (900 m). Although all mapped features cover targets larger than 172 m^2, smaller features were also sometimes identified indicating that the number of fluid flow expressions on the seabed may distinctly increase depending on the improvements in the lateral resolution.

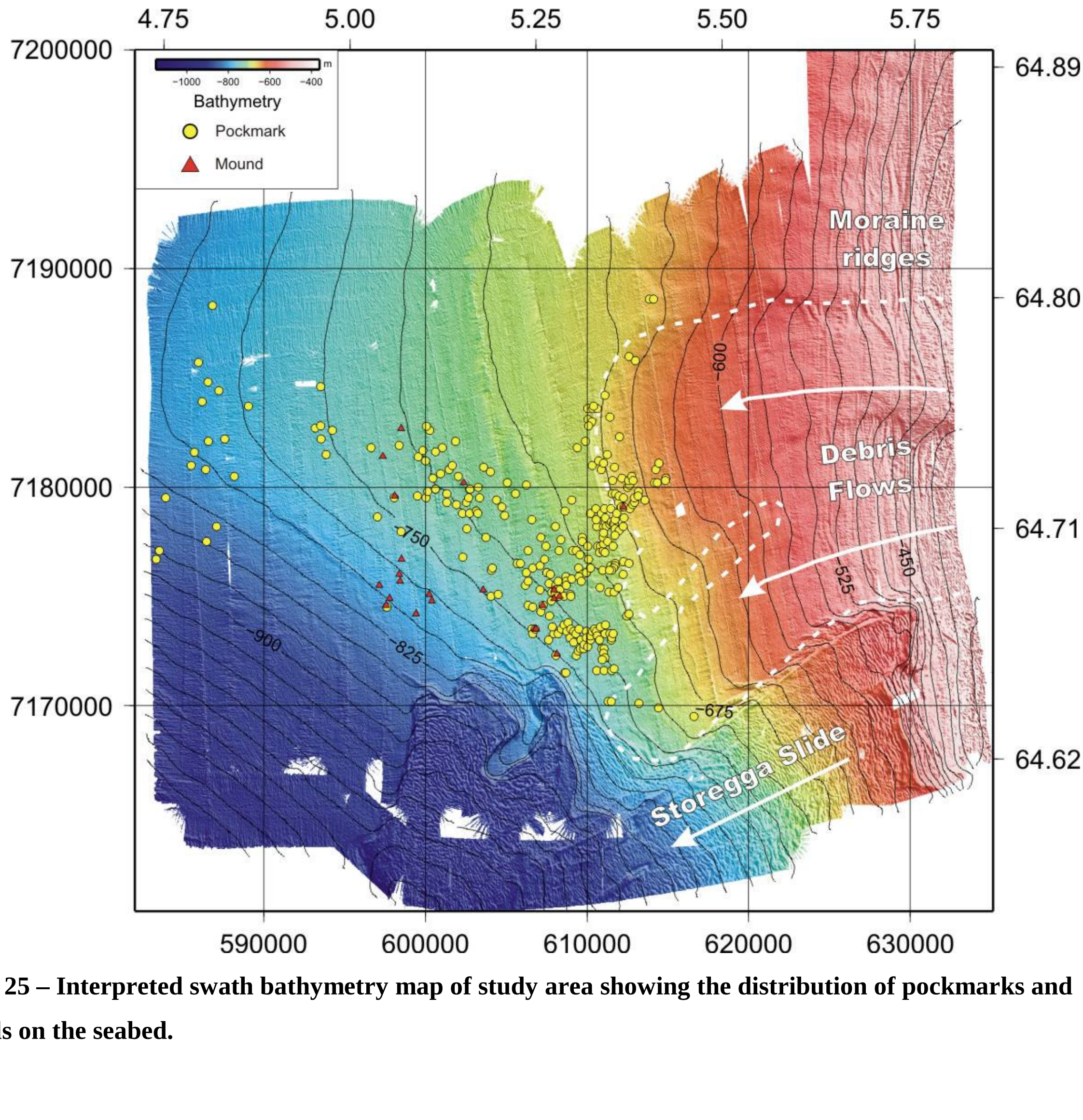

Figure 25 – Interpreted swath bathymetry map of study area showing the distribution of pockmarks and mounds on the seabed.

The spatial distribution of the mapped fluid flow expressions is shown in figure 25 and figure 26. The distribution of pockmarks and mounds indicates that they are not randomly located but may show a relationship to the previously described bathymetric elements. In the western part most of the fluid flow expressions are spread along and across the crest (labelled number 1 in figure 26). There is also a group of mainly mounded features (number 2 in figure 26) which are slightly offset to the south from this crest. In the east the distribution of fluid flow features is more complex with features lining up in different directions (numbers 3 through 5 in figure 26). Some of the features are located on GDF lobes, indicating that the processes forming were active during or after the Last Glacial Maximum (LGM) (Rise et al., 2005).

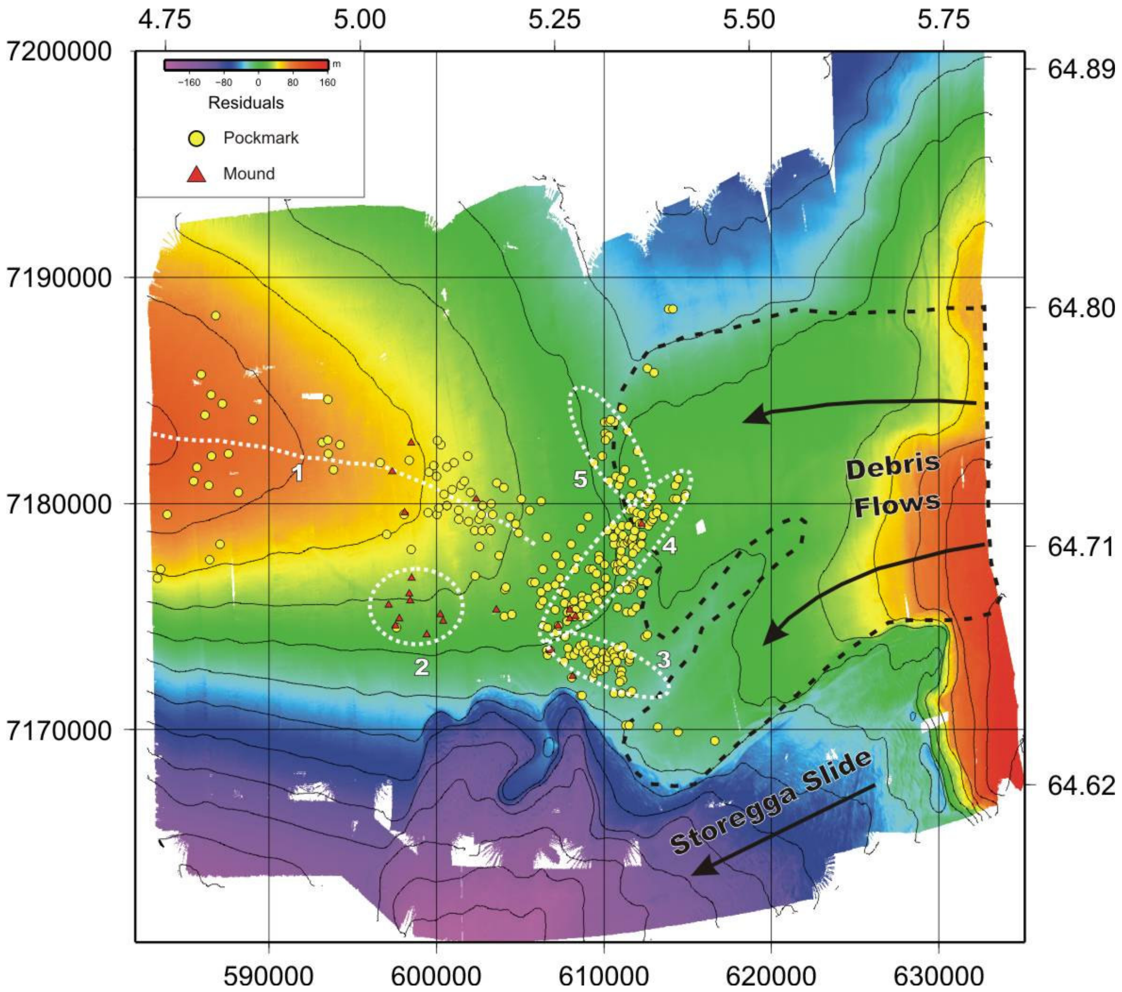

Figure 26 – Surface trend analysis of the high resolution swath bathymetry, with mapped fluid flow features.

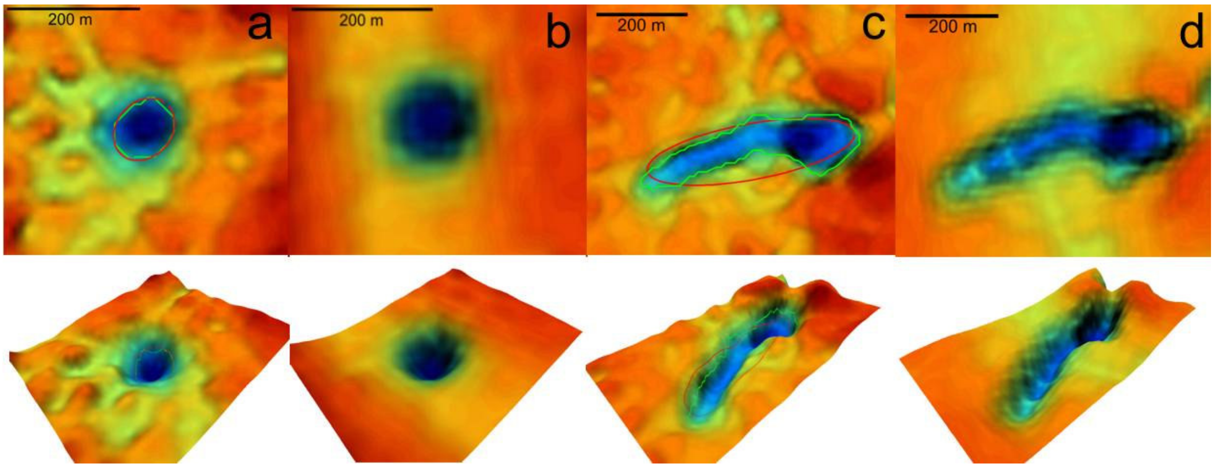

Figure 27 – a) and b) are examples of a rounded pockmark (obj 71) in the swath bathymetry and seafloor pick of 3D seismic data respectively, the top row shows the plan view and the bottom the perspective view (Vertical exaggeration is 20x); c) and d) are examples of an elongated pockmark (obj 151). Green contour around the pockmarks in the swath bathymetry are the 2 residual contours from which area and perimeter are collected; The mean residual and variance about the mean residual are computed from the grid cells inside this contour; The mean slope angle and variance of slope angle are computed from the values along the contour; The red line around the pockmarks represents the best fitting ellipse to the contour from which length of long axis and short axis, as well as orientation of long axis are computed (see also section 3.3.1 for explanation on the parameters).

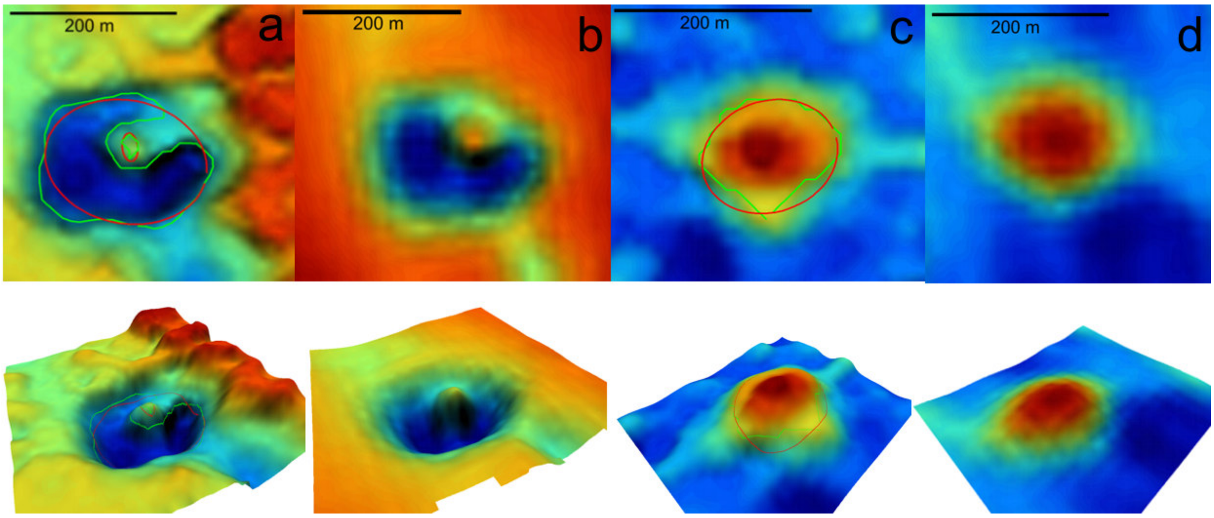

Figure 28 – Examples of how mounds appear in the bathymetry data. Figures (a) and (b) are shaded relief images of a mound (obj 31) inside a pockmark (obj 30), derived from swath bathymetry and 3D seismic respectively the top row shows the plan view and the bottom the perspective view (Vertical exaggeration is 20x). Figures (c) and (d) show a shade relief image of a typical isolated mound (obj 114). Green contour around the pockmarks and mounds in the swath bathymetry are the 2 residual contours from which area and perimeter are collected; The mean residual and variance about the mean residual are computed from the grid cells inside this contour; The mean slope angle and variance of slope angle are computed from the values along the contour; The red line around the pockmarks represents the best fitting ellipse to the contour from which length of long axis and short axis, as well as orientation of long axis are computed (see also section 3.3.1 for explanation on the parameters).

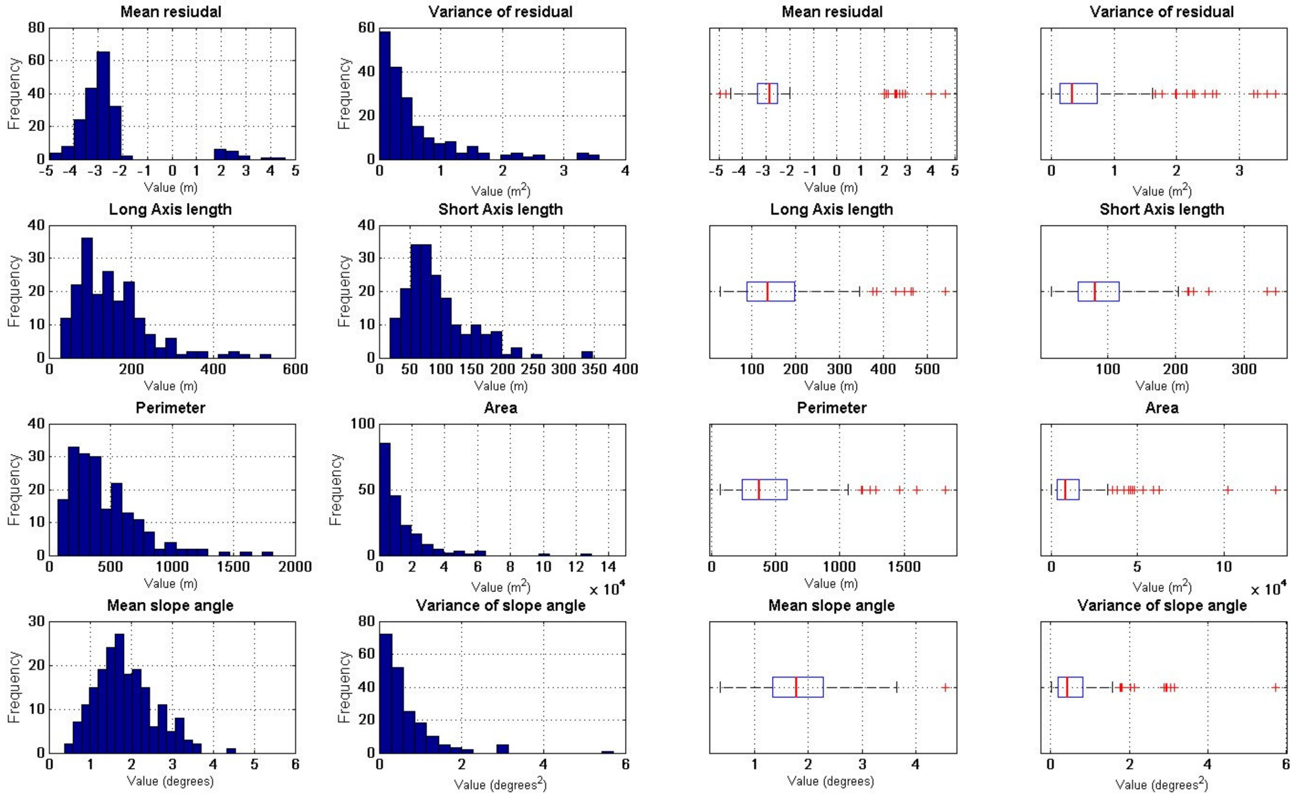

Figure 29 – Parameters mean residual, variance of residual, long axis length, short axis length, perimeter, area, mean slope angle and variance of slope angle are shown in form of: Frequency histograms (left); and Boxplots (right); In the box plots, the central red line represents the median of the dataset, the outer edges of the boxes are the 25 th and 75 th percentile (lower and upper quartiles), the ends of the error bars represent the 10 th and 90 th percentile and the individual crosses are outliers beyond these limits. The orientations of the long axis of the pockmarks and mounds are shown in figure 32.

The collected parameters for each target feature are arranged in a table in the appendix. The objects chosen for the statistical analysis were those contoured using the 2 residual. That is, there are 192 objects in total, of which 178 are pockmarks and 14 are mounds. The statistical distributions of the acquired parameters, in the form of frequency histograms and boxplots, are shown in figure 29.

The mean residual (depth or elevation) varies between approximately -5 and 4.6 m (figure 29), the negative values represent the depths of the pockmarks and the positive the elevation of the mounds. The mean depth inside pockmarks varied between -5 and -2 m (figure 29), and the mean height of the mounds varies between 2 and 4.5 m. The variance of residual (depth or elevation) represents a measure of the variability of the depths and heights within the pockmarks and mounds, this way it gives valuable information which is expected to help in the classification of these features through multivariate statistical analysis. The values are mostly below 2 m^2 with a mean of ~0.58 m^2 and a median of ~0.33 m^2, but some outliers reach values above 3 m^2 (figure 29). The spatial distribution of the residuals of the pockmarks and mounds show that apparently the deeper pockmarks and tallest mounds predominate at the central parts of the groups of pockmarks (numbered 1-5 in figure 26), decreasing in magnitude toward the peripheral (figure 30).

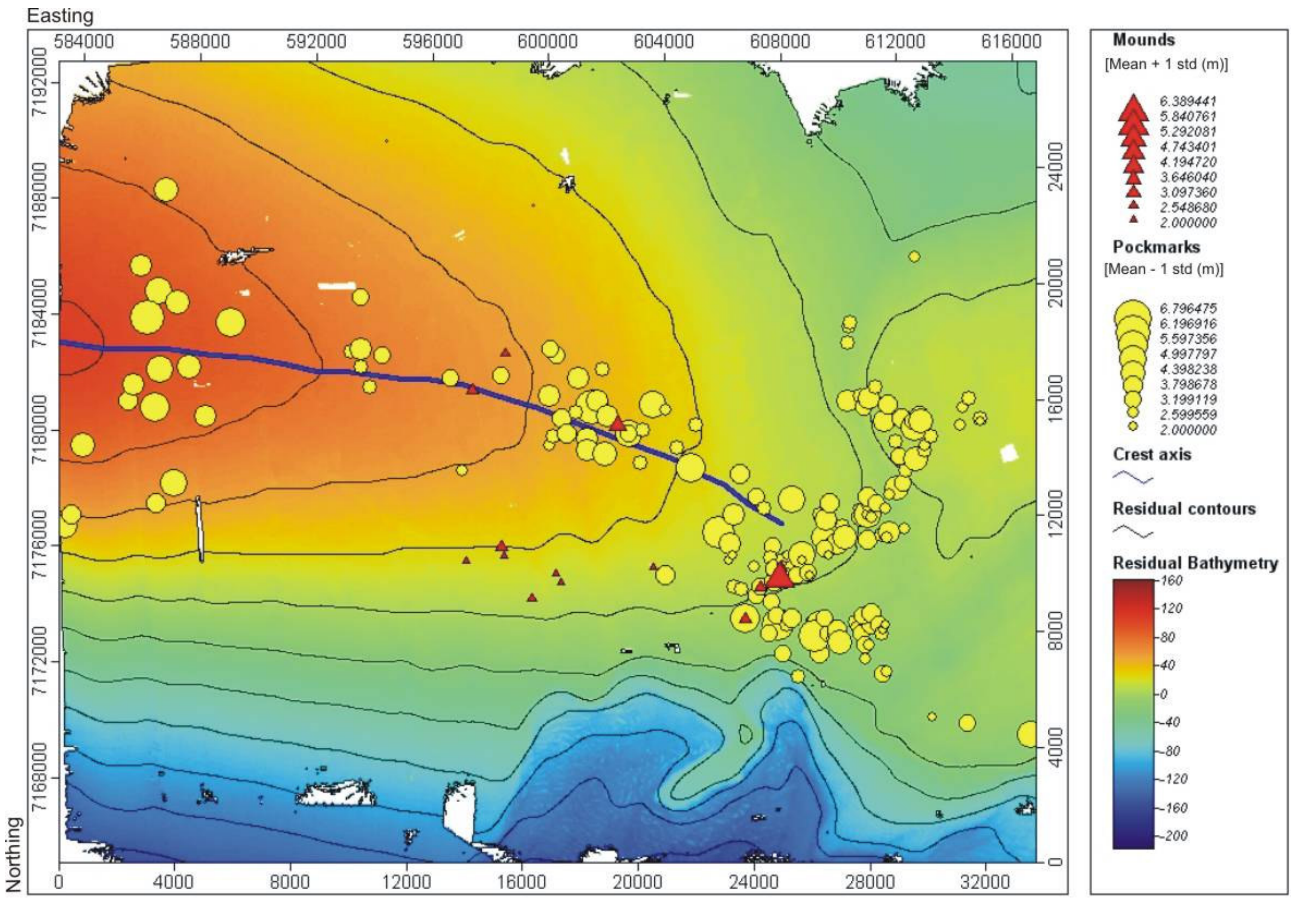

Figure 30 – Bullet map of mean residual minus 1 standard deviation (square root of the variance of residual) for pockmarks (yellow circles) and mean residual plus 1 standard deviation for mounds (red triangles) over residual (trend surface analysis) bathymetry map.

The measured long axis length of the pockmarks and mounds ranged from about 30 m to more than 500m (figure 29), while the short axis lengths ranged between 18 m and 345 m (figure 29). The mean length of the long axis and short axis were respectively 138 and 84 m, indicating that most of the features are elongated. Examples of circular and elongated pockmarks are shown in figure 27. The scatter plot of the measured long axis lengths versus the short axis lengths further shows that larger features tend to be more elongated than smaller features (figure 31). The long axis orientation distribution is shown in figure 32, in form of a histogram and a rose diagram. It shows that the orientation is highly variable. There is a slight preferred orientation between 0 and 100 degrees azimuth, although there are peaks in 110 degrees and 160 degrees. The mean orientation is about 73 degrees that is shown by the red arrow in the rose diagram of figure 32. Figure 33 shows the spatial distribution of the orientation. There appears to be a preferred orientation of some of the pockmarks and mounds in accordance to the strike of the lineated trains of fluid flow features (numbers 3, 4, and 5 in figure 26). While for the features across the crest (number 1 in figure 26) orientations seem to be much more variable, but with a large share of the features oriented roughly perpendicular to the strike of the crest.

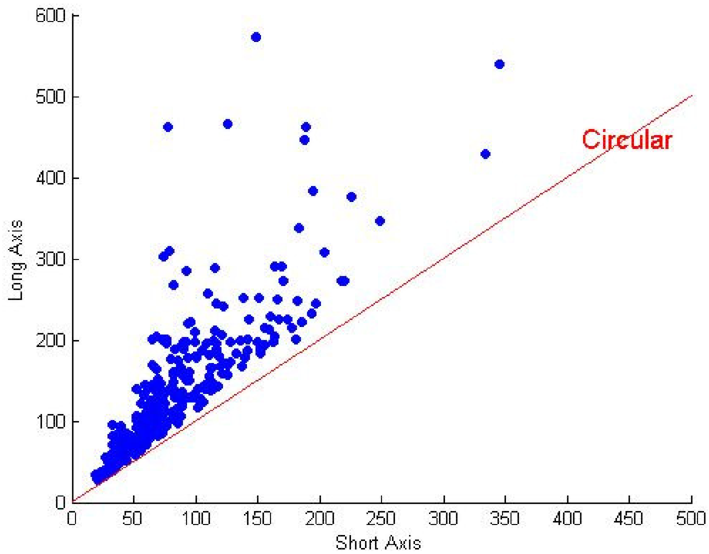

Figure 31- Scatter plot of long axis length vs. short axis length for the 192 target features considered in the statistical analysis (178 pockmarks and 14 mounds).

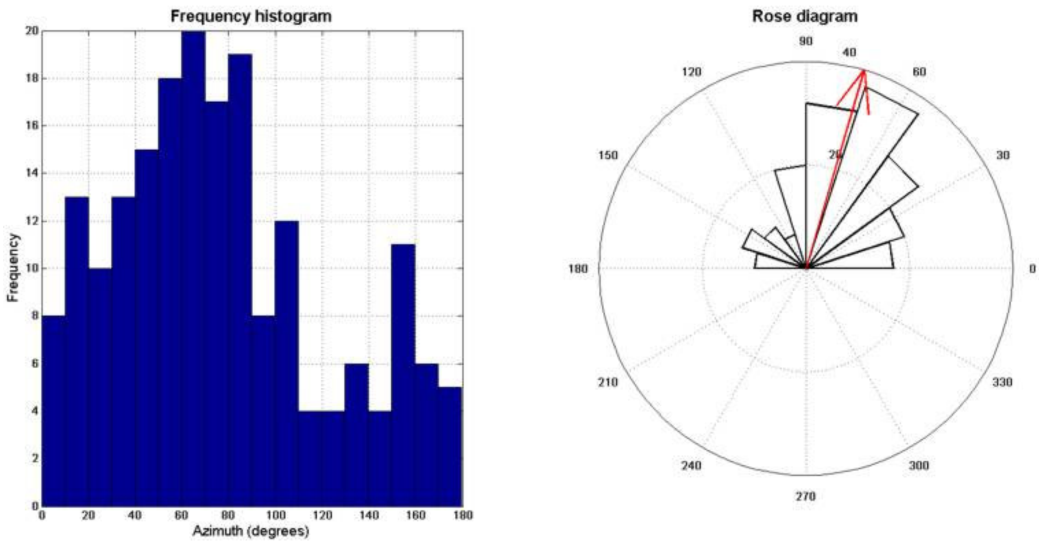

Figure 32 – Orientation of long axis (acquired from the best fitting ellipses) shown in a frequency histogram (left) and a rose diagram (right).

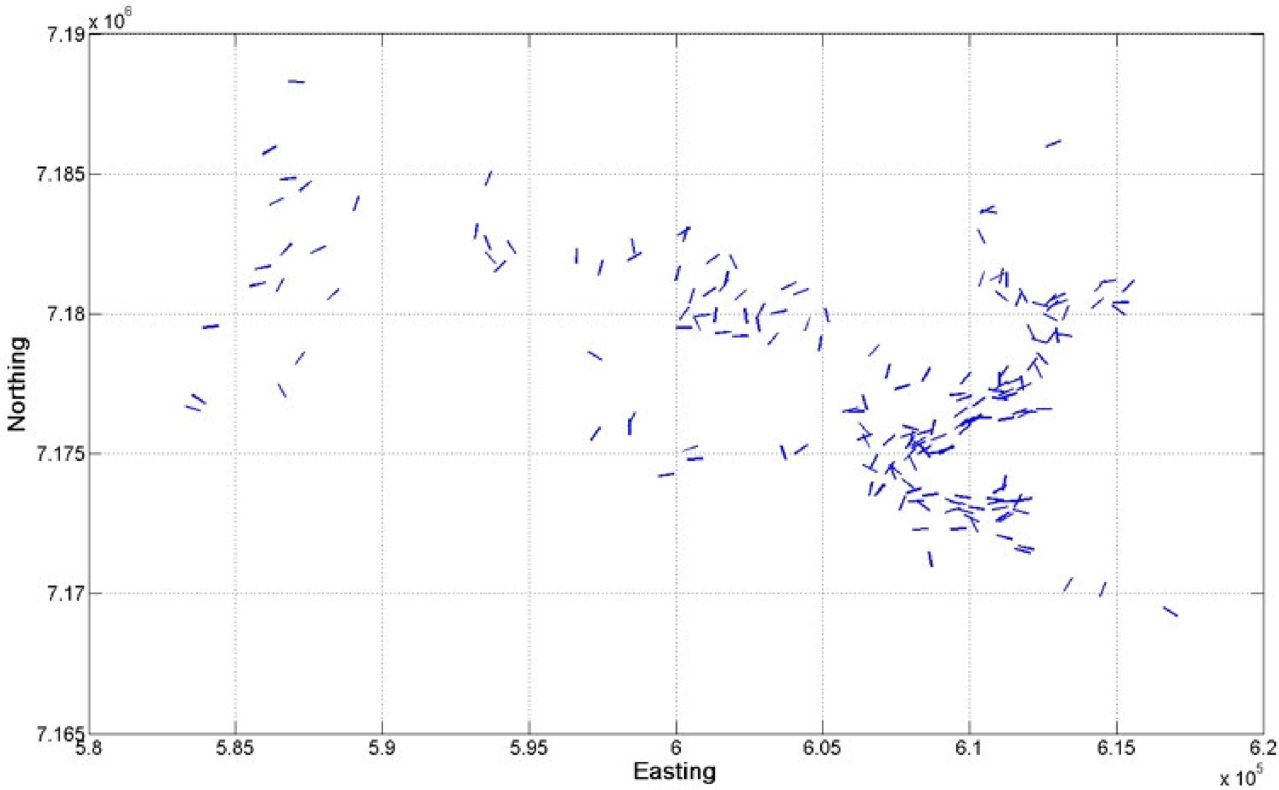

Figure 33 – Map of the orientation of the 178 pockmarks and 14 mounds chosen for the statistical analysis.

Measured perimeter values ranged from about 70 m up to about 1820 m, and the area values are between 300 m^2 up to about 130000 m^2 (figure 29). Figure 34 is a bullet map of the area values of the pockmarks and mounds. The largest features are pockmarks located in the western part of the study area close to the crest axis, and in the south-eastern part. Two relatively large mounds can be clearly distinguished, the smaller one is located over the crest axis and the larger is located along the features labelled number 4 in figure 26.

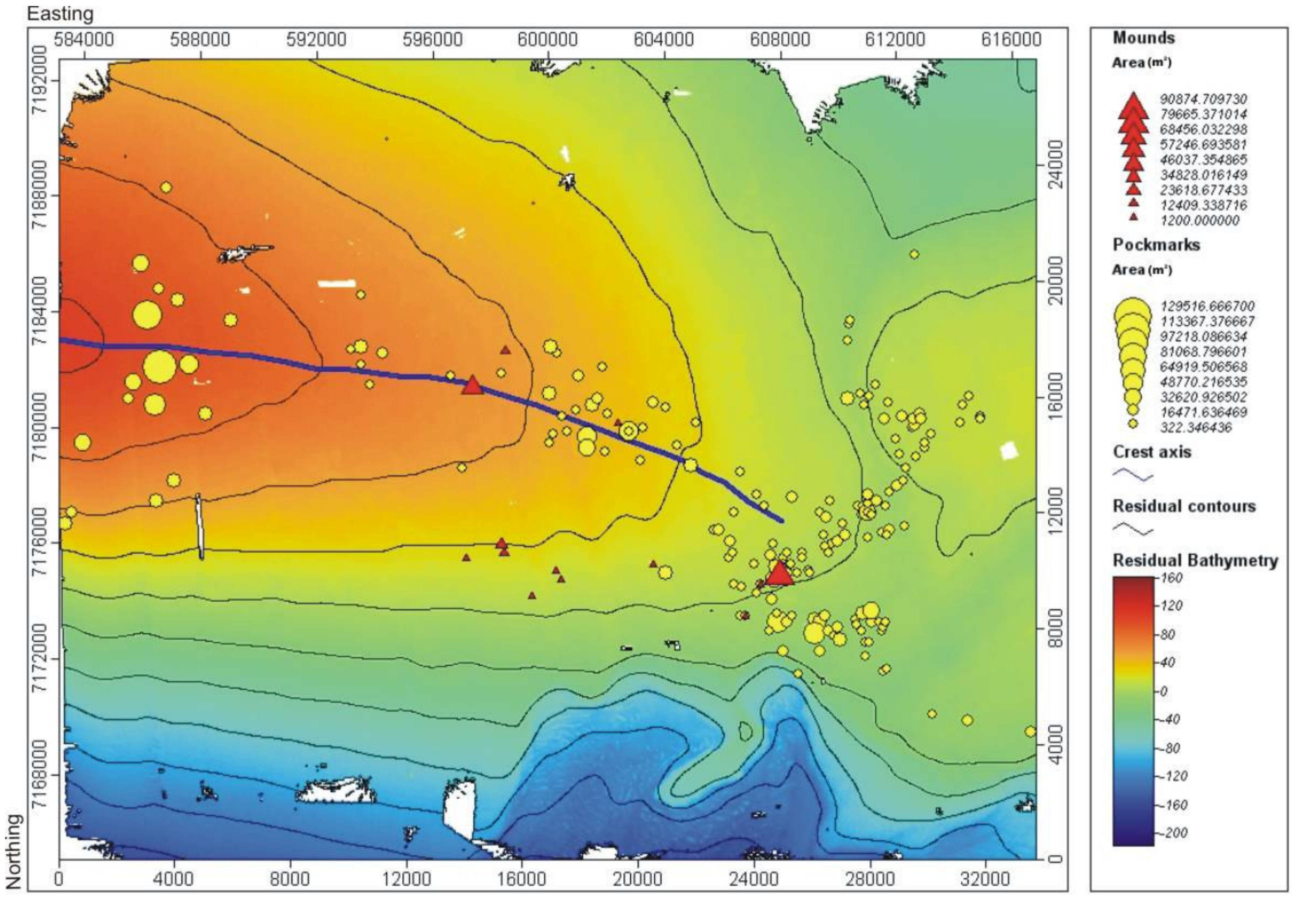

Figure 34 – Bullet map of area of the pockmarks and mounds over the residual bathymetry.

Mean slope angle values of pockmarks and mounds fall between 0.4 and 4.5 degrees (figure 29), with a mean of 1.85 degrees and a median of 1.78 degrees. The variance of the slope angle is a measure of the deviation from the mean of the slope along the rim of the pockmarks and mounds. The physical meaning of it is that it reflects the characteristic that some pockmarks and mounds happen to be sometimes steep in one side and have gentle slopes in the other. This information hopefully will be useful during the classification of these features by the multivariate statistical methods. Values are mostly between 0 and 2, with a mean of ~0.62 degrees^2 and a median of ~0.43 degrees^2, but with some outliers with more than 5 degrees^2.

4.1.2. Multivariate statistical analysis of pockmarks and mounds

4.1.2.1 Multidimensional scaling

The solutions of the multidimensional scaling are given in figure 35. The stress factor for the scaled 2 dimension solution was 0.05, which is good (Table 6). The solution shows that, as expected, the variables describing the size of fluid flow features (area, perimeter, short and long axis lengths) are closely related. The parameter variance of residual is also relatively closely related to the size, this may be partly due to the fact that variance was calculated from the grid cells inside the contour of the pockmarks and mounds, which implies that larger features have more grid cells and potentially more variance. The Mean slope angle and variance of slope angle also plot together indicating that they are positively correlated, that is larger mean slopes are generally accompanied by larger variance of the slopes. The mean residual and variance of residual plot distant from each other in figure 35 mainly due to the fact that the mean residual is split between positive (height of mounds) and negative values (depth of pockmarks), while the variance is a squared factor which means it is always positive. Had I used absolute values for the mean residuals, they would have plotted close meaning they are positively correlated. Orientation is not positively correlated with the other parameters.

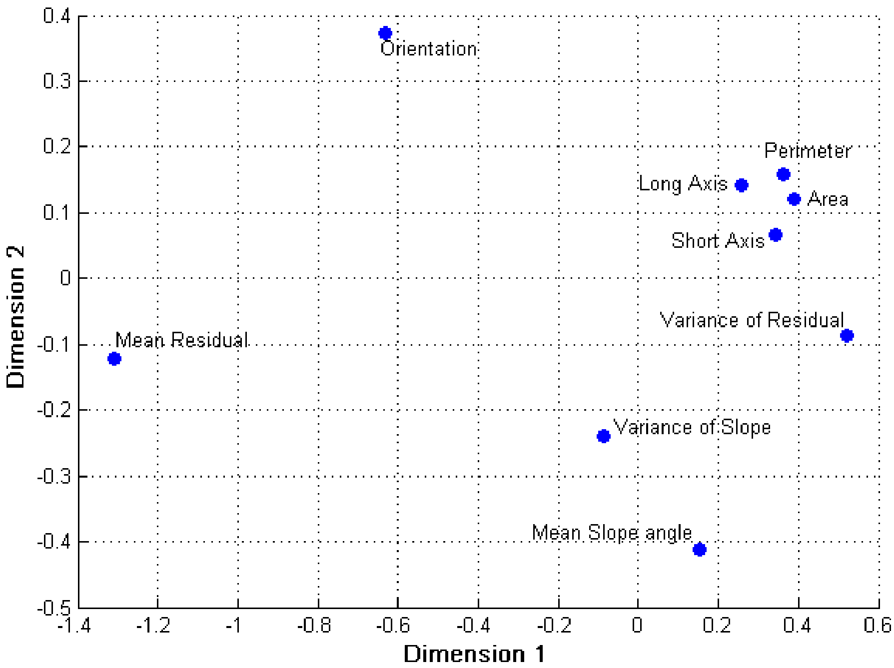

Figure 35 – R-mode multidimensional scaling solutions for the pockmarks and mounds data displayed in 2 dimensions. The R-mode multidimensional scaling solution produces 2D coordinates for the variables such that the distance between the variables is approximately equal to [1 - their Spearman's rank correlation value]. This means that variables that are closer to each other are more positively correlated than those more distant.

4.1.2.2. Cluster analysis

The results of the K-Means cluster analysis allowed classifying the pockmarks and mounds into 4 clusters comprising between 4.1 and 49.4 % of all observations (table 7). Most mounds were classified in one separate cluster, though one mound was classified within one of the other clusters.

The three clusters which comprise mainly pockmarks can be most easily distinguished by the relative size of the objects that range from small, medium to large pockmarks (figure 36d-g).

The small pockmarks cluster is the group with the largest number of observations (94 pockmarks). The elements of this cluster are absent within the westernmost mapped pockmarks and most densely distributed at the easternmost part of the area (figure 37). The small pockmarks are the ones with the shallowest depths, having a median mean depth of -2.7 m (figure 36b) and the median variance of the depth is close to 0.2 m^2 (figure 36c). The small pockmarks show the gentlest slopes of all classified features with a median mean slope of 1.4 degrees (figure 36h) and a median variance of slope of 0.25 $degrees^2$ (figure 36i). The median orientation of this group is 72 degrees azimuth (figure 36j).

The medium pockmarks cluster is the second largest group of pockmarks with 72 observations. They are densely distributed within the east, where they are intermingled with small pockmarks, while in the westernmost part they are not so densely distributed but are the predominant group (figure 37). The median mean depth is -3.3 m (figure 36b) and the median variance is 0.75 m^2 (figure 36c). The medium pockmarks have the steepest slopes with a median of mean slope of 2.35 degrees (figure 36h) and a variance of 0.8 $degrees^2$ (figure 36i). The median orientation is 74 degrees azimuth (figure 36j).

The large pockmarks are the rarest of the classified clusters with only 8 occurrences. They are predominantly found in the westernmost part which concentrates 50% of the occurrences (figure 37). This cluster has the deepest pockmarks with a median mean depth of about -3.7 m (figure 36b) and a median variance of depth of 1.4 m^2 (figure 36c). The median mean slope is 2.1 degrees (figure 36h) and a median variance about the mean slope of 0.75 $degrees^2$ (figure 36i). The Median orientation is of 42 degrees azimuth (figure 36j).

The mounds cluster consists only of mounds, although one mound was classified within the medium pockmarks (figure 36b). The mounds are found as one isolated patch in the middle of the map and in some other areas mixed mainly with small and medium pockmarks (figure 37). The median mean height is around 2.5 m and the median variance around the height is of about 0.05 m^2. The median mean slope within the mounds is about 1.5 degrees (figure 36h) and the variance about the mean slope is of around 0.5 $degrees^2$ (figure 36i). The orientation is of 58 degrees azimuth (figure 36j).

Table 7 – Results of the cluster analysis for the 192 pockmarks and mounds chosen for the statistical analysis, including cluster name, share of objects in each cluster and relative size, slope and orientation within each cluster, as interpreted from the cluster properties (figure 36).

Cluster name	Share of Objects (%)	Relative Residuals	Relative Size	Relative Slope	Orientation
Large pockmarks	4.1	Large negative mean, high variance.	Largest size	Steep slopes with high variance	Median of 42 degrees
Medium pockmarks	37.5	Medium negative mean, medium variance	Medium size	Steepest slopes, medium variance	Median of 74 degrees
Small pockmarks	49	Small negative mean, small variance	Small size	Small angles, small variance	Median of 72 degrees
Mounds	6.7	Positive mean residual, very small variance	Small size	Medium slopes, small to medium variance	Median of 58 degrees

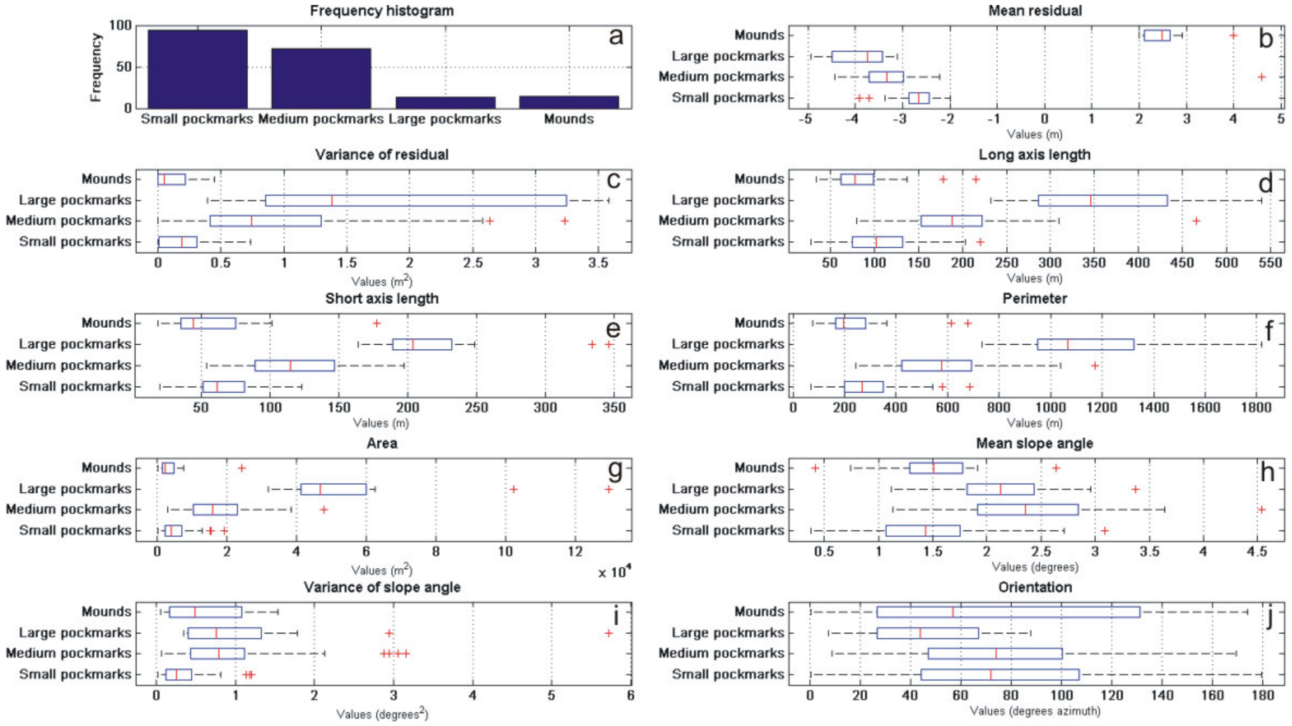

Figure 36 – Distribution of the parameters (x-axis) of 178 pockmarks and 14 mounds (y-axis) among the four clusters determined in the k-means cluster analysis. The central red line in the box plots represents the median value and the outer edges of the boxes are the 25 th and 75 th percentile. The max. error bars represent the 10 th and 90 th percentile and the individual crosses are outliers beyond these limits.

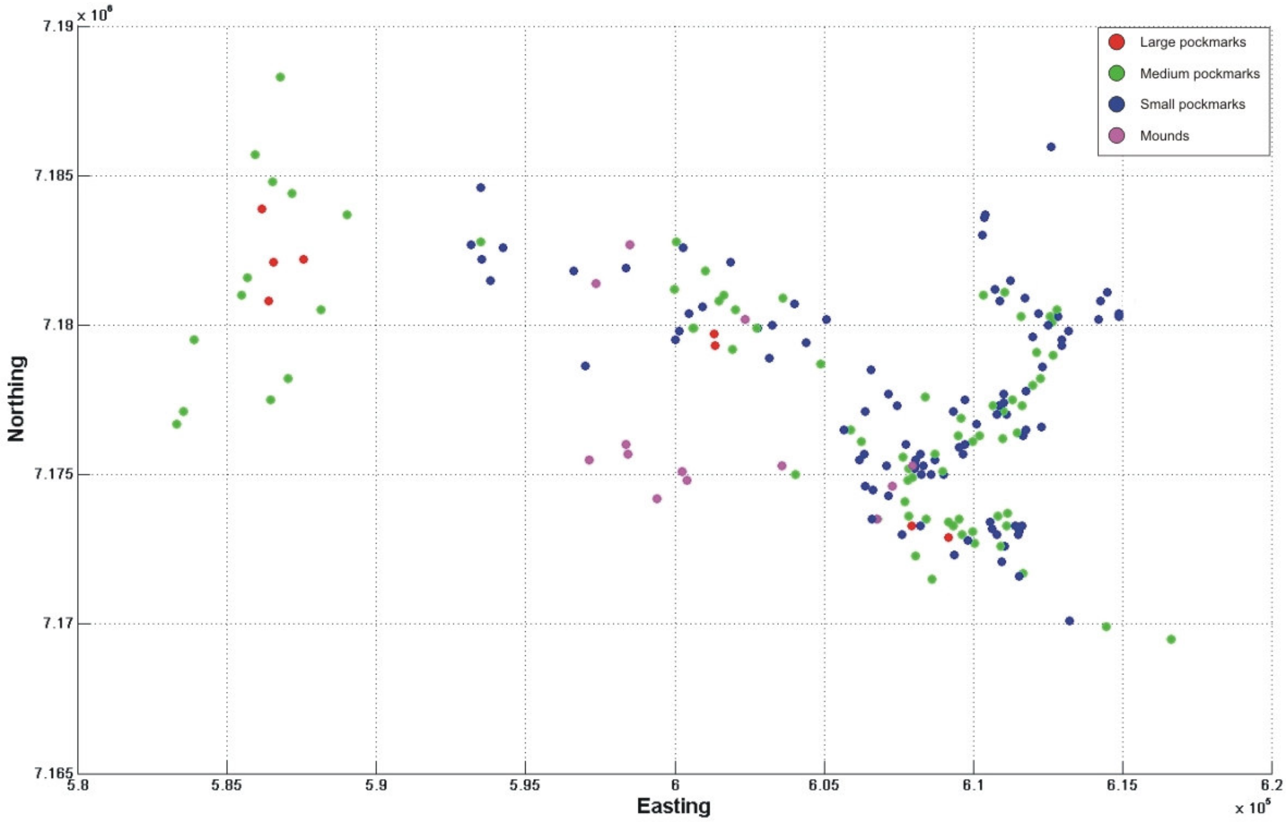

Figure 37 – Spatial distribution of the 4 clusters classified by the kmeans algorithm from the pockmarks and mounds data indicating that based on the classification of pockmarks and mounds there is a predominance of medium and large pockmarks in the western part of the map, while in the east there is a predominance of mounds, small and medium pockmarks.

4.2. 3D Seismic Interpretation and subsurface distribution of acoustic chimneys

The seismic interpretations are based on the tracking and analysis of a series of prominent reflections (figure 38) and the analysis of attribute maps derived from them. This resulted in the identification of shallow features relevant to the development of fluid flow pathways in the area. The most important prominent reflections are the BSR and high amplitude reflections. The geometry of the seal on top of the high amplitude reflections was also interpreted. Moreover, contourites, glacigenic debris flow deposits, major faults and acoustic chimneys could be distinguished on the basis of their particular seismic facies (Bünz et al., 2003; Berndt et al., 2004; Berndt, 2005; Bryn et al., 2005b; Cartwright et al., 2007). The stratigraphy used is that of Berg et al., (2005).

4.2.1. Description of stratigraphy within the area

The strong negative reflection at 2.8 s TWT (NE of figure 38A) is representing the base of the Brygge formation. This formation is thickest southeast of the Helland Hansen arch (figure 38; figure 39h). The Kai formation overlying the Brygge formation, is not only much thinner but also absent towards the crest of the Helland Hansen arch at the north-western part. Here, the Base Naust Unconformity (BNU) cuts into the Kai and Brygge formation (figure 38; figure 39g). The area beneath the BNU is affected by polygonal faults that concentrate in the Kai formation and uppermost 0.3 s TWT of the Brygge formation above the Helland Hansen Arch (figure 38).

Above the BNU, Naust W and U are characterized by thick prograding wedges (figure 38; figure 39f). These wedges completely cover the Helland Hansen arch with sediments filling the discrete basins between the domes positive topography. There is a large slide scar within these sequences, and also some high amplitude reflections mainly in the eastern part of the survey (figure 38).

Above reflection Top Naust U (TNU), the whole sequence of Naust S is characterized by contouritic deposits and high amplitude reflections. Reflection TNU marks the base of a series of high amplitude reflections that represent the lowermost part of the Naust S sequence. The top of these high amplitude reflections that have been named horizon “A” (figure 38) shows a strong reflection with negative polarity. The negative polarity has been attributed to a reduction in seismic velocity which is in turn interpreted by many authors to be caused by presence of free gas within the pore space of the sediments. (e.g. Bouriak et al., 2003; Mienert et al., 2005a; Hustoft et al., 2007). Intra Naust S2 (INS2) is the closest reflection to a major slide scar, named S2 (Solheim et al., 2005a), which cuts into sediments of Naust S3-4 in the southern part of the survey (figure 38; figure 39e). Above INS2, Naust S1-2 is laterally divided into two different seismic facies, in the south infilling contourite sediments partly buried the S2 slide scar and caused an associated moat striking SE-NW. The northwest area shows a thick package of mounded sediment drifts without any associated moat (figure 38; figure 39d). S1-2 is also partly characterized by high amplitude reflections. Some of these terminate abruptly in what is interpreted to be the base of the GHSZ. Also some attenuation of both amplitudes and frequencies of the seismic signal, as well as a large scale push down is affecting the reflections below the high amplitude areas within Naust S1-2.

The Top Naust S (TNS) marks the abrupt change from contouritic deposition to the deposition of relatively thick tongues of glacigenic debris flow deposits which comprise the Naust R3 unit. This contact is in many areas erosive, particularly within the domain of the infilling contourite deposits where debris flow channels cutting in the Naust S1-2 are found. The major depocenters of this unit is in the eastern part of the survey, over the moat of the S1-2 infilling contourites (figure 38; figure 39c). Contouritic deposition resumes after Intra-Naust R2 (INR2). Throughout the upper part of Naust R and Naust O reflections show patterns that may indicate the geometry of elongated mounded contourites. At the eastern area (figure 38B) the upper part of Naust O shows GDFs of Weichselian age, and in the south the northern escarpment of the Storegga Slide (figure 38A).

Particularly important for the fluid flow development in the area are the polygonal faults, the geometry of the sediment drifts that may act as potential shallow fluid reservoirs and the seal formed by the base of the gas hydrate stability zone. These were object of more detailed analysis during this master thesis.

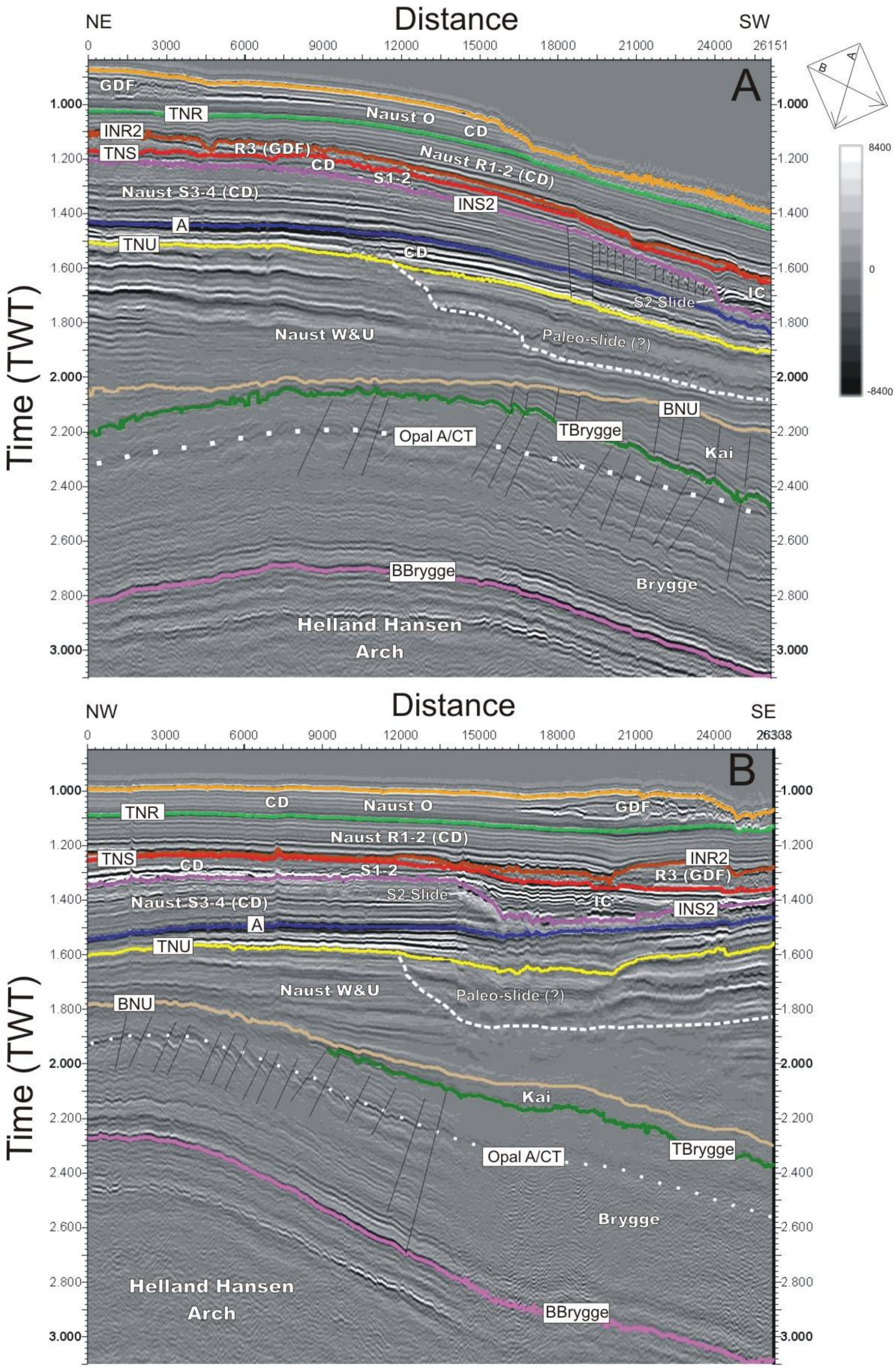

Figure 38 – Interpreted seismic sections across the ST0408 seismic survey: (A) Oriented along the dip of the margin; (B) Strike oriented. CD; Contourite drift; IC; Infilling contourite; GDF; glacigenic debris flows

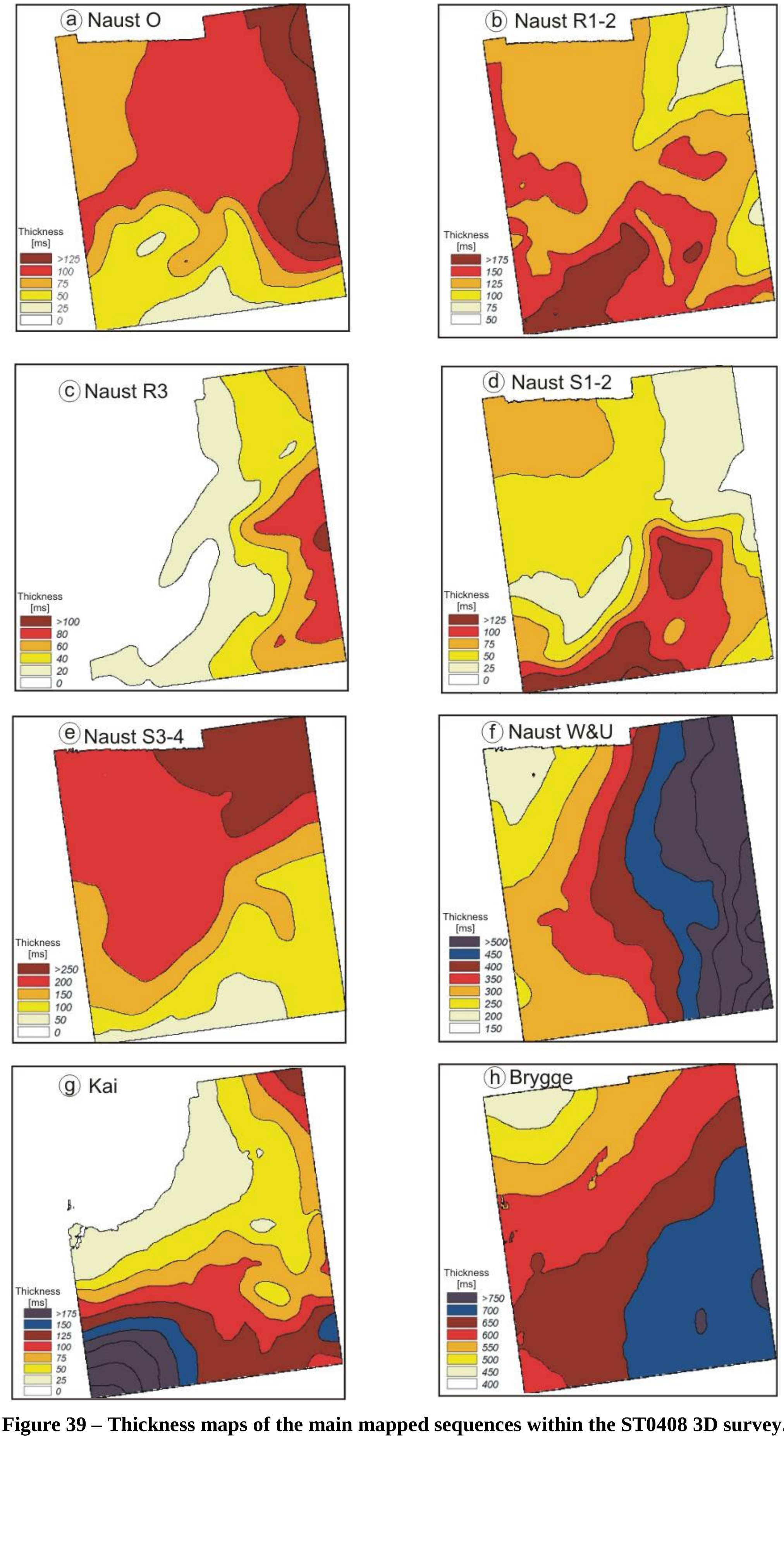

Figure 39 – Thickness maps of the main mapped sequences within the ST0408 3D survey.

4.2.2. The Polygonal faults

The polygonal faults that developed within part of the Brygge formation and Kai formation have their planar geometry best visualized at the Top Brygge (TBrygge, figure 38A) reflection (figure 40A). At this horizon polygonal faults seem to be more densely developed in the south-western part of the ST0408 survey area where also the largest fault offsets exist (>64 ms TWT) (>64 ms TWT) (figure 40B). The extracted RMS amplitudes from a 10 ms volume around the TBrygge (figure 38A) surface show the largest values also in the south-western part of the area (figure 41A). And a profile showing the reflection strength across a peak of RMS amplitude (figure 41B) shows a wide column of high amplitude reflections giving strong indications of fluid accumulation and migration starting from below the Base Brygge (BBrygge, figure 38A) reflection. If we look closer into the RMS amplitude map (figure 41A), we also notice a series of circular low amplitude anomalies, which could indicate focused fluid flow features. If this is the case, then fluid migration through the polygonal faulted Brygge formation might have occurred not exclusively along the faults but also by other vertical migration means.

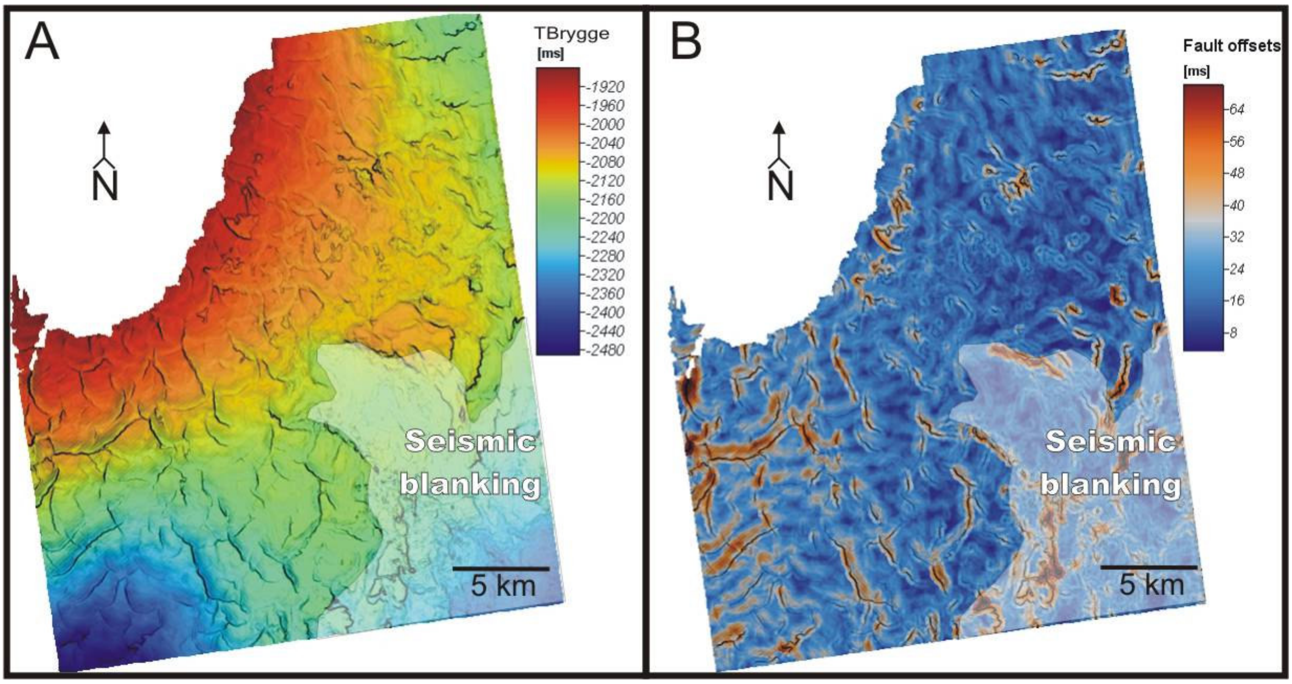

Figure 40 – (A) Time surface map of the Top Brygge reflection showing the geometry of the polygonal faults in plane view; (B) Map with the maximum offset of the faults. Both maps are shaded with the calculated slope of the Top Brygge time surface. Seismic blanking has affected the interpretation in the southeast part of the map, below the high amplitude zone of Naust S1-2.

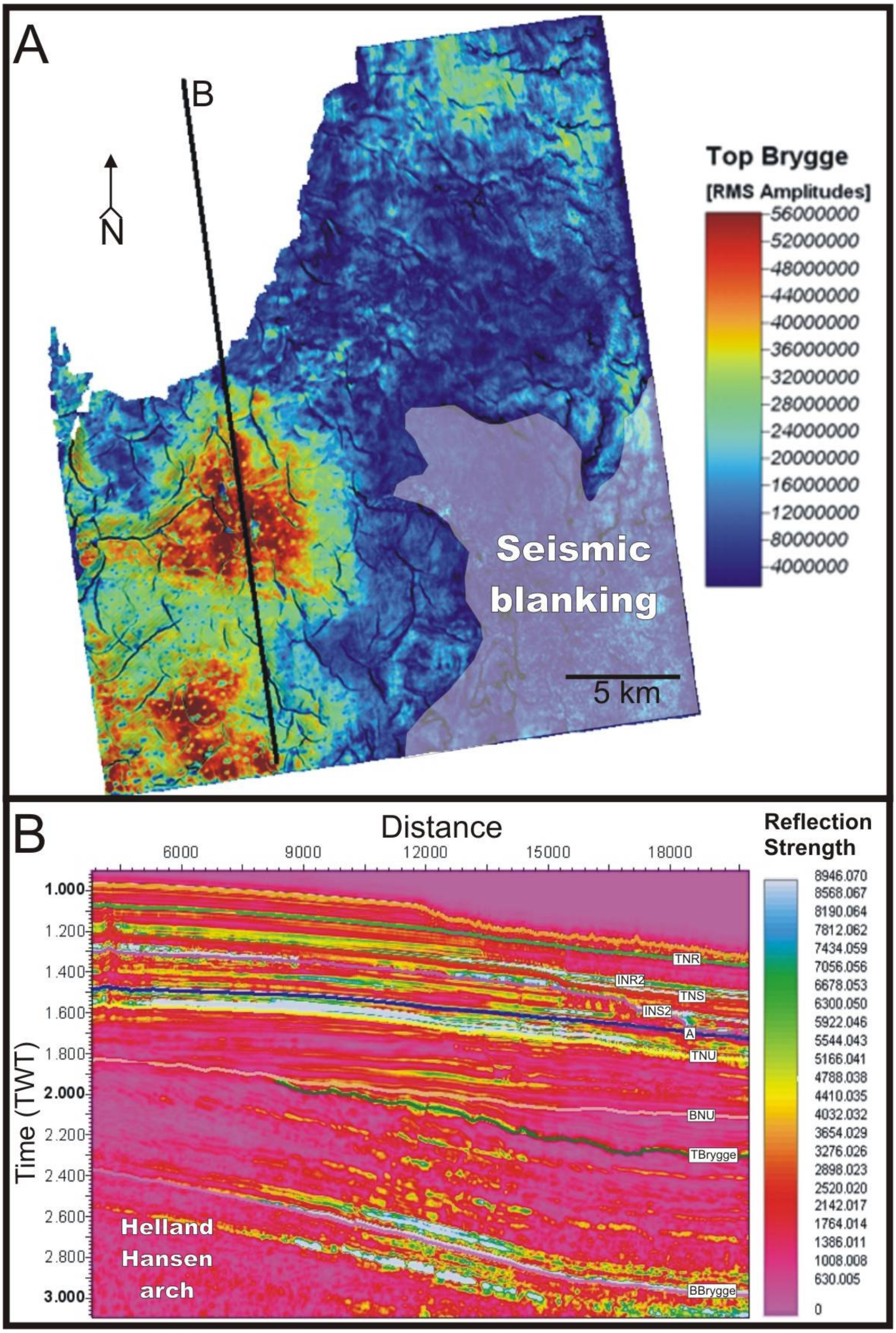

Figure 41 – (A) Map of root mean squared (RMS) amplitudes extracted from a volume of +- 5 ms around the Top Brygge surface, shaded with the slope of Top Brygge surface; (B) Reflection strength attribute section crossing a high amplitude zone within the map in A, and showing evidence of vertical fluid migration starting from below Base Brygge reflection.

4.2.3. Geometry of shallow reservoirs

There are distinct high amplitude reflections with negative polarity (“bright spots”) in the surveyed area, particularly within the Naust S sequence, but evidence for vertical fluid migration exists throughout the Brygge and also Kai formation (figure 41). The high amplitude reflections are occurring within contouritic sediments. The lowermost of these is the layer between TNU and reflection “A” (figure 41). This layer that is named Lower High Amplitude Zone (LHAZ), has already been suggested by several authors (Mienert et al., 1998a; Bouriak et al., 2003; Berndt et al., 2004) to be a zone of free gas accumulation. In the ST0408 data, indicators exists that this level is acting as a shallow fluid accumulation zone. A directional gradient map of the time surface of horizon A was created (figure 42). Assuming that there are no large differences in the capillary resistance within the sediments along this surface, and that the time surface closely resembles the depth surface, the directional gradients give a good approximation to which directions buoyant fluids would laterally migrate along the surface (Hindle, 1997). By connecting areas of convergent directional gradients, we can estimate the location of major transport pathways of buoyant fluids. In the comparison of the directions with the distribution of the RMS amplitudes extracted from a 10 ms volume window below horizon “A” we observe good correlation, which are high amplitudes in areas of convergence of the directional gradients (figure 42). Towards the southwest, it is also possible to identify a set of normal faults which are delimiting distinct changes in the amplitudes along the map (figure 42a-b). Such changes in amplitude give indications that these faults are acting as seals to lateral migration and at the same time give further evidence that the RMS amplitudes are indeed reflecting the distribution of fluids within this high amplitude zone (figure 42).

Above the LHAZ, within the sediments of Naust S1-2 there are two major high amplitude zones, which are separated by a band of low amplitudes (figure 44). We called the north-western high amplitude zone upper high amplitude zone 1 (UHAZ1) and the south-eatern bright spots UHAZ2. The seal of these potential fluid accumulation zones is more complex than in the case of LHAZ, because it is partially made by both the base of the R3 glacigenic debris flows and the base of the GHSZ (BGHSZ) (figure 45). The gas hydrate related BSR in the ST0408 seismic survey is usually not characterized by a continuous cross cutting reflection, but instead it is mostly characterized, where present, by the abrupt termination of high amplitude reflections (figure 43). This result is similar to previous descriptions of the BSR in the area (e.g. Bouriak et al., 2003; Bünz et al., 2003; Berndt et al., 2004; Hustoft et al., 2007).

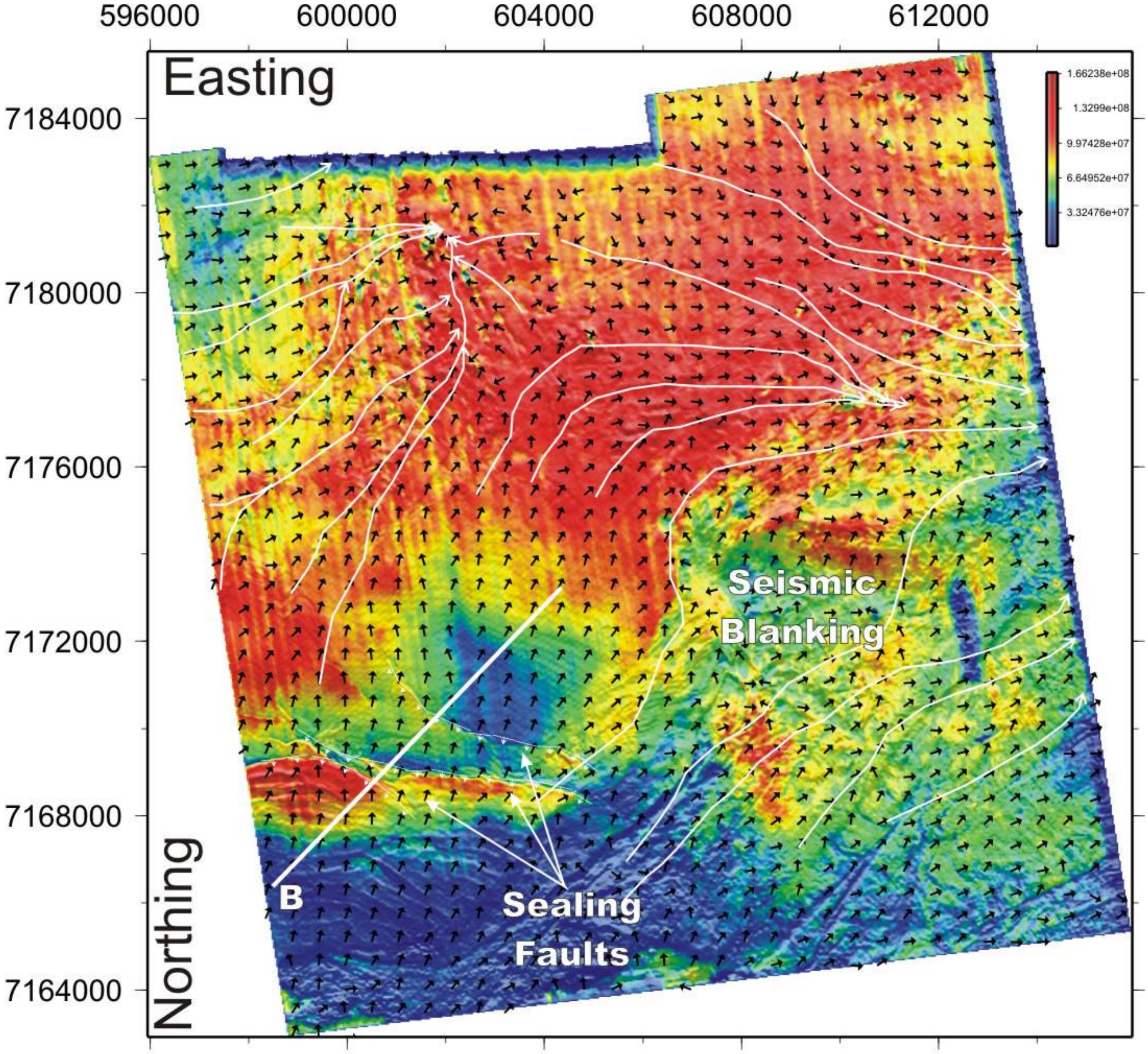

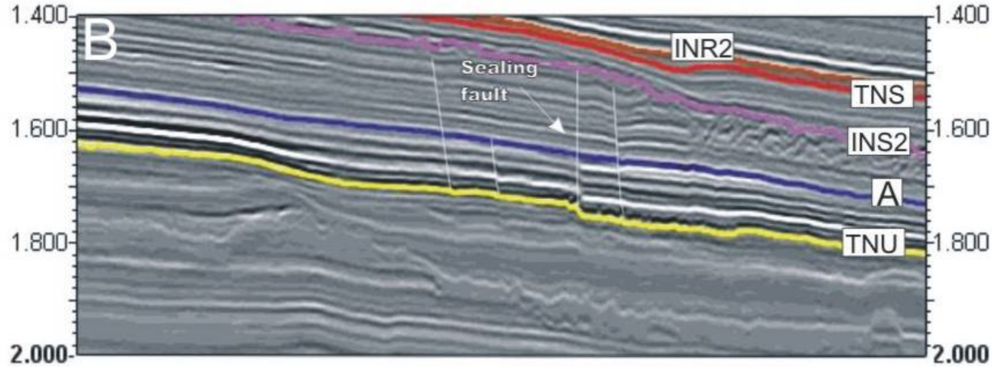

Figure 42 – (A) RMS amplitude extracted from a 10ms window below horizon A shaded with the northerly illuminated relief of horizon A; the small black arrows are the median directional gradient taken over a circular area of 540 m in diameter around the gridcells of horizon A; the white arrows are potential flow paths of buoyant fluids interpreted by connecting zones of convergent directional gradients; Normal faults marking sharp discontinuities in the amplitude map are marked by white symbols; (B) Cropped seismic section showing the extent of the large scale faults presumably acting as a seal to lateral fluid migration.

Within Naust S1-2 the BSR is visible as a boundary between two different seismic facies (figure 38; figure 43; figure 45). Below the BGHSZ, Naust S1-2 is characterized by strata with high amplitude reflections while above the BGHSZ acoustic blanking exists (Lee and Dillon, 2001). In the southeast, the BSR cross cuts the sediments of Naust S1-2 at the upper part of the slide scar and at the most distal parts where the recent Storegga Slide event forced a readjustment of the BGHSZ due to a removal of parts of the overburden (figure 43B; figure 45). The boundary (BGHSZ) lies in average 315 ms below the seafloor reflection, and runs parallel to the seafloor. A smoothed version of the seafloor reflection was used as an approximation to the geometry of the seal for potential fluid accumulations in the UHAZ1 and an approximation of the seal for UHAZ2 using either the geometry of the seafloor or the base of the glacigenic debris flows of R3 unit was applied, depending on which was the deeper. The resultant surface shows that the two Upper High Amplitude Zones are laterally separated by updip pinch-outs against the BGHSZ seal. The planar geometry of this pinch out follows the abrupt termination of the high RMS amplitudes (figure 44; figure 45).

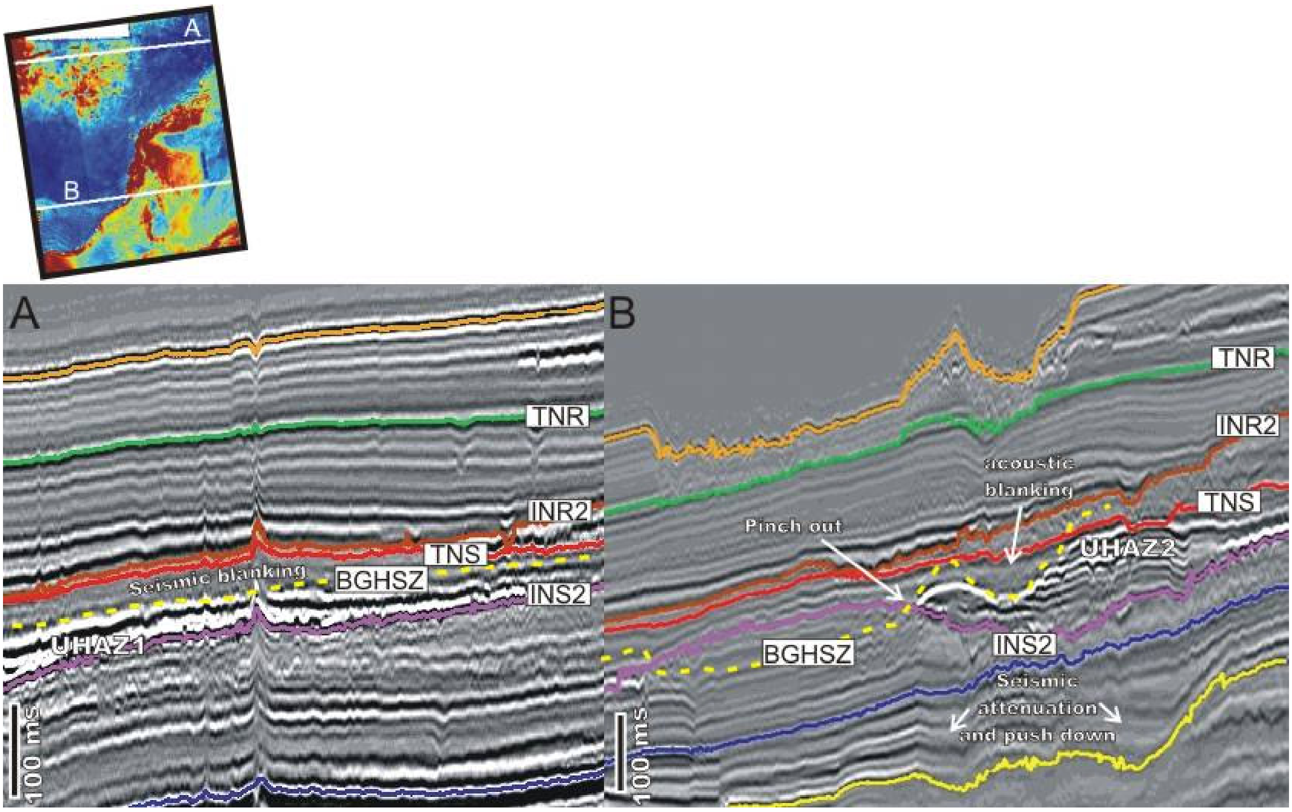

Figure 43 – Cropped seismic sections across: (A) Upper reservoir 1; (B) Upper reservoir 2; BGHSZ is the seafloor approximation to the base of gas hydrate stability zone.

The resultant seal or "trap" to fluid accumulations in the UHAZ1 and UHAZ2 was used to calculate the directional gradient, in a similar manner as in the case of the LHAZ, and estimate potential lateral fluid flow pathways assuming that fluids are free to migrate laterally. The resultant flow paths, once again showed an appreciable fit with the distributions of the RMS amplitudes of the Naust S1-2 unit (figure 44).

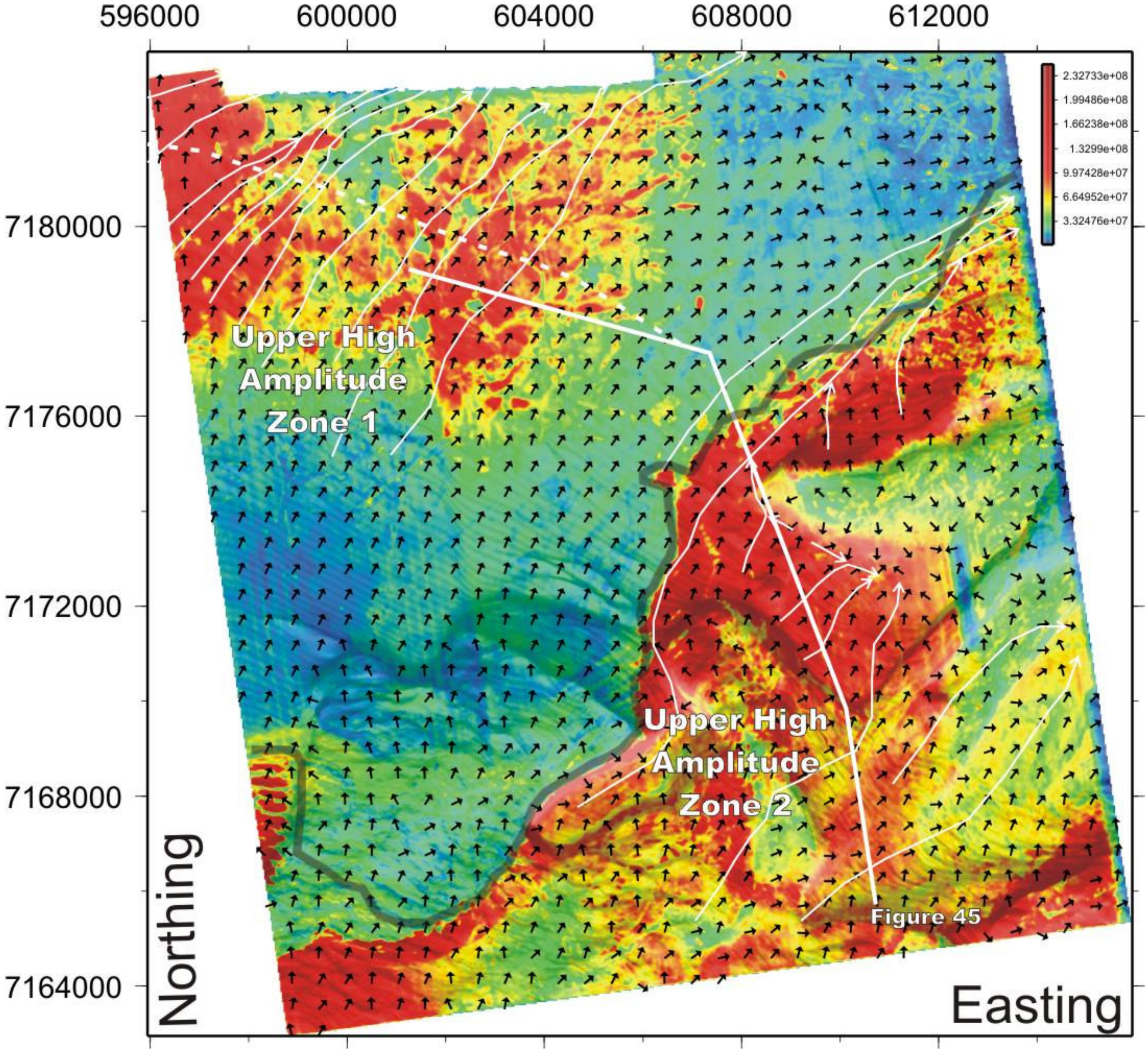

Figure 44 – RMS amplitude extraction map of Naust S1-2 shaded by the northerly illuminated top seal, showing the amplitude distribution of the two upper shallow reservoir units; short black arrows are the median directional gradient of the top seal taken over a circular area of 540 meters in diameter; long white arrows are potential flow paths interpreted by connecting zones of convergent directional gradients; white stippled line along UHAZ1 is the crest axis; broad semi-transparent black line marks the intersection between the seafloor approximation to the BGHSZ and the INS2 reflection at the upper part of the S2 slide scar. Note the sometimes dendritic pattern of the RMS amplitude distribution at UHAZ1 and close to the updip pinchout of the UHSZ2, and how this pattern fits well with the directional gradients.

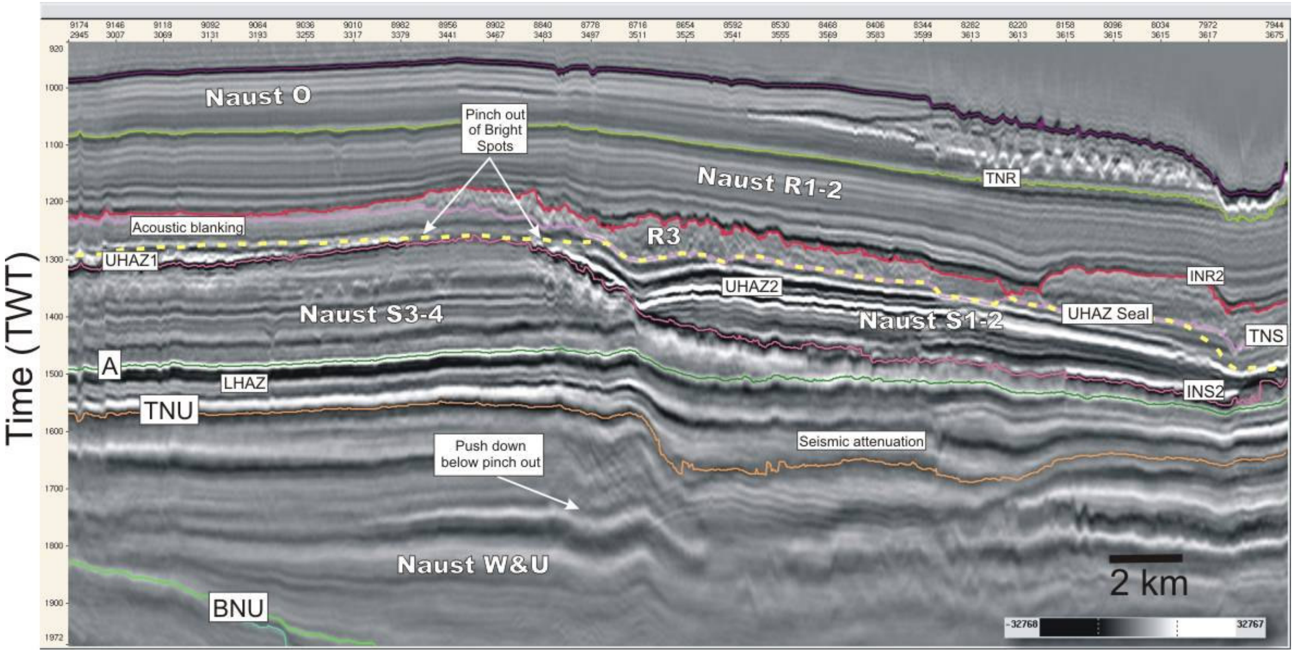

Figure 45 – Composite seismic section showing the stratigraphic expression of the high amplitude zones within Naust S. UHAZ; Upper high amplitude zone 1; LHAZ; Lower high amplitude zone; UHAZ Seal; Top seal formed partly by the seafloor approximation to the BGHSZ and the base of the R3 GDF unit; Location in figure 44.

4.2.4. Mapping and quantification of acoustic chimneys

A total of 441 acoustic chimneys were identified within the ST0408 3D seismic cube. The terminology used here is that of Cartwright et al., (2007), that is acoustic chimneys which terminate at the seafloor are called blowout pipes, while those terminating at deeper stratigraphic horizons are named seepage pipes. The quantified parameters are shown in a table in appendix, and examples of mapped pipes are shown in figure 47. The numbering of the horizons relative to the seismic data is according to table 8. The spatial distribution of the mapped features is shown in figure 46. The statistical distribution of the quantified parameters in form of frequency histograms, box plots, length relationships, and rose diagrams are shown in figure 48, figure 49, figure 50 and figure 52.

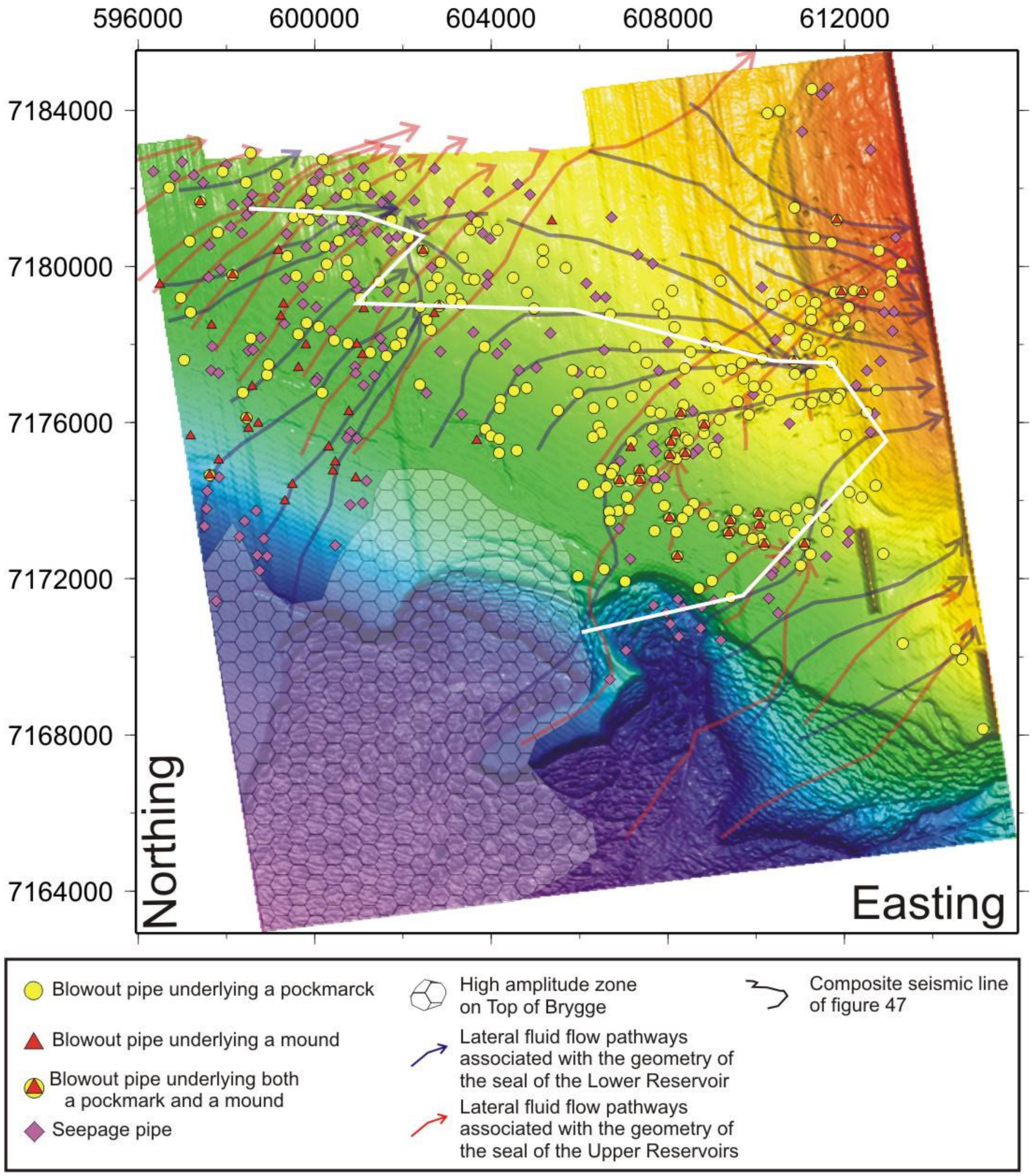

Figure 46 – Seafloor reflection time map with the spatial distribution of mapped acoustic chimneys in the ST0408 3D seismic survey.

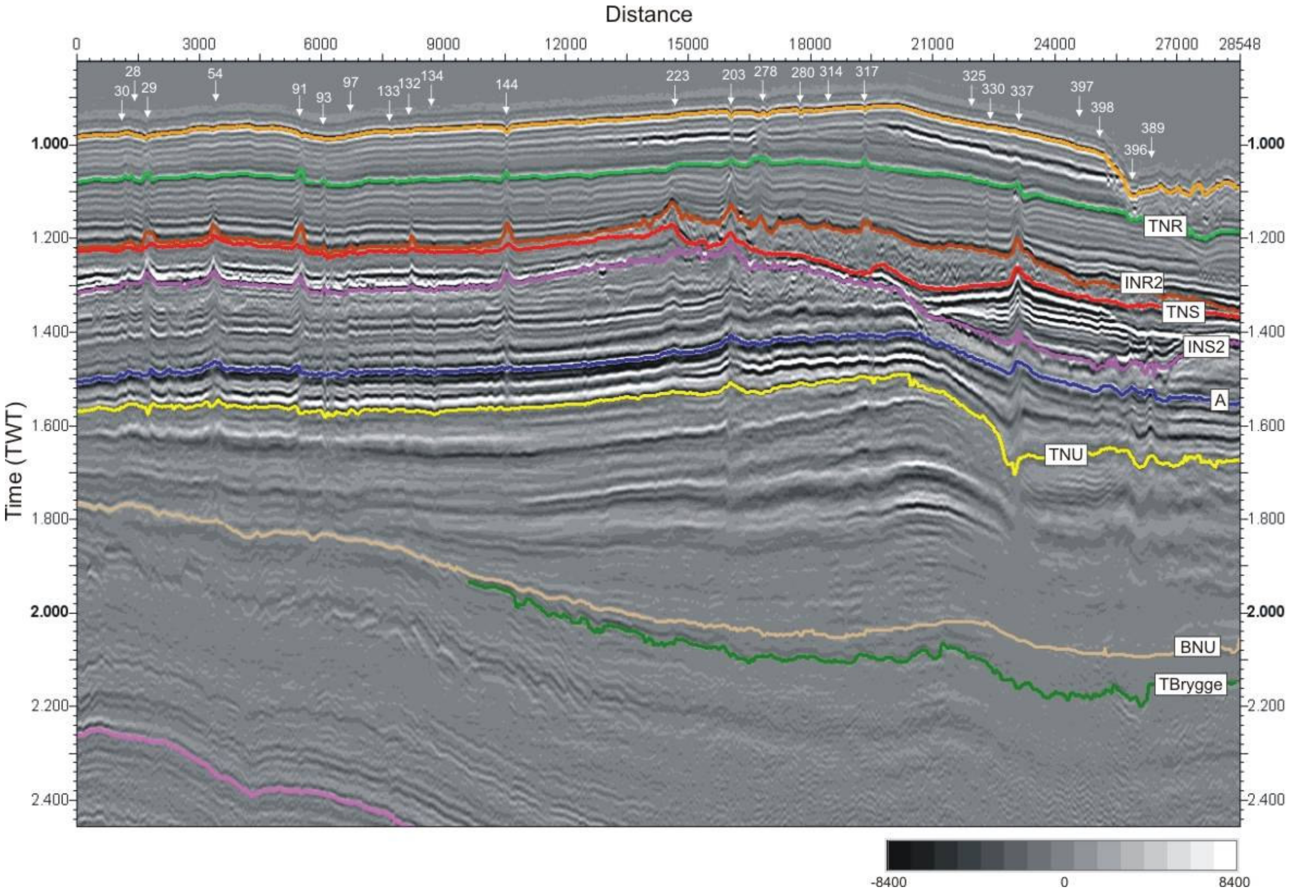

Figure 47 – Composite line crossing pipes in the ST0408 seismic cube. White arrows mark the pipes and the numbers are the reference numbers of the pipes in appendix B. Location in figure 46.

Table 8 – Correspondence between horizon numbering and seismic reflections within ST0408 survey (see also figure 38 and figure 47).

Horizon number	Reflection
1	**Seafloor**
2	**One reflection below Seafloor**
3	**Two reflections below seafloor**
4	**One reflection above TNR**
5	**Top Naust R (TNR)**
6	**Uppermost strong reflection above INR2**
7	**Lowermost strong reflection above INR2**
8	**Intra Naust R2 (INR2)**
9	**Top Naust S (TNS)**
10	**Intra Naust S2 (INS2)**
11	**Strong reflection below INS2**
12	**Strong reflection above horizon “A”**
13	**Horizon “A”**
14	**One reflection above TNU**
15	**Top Naust U (TNU)**
16	**Uppermost reflection below TNU**

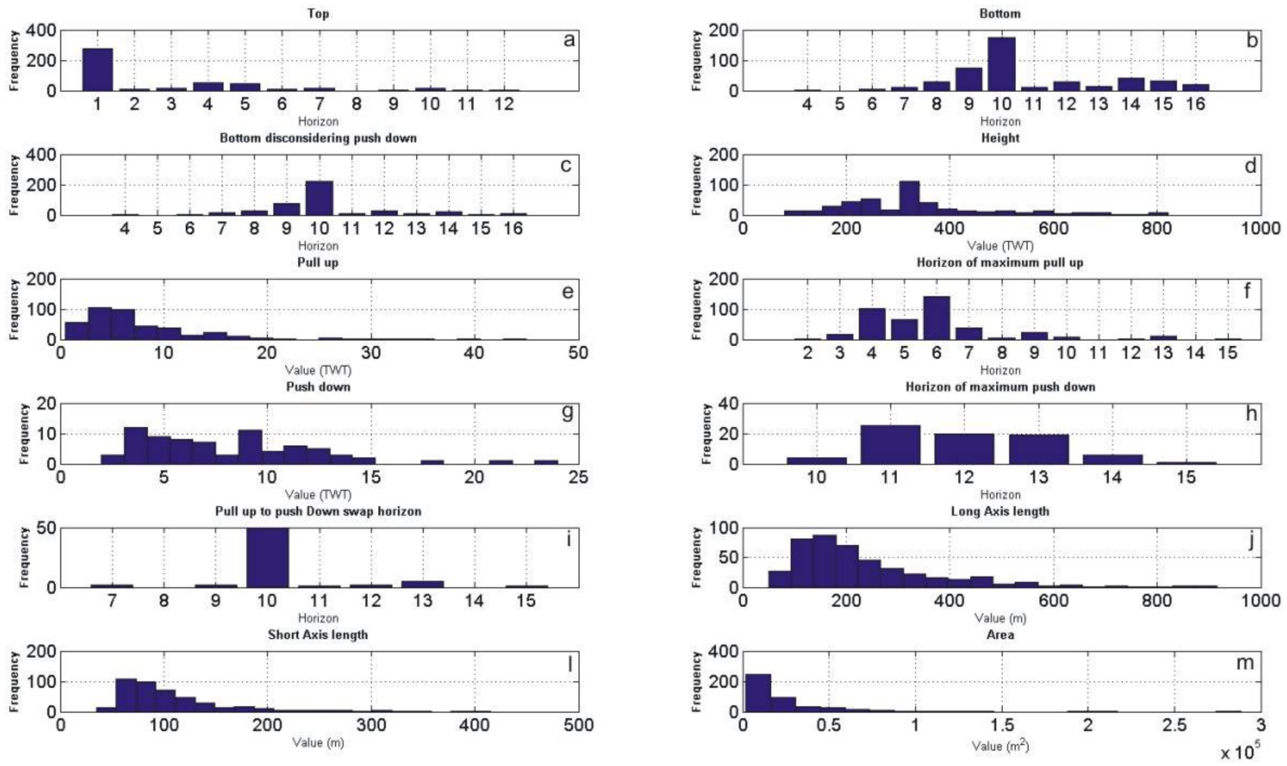

Figure 48 - Part of the collected parameters shown in frequency histograms. Correspondence between horizon numbers and seismic interpretation is given in table 8. Orientations of longest axis are shown in figure 52.

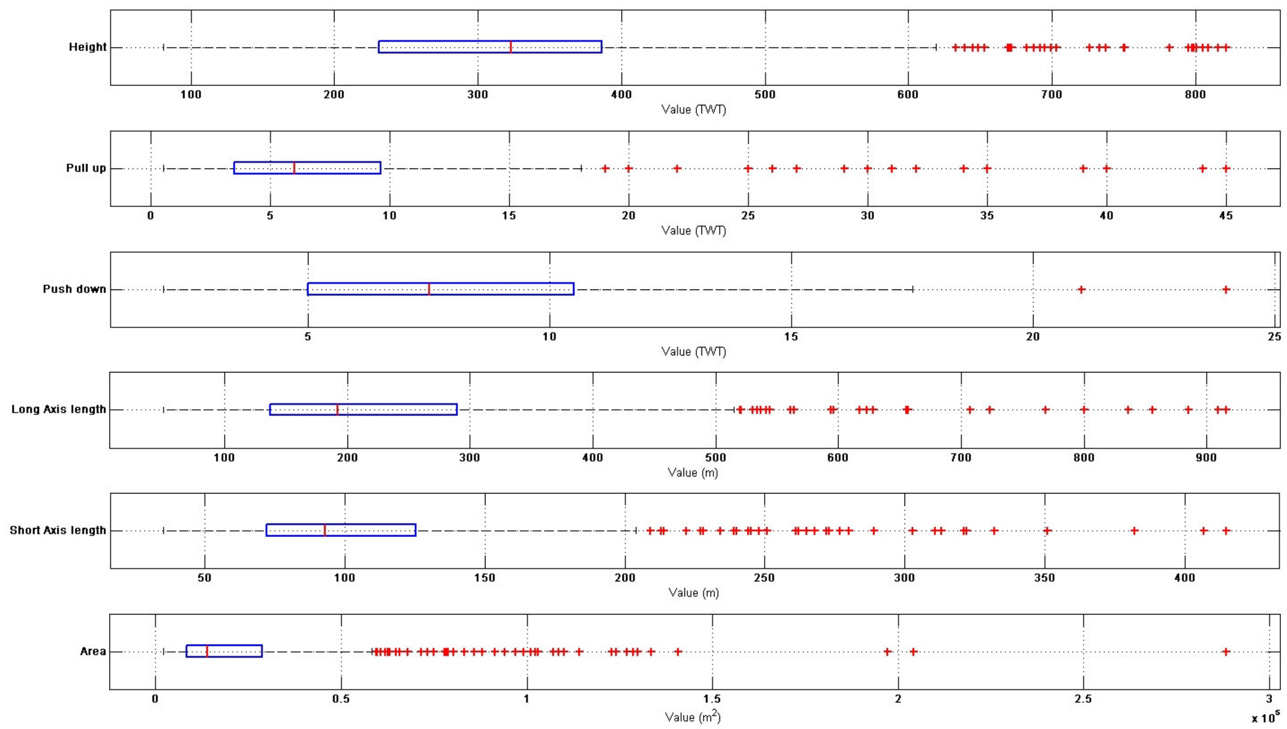

Figure 49 – Box plots of the parameters with continuous values. The central red line represents the median of the dataset, the outer edges of the boxes are the 25 th and 75 th percentile, the ends of the error bars represent the 10 th and 90 th percentile and the individual crosses are outliers beyond these limits.

Most of the pipes (~62%) terminate at the seafloor (figure 46 and figure 48a), where one or more pockmarks, mounds or both are usually present (figure 46). Others are terminating at different stratigraphic levels with predominance of 4 (One above TNR, table 8) and 5 (TNR, table 8) which together account for ~20 % of the upper termination of pipes. In fact most of the pipes drastically reduce in size above TNR. Thus it is possible that some of these pipes which are apparently terminating at these levels are actually falling below the seismic resolution.

The bottom (base) termination of the pipes is difficult to identify due to the fact that the seismic signal attenuation increases below some of these features (figure 47). This is particularly true for those pipes which present push down of reflections below some specific horizons. This way I have chosen to show two possible bottom interpretations, one considering extent with the push down and the other considering only the extent with pull up. In the first case (figure 48b), 246 (~55%) pipes appear to originate from horizons 9 (TNS, table 8) and 10 (INS2, table 8), and other 147 (~33%) pipes originate from horizons below. While in the second case (figure 48c), 297 (~67%) pipes originate from horizons 9 (TNS, table 8) and 10 (INS2, table 8), and only 81 (~18%) originate from horizons below 10 (INS2, table 8).

The height of the pipes (ms TWT) was computed using the whole range of identifiable features, including the area affected by push down. It ranged between ~80 and ~881 ms TWT, with a mean of 340 ms and a median of 323 ms (figure 48d; figure 49a). The mean and median height is reflecting the average depth to the base of the gas hydrate stability zone, where most of the pipes seem to originate from (figure 48b-c).

Pull up of reflections, is not necessarily caused by velocity distortions or seismic migration artifacts, because it could also be caused by real structural deformation. The push down effect is most likely a velocity distortion caused by localized concentration of free gas causing a decrease in seismic velocity. Note that 27 (~6%) of the pipes had either no associated up bending (pull up) or the effect was too small to be measured. Within pipes that showed pull up, the values varied between 0.5 and 45 ms, with a mean of 7.8 ms and a median of 6 ms (figure 48e; figure 49b). Maximum pull up was found to be dominantly within horizons 4 (One above TNR, table 8) to 7 (Lowermost strong reflection above INR2, table 8) with 347 pipes (~ 81%) showing maximum values at this levels (figure 48f), above the level of maximum pull up there is usually a very drastic reduction in the pull up effect (figure 47). Only 76 (~17%) pipes showed a push down of reflections, and the values measured were between 2 and 24 ms with a mean of 8.1 ms and a median of 7.5 ms (figure 48g; figure 49c). Maximum push down is approximately distributed evenly within horizons 11 (One reflection below INS2, table 8) to 13 (horizon A, table 8), which together concentrate 68 (89%) of the maximum push down observations (figure 48h). While the minority of pipes (17) showed only push down effect, the majority showed push down but also pull up. The dominant level where this change from pull up to push down of reflections occurred at was horizon 10 (INS2, table 8) with 81% of those pipes showing both pull up and push down, followed by horizon 13 (horizon A, table 8) with 8% of those pipes.

Long axis length of the pipes varied between 50 and 916 m with a mean of ~238 m and a median of 192 m (figure 48g; figure 49c), and the short axis lengths ranged from 35 to 415 m with a mean of ~111 m and a median of 93 m (figure 48g; figure 49c). The mean values of 238 and 111 m indicate that the pipes are, similar to seabed pockmarks and mounds, mostly elongated features (figure 50).

Area values ranged between ~ 2000 m^2 and ~ 290000 m^2, with a mean of 25491 m^2 and a median of 13854 m^2. The area values show a good correlation with the pull up values, giving an indication that the larger the feature the larger the associated pull up. This becomes obvious in the bullet map showing area and coloured pull up values (figure 51). There is also a tendency of pipes with larger area and pull up to have origin (bottom) in deeper horizons (figure 51). At the same time large pipes seem to occur mainly close to areas where there is a convergence of major fluid flow pathways along the top of the high amplitude zone LHAZ, but some occur also at convergent zones of the UHAZ seal (figure 51). The association between the major fluid flow pathways and the location of the acoustic chimneys is sometimes in contrast with the quantified bottom (figure 51), a situation which creates an ambiguity regarding the true extent (and thus origin) of the acoustic pipes.

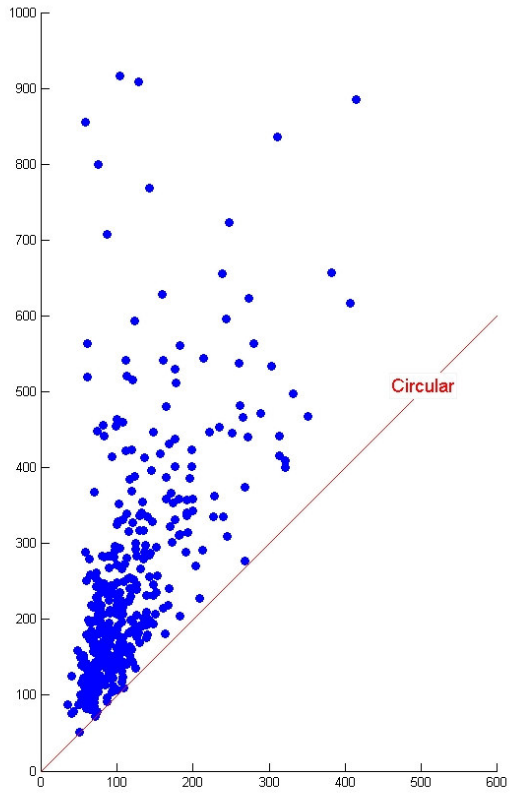

Figure 50 - Scatter plot of long axis length vs. short axis length for the 441 quantified acoustic chimneys within the ST0408 seismic cube.

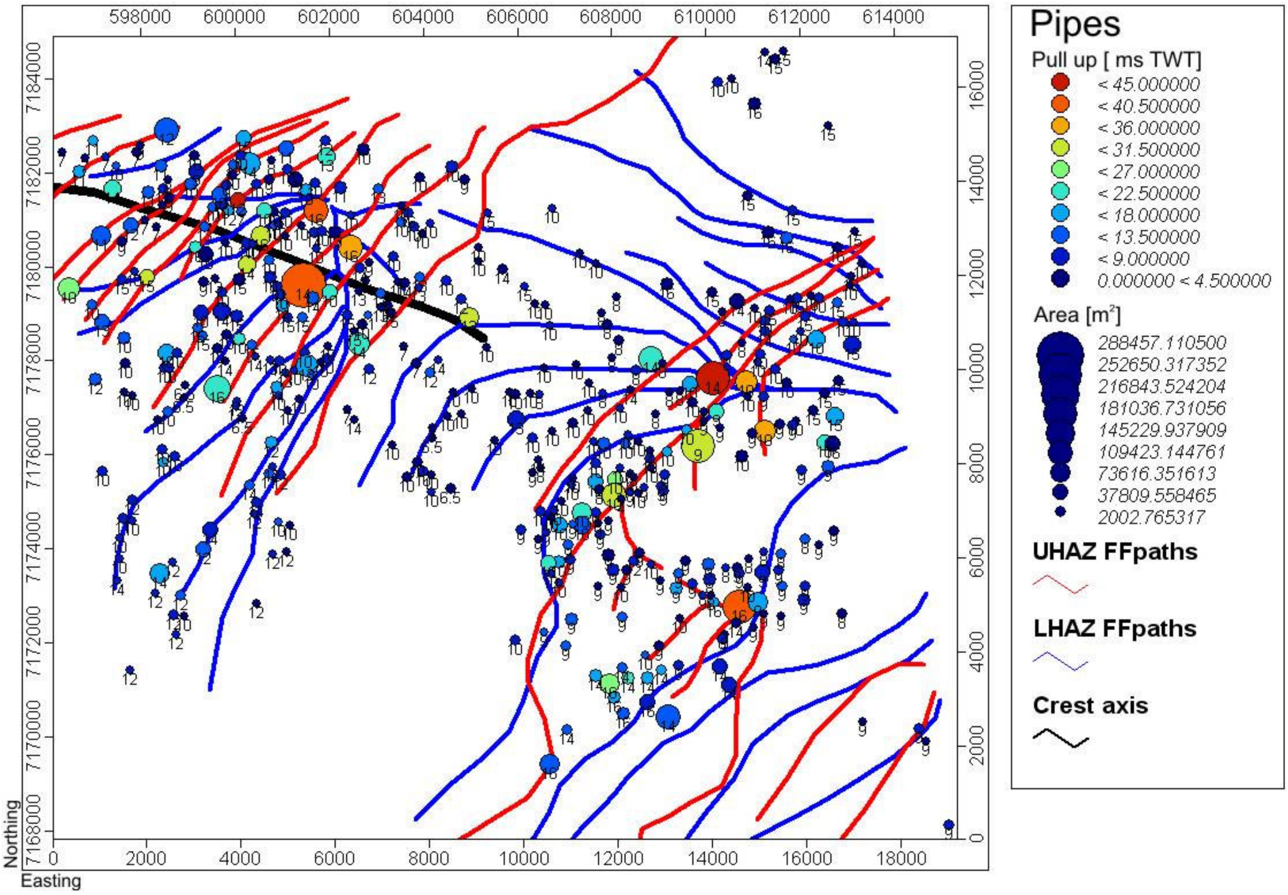

Figure 51 – Bullet map of the area of the 441 mapped pipes with color scale according to the maximum pull up value and labels according to bottom horizon (table 8). Red lines are interpreted major fluid flow pathways along the seal of the UHAZs 1 and 2; Blue lines are interpreted major fluid flow pathways along the seal of the LHAZ; Black line is the location of the bathymetric crest axis at the seabed (figure 26).

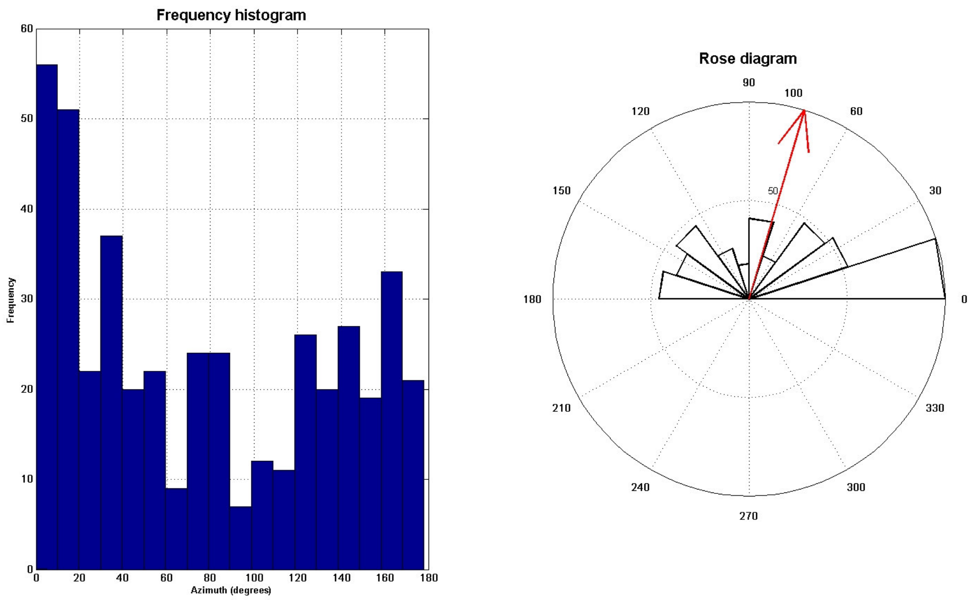

Figure 52 - Orientation of long axis in form of: Frequency historgram (left); Rose diagram (right).

The Orientation of the acoustic chimneys is shown in form of a frequency histogram and a rose diagram (figure 52) and as a map (figure 53). The orientation distribution as seen from the frequency histogram and rose diagram seems to be very random, there are a large number of pipes oriented within 0 and 20 degrees azimuth, but the mean is ~ 73 degrees. In the map the orientations seem to be, similarly to the pockmarks and mounds, aligning with the orientation of lineated trains of pipes. Factors controlling the orientation of the seepage pipes and blowout pipes must be the same since close features show similar orientations.

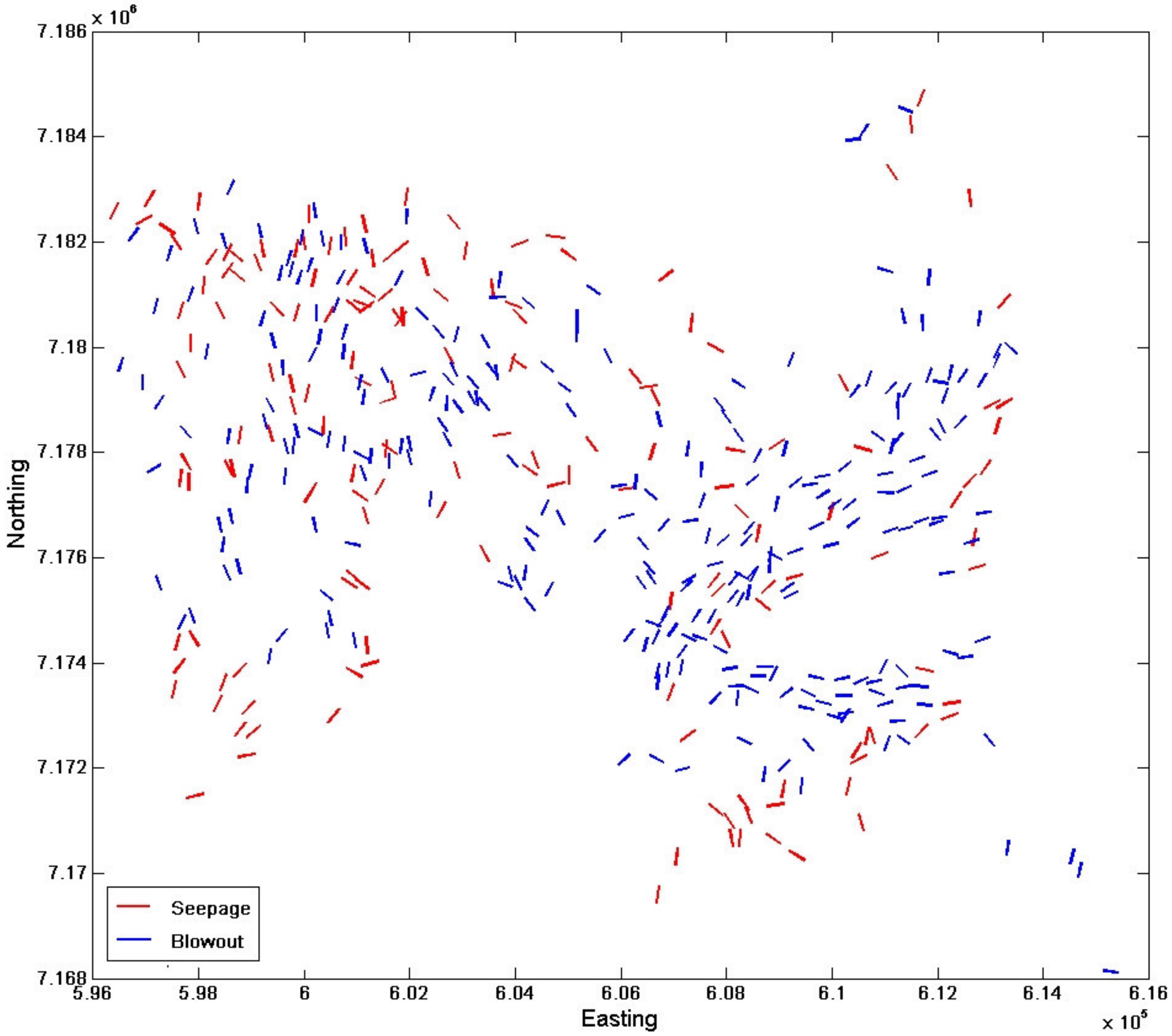

Figure 53 - Map of the orientation of the seepage pipes (red) and blowout pipes (blue).

4.2.5. Multivariate statistical analysis of the acoustic chimneys

4.2.5.1 Multidimensional scaling

Seven variables were used for the Multivariate statistical analysis, these were area, long axis length, short axis length, height, Orientation, Pull up and Push down. The Multidimensional scaling R-mode solutions to two dimensions of the 7 variables converged at a stress of 0.08, which is fairly good (Table 6). The coordinates of the 7 variables are displayed in figure 54. The most highly correlated are the size variables. The pull up has a close relationship to the size of the pipes, while the push down is highly independent from it. The push down is showing some correlation to the height. It reflects that within some pipes the larger push downs increases their height by extending their bottom. Orientation appears, in a similar manner to the orientation of the pockmarks and mounds, far from all other variables indicating that it is independent of any other parameter.

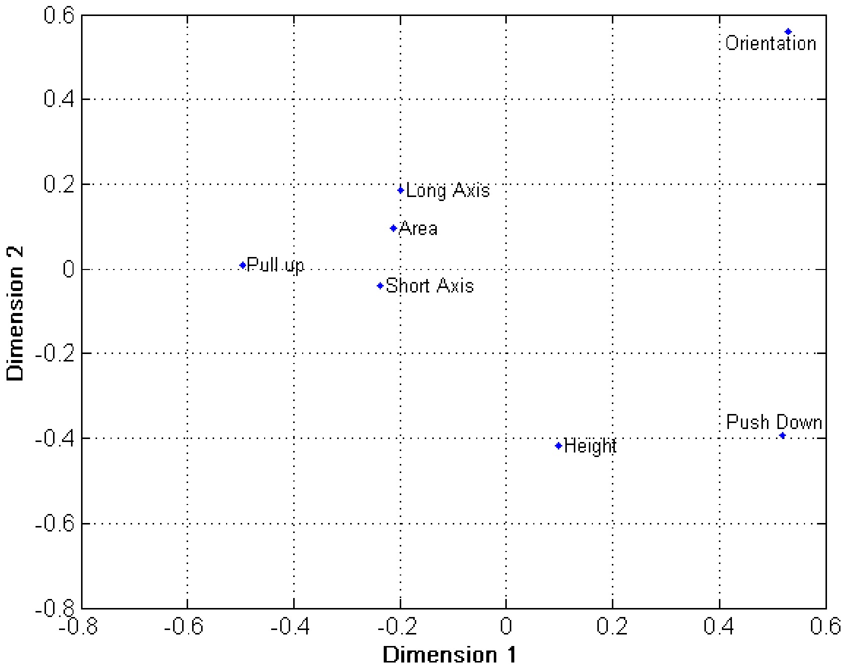

Figure 54 – The R-mode multidimensional scaling solution produces 2D coordinates for the variables such that the distance between the variables is approximately equal to [1 - their Spearman's rank correlation value]. This means that variables that are closer to each other are more positively correlated than those more distant.

The three dimensional scaling Q-mode solutions of the acoustic chimneys are shown in figure 55. The solution for 2 dimensional showed stress values above 0.15 (poor, Table 6), more than double of that of the 3D solution (0.06) and was therefore not used. The solution shows a considerable overlap between the observations of seepage pipes and the different blowout pipes, which indicates that the collected parameters are not enough to satisfy a separation of these groups.

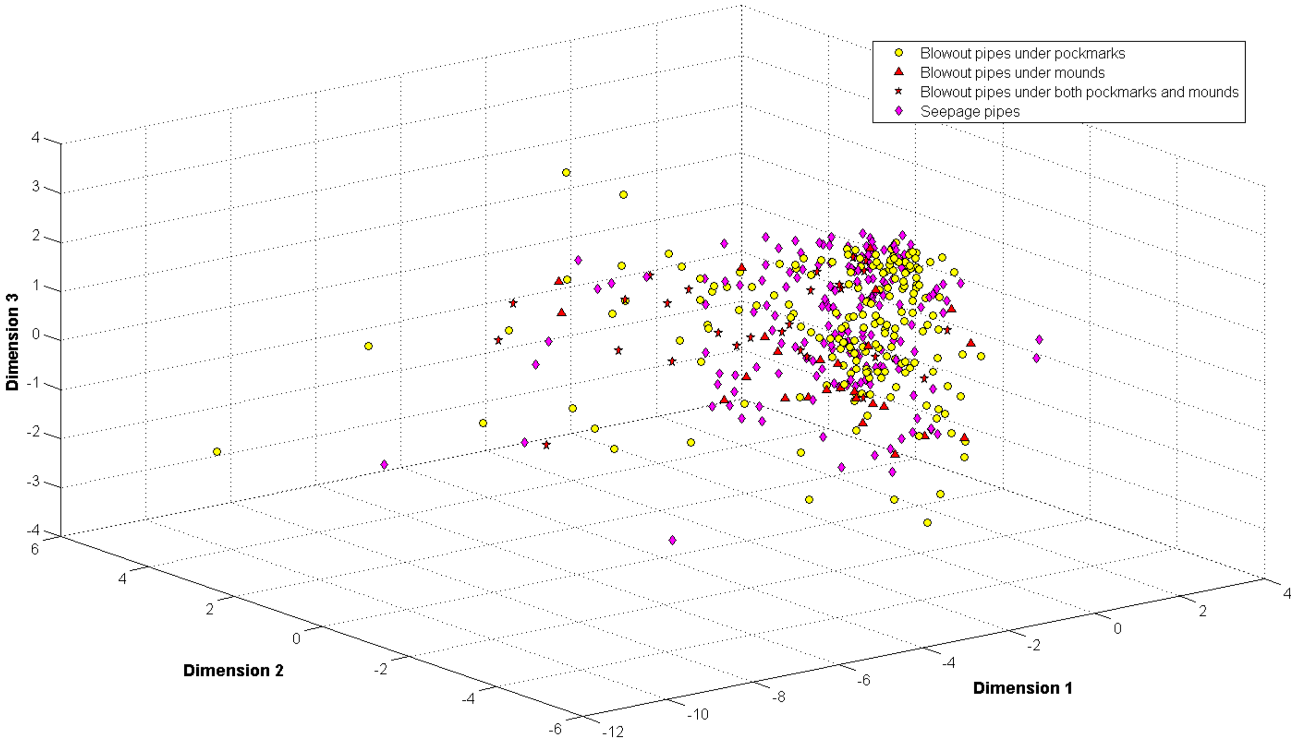

Figure 55 – Multidimensional scaling solution for the acoustic chimneys observations (Q-mode). The solution shows that except for some outliers, there is a great overlap between chimneys underlying different fluid flow features on the sea bed.

4.1.2.2. Cluster analysis

The K-means cluster solution classified the pipes in 4 clusters comprising between 6.1 and 60.7 percent of the observations (figure 56a). The pipe clusters were named after their median area as small, medium, large and very large pipes (table 9; figure 56d).

The small pipes are the most common type and are widely distributed over the survey area (figure 57). They have a median height less than 300 ms, making them the cluster with the smallest heights (figure 56e). They present usually a very low pull up (between 0 and 10 ms), and in the pipes with a push down, the push down is very small (less than 5 ms). The orientation is distributed between 0 and 180, but the median is around 70 degrees azimuth (figure 56h).

The medium pipes are much less common than the small pipes and slightly less numerous than the large pipes. They are mostly distributed over the UHAZ1 area and in the north eastern to mid eastern part of the survey (figure 57). They have the largest median height of all clusters (584 ms, figure 56e). This implies that most of these pipes are tall enough to be originating from the

LHAZ or below. The pull up values are varying from relatively small to medium (2 to 19 ms range), with a median of 7 ms (figure 56f). The push down is relatively large as we would expect from the height (figure 56g), falling in the range between 2 and 17 ms with a median of 8 ms. The orientation is 110 degrees from north, but all orientations seem to present (figure 56h).

The large pipes are the second most representative group after the small pipes with 88 members. The large pipes cluster is distributed widely over the survey area, but they seem to be less common in areas where there is a larger density of medium pipes (figure 57). They have a median height of 326 ms (figure 56e), which is close to the average depth of the BGHSZ in the area. The pulls up values vary between the same range as the medium pipes (2 to 20 ms), but with a median of 12 ms (figure 56f). The push-down values are small (less than 5 ms) and equivalent to the small pipes group (figure 56g). The median orientation is 70 degrees.

The very large pipes cluster is composed mostly of outliers. Despite their reduced number (27 pipes), they are distributed widely (figure 57). The heights are highly variable, but with a median height of 474 ms most of these pipes must originate at horizons deeper than the BGHSZ (figure 56e). Pull up values are mostly relatively large to very large (10 to 45 ms), with a median of 27 ms. The push down values are also relatively large falling in the range 12 and 24 ms, with a median of 14 ms (figure 56f; figure 56g). The median orientation of these pipes is around 50 degrees from north (figure 56h).

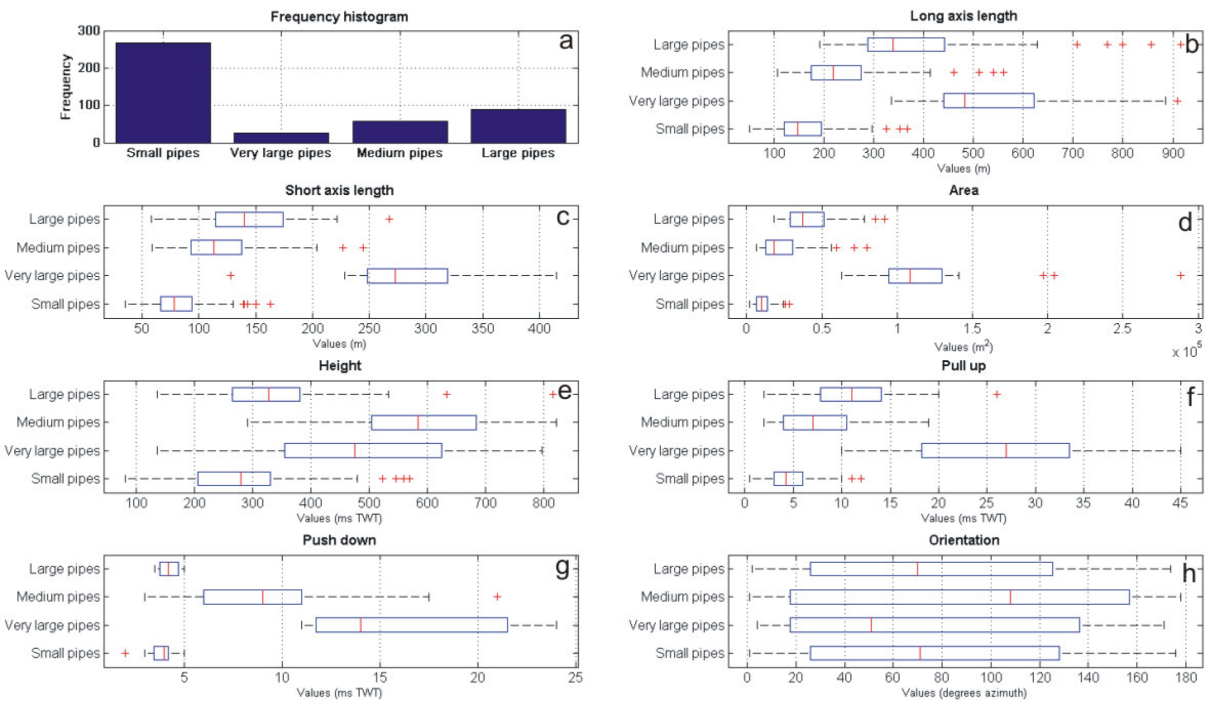

Figure 56 - Distribution of acoustic pipes parameters among the four clusters determined in the k-means cluster analysis.

Table 9 – Results of the cluster analysis for the 441 acoustic pipes, including cluster name, share of objects in each cluster and relative size, height, pull up, push down and orientation within each cluster, as interpreted from the cluster properties (figure 56).

Cluster name	Share of Objects (%)	Relative Size	Relative Height	Relative Pull up	Relative Push down	Orientation
Small pipes	60.7	Smallest	Short to medium	Small	Small push down	Median of 70 degrees
Medium pipes	13	Small to Medium	Medium to very tall	Small to medium	Medium push down	Median of 110 degrees
Large pipes	20	Medium to large	Short to medium	Small to medium	Small push down	Median of 70 degrees
Very large pipes	6.1	Large to very large	Short to very tall	Medium to very large	Large push down	Median of 50 degrees

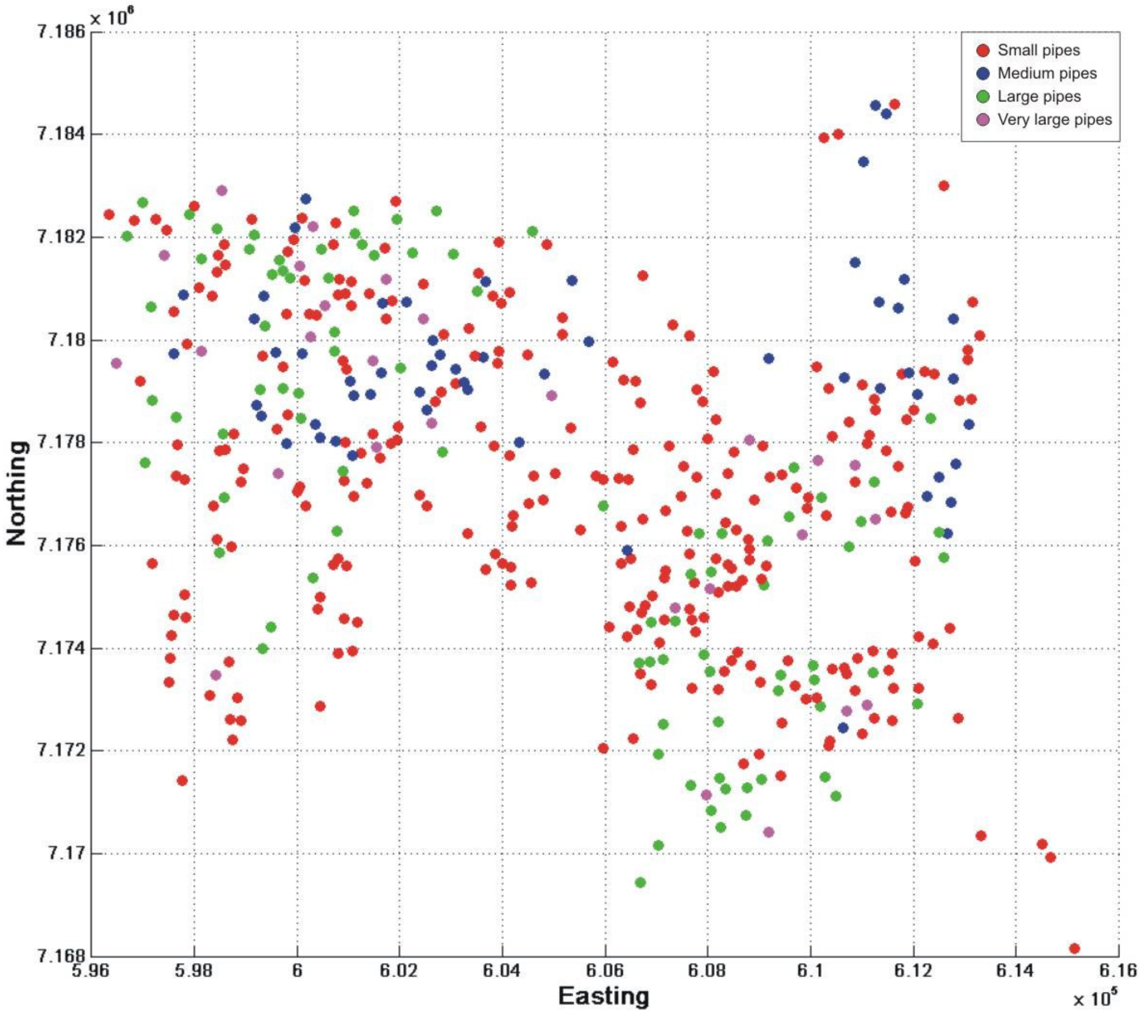

Figure 57 – Spatial distribution of the 4 clusters classified by the k-means cluster algorithm from the acoustic pipes data.

Similar to the multidimensional scaling analysis, the cluster analysis that is based on the quantified parameters from acoustic chimneys failed to distinguish between those blowout pipes that terminate in pockmarks, those that terminate in mounds and those that terminate in both mounds and pockmarks. Figure 58 shows the Q-mode multidimensional scaling solution of the acoustic chimneys that is in colour according to the classification done by the Kmeans clustering algorithm (figure 57). We can see that the clustering seems to be reasonable, but it does group within same clusters the different blowout pipes, and seepage pipes almost uniformly. This result shows for the second time that pipes underlying pockmarks, mounds or both show similar characteristics based on the parameters used in this study. It also shows that there is no particularity in the size of the pipes that underlie different fluid flow expressions on the sea bed.

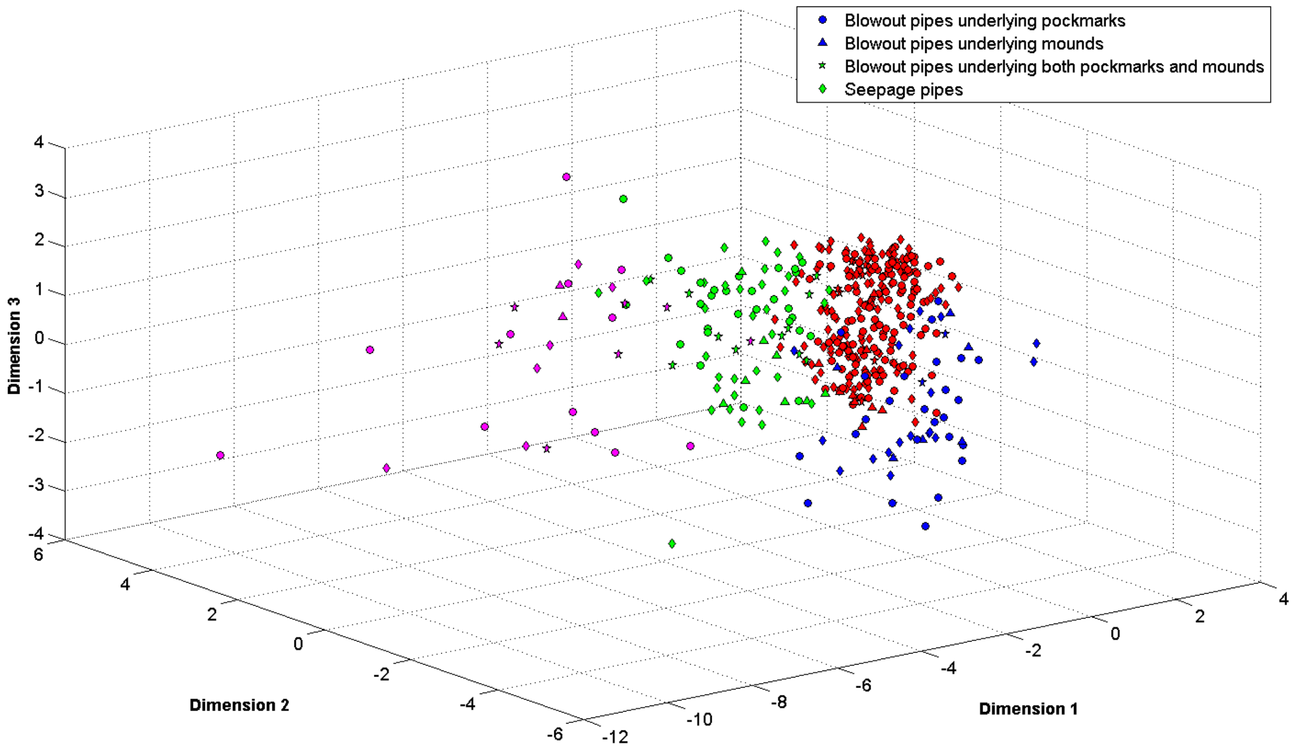

Figure 58 – Q-mode multidimensional scaling solution, with the different pipes colored according to the clusters classified by the kmeans cluster algorithm (figure 57). Again we see that pipes underlying mounds (triangles), pockmarks (circles) or both (stars) don't form clusters of their own.

4.2.7. Comparison of statistics of acoustic chimneys with the statistics of the respective overlying pockmarks and mounds

The comparison of the statistics of the mapped and quantified pockmarks and mounds at the seabed with those of the acoustic chimneys in the sub-seabed (ST0408 3D seismic cube) is presented out using R-mode multidimensional scaling. The solution presented in figure 59 shows that there is a relative large distance (poor positive correlation) between the size parameters of the seabed fluid features and the size parameters of the underlying acoustic chimneys. There is also a large distance within the orientation of both groups.

The large difference in size comes from the fact that many large pipes are overlain by small pockmarks and mounds and vice versa. This was observed during the quantification of the acoustic chimneys and may be related to the observation that the size of some pipes diminishes drastically above horizons 4 (One above TNR, table 8) and 5 (TNR, table 8), while others don’t show such drastic change.

The absolute differences in orientation present a median of 22 degrees, which is significantly large (figure 60A). Despite the overall difference in orientation between the acoustic chimneys and the overlying seabed fluid flow features, a map comparing the orientation of these groups illustrates that some areas show a very good agreement in orientation (figure 60B). Most of the features above the UHAZ2 show a very similar orientation, while the others show quite a large difference.

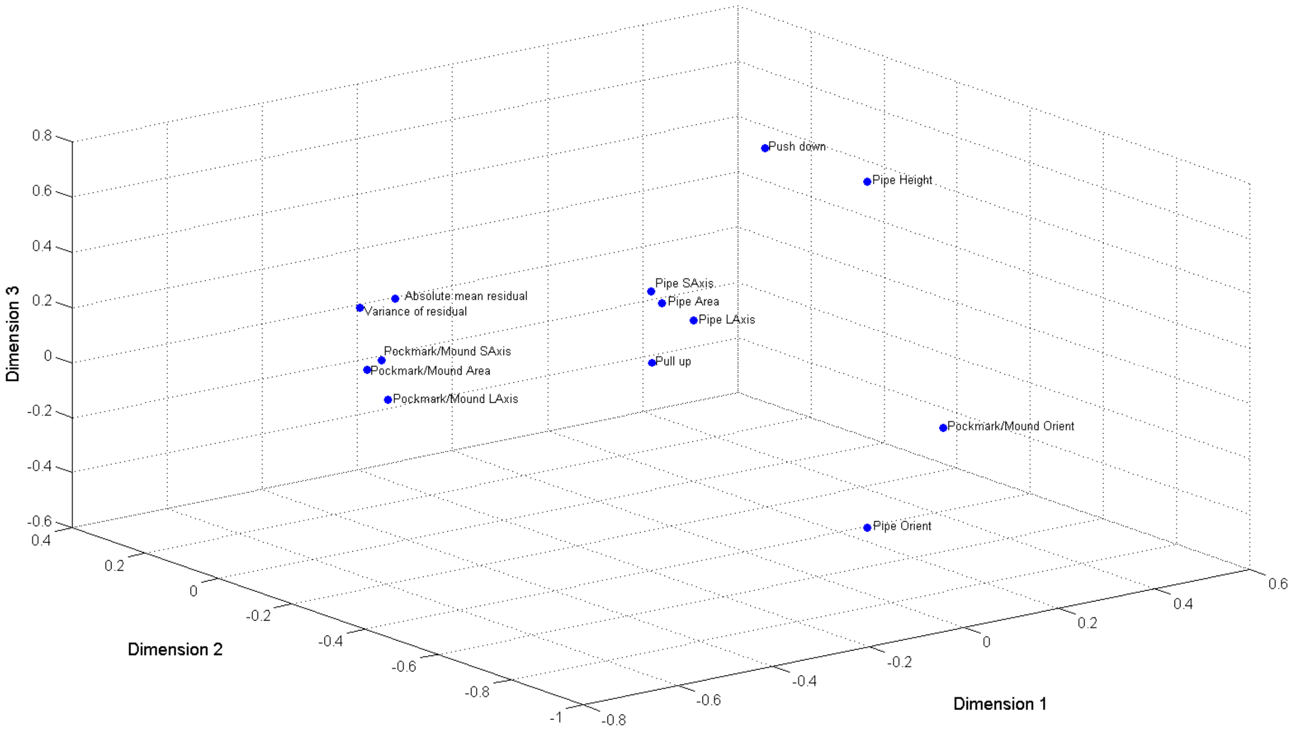

Figure 59 – Multidimensional scaling R-mode solutions for the pockmarks and mounds and acoustic chimneys data.

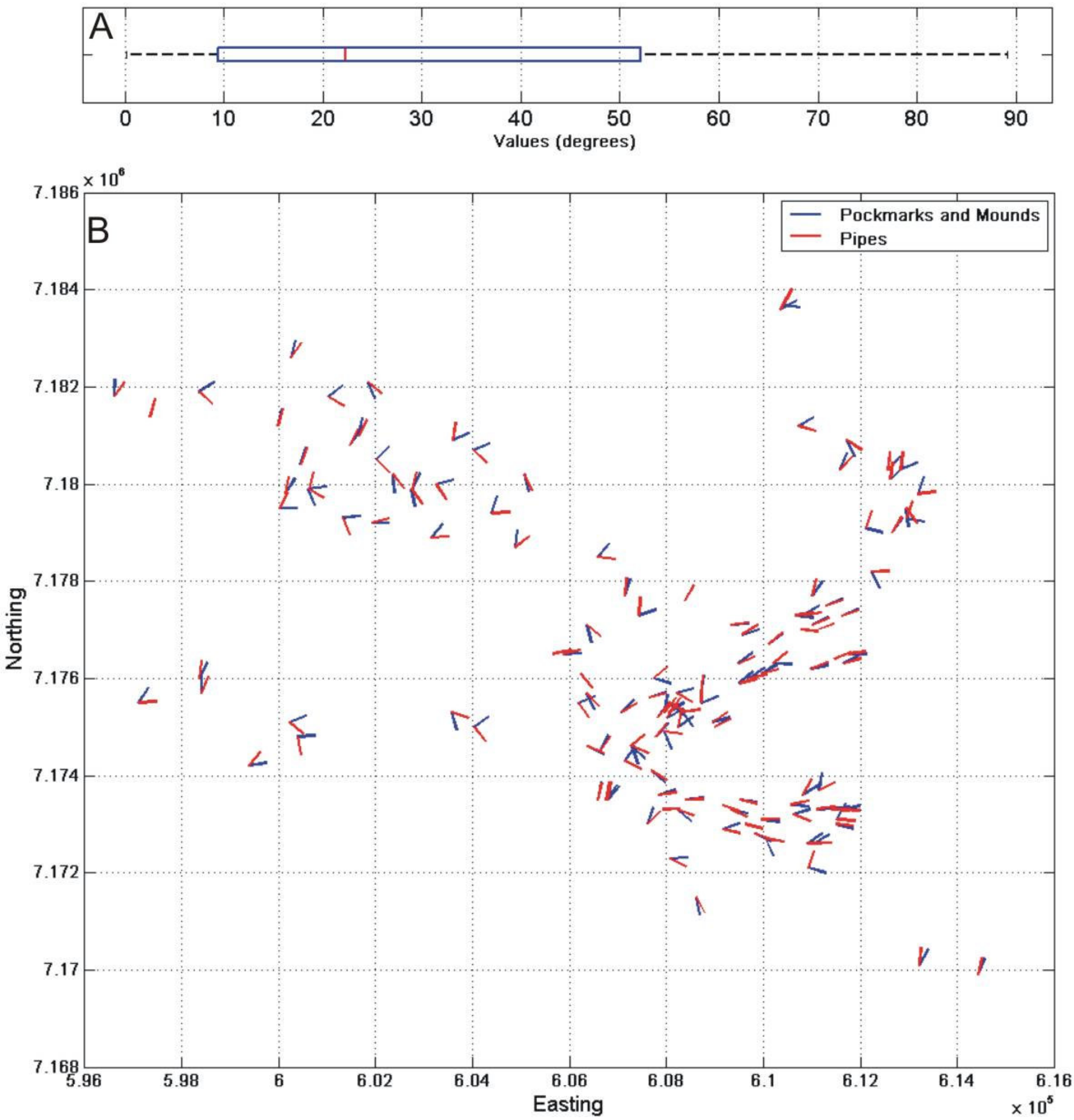

Figure 60 – (A) boxplot of the absolute difference between orientations of pockmarks and mounds and the respective underlying chimneys; (B) Map with the orientations of the pockmarks and mounds (blue) and those of the acoustic chimneys (red).

5. Discussion

This discussion is divided in three sections. In the first section we discuss the distribution of fluids (free gas?) as inferred from the results of the interpretation of the 3D seismic data. We also discuss the distribution of acoustic chimneys, pockmarks and mounds and the results of the quantification of the parameters collected from these features. In the second section, we discuss the possible origins of the fluids that are seeping through the pockmarks and mounds in respect to our results. In the final section we suggest timing and duration for the present fluid escape features in Nyegga.

5.1. Spatial distribution of geophysically inferred free gas and fluid flow expressions

The results indicate that there is a coincidence between acoustic chimneys, pockmarks and mound occurrences and the distribution of two major high amplitude zones within Naust S. The high amplitude zones are distributed at two major depth levels, at the base of Naust S3-4 (LHAZ) and at Naust S1-2 (UHAZs) where they are sometimes terminated by the BGHSZ (Figure 43; Figure 45). The high amplitudes within Naust S1-2 are further laterally divided by the pinch out of the sediments of Naust S1-2 below the BGHSZ against INS2 (Figure 43; Figure 44; Figure 45). The distinct lateral distribution of high amplitudes indicates that they are reflecting the fluid content (free gas?) along them (Figure 42; Figure 44). From this presumption, it may be inferred that the sediments have a relatively higher porosity within these two levels in comparison to the adjacent sediments within Naust S.

A conservative estimate of mean interval velocity of the sediments above the LHAZ indicates a compressional wave velocity of 2200 m/s (Mienert et al., 2005a). Temperatures at the level of Naust S are between 10 and 40 ^{o}C, based on a geothermal gradient of 55 ^{o}C/km (Bouriak et al., 2000). In such they are above the catagenesis zone and can be called shallow reservoirs.

5.1.1. Distribution and migration of fluids in the subsurface

Previous studies of the distribution of fluid flow expressions in form of acoustic chimneys, pockmarks and mounds in the Mid-Norwegian margin have shown that the shallow fluid flow system in Nyegga is part of a larger system associated with the distribution free gas trapped beneath the BGHSZ within contouritic sediments of the Naust formation (Bünz et al., 2003; Bünz and Mienert, 2004). The coincidence between the high density of fluid flow features and the crest in the bathymetry of Nyegga has already been pointed out by Bünz et al., (2003). This crest is likely to be a feature created by the interaction of the contour currents with the bathymetric high between the Møre and Vøring basins (Bünz et al., 2003). Time thickness maps of the ST0408 seismic cube indicates that the high developed first during the deposition of Naust S (Figure 39). Since the area is within the gas hydrate stability zone (water depth > 600 m and > 0 ^{o}C) and the BGHSZ tends to mimic the seafloor, this structural element at the seabed is likely to affect also the geometry of the BGHSZ in the subsurface. Moreover the concentration of seabed fluid flow expressions along this structural feature is an indication that lateral migration and accumulation of fluids beneath the seal formed by the BGHSZ plays an important role (Figure 25; Figure 26).

From the presented results (Figure 42) it is also evident that free gas within the LHAZ reservoir is migrating laterally mainly from the south and southwest of the study area, though there appears to be some northern component in the northeast of the survey area. The LHAZ extends beyond the ST0408 seismic survey and may be a part of a larger fluid migration system, such that it could be receiving fluids from areas as far as the adjacent Ormen Lange dome (e.g. Bünz et al., 2005) which is about 100 km to the south. But the distribution of amplitudes in the subsurface (Figure 42) agree very well with a model in which buoyant fluid sources in the south and southwest, such as the high amplitude areas within the Top Brygge reflection, are redistributed by the LHAZ reservoir (Figure 46).

The combined effect of the influence of the Helland Hansen dome topography and the polygonal faulted system of Brygge and Kai formations, contributed to create in the subsurface series of north- south oriented ridges within the contourites of Naust S. Within free gas zones, such as the LHAZ shallow reservoir, these ridges are major areas of convergence which convey buoyant fluids toward broader structural highs where they encounter a closure. The distribution of the free gas along the top of the LHAZ reservoir (reflection A) is coinciding very well with the directional gradient along the surface and points towards two major convergent zones representing broad areas of potential trapping of fluids. One lies beneath the UHAZ1 reservoir and the other is located beneath the easternmost part of UHAZ2 reservoir (Figure 42; Figure 46).

The UHAZ reservoirs seem to be charged by free gas through the migration of fluids out of the LHAZ reservoir. This migration would be occurring through vertical migration at the areas of convergence of the lateral buoyant fluid flow pathways on top of the LHAZ reservoir (Figure 46), but could also be occurring through the S2 slide scar where a dense set of extensional faults is sometimes observed (Figure 38a). The distribution of high amplitudes and inferred free gas along the top of UHAZ1 reservoir shows a very discontinuous and sometimes dendritic pattern (Figure 44). It is possibly influenced by the thinning of the sediment layers beneath the BGHSZ, by lateral permeability variations and by the acoustic chimneys which cause attenuation of the amplitudes.

The dendritic amplitude distribution tends to follow the directional gradient (Figure 44), while major fluid pathways are roughly parallel and are directed from southwest to northeast indicating that this would be the principal direction of redistribution of free gas within this level. Although these directions do not point toward any true structural closure, the change from a 1 degree slope to a flat surface may create a trap, as evidenced by the local distribution of the fluids at this level and of the pockmarks and mounds at the sea bed (Figure 44; Figure 46).

At the UHAZ2 reservoir free gas seems to concentrate in two major areas within the infilling contourites. One area extents along the S2 slide scar up to the pinch out of the BGHSZ against INS2 (Figure 44) concentrating mainly at the upper part of the S2 slide scar. At the easternmost part of this scar the distribution of high amplitudes appears to be dendritic until their abrupt northern termination at the pinch out zone (Figure 44). At this area the slide scar is broader and less steep than other parts of the study area and the rough topography of the slide scar and the high variability in thickness of the free gas zone squeezed between INS2 and the base of the BGHSZ may be contributing to create series of scar-aligned traps which step up along the scar (Figure 44; Figure 46; Figure 47). The second high amplitude concentration occurs at the thickest accumulation of the infilling contourites that occurs roughly as a SE-NW ridge slightly tilted updip towards NW (Figure 44). In the east, the two high amplitude zones are separated by a wedge of GDFs deposited over the moat of the infilling contourites (Figure 44; Figure 47). The interpreted fluid flow pathways indicate a principal spill point out of this ridge towards the updip pinchout in the north (Figure 44; Figure 46). But spilling of free gas beneath the lowermost parts of the wedge of GDFs deposited at the moat is also a possible and likely migration pathway, but implies large fluxes of free gas to this trapping area in order to fill it to these deeper spill points (Figure 44; Figure 45).

5.1.2. Origin and distribution of acoustic chimneys, pockmarks and mounds

Two major models have been previously proposed to explain the origin and distribution of pockmarks and mounds in Nyegga (Bouriak et al., 2000; Berndt et al., 2003; Bünz et al., 2003; Hustoft et al., 2007). The first model, pockmarks and mounds are linked to leakage systems in form of vertical pipes from over pressured shallow reservoirs (e.g. Bouriak et al., 2000; Bünz et al., 2003; Hustoft et al., 2007). The second model suggests that seabed fluid flow expressions have been produced by vertical migration of fluids through pipes connected directly to polygonal faults at depth (e.g. Berndt et al., 2003; Berndt, 2005). In both models fluids are breaching the seal that is represented by the gas hydrated sediment layer.

It is evident from the results of the seismic interpretation that more than one stratigraphic level is acting as a fluid reservoir. This situation may cause fluids to be stored in different levels before they are finally expelled to the seafloor. Most of the acoustic chimneys are located along small or large scale crests within the shallow reservoirs and/or at their updip pinch-outs (Figure 46), which are the typical areas for building up focused overpressure (Cartwright et al., 2007; Hustoft et al., 2007). Although evidence exists for fluids to be partially originating from beneath the polygonal faulted system (Figure 40; Figure 41) in the southwestern part of the area, no clear evidence was found that acoustic chimneys can be directly connected to these faults. Additionally, no pockmark or mound was observed over these areas (Figure 46).

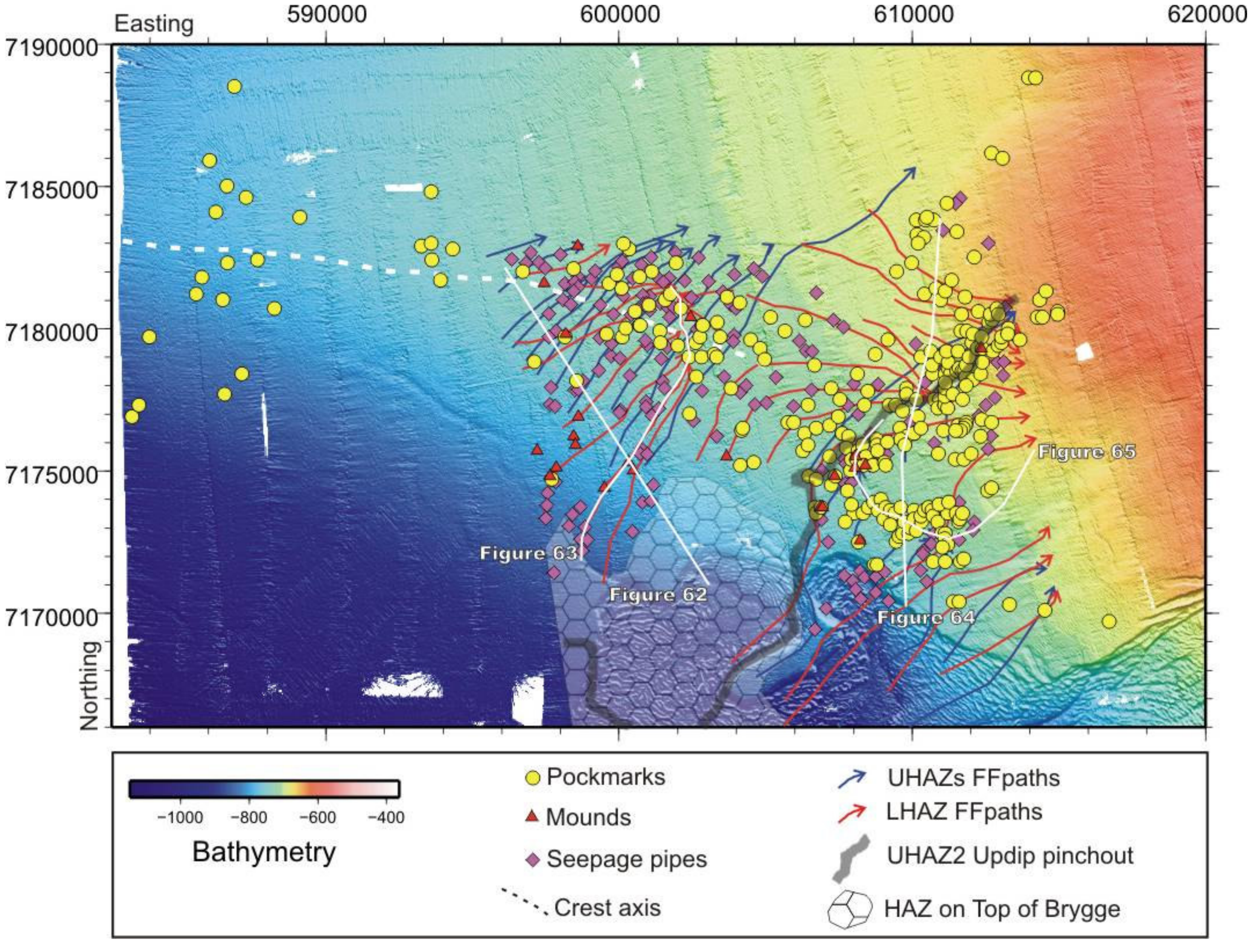

Figure 61 – Bathymetric map of the Nyegga study area showing the distribution of pockmarks, mounds and seepage pipes. Blue arrows are interpreted major directions of lateral migration along the UHAZs, while red lines are major directions of lateral migration along the LHAZ. The broad black line indicates the updip pinchout of the Naust S1-2 against the INS2 and the BGHSZ approximation.

The distribution of the fluid flow features at the seabed in the study area is thus interpreted to be a complicated combination of lateral and vertical migration originating from locally over-pressured shallow reservoirs (figure 61). Lateral migration of fluids conveys the fluids through geological settings that allow a focused flow towards structural traps or stratigraphic pinch outs. "*Given sufficiently focused fluid flow and high pressure, the fluid may support the creation of permeable pathways by hydraulic fracturing, which requires that fluid pressure exceeds the least principal stress*" (Zühlsdorff and Spieß, 2004). The formation of the vertical seepage and blowout pipes represented by the acoustic chimneys are thus interpreted to be resultant from hydraulic fracturing of the "impermeable" overburden (Aydin, 2000; Zühlsdorff and Spieß, 2004; Cartwright et al., 2007; Hustoft et al., 2007). Acoustic chimneys are found both along the major fluid flow paths (figure 62; figure 63) and at the structural traps (figure 63; figure 64; figure 65) and stratigraphic pinch outs (figure 64; figure 65). Overpressure then seems to develop not only in areas of fluid entrapment but also along areas of lateral fluid migration.

The swath bathymetry data to the west of the 3D seismic area (figure 61) show pockmarks distributed mainly along and across the crest. This may suggest that they are related to blowout events associated with lateral migration and accumulation of fluids at the BGHSZ. Another evidence comes from the area of the ST0408 3D seismic cube where pockmarks and mounds may indicate similar blowout events originating from the UHAZ1 (figure 62; figure 63). However, areas between the UHAZs (band of low amplitudes) show pockmarks and mounds which are genetically related to the LHAZ (figure 62; figure 63; figure 64), which let us conclude that overpressure develops also at this level. This way pockmarks and mounds found over the UHAZs can also be product of fluid expulsion from the level of the LHAZ, in which case pipes coming from this level must be capable of continuing to the seabed after piercing the UHAZ (figure 62; figure 63). The distinction between the sources of the acoustic chimneys, when possible, can be made mainly through the interpretation of the directional gradient maps and through the quantification of the bottom termination of the acoustic chimneys (Figure 51). Over the UHAZ2 pockmarks and mounds are striking in two major directions paralleling the updip pinchout and the crest of the infilling contourites (figure 61; figure 64; figure 65), indicating that they are originating mainly from the level of the UHAZ2. Although less numerous, acoustic chimneys originating from the LHAZ are also found at this area (figure 64; figure 65).

A new approach based on statistical analysis enabled to study fluid migration and seafloor seepages. It allowed a quantification of several parameters within 178 pockmarks, 14 mounds and 441 acoustic chimneys with a primarily exploratory objective. Rudimentary and mainly exploratory multivariate statistical analysis methods were used in an attempt to capture the basic relationships within the parameters defining fluid escape features, and the similarities and dissimilarities between the studied targets of fluid flow expressions.

The quantification of the pockmarks and mounds in the study area showed that the largest and deepest pockmarks (classified as large and medium pockmarks) are distributed mainly close to the crest axis, paralleling the updip pinchout and at the crest axis of the infilling contourites and are surrounded by smaller pockmarks (classified as small pockmarks) (Figure 30; Figure 34; Figure 37).

The size and depth of active seeping pockmarks has been attributed to several factors including degree of overpressure, grain size of the seabed sediments (Hovland and Judd, 1988), and duration of fluid flow seepage (Bøe et al., 1997; Gay et al., 2006a).

Changes in grain size are unlikely to cause differences in the area and depth of pockmarks which are close to each other, unless mud extrusion is involved. But mud extrusion is mainly associated with mud mounds and mud volcanoes, and only rarely forms pockmarks (Kopf, 2002).

Timing and duration of fluid flow in Nyegga can be speculated from large scale geological events such as the Neogene glacial and interglacial cycles (Bünz et al., 2003; Hustoft et al., 2007), but the timing and duration of seepage within individual fluid flow targets is contrained largely through sampling and dating methods, such data is not available. However, duration of flow within individual pockmarks could be an important factor controlling pockmarks size and depth at Nyegga (Bøe et al., 1997).

Pockmarks to which fluid migration have ceased are susceptible to burial. The size and depth of these features will then be determined by largest attained size, the time since ceased activity and the sedimentation rate. It is intuitive to assume that sedimentation rates are largest at the crest, since this positive topography is suggested to be a sedimentary and not a tectonic feature. Thus it is contradictory to find the largest and deepest pockmarks over the areas where we consider the largest sedimentation rates, suggesting that either these features are active or burial of unactive pockmarks is not a major controlling factor for the present size and depth distribution of the pockmarks.

The degree of overpressure can be an important control in the size and depth developments of pockmarks at the seabed, since relatively stronger pressures imply in a relatively more powerful flow capable of sediment suspension and erosion. The level of overpressure within buoyant trapped fluids is highest at the top of the trap or where the gas column is higher. Our observations suggest that the largest pockmarks and mounds could derive from such overpressure areas, since the largest seabed fluid flow features are either distributed at the top of the bathymetric crest or over the two major traps within the UHAZ2 (top of the infilling contourites and updip pinchout against BGHSZ).

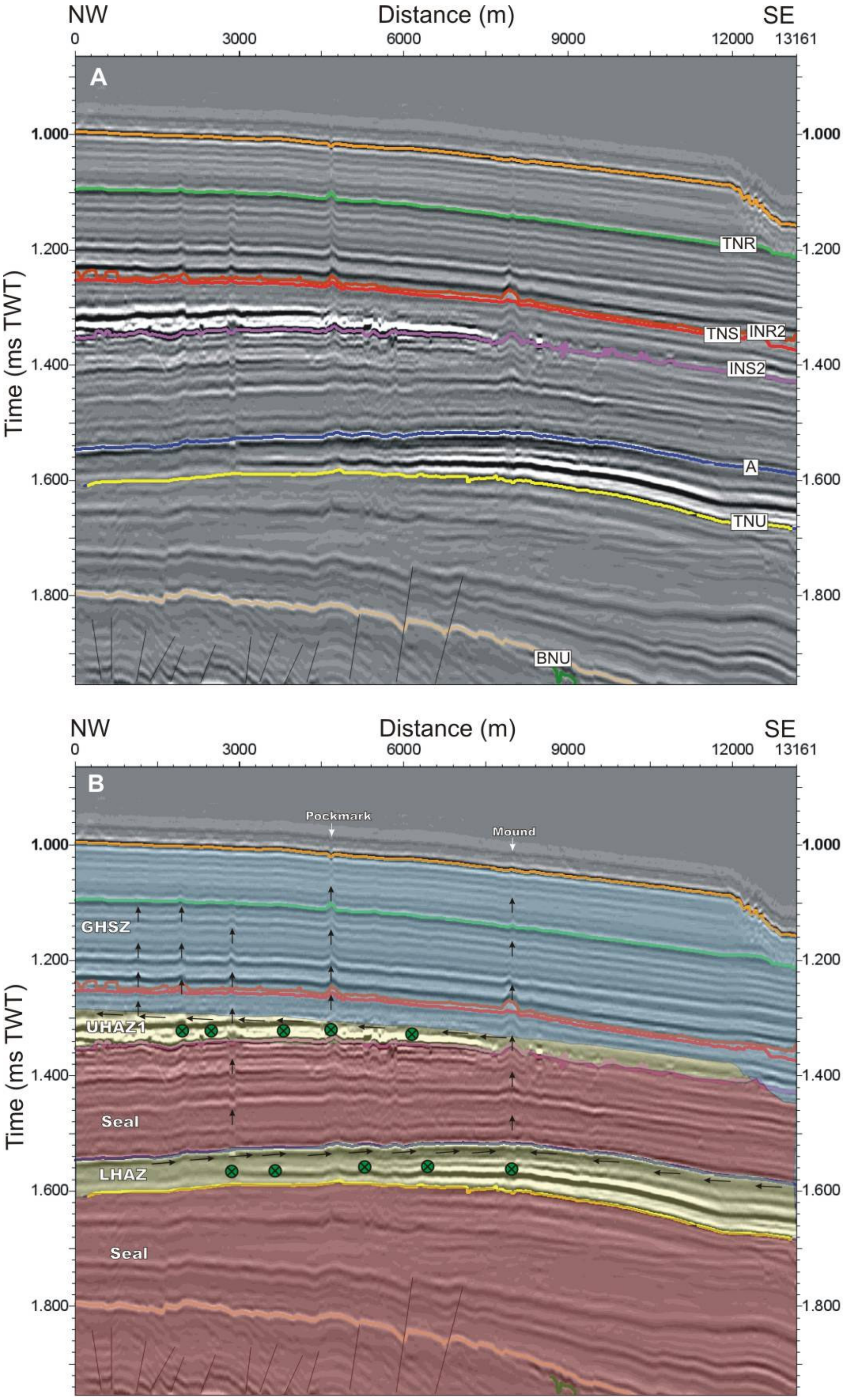

Figure 62 – Arbitrary seismic section from the ST0408 3D seismic survey showing: (A) Stratigraphy; (B) Interpreted fluid flow features, including the GHSZ and the UHAZ1 and LHAZ and sealing intervals. Black arrows indicate lateral migration pathways in the plane of the section, while green circles with cross or dot inside represent major lateral migration pathways perpendicular to the plane of the section, where the cross represents flow into the section, while the dot represents migration out of the section.

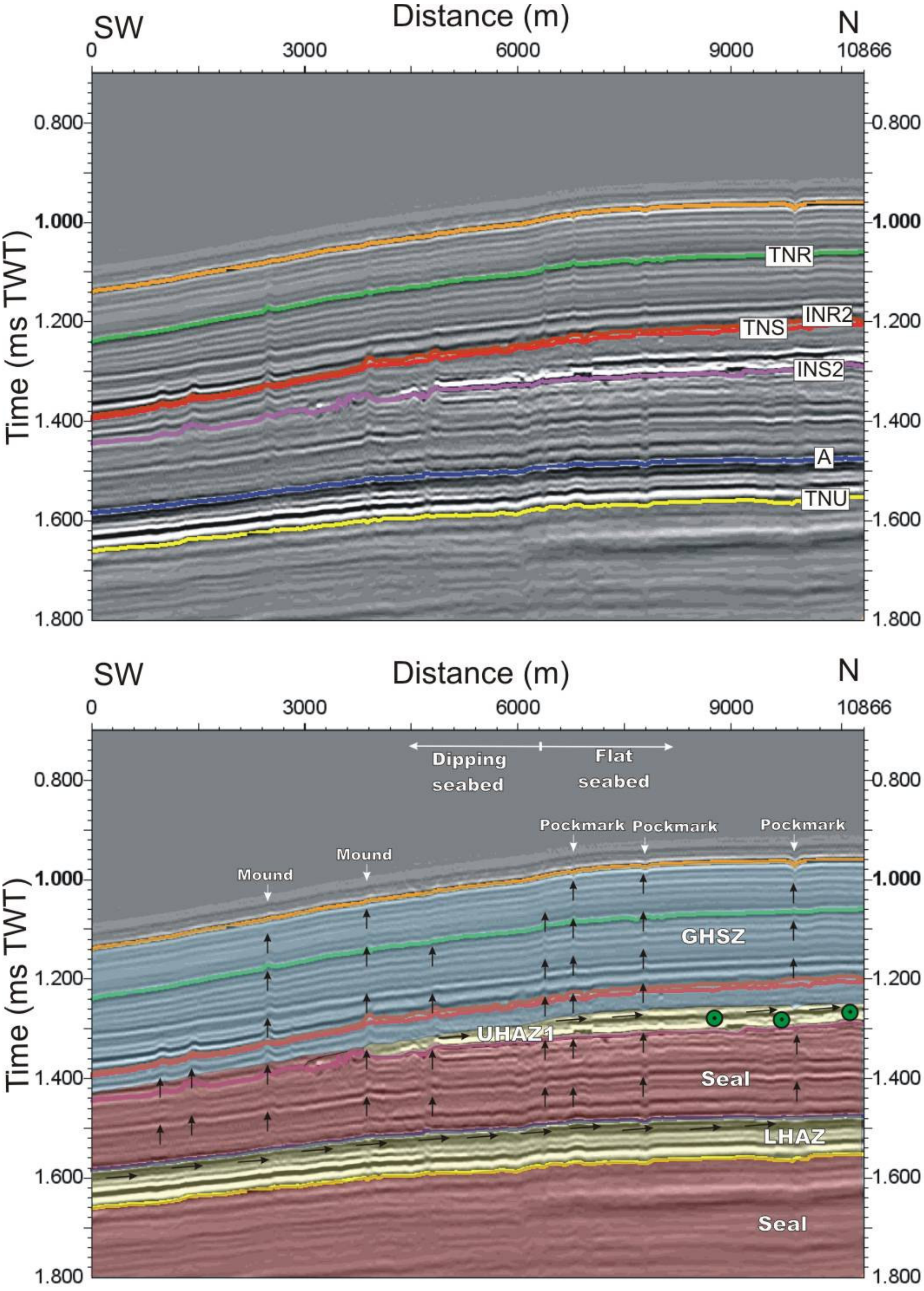

Figure 63 – Arbitrary seismic section from the ST0408 3D seismic survey along an interpreted major fluid flow pathway within the LHAZ showing: (A) Stratigraphy; (B) Interpreted fluid flow features, including the GHSZ and the UHAZ1 and LHAZ and sealing intervals. Black arrows indicate lateral migration pathways in the plane of the section, while green circles with cross or dot inside represent major lateral migration pathways perpendicular to the plane of the section, where the cross represents flow into the section, while the dot represents migration out of the section.

The origin of mounds in Nyegga have been ascribed to mud volcanism (Mienert et al., 1998a), mud diapirism (Mienert et al., 1998a; Bouriak et al., 2000) and carbonate build up (Hovland et al., 2005; Mazzini et al., 2005).

Bouriak et al., (2000) took sediment cores from one of the mounds in the studied area and found fossils of Eocene age within a matrix of distinctly consolidated mud, suggesting that mud mobilization through the fluid conduits represented by the acoustic chimneys could be contributing to the formation of some of the mounds. While Gravdal et al., (2003) investigated the area using Tobi Side-scan sonar and high resolution seismic. Their results did not support large scale mud volcanism, since there was no evidence of mobilized mud in the fluid flow features at the seabed.

There are two major theories for the formation of carbonate mounds, although one does not rule out the other. In one theory mounds grow by authigenic precipitation of carbonates related to long term (tens of thousands of years) continued methane seepage (e.g. Hovland and Judd, 1988; Naeth et al., 2005). In another theory, it is suggested that mounds grow by the vertical building capability of cold water corals, in particular *Lophelia sp*., in the presence of strong bottom currents which can provide a large supply of nutrient rich waters (Wheeler et al., 2007). But cold water corals cannot colonize mud sea beds because they need a hard ground where they can fixate and grow. So it can be assumed that cold water coral colonization must postdate the carbonate formation, especially where no other potential fixation ground exists. Moreover, Hovland et al., (2005) investigated methane derived authigenic carbonates within pockmarks in the study area and found no evidence of the presence of *Lophelia sp*. Thus we rule out the contribution of cold water coral growth to the development of the size of the mounds observed in the study area that are at water depths between 600 and 900m.

Although the mounds in the study area are not as numerous as the pockmarks, the largest and tallest mapped features are occurring close to the same areas where we find the largest and deepest pockmarks and also line up with the same major traps within the UHAZ. This supports the idea that they may be fluid flow related and also that the areas and heights of these features are, similarly to the areas and depths of pockmarks, possibly controlled by the degree of overpressure, and duration of fluid flow.

One of the objectives with the quantification of the pockmarks and mounds was to try to identify possible dissimilarities within the acoustic chimneys underlying different seabed expressions of fluid flow such as mounds and pockmarks. The results from the multidimensional scaling and the cluster analyses show that the quantified parameters within the acoustic chimneys do not help much in this distinction. But the group of isolated mounds to the south of the crest is an interesting source for a hypothesis. Although the quantified parameters within the mainly small acoustic chimneys underlying those features do not significantly differ from those of other small acoustic chimneys elsewhere, there is clearly something particular to that area which makes it susceptible for the development of isolated mounds with no associated pockmarks. The isolated mounds lie down slope from the crest in an area where there is clear evidence of fluid flow chimneys connected to the deeper LHAZ shallow reservoir (figure 61; figure 62; figure 63). Particularly interesting is the fact that the acoustic chimneys are not crossing the UHAZ, due to the fact that the UHAZ pinches out to the north (figure 63). These features are some of the closest features to the high amplitude zone observed within the Top Brygge formation (Figure 41; figure 61). Major lateral migration pathways exist, which are originating directly from above these high amplitudes. Once hydraulic fractures are developed at the overpressured free gas zones, the resultant “permeable pathways” could also be conduits for fluids such as formation water and mud (e.g. Dimitrov, 2002; Kopf, 2002). This could be used to explain why Bouriak and his co-authors found anomalous consolidated mud with fossils of Eocene age in a shallow sample (1.3 m) taken from a mound in this area. Based on these facts we can speculate that the composition of the fluids within these pipes and which is seeping at the seabed could be largely derived from the de-watering of the Oligocene-Eocene polygonal faults system (Berndt et al., 2003), possibly also including gases of thermogenic origin. This could then be a controlling factor in the formation of these particular mounds. The fact that there are no associated pockmarks suggests that the rate of seepage must be very low (microseepage?), or that mud extrusion is occurring (mud mounds?).

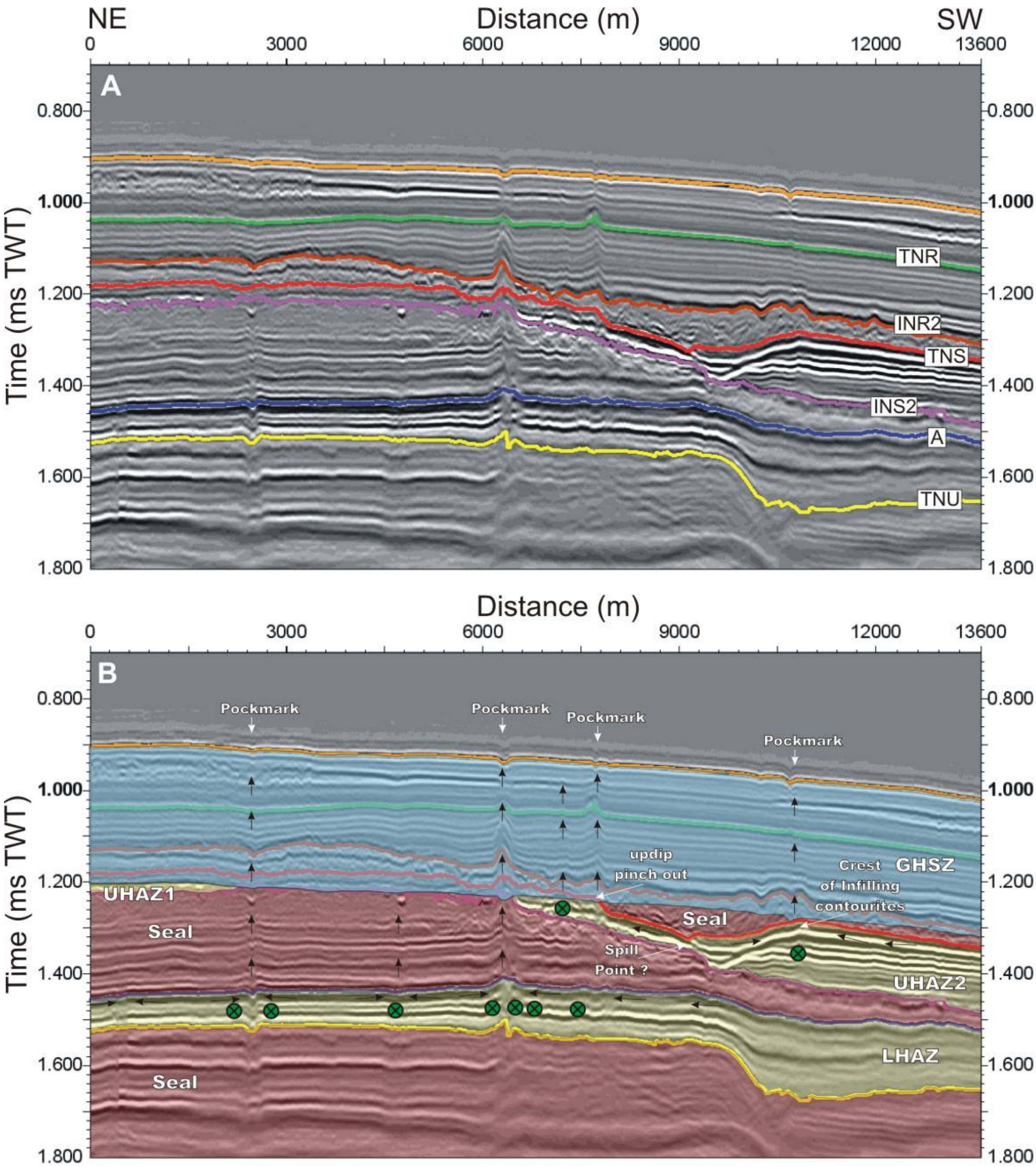

Figure 64 – Arbitrary seismic section from the ST0408 3D seismic survey showing: (A) Stratigraphy; (B) Interpreted fluid flow features, including the GHSZ and the UHAZs and LHAZ and sealing intervals. Black arrows indicate lateral migration pathways in the plane of the section, while green circles with cross or dot inside represent major lateral migration pathways perpendicular to the plane of the section, where the cross represents flow into the section, while the dot represents migration out of the section.

Most pockmarks described in the literature are circular features (Hovland and Judd, 1988; Hovland et al., 2002; Judd et al., 2002). Elongated pockmarks are normally attributed to posterior modification, as it is thought that gas escape and erosion from a point source normally will produce circular depressions (Hovland and Judd, 1988). The modifications are in turn attributed to bottom currents (Andresen et al., 2008), to amalgamation of pockmarks formed along linear sources, such as faults, or merging of individual pockmarks (Pilcher and Argent, 2007).

This study shows that pockmarks and mounds in the study area are mostly elongated features (Figure 31) and that in some areas elongation is oriented in the same direction as subsurface settings from which they are interpreted to originate (Figure 33; figure 61). No observable major faults are associated with the location of the pockmarks and mounds, but the features are instead connected to acoustic chimneys. The acoustic chimneys show also elongated shapes (Figure 50) and most importantly show similar orientation as the pockmarks and mounds in some areas (Figure 53; Figure 60). This suggests that the orientation and elongation of pockmarks and mounds is inherited from the acoustic chimneys.

It can be speculated that the elongation and orientation of the acoustic chimneys in Nyegga reflect the geometry of the distribution of the overpressured fluids, or simply put the geometry of the trap where fluids are susceptible to pressure build up and form hydraulic fractures. The orientation of pockmarks and mounds overlying the UHAZ2 is in accordance with the orientation of the major traps found at the UHAZ2 level, namely the updip pinchouts against the INS2 and the BGHSZ at the upper part of the S2 slide scar and the ridge formed by the infilling contourite sediments (figure 61; figure 64; figure 65). Therefore, the orientation of the pockmarks and mounds suggests a relationship to the geometry of the trap from which fluids are vertically migrating. This also supports the notion that the pockmarks and mounds in this area are mainly product of vertical migration from the level of the UHAZ2.

However, above UHAZ1 the orientation of acoustic chimneys and overlying pockmarks and mounds significantly differ from each other (Figure 60). Given the speculative nature of this issue it seems presently too early to come up with plausible explanations. Nevertheless, it appears that the orientation of pockmarks and mounds over the UHAZ1 is not defined by the orientation of acoustic chimneys as for example seen over the UHAZ2.

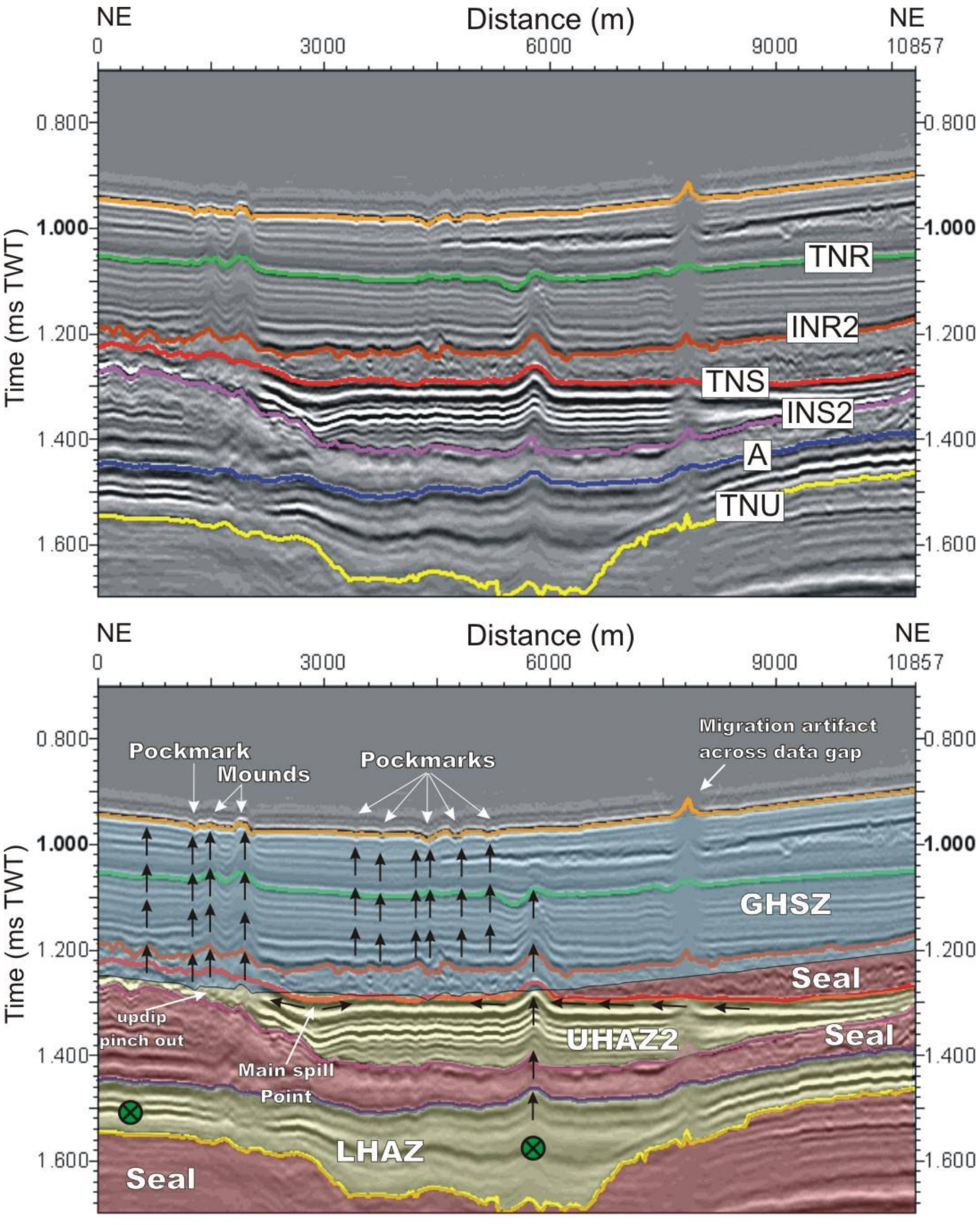

Figure 65 – Arbitrary seismic section from the ST0408 3D seismic survey along the ridge formed by the infilling contourite sediments showing: (A) Stratigraphy; (B) Interpreted fluid flow features, including the GHSZ and the UHAZs and LHAZ and sealing intervals. Black arrows indicate lateral migration pathways in the plane of the section, while green circles represent major lateral migration pathways perpendicular to the plane of the section, where the cross represents flow into the section, while the dot represents migration out of the section.

There is little or none published information on what controls the size of acoustic chimneys, making any discussion highly speculative. This may change in the next few years since detailed studies on these fluid flow features are being carried out at the moment (e.g. Plaza-Faverola et al., 2008; Westbrook et al., 2008).

Based on the presented data, there may be a possible association between the locations of some of the largest acoustic chimneys with areas close to convergence of the interpreted major fluid flow pathways, especially within the LHAZ reservoir (Figure 51). This observation suggests that the larger acoustic chimneys may be related to higher gas fluxes. This higher flux would imply a possible stronger flow towards the seabed. But the statistical results show that there is a poor correlation of the size of the acoustic chimneys with the size of the fluid flow features at the seabed (Figure 59). This contradiction could be related to differences in fluid compositions and heat advection through particular chimneys which may decrease or enhance flow depending whether they enhance or hinder hydrate formation (Liu and Flemings, 2007). The observed correlation between acoustic chimneys size with the pull up, could then be a consequence of higher rate of gas hydrate formation within these particular large chimneys, which could then imply in less gas flow to the seabed and hence explain why large chimneys are sometimes related to small pockmarks. This may also partly explain the observation that some particular chimneys decrease drastically in area within the GHSZ (ex. figure 65). Also, some acoustic chimneys may distinctly decrease their activity over time. In which case the potential hydrate formation and/or the precipitation of authigenic carbonates within these abandoned vertical fluid flow pipe structures may cease, while distortion (pull up) of reflections due to higher velocity material may still prevail.

Pull-up and Push-down are terms commonly used for seismic velocity distortions, in which lateral changes in lithology, physical properties or fluid content of sediments and rocks cause the seismic signal to be delayed or rushed when traveling through them. This causes distortions in the reflections underneath, which may appear up bent (pull up) or down bent (push down) depending whether there is a local faster medium or slower medium respectively, even though the reflectors from which they originate are flat. Structural deformations due to forced deformation and upward movement of sediment layers , or, and collapse structures due to loss of pore water and gases (Judd and Hovland, 2007) could also show similar results with up bending and down bending of reflections, respectively.

Large scale structural deformation within the acoustic chimneys would imply that once a pipe is formed it would disturb the sediments in such a way as to be visible in the seismic even after ceased activity. But recent work in paleo-pockmarks does not support that. Andresen et al., (2008) mapped hundreds of paleo-pockmarks in 10 different 3D seismic surveys spread between the

Danish central graben and the Danish North Sea. The pockmarks were suspected to have been formed by vertical migration from underlying reservoirs. They were dated to have formed 9.5 to 5 Myrs ago and are now deeply buried beneath 500 to 1500 m of sediments. The fact that the authors found no disturbance in the reflections beneath those features implies that no resolvable structural deformation occurred vertically beneath them.

In this study we observed a large variability in the pull up and push down characteristics of the acoustic chimneys, but we can generally separate them into four groups: (1) Push down beneath BGHSZ; (2) Pull up within GHSZ swapping to push down below BGHSZ; (3) Pull up within GHSZ; (4) Pull up extending beneath BGHSZ.

The push down observed within the acoustic chimneys in the study area occurred only beneath the BGHSZ, and was commonly observed below updip pinch-outs and focusing elements within the UHAZs. In these areas we would expect a larger accumulation of free gas. This supports the idea that the push down observed within the deep parts of some acoustic chimneys and also below updip pinchouts is most likely produced by velocity distortion due to free gas causing a delay in the seismic signal.

Pull up occurring within the gas hydrate stability zone can be related to an increased concentration of gas hydrates within the acoustic chimneys, since gas hydrate increases the seismic velocity within the sediments (Andreassen et al., 2003; Bünz and Mienert, 2004; Mienert et al., 2005a; Westbrook et al., 2008). It could also be related to authigenic carbonate formation since it increases the compressional wave velocity as well, but this phenomenon is restricted to the uppermost tens of meters (e.g. Mazzini et al., 2004), and as such does not explain the extent of the up bending observed in the study area. The sometimes change from pull up to push down occurring beneath the BGHSZ (Figure 48i) is commonly attributed to a change from localized hydrate concentration to localized accumulation of free gas across the hydrate stability boundary (Hovland and Judd, 1988; Kvenholden, 1998). In the case there is no significant free gas concentration beneath the BGHSZ, the push down caused by the free gas may not be able to fully compensate for the pull up effect, and the distortion could then extend deep beneath the GHSZ. This may explain why we observe pull up occurring beneath the GHSZ (ex. Figure 47; Figure 65).

Cluster analysis of the acoustic chimneys showed that similar features are usually not forming patches in the map, and instead appear to be highly intermingled. One exception is a large pipes patch lying in the southeast of the study area. The acoustic chimneys that compose a patch in the southeast are associated with large pull ups which appear beneath the S2 slide scar. The best examples are represented by features 398, 396, 389 (Figure 47). The occurrence of pull ups restricted to beneath the GHSZ may be related to the fact that these features are lying in an area where the removal of sediments by the Storegga slide forced the BGHSZ to readjust to new equilibrium. This caused a deepening of BGHSZ and the crosscut at the Naust S1-2 (Figure 47). As a consequence of this readjustment, the free gas within Naust S1-2 allowed gas hydrate to grow producing local high velocity anomalies. This way, these particular acoustic chimneys may not represent focused fluid flow pathways but instead could be major velocity distortions caused by local gas hydrate accumulations. This observation supports the notion that gas hydrate accumulation may be playing an important in the size and pull up characteristics of the acoustic chimneys quantified from the ST0408 seismic data.

In some areas we found a clear coincidence between the location of acoustic chimneys, pockmarks and mounds with some focusing elements and/or updip pinch outs within one of the two mentioned high amplitude levels within Naust S, but the determination of the bottom (base) of these acoustic chimneys from the seismic data sometimes show other sources. In the quantified bottom of the acoustic chimneys, the largest features were mainly computed to originate from deeper levels (Horizon A to Uppermost reflection below TNU, figure), including those that are coinciding with subsurface structures at a shallower level (crest of infilling contourite and updip pinchout). And most of the smaller features originate at the level of the BSR (horizon 10), including features that are clearly associated with major migration pathways along the LHAZ seal (horizon A) (Figure 51). This contradiction is most likely explained by a difficulty in the visualization of the real bottom (base) of the acoustic chimneys in the seismic data, since it would be unlikely that the coincidences of the location of acoustic chimneys with subsurface structures and migration pathways could all be accidental. Also as stated above, velocity distortions can extend deep beneath the associated velocity anomaly, making it difficult to quantify the true bottom termination of the fluid flow conduits. For these reasons, the quantification of the actual base of the blowout and seepage pipes could have failed to capture their true origin (source of fluids).

5.2. Origin of fluids to the seabed pockmarks and mounds

The source of the fluids in Nyegga has been attributed to different sources. Berndt et al. (2003) concluded that the fluid escape features in Nyegga are attributed to de-watering through the Eocene-Oligocene polygonal fault systems of the Brygge and Kai formation. The presence of free gas beneath the BSR, the formation of gas hydrates above and the depth variations of the BSR towards hydrocarbon provinces has been attributed to methane gas mixtures of thermogenic and biogenic origin (e.g. Posewang and Mienert, 1999; Bünz et al., 2003). Gas hydrate dissociation and subsequent accumulation of free gas under the BSR has also been proposed as a source for the overlying pockmarks and mounds (Paull et al., 1994).

The thermogenic fluids are suspected to be originating from deeper sources through leakage out of structural traps such as the Tertiary domes (Doré and Lundin, 1996; Bünz et al., 2003). There is some evidence that supports thermogenic fluid migration from below the base of Brygge Formation (Figure 41). From the amplitude distribution, the fluid migration seems to be focused in the southwest of the 3D seismic survey area (Figure 41). This area shows also the largest fault offsets within the polygonal faults affecting the Top Brygge surface (Figure 40b) suggesting a relationship between fault offsets and fluid migrations. More interestingly, the pattern of circular low RMS amplitude anomalies within the high amplitudes may indicate that fluid flow may not be restricted to the fractures manifested by the polygonal fault system (Figure 41). This pattern of low amplitude anomalies is to date undocumented from other studied polygonal fault systems. It could be produced by hydraulic fracturing associated with overpressure, but no acoustic chimneys were observed neither within the Kai and Brygge formation nor originating directly from it. Alternatively, these could represent paleo-pockmarks formed during the time this surface was at the seafloor, but no bathymetric expression was found within the circular anomalies.

Microbial gas generation is also a possible, though likely minor, source of fluids within the Naust formation (Paull et al., 1994; Bünz et al., 2003; Hovland et al., 2005; Mazzini et al., 2005). Bünz et al., (2003) discusses that the bacterial degradation of organic matter in the Naust formation sediments is not enough to explain the distribution and amount of free gas under the BSR, since the presence of BSR is observed at depths close to the base of Naust formation and also because of the low total organic content (less than 1%) of the Naust sediments. While carbon isotopic analyses from carbonates retrieved from inside pockmarks in the study area suggest mixed biogenic and thermogenic gases (δ13C = -52 ‰ to -58 ‰ PDB, Hovland et al., 2005). This in turn, does not necessarily implicate a bacterial degradation of *in situ* organic material within Naust sediments. Brekke et al., (1997) discusses that biodegradation of thermogenic gases into CO_2 and subsequent methane production by methanogens can lead to isotopically light methane. These authors tried to explain why the methane rich fluids within shallow sediments overlying known leaking petroleum reservoirs were depleted in ^{13}C.

One mechanism accounting for free gas accumulation beneath the BSR is the readjustment of the BGHSZ, causing gas hydrate dissociation at the base in a process called gas hydrate recycling. This can be caused by sediment removal relative to the seabed (pressure reduction), or by pressure and temperature changes in response to sea-level fall or bottom-water warming (both of which cause the base of the GHSZ to move upward relative to the seabed). The decrease of the thickness of the HSZ and the dissociation of gas hydrates at the BGHSZ may cause resultant buoyant gas to migrate upward, to increase the thickness of the free gas zone beneath the new BGHSZ or to form hydrates in the GHSZ, whereas some free gas residue remains in the pore space of the sediments beneath the BGHSZ (Haacke et al., 2007). The results of this thesis do not support the idea of gas hydrate recycling. This conclusion is based on observations of the presence of thick free gas zones within Naust S1-2 beneath the BGHSZ, and also based on the discontinuity in the UHAZs across the study area without any co-relatable discontinuity in the conditions for hydrate recycling. The existence of a deeper level of free gas accumulation represented by the LHAZ which are not associated to the GHSZ further supports the idea that the free gas beneath the BGHSZ could be coming mainly from deeper levels, and not from gas hydrate recycling.

5.3. Suggestions for the timing and duration of seafloor seepage

Three observations are considered when trying to constrain the timing and duration of seepage through pockmarks and mounds at Nyegga. (1) Seabed fluid flow features in the eastern part of the study area pierce through Weichselian GDFs; (2) Buried pockmarks and mounds (paleo-features) are not observed in seismic data; (3) Methane derived authigenic carbonates have been sampled in some of the Nyegga pockmarks (Hovland et al., 2005; Mazzini et al., 2005; Mazzini et al., 2006) .

The youngest fluid flow activity in Nyegga must be younger than the GDFs and is therefore younger than the LGM. Datings of foraminifera and crusts sampled from pockmarks confirm an age of < 18 ka (Paull et al., 2008b). These age constraints should be valid for features connected to acoustic chimneys interpreted to originate from both the UHAZ and the LHAZ reservoir.

Within the sediments of the Naust formation, no seismic evidence exits for buried isolated or stacked pockmarks or mounds. Since the chimneys penentrate through the Naust formation, a younger generation of fluid flow activity than the upper Naust may be suggested.

The precipitation of authigenic carbonates is the result of coupled anaerobic methane oxidation (AOM) and sulphate reduction operated by a consortium of archaea and sulphate-reducing bacteria (Judd and Hovland, 2007), a process that takes 10-100 kyrs to form significant carbonate crusts (Andresen et al., 2008). Methane derived authigenic carbonates (MDAC) have been reported from a number of gas hydrate provinces around the world (reference). Samples taken from some of the Nyegga mounds mapped in the study area clearly allowed to identify the MDAC (Hovland et al., 2005; Mazzini et al., 2005; Mazzini et al., 2006), but without age datings. Mounds are distributed in the study area without showing a systematic pattern. The near vicinity of some of these mounds to the pockmarks in the study area may indicate a similar timing for both types of seabed fluid expressions.

The above consideration suggests that the fluid flow features in Nyegga constitute a generation of fluid expulsion that is probably active at least from the LGM to the present.

6. Conclusion

- Swath bathymetry and 3D seismic data allowed mapping of 287 pockmarks, 23 mounds, 441 acoustic chimneys. Additionally several important elements of the geological fluid flow system at Nyegga were identified and analyzed, including GHSZ, GDFs, HAZs and the Polygonal fault system.
- Pockmarks and mounds at Nyegga are interpreted to be the result of fluid seepage from two overpressured shallow reservoirs within Naust S sediments. The pockmarks and mounds at the seabed are connected to acoustic chimneys distributed over major accumulation areas for free gas within these reservoirs. These acoustic chimneys are inferred to represent permeable pathways created by hydraulic fracturing of sealing sediments due to pore pressure build up. Overpressure occurs at both shallow reservoirs as evidenced by the observation of acoustic chimneys reaching the seafloor which are interpreted to be originating from both levels.
- New statistical approach to fluid flow studies presented evidence that the size of both pockmarks and mounds could be partially controlled by the degree of overpressure at the UHAZs, as evidenced by the quantification of the largest features over the crest of structural highs and at updip pinchouts. Also quantification of the orientation of fluid flow expressions, provided evidence that the orientation of pockmarks and mounds in particular areas is inherited from the acoustic chimneys. The orientation of the acoustic chimneys over UHSZ2 are parallel to the orientation of underlying traps from which they are inferred to originate (the updip pinch out of the Naust S1-2 under the BGHSZ against the INS2 reflection and the structural crest formed by infilling contourite sediments of Naust S1-2). This indicates that the orientation of acoustic chimneys, pockmarks and mounds at Nyegga could reflect the geometry of the trap where overpressure develops and hydraulic fractures form.
- Geophysical evidence for the contribution of fluids of thermogenic origin for the shallow fluid flow system in Nyegga was found. Migration appears to be associated with large offset (> 40 ms TWT) polygonal faults. However, previously undocumented circular low RMS amplitude anomalies found within the Top Brygge surface could be evidence for hydraulic fracturing processes. The thermogenic fluids are probably laterally distributed by the LHAZ, while the thick free gas zone represented by the UHAZ is concluded to be mainly product of advection of fluids through acoustic chimneys originating from overpressured areas within the LHAZ.

- The fluid flow features in Nyegga constitute a generation of fluid expulsion that is probably active at least from the LGM to the present.

References

Andreassen, K., Berteussen, K.A., Sognnes, H., Henneberg, K., Langhammer, J. and Mienert, J., 2003. Multicomponent ocean bottom cable data in gas hydrate investigation offshore of Norway. Journal of Geophysical Research, 108(B8).

Andreassen, K., Laberg, J.S. and Vorren, T.O., 2008. Seafloor geomorphology of the SW Barents Sea and its glaci-dynamic implications Geomorphology, 97(1-2): 157-177.

Andresen, K.J., Huuse, M. and Clausen, O.R., 2008. Morphology and distribution of Oligocene and Miocene pockmarks in the Danish North Sea - implications for bottomcurrent activity and fluid migration. Basin Research, 20: 445-466.

Aydin, A., 2000. Fractures, faults, and hydrocarbon entrapment, migration and flow. Marine and Petroleum Geology, 17: 797-814.

Berg, K., Solheim, A. and Bryn, P., 2005. The Pleistocene to recent geological development of the Ormen Lange area. Marine and Petroleum Geology, 22: 45-56.

Berndt, C., 2005. Focused fluid flow in passive continental margins. Philosophical Transactions - Royal Society Mathematical, Physical and Engineering Sciences, 363(1837): 2855-2871.

Berndt, C., Buenz, S., Clayton, T., Mienert, J. and Saunders, M., 2004. Seismic character of bottom simulating reflectors; examples from the mid-Norwegian margin. Marine and Petroleum Geology, 21(6): 723-733.

Berndt, C., Mienert, J. and Bünz, S., 2003. Polygonal fault systems on the mid-Norwegian margin: a long term source for fluid flow. In: P.v. Rensbergen, R.R. Hillis, A.J. Maltman and C.K. Morley (Editors), Subsurface sediment mobilization. Geological Society of London, London, pp. 283-290.

Bjørkum, P.A. and Nadeau, P.H., 1998. Temperature controlled porosity/permeability reduction, fluid migration, and petroleum exploration in sedimentary basins. Aust. Pet. Prod. & Expl. Assoc. Journal., 38: 453-464.

Bjørlykke, K., 2006. Modelling of fluid flow and overpressure - A discussion. Norwegian Journal of Geology, 86: 439-441.

Booth, J.S., Winters, W.J., Dillon, W.P., Clennell, M.B. and Rowe, M.M., 1998. Major occurerences and reservoir concept of marine clathrate hydrates: Implications of field evidence. In: J.P. Henriet and J. Mienert (Editors), Gas Hydrates: Relevance to World Margin Stability and Climate Change. Special Publications. Geological Society, London, pp. 113-127.

Bouriak, S., Vanneste, M. and Saoutkine, A., 2000. Inferred gas hydrates and clay diapirs near the Storegga Slide on the southern edge of the Vøring Plateau, offshore Norway. Marine Geology, 163: 125-148.

Bouriak, S., Volkonskaia, A. and Galaktionov, V., 2003. 'Split' strata-bounded gas hydrate BSR below deposits of the Storegga Slide and at the southern edge of the Vøring Plateau. Marine Geology, 195: 301-318.

Brekke, H., 2000. The tectonic evolution of the Norwegian Sea Continental Margin with emphasis on the Vøring and Møre Basins. In: A. NØTTVEDT (Editor), Dynamics of the Norwegian Margin. Geological Society, London, pp. 327-378.

Bryn, P., Berg, K., Forsberg, C.F., Solheim, A. and Kvalstad, T.J., 2005a. Explaining the Storegga Slide. Marine and Petroleum Geology, 22: 11-19.

Bryn, P., Berg, K., Stoker, M.S., Haflidason, H. and Solheim, A., 2005b. Contourites and their relevance for mass wasting along the mid-Norwegian margin. Marine and Petroleum Geology, 22(1-2): 85-96.

Buenz, S., Mienert, J. and Berndt, C., 2003. Geological controls on the Storegga gas-hydrate system of the mid-Norwegian continental margin. Earth and Planetary Science Letters, 209(3-4): 291-307.
Bugge, T., Befring, S., Belderson, R.H., Eidvin, T., Jansen, E., Kenyon, N.H., Holtedahl, H. and Sejrup, H.P., 1987. A giant three-stage submarine slide off Norway. Geo-Marine Letters, 7(191-198).
Bukovics, C. and Ziegler, P.A., 1985. Tectonic development of the Mid-Norway continental margin. Marine and Petroleum Geology, 2(1): 2-22.
Bünz, S. and Mienert, J., 2004. Acoustic imaging of gas hydrate and free gas at the Storegga Slide. JOURNAL OF GEOPHYSICAL RESEARCH, 109.
Bünz, S., Mienert, J. and Berndt, C., 2003. Geological controls on the Storegga gas-hydrate system of the mid-Norwegian continental margin. Earth and Planetary Science Letters, 209(3-4): 291-307.
Bünz, S., Mienert, J., Bryn, P. and Berg, K., 2005. Fluid flow impact on slope failure from 3D seismic data; a case study in the Storegga Slide. Basin Research, 17(1): 109-122.
Bøe, R., Rise, L. and Ottesen, D., 1997. Elongate depressions on the southern slope of the Norwegian Trench (Skagerrak): morphology and evolution Marine Geology, 146(1-4): 191-203.
Cartwright, J., Huuse, M. and Aplin, A., 2007. Seal bypass systems. AAPG Bulletin, 91(8): 1141–1166.
Cartwright, J., James, D. and Bolton, A., 2003. The genesis of polygonal fault systems; a review. Geological Society Special Publications, 216: 223-243.
Cartwright, J.A. and Dewhurst, D.N., 1998. Layer-bound compaction faults in fine-grained sediments. Geological Society of America Bulletin, 110(10): 1242-1257.
Cartwright, J.A. and Huuse, M., 2005. 3D seismic technology; the geological "Hubble". Basin Research, 17(1): 1-20.
Chand, S., Mienert, J., Andreassen, K., Knies, J., Plassen, L. and Fotland, B., 2008. Gas hydrate stability zone modelling in areas of salt tectonics and pockmarks of the Barents Sea suggests an active hydrocarbon venting system. Marine and Petroleum Geology, 25(7): 625-636.
Chen, J. and Schuster, G.T., 1999. Resolution limits of migrated images. GEOPHYSICS, 64(4): 1046–1053.
Clarke, J.E.H., Gardner, J.V., Torresan, M. and Mayer, L., 1998. The limits of spatial resolution achievable using a 30kHz multibeam sonar: model predictions and field results.
Dalland, A., Worsley, D. and Ofstad, K., 1988. A lithostratigraphic scheme for the Mesozoic and Cenozoic succession offshore mid- and northern Norway. NPD-Bulletin, 4.
Davies, R.J. and Posamentier, H.W., 2005. Geologic processes in sedimentary basins inferred from three-dimensional seismic imaging. GSA Today, 15(10).
Davis, J.C., 1986. Statistics and data analysis in geology 2 ed. John Wiley & Sons, New York, 646 pp.
Dimitrov, L.I., 2002. Mud volcanoes—the most important pathway for degassing deeply buried sediments. Earth-Science Reviews, 59: 49-76.
Doré, A.G. and Lundin, E.R., 1996. Cenozoic compressional structures on the NE Atlantic margin: nature, origin, and potential significance for hydrocarbon exploration. Petroleum Geoscience, 2: 299-311.
Egeberg, P.K., 2000. Hydrates associated with fluid flow above salt diapirs (site 996). In: C.K. Paull, P.J. Matsumoto and W.P. Dillon (Editors), Proceedings of the Ocean Drilling Program, Scientific Results, pp. 219-228.
Eidvin, T. and Rundberg, Y., 2001. Late Cainozoic stratigraphy of the Tampen area (Snorre and Visund fields) in the northern North Sea, with emphasis on the chronology of early Neogene sands. Norsk Geologisk Tidsskrift, 81: 119-160.

Eldholm, O., Thiede, J. and Taylor, E., 1987. Summary and preliminary conclusions, ODP Leg 104. In: O. Eldholm, J. Thiede and E. Taylor (Editors), Proceedings, Initial Reports of the Ocean Drilling Program. College Station, Texas.
Eldholm, O., Thiede, J. and Taylor, E., 1989. Evolution of the Vøring Volcanic Margin. Proceedings of the Ocean Drilling Program, Scientific Results, 104.
Eldholm, O. and Thomas, E., 1993. Environmental impact of volcanic margin formation. Earth and Planetary Science Letters, 117: 319-329.
England, W.A., Mackenzie, A.S., Mann, D.M. and Quingley, T.M., 1987. The movement and entrapment of petroleum fluids in the subsurface. Journal of Geological Society of London, 144(2): 327-347.
Evans, D., McGiveron, S., Harrison, Z., Bryn, P. and Berg, K., 2002. Along-slope variation in the late Neogene evolution of the mid-Norwegian margin in response to uplift and tectonism. Geological Society Special Publications, 196: 139-151.
Gay, A., 2006. Seafloor facies related to upward methane flux within a giant pockmark of the Lower Congo Basin; reply. Marine Geology, 232(1-2): 103-104.
Gay, A., Lopez, M., Cochonat, P., Seranne, M., Levache, D. and Sermondadaz, G., 2006a. Isolated seafloor pockmarks linked to BSRs, fluid chimneys, polygonal faults and stacked Oligocene-Miocene turbiditic palaeochannels in the Lower Congo Basin. Marine Geology, 226(1-2): 25-40.
Gay, A., Lopez, M., Ondreas, H., Charlou, J.L., Sermondadaz, G. and Cochonat, P., 2006b. Seafloor facies related to upward methane flux within a giant pockmark of the Lower Congo Basin. Marine Geology, 226(1-2): 81-95.
Gernon, T.M., Sparks, R.S.J. and Field, M., 2007. Degassing structures in volcaniclastic kimberlite: Examples from southern African kimberlite pipes. Journal of Volcanology and Geothermal Research, 174(1-3): 186-194.
Ginsburg, G.D. and Soloviev, V.A., 1997. Methane migration within the submarine gas-hydrate stability zone under deep-water conditions. Marine Geology, 137(1-2): 49-57.
Gjelberg, J.G., Enoksen, T., Kjærnes, P., Mangerud, G., Martinsen, O.J., Roe, E. and Vågnes, E., 2001. The Maastrichtian and Danian depositional setting, along the eastern margin of the Møre Basin (mid-Norwegian Shelf): implications for reservoir development of the Ormen Lange Field. In: O.J. Martinsen and T. Dreyer (Editors), Sedimentary Environments Offshore Norway — Palaeozoic to Recent. NPF Special Publication, pp. 421-440.
Gravdal, A., Haflidason, H. and Evans, D., 2003. Seabed and subsurface features on the southern Vøring Plateau and northern Storegga Slide Escarpment. In: J. Mienert and P. Weaver (Editors), European Margin Sediments Dynamics, Side-Scan and Seismic Images. . Springer-Verlag, Berlin, pp. 111-117.
Haflidason, H., Lien, R., Sejrup, H.P., Forsberg, C.F. and Bryn, P., 2005. The dating and morphometry of the Storegga Slide. Marine and Petroleum Geology, 22: 123-136.
Haflidason, H., Sejrup, H.P., Nygard, A., Mienert, J., Bryn, P., Lien, R., Forsberg, C.F., Berg, K. and Masson, D., 2004. The Storegga Slide: architecture, geometry and slide development Marine Geology, 213(1-4): 201-234.
Hansen, J.P.V., Cartwright, J.A., Huuse, M. and Clausen, O.R., 2005. 3D seismic expression of fluid migration and mud remobilization on the Gjallar Ridge, offshore mid-Norway. Basin Research, 17(1): 123-139.
He, T., Spence, G.D., Riedel, M., Hyndman, R.D. and Chapman, N.R., 2007. Fluid flow and origin of a carbonate mound offshore Vancouver Island: Seismic and heat flow constraints. Marine Geology, 239: 83-98.
Heggland, R., 1997. Detection of gas migration from a deep source by the use of exploration 3D seismic data. Marine Geology, 137: 41-47.

Heggland, R., 1998. Gas seepage as an indicator of deeper prospective reservoirs. A study based on exploration 3D seismic data. Marine and Petroleum Geology, 15: 1-9.

Henriksen, S. and Vorren, T.O., 1996. Late Cenozoic sedimentation and uplift history on the mid-Norwegian continental shelf. Global and Planetary Change. , 12: 171-199.

Hindle, A.D., 1997. Petroleum migration pathways and charge concentration: a three-dimensional model. Bulletin of American Association of Petroleum Geologists, 8(9): 1451-1481.

Hjelstuen, B.O., Eldholm, O. and Skogseid, J., 1997. Voring Plateau diapir fields and their structural and depositional settings. Marine Geology, 144(1-3): 33-57.

Hjelstuen, B.O., Eldholm, O. and Skogseid, J., 1999. Cenozoic evolution of the northern Vøring Margin. Geological Society of America Bulletin, 111: 1792-1807.

Hjelstuen, B.O., Sejrup, H.P., Haflidason, H., Berg, K. and Bryn, P., 2004a. Neogene and Quaternary depositional environments on the Norwegian continental margin, 62 degrees N-68 degrees N. Marine Geology, 213(1-4): 257-276.

Hjelstuen, B.O., Sejrup, H.P., Haflidason, H., Nygard, A., Ceramicola, S. and Bryn, P., 2005. Late Cenozoic glacial history and evolution of the Storegga Slide area and adjacent slide flank regions, Norwegian continental margin. Marine and Petroleum Geology, 22(1-2): 57-69.

Hjelstuen, B.O., Sejrup, H.P., Haflidason, H., Nygård, A., Berstad, I.M. and Knorr, G., 2004b. Late Quaternary seismic stratigraphy and geological development of the south Vøring margin, Norwegian Sea. Quaternary Science Reviews, 23: 1847-1865.

Hovland, M., 1981. Characteristics of pockmarks in the Norwegian Trench Marine Geology, 39(1-2): 103-117.

Hovland, M., 2003. Geomorphological, geophysical, and geochemical evidence of fluid flow through the seabed. Journal of Geochemical Exploration: 78-79.

Hovland, M., Gardner, J.V. and Judd, A.G., 2002. The significance of pockmarks to understanding fluid flow processes and geohazards. Geofluids, 2(2): 127-136.

Hovland, M. and Judd, A.G., 1988. Seabed pockmarks and seepages: impact on geology, biology and the marine environment. Graham & Trotman Ltd., London.

Hovland, M. and Svensen, H., 2006. Submarine pingoes; indicators of shallow gas hydrates in a pockmark at Nyegga, Norwegian Sea. Marine Geology, 228(1-4): 15-23.

Hovland, M., Svensen, H., Forsberg, C.F., Johansen, H., Fichler, C., Fossa, J.H., Jonsson, R. and Rueslatten, H., 2005. Complex pockmarks with carbonate-ridges off mid-Norway; products of sediment degassing. Marine Geology, 218(1-4): 191-206.

Hovland, M., Talbot, M., Olaussen, S. and Aasberg, L., 1985. Recently formed methane-derived carbonates from the North Sea floor. In: B.M. Thomas (Editor), Petroleum Geochemistry in Exploration of the Norwegian Shelf. Norwegian Petrol. Soc. Graham & Trotman, pp. 263-266.

Hustoft, S., Mienert, J., Bünz, S. and Hervé, N., 2007. High-resolution 3D-seismic data indicate focussed fluid migration pathways above polygonal fault systems of the mid-Norwegian margin. Marine Geology, 245: 89–106.

Huuse, M. and Mickelson, M., 2004. Eocene sandstone intrusions in the Tampen Spur area (Norwegian North Sea Quad 34) imaged by 3D seismic data Marine and Petroleum Geology, 21(2): 141-155.

Haacke, R.R., Westbrook, G. and Hyndman, R.D., 2007. Gas hydrate, fluid flow and free gas: Formation of the bottom-simulating reflector. Earth and Planetary Science Letters, 261: 407-420.

Ivanov, M.K., Westbrook, G., Blinova, V., Kozlova, A., Mazzini, A., Nouzé, H. and Minshull, T., 2007. First Sampling of Gas Hydrate From the Vøring Plateau. EOS, TRANSACTIONS, AMERICAN GEOPHYSICAL UNION, 88(19): 209-216.

Japsen, P. and Chalmers, J.A., 2000. Neogene uplift and tectonics around the North Atlantic: overview. Global and Planetary Change, 24: 165–173.

Johnson, R., A and Wichern, D., W, 2002. Applied Multivariate Statistical Analysis. Prentice-Hall, New Jersey.
Jones, G.B., Floodgate, G.D. and Bennell, J.D., 1986. Chemical and microbiological aspects of acoustically turbid sediments preliminary investigations**.** Marine Geotechnology, 6: 315-332.
Judd, A.G. and Hovland, M., 2007. Seabed Fluid Flow: Impact on Geology, Biology an the Marine Environment. Cambridge, London.
Judd, A.G., Hovland, M., Dimitrov, L.I., Gil, S.G. and Jukes, V., 2002. The geological methane budget at continental margins and its influence on climate change. Geofluids, 2(2): 109-126.
King, L.H. and MacLean, B., 1970. Pockmarks on the Scotian Shelf. . Geological Society of America Bulletin, 81: 3141-3148.
Kjeldstad, A., Skogseid, J., Langtangen, H.P., Bjørlykke, K. and Høeg, K., 2003. Differential loading by prograding sedimentary wedges on continental margins: An arch-forming mechanism. JOURNAL OF GEOPHYSICAL RESEARCH, 108(B1, 2036).
Kopf, A.J., 2002. Significance of mud volcanism. Reviews of Geophysics, 40(2).
Kvenholden, K.A., 1998. A primer on the geological occurerence of gas hydrate. In: J.P. Henriet and J. Mienert (Editors), Gas Hydrates: Relevance to World Margin Stability and Climate Change. Special Publications. Geological Society, London, pp. 9-30.
Laberg, J.S., Stoker, M.S., Dahlgren, T., de Haas, H., Haflidason, H., Hjelstuen, B.O., Nielsen, T., Shannon, P.M., Vorren, T.O., van Weering, T.C.E. and Ceramicola, S., 2005. Cenozoic alongslope processes and sedimentation on the NW European Atlantic margin. Marine and Petroleum Geology, 22: 1069-1088.
Laberg, J.S., Vorren, T.O., Mienert, J., Bryn, P. and Lien, R., 2002. The Trænadjupet Slide: a large slope failure affecting the continental margin of Norway 4000 years ago. Geo-Marine Letters 22: 19–24.
Lee, M.W. and Dillon, W.P., 2001. Amplitude blanking related to pore-filling of gas hydrate in sediments. Marine Geophysical Research, 22: 101-109.
Liu, X. and Flemings, P.B., 2007. Dynamic multiphase flow model of hydrate formation in marine sediments. JOURNAL OF GEOPHYSICAL RESEARCH, 112.
Liu, X., Zhong, G., Yin, J., He, Y. and Li, X., 2008. GIS-based modeling of secondary hydrocarbon migration pathways and its application in the northern Songliao Basin, northeast China. Computers & Geosciences, 34: 1115-1126.
Lundin, E. and Doré, A.G., 2002. Mid-Cenozoic post-breakup deformation in the 'passive' margins bordearing the Norwegian-Greenland Sea. Marine and Petroleum Geology, 19: 79-93.
Løseth, H., L, W., Arntsen, B., Hanken, N., Basire, C. and Graue, K., 2001. 1000m long gas blow out pipes, 63rd EAGE Conference & Excibition, Amsterdam, pp. 524.
MacDonald, I.R., Leifer, I., Sassen, R., Stine, P., Mitchell, R. and Guinasso, N., Jr., 2002. Transfer of hydrocarbons from natural seeps to the water column and atmosphere. Geofluids, 2(2): 95-107.
Mazzini, A., Aloisi, G., Akhmanov, G.G., Parnell, J., Cronin, B.T. and Murphy, P., 2005. Integrated petrographic and geochemical record of hydrocarbon seepage on the Voring Plateau. Journal of the Geological Society of London, 162(5): 815-827.
Mazzini, A., Ivanov, M.K., Parnell, J., Stadnitskaia, A., Cronin, B.T., Poludetkina, E., Mazurenko, L. and van Weering, T.C.E., 2004. Methane-related authigenic carbonates from the Black Sea: geochemical characterisation and relation to seeping fluids. Marine Geology, 212(1-4): 153-181.
Mazzini, A., Svensen, H., Hovland, M. and Planke, S., 2006. Comparison and implications from strikingly different authigenic carbonates in a Nyegga Complex pockmark, G11, Norwegian Sea. Marine Geology, 231(1-4): 89-102.

Mienert, J., Bunz, S., Guidard, S., Vanneste, M. and Berndt, C., 2005a. Ocean bottom seismometer investigations in the Ormen Lange area offshore mid-Norway provide evidence for shallow gas layers in subsurface sediments. Marine and Petroleum Geology, 22(1-2): 287-297.

Mienert, J., Bünz, S., Iversen, S., Hustoft, S., Thingnes, V., Perez-Garcia, C., Faverola, A.P., Eriksen, F.N., Planke, S., Berndt, C., Huggins, R., Royal, R. and Fløystad, K., 2006. Quantification of Geological Processes that Govern Basin Scale Fluid Flow at Nyegga, University of Tromsø, Ålesund-Tromsø aboard R/V Jan Mayen.

Mienert, J., Posewang, J. and Baumann, M., 1998a. Gas hydrates along the north-eastern Atlantic Margin: possible hydrate bound margin instabilities and possible release of methane. In: J.P. Henriet and J. Mienert (Editors), Gas Hydrates: Relevance to World Margin Stability nad Climate Change. Special Publication. Geological Society of London, London, pp. 275-291.

Mienert, J., Posewang, J. and Baumann, M., 1998b. Gas hydrates along the northeastern Atlantic Margin; possible hydrate-bound margin instabilities and possible release of methane. Geological Society Special Publications, 137: 275-291.

Mienert, J., Vanneste, M., Andreassen, K., Haflidason, H. and Sejrup, H.P., 2005b. Ocean warming and gas hydrate stability on the mid-Norwegian margin at the Storegga Slide. Marine and Petroleum Geology, 22: 233-244.

Mosher, D., Bigg, S. and LaPierre, A., 2006. 3D seismic versus multibeam sonar seafloor surface renderings for geohazards assessment: Case examples from central Scotian Slope. The Leading Edge, 25(12): 10.

Mulchrone, K.F. and Choudhury, K.R., 2004. Fitting an ellipse to an arbitrary shape: implications for strain analysis. Journal of Structural Geology, 26: 143-153.

Myhre, A.M., Eldholm, O., Faleide, J.I., Skogseid, J., Gudlaugsson, S.T., Planke, S., Stuevold, L.M. and Vågnes, E., 1992. Norway-Svalbard Continental Margin: Structural and Stratigraphical styles. In: C.W. Poag and P.C. de Graciansky (Editors), Geological Evolution of Atlantic Continental Margins. van Nostrand Reinhold, New York van Nostrand Reinhold, pp. 157-185

Nadeau, P.H., Bjørkum, P.A. and Walderhaug, O., 2005. Petroleum system analysis: Impact of shale diagenesis on reservoir fluid pressure, hydrocarbon migration and biodegradation risks. In: A.G. Doré and B. Vining (Editors), 6th Petroleum Geology Conference - Petroleum Geology: North-West Europe and Global Perspectives. Geological Society, London, pp. 1267-1274.

Naeth, J., di Primio, R., Horsfield, B., Schaefer, R.G., Shannon, P.M., Bailey, W.R. and Henriet, J.P., 2005. Hydrocarbon seepage and carbonate mound formation: a basin modelling study from the porcupine basin (offshore ireland). Journal of Petroleum Geology, 28(2): 147-166.

Orvik, K.A. and Niiler, P., 2002. Major pathways of Atlantic water in the northern North Atlantic and Nordic Seas toward Arctic. . Geophysical Research Letters., 29: X1–X4.

Paull, C.K., Normark, W.R., Ussler III, W., Caress, D.W. and Keaten, R., 2008a. Association among active seafloor deformation, mound formation, and gas hydrate growth and accumulation within the seafloor of the Santa Monica Basin, offshore California. Marine Geology, 250: 258-275.

Paull, C.K., Ussler III, W. and Borowski, W.S., 1994. Sources of biogenic methane to form marine gas hydrates. In: E.D. Sloan, H. J and M.A. Hnatow (Editors), International Conference on Natural Gas Hydrates, Plenum, New York, pp. 393– 409.

Paull, C.K., Ussler III, W., Holbrook, W.S., Hill, T.M., Keaten, R., Mienert, J., Haflidason, H., Johnson, J.E., Winters, W.J. and Lorenson, T.D., 2008b. Origin of pockmarks and chimney structures on the flanks of the Storegga Slide, offshore Norway. Geo-Mae Lett, 28: 43-51.

Perrodon, A., 1983. Dynamics of oil and gas accumulations. Elf Aquitaine, Pau.

Pilcher, R. and Argent, J., 2007. Mega-pockmarks and linear pockmark trains on the West African continental margin. Marine Geology, 244: 15-32.

Planke, S., Svensen, H., Hovland, M., Banks, D.A. and Jamtveit, B., 2003. Mud and fluid migration in active mud volcanoes in Azerbaijan. Geo-Marine Letters, 23(3-4): 258-268.
Plaza-Faverola, A., Ker, S., Westbrook, G., Exley, R., Broto, K., Gailler, A. and Jose, T., 2008. Reflection Tomography for the Investigation of Vp Variation Within the CNE03 Chimney in the Nyegga Region of the Mid-Norwegian Margin, 2008 AGU Fall Meeting. AGU, San Francisco, CA.
Poole, D.A.R. and Vorren, T.O., 1993. Miocene to Quaternary paleoenvironments and uplift history on the mid Norwegian shelf. Marine Geology, 115: 173-205.
Posewang, J. and Mienert, J., 1999. The enigma of double BSRs: indicators for the gas hydrate stability field? In: J.M. Gardner and P.R. Vogt (Editors), High Latitude Gas Venting, Hydrates and Mass Wasting. Geomarine Letters, pp. 157-163.
Rafaelsen, B., Elvebakk, G., Andreassen, K., Stemmarik, L., Colpaert, A. and Sammuelsberg, T.J., 2008. From detached to attached carbonate buildup complexes — 3D seismic data from the upper Palaeozoic, Finnmark Platform, southwestern Barents Sea. Sedimentary Geology, 206(1-3): 17-32.
Riedel, M., Spence, G.D., Chapman, N.R. and Hyndman, R.D., 2002. Seismic investigations of a vent field associated with gas hydrates, offshore Vancouver Island. JOURNAL OF GEOPHYSICAL RESEARCH, 107(B9).
Rise, L., Ottesen, D., Berg, K. and Lundin, E., 2005. Large-scale development of the mid-Norwegian margin during the last 3 million years. Marine and Petroleum Geology, 22(1-2): 33-44.
Rock, N.M.S., 1988. Numerical geology. Springer-Verlag, Heidelberg, Germany.
Schmitz, T. and Jokat, W., 2007. Amplitude versus offset analyses of the deep sedimentary structures at the northern flank of the Porcupine Basin, SW of Ireland. Intenational Journal of Earth Science, 96: 171-184.
Selley, R.C., 1998. Elements of Petroleum Geology. Academic Press, San Diego, USA.
Skogseid, J., Planke, S., Faleide, J.I., Pedersen, T., Eldholm, O. and Neverdal, F., 2000. NE Atlantic continental rifting and volcanic margin formation. Geological Society Special Publications, 167: 295-326.
Sloan, E.D., 1998. Clathrate hydrates of natural gases. Chemical industries 73. Marcel Dekker, New York, XII, 705 s. pp.
Smith, W.H.F. and Sandwell, D.T., 1997. Global seafloor topography from satellite altimetry and ship depth soundings. Science, 277: 1957-1962.
Solheim, A., Berg, K., Forsberg, C.F. and Bryn, P., 2005a. The Storegga Slide Complex; repetitive large scale sliding with similar cause and development. Marine and Petroleum Geology, 22(1-2): 97-107.
Solheim, A., Bryn, P., Sejrup, H.P., Mienert, J. and Berg, K., 2005b. Ormen Lange — an integrated study for the safe development of a deep-water gas field within the Storegga Slide Complex, NE Atlantic continental margin; executive summary. Marine and Petroleum Geology, 22(1-2): 1-9.
Stahl, W., Faber, E., Carey, B.D. and Kirksey, D.L., 1981. Near-surface evidence of migration of natural gas from deep reservoirs and source rocks. AAPG Bulletin, 65: 1543-1550.
Stoker, M.S., Hoult, R.J., T, N., Hjelstuen, B.O., Laberg, J.S., Shannon, P.M., Praeg, D., Mathiesen, A., Van Weering, T.C.E. and McDonnell, A., 2005a. Sedimentary and oceanographic responses to early Neogene compression on the NW European margin. Marine and Petroleum Geology, 22: 1031–1044.
Stoker, M.S., Praeg, D., Hjelstuen, B.O., Laberg, J.S., Nielsen, T. and Shannon, P.M., 2005b. Neogene stratigraphy and the sedimentary and oceanographic development of the NW European Atlantic margin. Marine and Petroleum Geology, 22: 977–1005.

Stuevold, L.M., Faerseth, L., Arnsen, L., Cartwright, J. and Moller, N., 2003. Polygonal faults in the Ormen Lange field, offshore Norway In: P.v. Rensbergen, R.R. Hillis, A.J. Maltman and C.K. Morley (Editors), Subsurface sediment mobilisation. Special publications. Geological Society, London, pp. 263-282.

Svensen, H., Planke, S., Jamtveit, B. and Pedersen, T., 2003. Seep carbonate formation controlled by hidrothermal vent complexes: a case study from the Vøring Basin, the Norwegian Sea. Geo-Marine Letters, 23: 351-358.

Thomas, Y., Masset, B., Didailler, S., Régnault, J.P., Le Conte, S., Le Roux, D., Farcy, P., Magueur, M., Viollette, P., Hervéou, J., Guedes, J.C., Jégot, B., Gascon, G., Prud'homme, C., Nouzé, H., Thereau, E., Contruci, I. and Foucher, J.P., 2004. Sismique marine haute résolution 3D: un nouvel outil de reconnaissance à destination de la communauté scientifique. Comptes Rendus Géosci., 336: 579–585.

Vanneste, M., De Batist, M., Golmshtok, A., Kremlev, A. and Versteeg, W., 2001. Multi-frequency seismicnext term study of gas hydrate-bearing sediments in Lake Baikal, Siberia Marine Geology, 172(1-2): 1-21.

Viana, A.R., Almeida JR, W., Nunes, M.C.V. and Bulhões, E.M., 2007. The economic importance of contourites. In: A.R. Viana and M. Rebesco (Editors), Economic and Palaeoceanographic Significance of Contourite Deposits. Special Publications. Geological Society, London, pp. 1-23.

Vågnes, E., Gabrielsen, R.H. and Haremo, P., 1998. Late Cretaceous–Cenozoic intraplate contractional deformation at the Norwegian continental shelf: timing, magnitude and regional implications. Tectonophysics, 300: 29-46.

Wessel, P. and Smith, W.H.F., 1991. Free software helps map and display data. EOS transactions of the American Geophysical Union, 72(441).

Wessel, P. and Smith, W.H.F., 1998. New, improved version of the Generic Mapping Tools released. EOS transactions of the American Geophysical Union, 79(579).

Westbrook, G., Exley, R., Minshull, T., Nouzé, H., Gailler, A., Tesmi, J., Ker, S. and Plaza, A., 2008. High-resolution 3D seismic investigations of hydrate-bearing fluid-escape chimneys in the Nyegga region of the Vøring Plateau, Norway, 6th International Conference on Gas Hydrates, Vancouver, British Columbia, Canada.

Wheeler, A.J., Beyer, A., Freiwald, A., de Haas, H., Huvenne, V.A., Kozachenko, M. and Olu-Le Roy, K., 2007. Morphology and environment of cold-water coral carbonate mounds on the NW European margin. Intenational Journal of Earth Science, 96: 37-56.

Wood, W.T., Gettrust, J.F., Chapman, N.R., Spence, G.D. and Hyndman, R.D., 2002. Decreased stability of methane hydrates in marine sediments owing to phase boundary roughness. Nature, 420: 656-660.

Yuan, F., Bennell, J.D. and Davis, A.M., 1992. Acoustic and physical characteristics of gassy sediments in the western Irish Sea. Continental Shelf Research, 12(10): 1121-1134.

Zühlsdorff, L. and Spieß, V., 2004. Three-dimensional seismic characterization of a venting site reveals compelling indications of natural hydraulic fracturing. Geology, 32(2): 101-104.

Appendix

Statistics of fluid flow expressions

Statistics of Pockmarks and Mounds

Notation:

Onr = Object number
P = Pockmark
M = Mound
Mres = Mean residual
Vres = Variance of residual

Per = Perimeter
MSl = Mean slope angle
VSl = Variance of slope angle
SA = Short axis length
LA = Long axis length

Orient = Orientation
Src = Data source
BL = base level for contouring
C = Number of underlying chimney
NA = Chimney data not available

Onr	P	M	Mres	Vres	Per	Area	MSl	VSl	X	Y	LA	SA	Orient	Depth	Src	BL	C
1	1	0	-3.585366	1.189054	617.40325	20022.9167	2.263932	0.524478	586800.00	7188300.00	182.63	152.08	93.128	-792.709	MB	-2	NA
2	1	0	-3.603104	0.931166	937.783196	44700	2.73911	0.357933	585940.00	7185700.00	308.4	203.63	56.479	-793.988	MB	-2	NA
3	1	0	-3.903061	1.363052	605.148637	20137.5	2.636503	0.809564	586530.00	7184800.00	187.76	152.77	84.766	-792.419	MB	-2	NA
4	1	0	-4.939698	3.44762	1600.02722	102316.584	2.124066	0.757216	586160.00	7183900.00	428.29	333.69	63.335	-796.628	MB	-2	NA
5	1	0	-3.706667	1.160622	785.280091	30162.5	1.881678	0.461559	587190.00	7184400.00	249.39	166.15	47.943	-786.723	MB	-2	NA
6	1	0	-2.867647	0.203071	320.416306	6750	1.568062	0.065307	593510.00	7184600.00	110.29	84.664	21.164	-754.429	MB	-2	NA
7	1	0	-4.031563	1.767287	1819.05365	129516.667	1.119617	0.342301	586560.00	7182100.00	539.93	345.87	41.096	-797.752	MB	-2	NA
8	1	0	-3.745303	1.383981	1277.83347	46766.6667	1.849614	1.166304	587580.00	7182200.00	383.55	194.49	65.662	-788.582	MB	-2	NA
9	1	0	-4.165017	2.58003	731.771935	30200	2.216856	0.45668	589020.00	7183700.00	221.91	185.53	19.402	-780.698	MB	-2	NA
10	1	0	-2.727273	0.198347	179.6399	2150	1.83526	0.166024	593160.00	7182700.00	58.133	50.938	8.8789	-759.012	MB	-2	NA
11	1	0	-3.403433	0.712778	674.700867	23187.5	1.618461	0.467223	593500.00	7182800.00	224.9	142.74	159.46	-757.471	MB	-2	NA
12	1	0	-2.820755	0.147116	508.700577	10750	1.333517	0.397506	593520.00	7182200.00	175.98	80.347	140.01	-757.942	MB	-2	NA
13	1	0	-2.961538	0.22929	581.652501	15483.3335	1.228494	0.478458	594240.00	7182600.00	179.36	119.41	146.13	-751.483	MB	-2	NA
14	1	0	-3.097561	0.331945	266.076989	4300	1.06066	0.357168	600260.00	7182600.00	103.56	57.273	15.195	-721.536	MB	-2	44
15	1	0	-2.6	0.24	90.710678	550	1.24848	0.076442	601850.00	7182100.00	35.117	24.098	156.8	-715.858	MB	-2	48
16	1	0	-3.270408	0.472798	571.126984	19600	1.798294	0.455736	585490.00	7181000.00	186.88	142.27	78.13	-811.481	MB	-2	NA
17	1	0	-3.578348	0.842152	838.406204	35250	1.922607	0.403951	585680.00	7181600.00	290.48	169.16	77.683	-804.1	MB	-2	NA
18	1	0	-4.4336	2.251991	1012.54834	62500	1.764342	0.384325	586390.00	7180800.00	345.79	248.57	28.917	-810.372	MB	-2	NA
19	1	0	-3.380342	0.637391	600.558731	23137.5	2.376614	0.879682	588160.00	7180500.00	196.84	163.2	43.199	-798.985	MB	-2	NA
20	1	0	-2.705882	0.207612	161.465483	1696.87988	1.608818	0.408183	593830.00	7181500.00	52.414	44.786	44.286	-759.105	MB	-2	NA
21	1	0	-2.910112	0.284055	375.563492	8750	1.23244	0.12036	596620.00	7181800.00	133.32	89.695	1.5452	-740.836	MB	-2	6
22	0	1	2.467213	0.339089	678.735809	24225.3152	1.711854	1.207542	597360.00	7181400.00	215.63	177.52	16.575	-734.844	MB	-2	10
23	1	0	-2.72043	0.351948	425.603612	8683.9314	1.019811	0.099786	598360.00	7181900.00	130.9	90.74	57.835	-731.044	MB	-2	4

24	1	0	-3.196126	0.969127	686.852957	26511.9407	2.078229	0.303964	599990.00	7181200.00	225.35	166.94	15.329	-732.231	MB	-2	29
25	1	0	-3.222222	0.518519	349.705627	8100	2.150096	0.369993	600460.00	7180400.00	132.7	84.345	17.992	-726.895	MB	-2	78
26	1	0	-3.521008	0.921828	417.989899	11800	2.25733	0.250042	601030.00	7181800.00	143.83	113.98	53.496	-722.369	MB	-2	40
27	1	0	-4.707317	3.23141	733.487663	32750	2.173446	0.408943	601470.00	7180800.00	232.94	193.14	36.735	-727.319	MB	-2	54
28	1	0	-3.39726	0.664102	505.137665	14600	2.05186	0.299023	601650.00	7181000.00	187.57	104.86	13.311	-723.426	MB	-2	54
29	1	0	-3.272461	1.247064	389.64182	10378.8196	2.575267	0.065899	602020.00	7180500.00	138.74	107.35	45.847	-724.263	MB	-2	109
30	1	0	-3.918067	1.604632	1038.04611	47850	1.480546	0.080475	602740.00	7179900.00	88.828	62.663	169.59	-720.943	MB	-2	118
31	0	1	4	0	76.568542	300	2.637727	0.118726	602350.00	7180200.00	34.346	18.503	173.94	-719.733	MB	2	117
32	1	0	-3.881657	1.666468	529.345528	16600	2.081163	0.152829	603600.00	7180900.00	167.36	136.97	63.992	-717.982	MB	-2	112
34	1	0	-2.666667	0.222222	130.710678	1250	1.647407	0.809598	605070.00	7180200.00	47.118	37.586	167.16	-711.074	MB	-2	139
35	1	0	-2.708369	0.004894	210.655074	3019.2583	1.187085	0.249572	604020.00	7180700.00	77.699	54.138	67.419	-714.253	MB	-2	114
36	1	0	-3.439628	0.970813	953.193291	32000	1.953733	1.78751	610320.00	7181000.00	290.58	163.84	19.154	-692.584	MB	-2	NA
37	1	0	-2.774194	0.174818	229.705627	3200	1.190118	0.243276	610720.00	7181200.00	76.318	56.486	60.875	-684.573	MB	-2	151
38	1	0	-2.775	0.274375	256.142716	3750	1.969906	0.513217	610880.00	7180800.00	92.735	55.432	130.38	-681.535	MB	-2	NA
39	1	0	-3.455882	0.718642	313.836518	6668.75	3.142514	1.000555	611030.00	7181100.00	109.21	85.209	10.963	-684.275	MB	-2	NA
40	1	0	-2.714286	0.204082	173.137085	2100	1.91425	0.484578	611250.00	7181500.00	62.575	47.01	179.59	-673.859	MB	-2	NA
41	1	0	-3.414474	0.861106	499.345528	15300	1.859946	0.877506	611580.00	7180300.00	169.91	125.29	20.687	-674.083	MB	-2	155
42	1	0	-3.252874	0.510768	352.132034	8650	1.62234	0.440339	611710.00	7180900.00	117.15	101.86	153.08	-667.171	MB	-2	154
43	1	0	-3.237705	0.427103	480.427277	12487.5	0.719486	0.116532	612160.00	7180400.00	143.7	117.27	106	-664.58	MB	-2	NA
44	1	0	-3.096154	0.471524	326.787667	5150	0.786094	0.190429	612510.00	7180000.00	104.8	68.709	117.5	-662.22	MB	-2	157
45	1	0	-3.845	1.980975	753.193291	19900	1.129364	0.271674	612630.00	7180100.00	198.72	135.71	44.634	-662.846	MB	-2	157
46	1	0	-2.982759	0.3043	727.138245	17400	1.153285	0.213354	612580.00	7180300.00	182.77	132.41	43.319	-662.42	MB	-2	157
47	1	0	-3.1875	0.371094	539.367104	13842.3491	1.916046	0.820201	612780.00	7180500.00	197.3	92.028	64.303	-661.682	MB	-2	NA
48	1	0	-3.906977	0.735533	459.730904	12814.6245	0.88466	0.180122	612840.00	7180300.00	154.83	110.78	66.423	-660.293	MB	-2	157
49	1	0	-3.782486	1.2041	810.121933	35450	1.680233	0.218174	583900.00	7179500.00	245.42	197.27	83.175	-836.583	MB	-2	NA
50	1	0	-4.061538	1.61929	700.189229	26116.6667	2.243564	0.56629	587050.00	7178200.00	200.79	181.12	36.467	-838.381	MB	-2	NA
51	1	0	-2.393295	0.0708	237.538768	3893.61133	1.437893	0.122468	600020.00	7179500.00	81.444	69.388	88.864	-735.307	MB	-2	89
52	1	0	-2.829268	0.190363	369.705627	8100	2.057649	0.698401	600140.00	7179800.00	123.66	88.647	33.444	-734.21	MB	-2	87
53	1	0	-3.344444	0.336914	397.664369	9910.05664	2.93241	0.321196	600610.00	7179900.00	129.61	98.889	157.17	-730.9	MB	-2	88
54	1	0	-3.196918	0.80687	396.370634	9580.19043	3.200382	0.257618	600630.00	7179900.00	156.73	88.723	81.953	-730.257	MB	-2	88
55	1	0	-3.409006	0.67324	1461.18319	53150	1.835613	1.05782	601310.00	7179700.00	462.98	189.07	7.2646	-728.159	MB	-2	NA
56	1	0	-3.632159	0.910948	1170.53824	45700	1.330808	0.7337	601330.00	7179300.00	337.87	183.26	83.281	-730.108	MB	-2	91
57	1	0	-3.627451	1.057286	395.203392	10200	2.786191	0.139928	601920.00	7179200.00	139.2	101.47	89.192	-731.112	MB	-2	125
58	1	0	-1.089286	0.367028	406.27417	11200	1.305655	0.354162	602290.00	7178800.00	137.57	111.89	50.25	-729.003	ST0408	0	133

B

59	1	0	-0.819672	0.14781	295.563492	6150	1.338509	0.23022	602520.00	7179300.00	100.77	84.191	31.865	-724.206	ST0408	0	127
60	1	0	-1.952055	0.168934	611.900126	14508.634	1.182714	0.137708	602550.00	7178100.00	157.11	125.29	138.46	-733.482	MB	-1	189
61	1	0	-0.890625	0.253662	309.705627	6400	1.434018	0.456428	602670.00	7179500.00	106.67	82.225	22.308	-722.178	ST0408	0	124
62	1	0	-0.615385	0.236686	130.710678	1250	0.945014	0.155998	602730.00	7178800.00	47.804	37.768	36.955	-723.384	ST0408	0	132
63	1	0	-3.074468	0.302965	366.076989	9450	1.262544	0.073999	602760.00	7179900.00	126.74	104.56	27.46	-719.076	MB	-2	118
64	1	0	-2.756757	0.184076	233.137085	3700	1.667042	0.530557	603150.00	7178900.00	85.348	59.927	39.713	-723.529	MB	-2	130
65	1	0	-1.774194	0.174818	207.279221	3150	1.420413	0.348108	603230.00	7178800.00	73.519	60.137	62.81	-722.946	ST0408	-1	134
66	1	0	-0.804348	0.200851	255.563492	4550	0.893369	0.108792	603360.00	7179500.00	91.851	68.696	7.1267	-719.25	ST0408	0	122
67	1	0	-2.72	0.2016	187.213494	2450	1.764998	0.033642	604400.00	7179400.00	70.228	48.171	18.141	-720.362	MB	-2	141
68	1	0	-1.840426	0.13411	381.421356	9500	1.09683	0.167035	604720.00	7179100.00	131.98	98.491	179.6	-717.173	ST0408	-1	142
69	1	0	-4.219409	2.16283	605.324687	24556.4692	2.953049	0.44396	604880.00	7178700.00	204.12	163.76	8.7231	-723.02	MB	-2	144
70	1	0	-2.060345	0.332565	420.416306	11650	1.101037	0.129275	605570.00	7179700.00	141.65	113.79	16.923	-710.541	ST0408	-1	147
71	1	0	-3.245902	0.54609	287.924172	6050	2.404785	0.433808	606580.00	7178500.00	102.2	82.359	42.011	-716.613	MB	-2	202
72	1	0	-1.631006	0.000933	225.023559	2188.13184	0.529381	0.052438	607510.00	7176100.00	85.747	37.041	3.6285	-719.16	MB	-1	234
73	1	0	-1.123077	0.354083	170	2300	1.161995	0.146935	608640.00	7178900.00	106.61	87.99	3.3116	-701.635	MB	0	NA
74	1	0	-1.185714	0.494082	454.558441	14100	1.278275	0.301326	609070.00	7179400.00	159.37	121.33	21.353	-698.198	ST0408	0	153
75	1	0	-1.633567	0.253006	423.913821	10779.6631	1.28106	0.266084	610210.00	7178800.00	161.12	95.107	92.702	-694.58	MB	-1	267
76	1	0	-1.668327	0.536332	305.952015	5609.521	1.353315	0.146323	610540.00	7179000.00	114.17	74.153	158.83	-693.872	MB	-1	266
77	1	0	-2.123596	0.502381	491.236113	14154.7388	1.541992	0.418394	610600.00	7178200.00	167.84	120.18	75.681	-694.895	MB	-1	272
78	1	0	-2	0	197.498248	2356.17603	1.315971	0.083501	610580.00	7178500.00	74.999	44.943	92.212	-692.073	MB	-1	NA
79	1	0	-2.058266	0.084961	253.55622	4075.73584	1.042305	0.105509	610880.00	7178800.00	93.255	59.076	43.591	-691.551	MB	-1	268
80	1	0	-2.305797	0.22715	531.912534	15800.4768	1.342601	0.293345	611030.00	7178200.00	195.9	108.38	48.853	-692.738	MB	-1	271
81	1	0	-2	0	88.558901	519.0625	1.064719	0.006029	611140.00	7178400.00	31.166	23.779	138.67	-691.927	MB	-1	271
82	1	0	-2.084621	0.110284	514.632042	12171.4998	1.396492	0.519836	611200.00	7178200.00	192.6	87.72	64.486	-692.631	MB	-1	271
83	1	0	-2.676179	0.859059	400.722961	10388.5935	2.233073	0.471499	611130.00	7178600.00	149.77	94.908	31.601	-693.543	MB	-1	270
84	1	0	-2	0	229.459253	3670.81543	1.33412	0.136191	611080.00	7179000.00	81.286	63.068	83.411	-692.072	MB	-1	268
85	1	0	-1.753885	0.12816	284.562094	5450.85474	1.662981	0.199693	611470.00	7179000.00	106.84	72.441	1.8929	-686.79	MB	-1	304
86	1	0	-2	0	188.10877	2509.35742	0.824808	0.238726	611430.00	7178300.00	69.727	50.983	39.164	-691.407	MB	-1	271
87	1	0	-1.191919	0.052469	366.708841	5903.71924	1.130211	0.355653	611500.00	7178400.00	138.12	68.771	84.194	-690.412	MB	-1	NA
88	1	0	-2	0	140.704454	1313.07544	1.023781	0.260698	611610.00	7178300.00	52.529	34.901	58.815	-691.445	MB	-1	310
89	1	0	-2	0	149.168465	1401.49609	2.32506	1.125456	611690.00	7178300.00	59.074	35.422	86.45	-689.672	MB	-1	310
90	1	0	-2.213178	0.338944	456.766966	13449.6306	2.433234	1.340069	611730.00	7178100.00	165.26	113.35	91.075	-691.836	MB	-1	310
91	1	0	-0.623551	0.018527	141.289807	1058.31836	0.989003	0.044467	611740.00	7178500.00	47.569	34.86	101.71	-684.995	MB	-1	306
92	1	0	-1.607794	0.027712	149.930821	1410.7666	0.805189	0.313675	611570.00	7179700.00	56.808	36.071	66.422	-677.361	MB	-1	NA

C

93	1	0	-1.509498	0.007178	198.286963	2451.18481	0.795646	0.228338	611770.00	7179700.00	74.694	46.541	114.94	-672.824	MB	-1	NA
94	1	0	-1.378762	0.014711	119.834217	860.087646	1.317096	0.258878	611940.00	7179300.00	40.001	33.861	136.74	-672.808	MB	-1	303
95	1	0	-1.257999	0.026938	136.086954	1205.40332	1.051923	0.432053	611840.00	7178800.00	53.511	34.952	113.91	-680.398	MB	-1	305
96	1	0	-3.75039	1.449996	534.803905	16117.5842	2.774859	0.956754	611980.00	7178000.00	195.25	116.8	37.761	-692.682	MB	-2	NA
97	1	0	-2.700937	0.251676	255.289286	3980.84106	1.615207	0.561732	611970.00	7179600.00	97.958	57.886	155.01	-672.547	MB	-2	NA
98	1	0	-3.12869	0.34745	430.434215	8696.92383	3.607483	0.615399	612110.00	7179100.00	157.76	82.248	105.62	-676.798	MB	-2	301
99	0	1	1.438282	0.103986	348.426245	4270.76172	1.522048	1.079639	612260.00	7179100.00	101.43	67.211	137.98	-667.841	MB	1	302
100	1	0	-1.415298	0.013587	92.339394	585.819092	0.942797	0.017274	612290.00	7179100.00	32.981	26.699	47.729	-670.624	MB	-1	302
101	1	0	-3.017188	0.397357	272.567653	5023.31494	3.176385	2.874228	612230.00	7178200.00	93.135	74.434	154.93	-682.924	MB	-2	309
102	1	0	-1.808261	0.000934	114.746817	929.680664	0.647349	0.003268	612270.00	7179500.00	40.565	32.563	5.9346	-670.921	MB	-1	NA
103	1	0	-2.579937	0.130269	300.255437	5856.1167	1.816	0.426369	612300.00	7178600.00	110.52	73.839	139.93	-676.464	MB	-2	NA
104	1	0	-3.610114	1.185406	293.639669	6391.52075	2.700269	1.301368	612660.00	7179000.00	111.7	80.587	35.562	-672.705	MB	-2	300
105	1	0	-1.68371	0.002772	194.409706	2633.72363	0.910337	0.309104	612820.00	7179200.00	67.51	54.686	83.028	-665.296	MB	-1	300
106	1	0	-2.43327	0.198361	286.694787	3405.83106	1.376625	0.191094	612950.00	7179300.00	105.1	51.727	102.36	-665.191	MB	-2	299
107	1	0	-2.636853	0.000482	148.547729	1496.40088	1.576528	0.106394	612940.00	7179500.00	55.54	38.29	173.31	-664.384	MB	-2	298
108	1	0	-2.919385	0.000707	92.165295	638.721191	2.280744	0.178827	613180.00	7179800.00	34.082	28.537	19.624	-660.067	MB	-2	297
109	1	0	-1.729936	0.003159	232.304682	3379.92676	1.264963	0.062792	613160.00	7179600.00	91.545	52.245	88.614	-661.136	MB	-1	298
110	1	0	-2.543744	0.144447	265.891079	4362.23682	1.97366	0.734474	613580.00	7179400.00	88.894	68.929	112.53	-657.894	MB	-1	NA
111	1	0	-3.710432	1.21901	784.611346	31302.1182	2.843853	0.968141	583310.00	7176700.00	248.88	182.29	107.69	-891.808	MB	-2	NA
112	1	0	-3.186112	0.595728	583.68199	21141.3662	2.131002	1.050725	583530.00	7177100.00	197.15	150.43	124.33	-878.367	MB	-2	NA
113	1	0	-3.401828	0.428	793.684808	24988.6021	1.727752	1.250264	586450.00	7177500.00	229.73	160.18	152.72	-852.468	MB	-2	NA
114	0	1	1.901227	0.192282	418.30066	11284.1052	1.860969	0.478664	598510.00	7176700.00	140.04	114.32	70.166	-764.313	MB	1	163
115	0	1	2.643781	0.210841	365.14149	7545.65894	1.334725	0.342531	598370.00	7176000.00	136.86	79.987	26.463	-774.463	MB	2	165
116	1	0	-2	0	208.667419	2761.61157	1.355548	0.094173	602300.00	7176800.00	74.126	52.076	72.543	-746.69	ST0408	-1	197
117	1	0	-2	0	374.954443	7506.61646	0.64676	0.076236	603730.00	7177700.00	146.74	71.32	115.69	-727.505	ST0408	-1	195
118	1	0	-1.761042	0.147586	325.126839	5596.51123	1.123322	0.161232	604090.00	7176200.00	125.26	63.47	68.744	-739.883	MB	-1	200
119	1	0	-0.852483	0.000101	142.981163	1338.54126	0.544624	0.062302	604130.00	7176300.00	54.659	37.006	43.736	-736.833	MB	-1	199
120	1	0	-2.383801	0.16905	273.97085	4767.57593	1.283613	0.195891	605670.00	7176500.00	111.08	60.89	76.119	-729.075	MB	-2	214
121	1	0	-4.440279	2.447895	518.245263	17434.9592	3.039987	1.445641	605870.00	7176500.00	177.48	139.57	88.462	-733.329	MB	-2	214
122	1	0	-3.410256	0.741946	547.695526	15600	2.754533	0.620337	606230.00	7176100.00	209.19	99.352	139.5	-728.58	MB	-2	363
123	1	0	-3.709955	0.595983	368.600166	9455.64478	2.088327	0.183019	606360.00	7177100.00	124.21	105.84	166.16	-724.306	MB	-2	211
124	1	0	-1.808824	0.154628	357.989899	6900	1.05293	0.111205	606630.00	7176300.00	133.32	69.044	41.502	-723.432	MB	-1	362
125	1	0	-1.88	0.2256	275.563492	5150	1.736946	0.397098	607090.00	7176400.00	93.487	76.057	120.04	-720.826	MB	-1	231
126	1	0	-3	0.388889	231.355629	3700	1.356513	0.448993	607150.00	7177700.00	87.232	59.117	16.197	-714.763	MB	-2	220

D

127	1	0	-1.5	0.25	76.687531	404.41748	0.813404	0.117739	607380.00	7176700.00	28.303	20.944	76.768	-716.127	MB	-1	229
128	1	0	-2.666667	0.222222	144.852814	1500	1.72918	1.202383	607440.00	7177300.00	51.376	42.08	72.433	-714.025	MB	-2	224
129	1	0	-1.793103	0.16409	207.279221	3050	0.774842	0.1177	607520.00	7176100.00	70.418	60.754	101.27	-718.932	ST0408	-1	234
130	1	0	-3.138595	0.328028	272.066562	4849.99463	2.332091	0.341304	607740.00	7176000.00	101.53	68.035	105.96	-721.713	MB	-2	235
131	1	0	-3.880956	1.585557	405.992043	11141.2803	2.566591	0.229462	608390.00	7177600.00	144.07	107.48	30.133	-712.512	MB	-2	222
132	1	0	-1	0	261.421356	4400	0.506111	0.038862	608260.00	7177100.00	93.148	64.886	69.526	-709.028	ST0408	0	225
133	1	0	-1.263286	0.023928	232.546575	3514.77002	0.849566	0.109177	609110.00	7177100.00	87.912	57.517	53.848	-704.621	MB	-1	227
134	1	0	-2.572206	0.223521	218.054411	3147.60986	1.793258	0.172195	609330.00	7177100.00	79.401	57.842	84.013	-705.052	MB	-2	228
135	1	0	-3.925668	1.248482	326.648709	7582.54907	3.095561	0.450572	609490.00	7176300.00	117.94	89.129	51.605	-712.004	MB	-2	287
136	1	0	-3.333021	1.233379	580.089285	13973.6604	2.021236	1.571232	609570.00	7176900.00	222.75	95.727	70.876	-706.313	MB	-2	281
138	1	0	-1	0	295.563492	6050	1.025849	0.36869	609710.00	7177500.00	102.56	81.177	38.747	-697.753	ST0408	0	277
139	1	0	-1	0	329.705627	5300	1.473239	0.29636	609710.00	7177700.00	116.08	61.843	133.82	-698.871	ST0408	0	NA
140	1	0	-3.014508	0.56036	350.52398	7490.0061	1.025849	0.36869	609710.00	7177500.00	102.56	81.177	38.747	-697.753	MB	-2	277
141	1	0	-2.968268	0.74852	525.888184	14517.9407	2.651494	0.200864	609960.00	7176100.00	129.4	82.847	62.289	-708.715	MB	-2	294
142	1	0	-1.755907	0.142603	265.794823	4340.52246	2.214509	0.718832	610040.00	7177300.00	170.39	124.42	175.72	-702.451	MB	-1	276
143	1	0	-2.934459	0.449803	379.652971	8622.85254	2.095342	0.470369	609720.00	7176000.00	101	60.867	54.243	-709.06	MB	-2	294
144	1	0	-3.378101	0.879051	621.244	14219.3601	2.707923	0.142701	609960.00	7176100.00	148.52	81.828	55.241	-708.626	MB	-2	294
145	1	0	-2.668478	0.149703	301.584806	3821.37573	2.173223	0.328872	610110.00	7176700.00	220.11	93.327	53.895	-704.7	MB	-2	285
146	1	0	-3.45318	1.473599	519.046281	16037.7505	1.803502	0.986354	610210.00	7176300.00	103.93	53.598	91.736	-704.207	MB	-2	288
147	1	0	-2.219598	0.014833	361.944994	6006.35523	3.152486	1.17975	610660.00	7177300.00	198.29	114.62	98.408	-701.454	MB	-2	278
148	1	0	-2.596938	0.001177	344.489883	5345.74292	1.664139	0.159343	610840.00	7177300.00	144.92	65.506	58.976	-697.273	MB	-2	278
149	1	0	-3.374416	0.541189	340.419405	6919.39673	1.413593	0.266975	610770.00	7177000.00	139.37	52.519	95.688	-698.396	MB	-2	282
150	1	0	-3.967401	1.579145	1173.02809	38406.5037	3.086681	0.777885	611010.00	7177100.00	131.68	73.9	63.266	-699.433	MB	-2	283
151	1	0	-3.374416	0.541189	340.419405	6919.39673	3.640486	1.761459	610980.00	7176200.00	466.31	126.05	79.303	-702.054	MB	-2	292
152	1	0	-2.754327	0.000219	184.868226	2236.74292	3.086681	0.777885	611010.00	7177100.00	131.68	73.9	63.266	-699.433	MB	-2	283
153	1	0	-2.417869	0.000194	270.167889	3750.13281	1.435308	0.088819	611110.00	7177000.00	70.784	44.605	71.377	-698.133	MB	-2	283
154	1	0	-2.401568	0.000553	159.201975	1611.24707	1.301951	0.533467	611020.00	7177400.00	94.863	60.272	0.36789	-695.952	MB	-2	278
155	1	0	-3.243228	0.733296	685.626075	19162.1079	1.013235	0.022524	611010.00	7177700.00	59.889	38.605	35.272	-694.892	MB	-2	275
156	1	0	-2.809262	0.366708	739.889532	15801.6265	2.749952	0.73884	611290.00	7177500.00	284.97	92.67	66.76	-696.337	MB	-2	279
157	1	0	-2.769263	0.183087	401.256341	9861.30859	1.955991	0.411548	611470.00	7176400.00	301.86	73.997	64.864	-700.444	MB	-2	290
158	1	0	-3.277597	1.066775	462.512125	13332.804	1.491579	0.478691	611750.00	7176500.00	150.43	92.201	89.612	-700.065	MB	-2	289
159	1	0	-2.501664	0.001337	570.066606	10633.186	2.339832	0.861126	611620.00	7177300.00	166.62	112.53	67.121	-698.171	MB	-2	280
160	1	0	-2.511832	0.000622	179.592848	2166.17114	1.327707	0.475631	611740.00	7177800.00	188.69	89.744	171.73	-692.899	MB	-2	NA
161	1	0	-1.459099	0.002088	203.413567	2492.56397	0.72844	0.027936	611720.00	7176400.00	70.625	43.661	56.393	-700.88	MB	-1	293

162	1	0	-2.578953	0.000191	72.880301	400.027588	0.375321	0.025507	611650.00	7176300.00	80.846	43.496	62.242	-699.785	MB	-2	293
163	1	0	-1.783048	0.000413	94.288301	599.409424	0.73764	0.098669	611540.00	7176200.00	27.56	21.393	23.824	-700.743	MB	-1	290
164	1	0	-1.714286	0.204082	198.994949	2750	1.03736	0.155784	611390.00	7176200.00	38.092	24.092	17.266	-700.299	ST0408	-1	291
165	1	0	-1.903281	0.546053	1486.80138	62473.4329	0.491736	0.015821	611030.00	7177900.00	74.221	51.563	43.774	-692.034	ST0408	-1	274
166	1	0	-1.357239	0.260787	469.785021	9209.67212	2.072642	1.634847	612240.00	7176000.00	573.52	148.31	75.302	-697.904	ST0408	-1	316
167	1	0	-2.361086	0.001307	129.205431	1194.88672	2.139297	0.307889	612270.00	7176600.00	200.94	64.987	90.142	-690.692	MB	-2	NA
168	1	0	-1.357016	0.031803	469.785021	9209.67212	1.918259	0.221629	612610.00	7176500.00	46.98	36.993	143.32	-686.376	ST0408	-1	315
169	0	1	2.112718	0.00183	258.414989	4596.14209	1.474932	1.012161	598420.00	7175700.00	97.775	68.2	0.25125	-779.68	MB	2	166
170	0	1	2.511606	0.001753	128.213746	1036.53003	1.553395	0.642897	599400.00	7174200.00	50.648	29.244	80.715	-791.306	MB	2	411
171	0	1	2	0	176.568542	2200	1.541871	1.076354	597120.00	7175500.00	62.602	52.943	33.97	-791.55	MB	2	168
172	0	1	1.386174	0.00003	282.953549	5169.39136	0.765049	0.31946	597550.00	7174600.00	110.62	65.877	30.245	-804.37	ST0408	1	408
173	0	1	1.420609	0	97.85715	579.758301	0.968136	0.04367	597770.00	7174900.00	35.117	26.588	150.35	-797.413	ST0408	1	407
174	1	0	-0.817073	0.149465	366.27417	8100	1.549376	0.316794	597610.00	7174500.00	139.54	78.173	39.032	-805.625	ST0408	0	408
175	0	1	2	0	178.994949	1650	1.40126	0.648638	600230.00	7175100.00	75.848	35.261	69.908	-774.922	MB	2	422
176	0	1	2.084205	0.003106	200.229098	1416.6521	0.416042	0.055665	600390.00	7174800.00	81.184	32.216	86.53	-778.223	MB	2	423
177	0	1	2.17975	0.01119	166.162873	1857.66455	0.742731	0.105513	603570.00	7175300.00	64.077	42.955	163.17	-746.224	MB	2	431
178	1	0	-3.225414	0.519113	647.808571	23896.5354	2.494906	1.490012	604040.00	7175000.00	214.72	155.33	54.895	-754.759	MB	-2	433
179	0	1	2.549996	0.218789	191.870084	2289.43774	1.858835	0.268849	607970.00	7175300.00	75.834	44.964	9.0605	-719.071	MB	2	246
180	1	0	-1.438741	0.211312	275.296186	3345.75684	1.473295	0.466478	604490.00	7175100.00	78.974	63.744	154.6	-747.401	MB	-1	434
181	1	0	-2.221853	0.003045	341.796329	5931.21069	0.946629	0.107869	606180.00	7175500.00	139.34	61.938	68.984	-733.181	MB	-2	367
182	1	0	-2.276397	0.000765	237.352231	3514.44238	1.164505	0.38942	606350.00	7175700.00	82.506	64.759	152.88	-729.519	MB	-2	365
183	1	0	-2.510369	0.184805	485.33157	10008.906	1.676755	1.132781	606370.00	7174600.00	139.31	109.91	117.38	-739.171	MB	-2	369
184	1	0	-2.436094	0.194518	446.129708	9508.92847	1.332005	0.3011	606640.00	7174500.00	166	88.125	23.589	-740.639	MB	-2	371
185	1	0	-2.487653	0.000297	237.913458	3714.53589	1.396572	0.522971	607080.00	7175300.00	87.316	62.127	44.199	-729.288	MB	-2	243
186	1	0	-3.066092	0.390213	307.736146	5926.6167	1.528872	0.319965	607140.00	7174300.00	104.55	81.727	36.26	-739.541	MB	-2	376
187	0	1	2.798531	0.000605	239.43496	2730.48389	1.291308	0.170058	607270.00	7174600.00	94.403	40.079	131.27	-729.034	MB	2	260
188	1	0	-2.73186	0.57561	264.048888	4007.39111	2.716955	0.272678	607290.00	7174600.00	97.336	59.154	161.77	-734.437	MB	-2	260
189	1	0	-2.496946	0.203566	765.306833	16682.6243	1.441817	0.440402	607650.00	7175600.00	309.74	78.806	71.968	-724.496	MB	-2	240
190	1	0	-2.851816	0.243942	531.57346	15295.7197	1.906363	0.548604	607690.00	7174100.00	173.48	127.66	129.9	-737.532	MB	-2	264
191	1	0	-3.121158	0.392778	985.61152	38030.1885	2.268783	1.153747	607790.00	7174800.00	272.35	217.32	43.81	-730.622	MB	-2	254
192	1	0	-3.054299	0.642262	679.95265	23118.5891	1.994279	0.8013	607830.00	7175200.00	212.42	158.73	33.824	-727.61	MB	-2	246
193	1	0	-2.617232	0.100027	427.340112	7109.75513	1.790162	0.554826	608060.00	7175500.00	152.04	69.044	131.94	-723.909	MB	-2	242
194	1	0	-2.296526	0.167614	162.030386	1375.62061	0.914984	0.03848	608060.00	7175300.00	61.347	33.331	56.805	-724.405	MB	-2	246
195	0	1	4.591915	3.2311	589.045549	19790.155	4.537471	3.152621	607960.00	7174900.00	200.54	141.42	157.83	-718.276	MB	2	254

F

196	1	0	-2.227514	0.001208	123.408541	968.405273	1.066412	0.143295	608020.00	7175200.00	48.143	30.828	62.848	-725.159	MB	-2	246
197	1	0	-4.503342	3.292732	1065.79596	59300.2336	3.375078	5.719292	607920.00	7173300.00	376.09	226.2	87.506	-746.975	MB	-2	349
198	1	0	-2.080155	0.00201	212.217638	2495.43701	1.016565	0.121757	608210.00	7175700.00	84.299	44.016	75.27	-719.997	MB	-2	242
199	1	0	-2.302042	0.140795	317.764015	5431.47827	1.435692	0.539098	608330.00	7175300.00	105.26	70.328	143.46	-721.298	MB	-2	247
200	1	0	-2.673927	0.367163	333.58698	6549.48535	1.819984	0.438538	608250.00	7175000.00	130.03	72.389	56.522	-725.755	MB	-2	255
201	0	1	0.881406	0.000825	200.295393	2248.67236	1.26638	0.460123	608310.00	7175000.00	71.2	43.506	51.963	-721.472	MB	0	255
202	1	0	-2.672984	0.514037	263.2282	4093.63403	1.736878	0.312189	608570.00	7175000.00	104.17	57.333	81.799	-724.022	MB	-2	255
203	1	0	-1.987109	0.000695	201.545433	2787.28711	1.067539	0.228633	608690.00	7175900.00	75.035	52.836	80.992	-715.689	MB	-2	238
204	1	0	-3.860304	1.997072	408.336283	10040.3735	3.029817	1.008416	608710.00	7175700.00	157.81	89.79	11.693	-721.695	MB	-2	241
205	1	0	-2	0	138.551177	1252.1919	0.803749	0.067383	608720.00	7175500.00	54.086	36.999	69.083	-718.186	MB	-2	244
206	1	0	-2.780711	0.502069	403.992703	10285.8184	2.377695	0.425418	608960.00	7175100.00	156.32	93.993	75.26	-720.474	MB	-2	253
207	1	0	-2.161946	0.000045	153.996	1599.25293	0.646987	0.183852	609000.00	7175000.00	58.019	40.958	57.062	-719.258	MB	-2	257
208	1	0	-2.008238	0.00033	213.003336	2955.64233	1.206686	0.250339	609050.00	7175800.00	72.513	58.434	132.35	-712.667	MB	-2	239
209	1	0	-2.876219	0.43053	376.962005	8227.50464	2.20087	0.272118	609510.00	7175900.00	140.92	80.118	50.075	-712.323	MB	-2	294
210	1	0	-2.224215	0.000641	137.714341	1136.36328	0.734985	0.117161	609660.00	7175700.00	54.45	32.322	45.296	-710.032	MB	-2	NA
211	1	0	-1.813534	0.00106	250.636131	4190.66187	0.76729	0.228849	610800.00	7175400.00	92.739	62.339	42.518	-702.274	ST0408	-1	NA
212	1	0	-0.883769	0.027701	353.374128	8343.85376	0.745946	0.171253	611360.00	7175200.00	127.5	91.167	34.052	-703.338	ST0408	0	NA
213	1	0	-1.125175	0.003775	507.238059	12398.3101	0.518024	0.055498	611670.00	7175200.00	197.77	90.223	53.266	-702.37	ST0408	-1	NA
214	1	0	-1.989777	0.250437	278.570634	4904.4458	1.407108	0.428313	611920.00	7175400.00	102.92	67.092	72.755	-702.661	ST0408	-1	296
215	1	0	-1	0	105.353529	664.068604	0.997	0.007137	612470.00	7174100.00	38.994	27.174	19.995	-702.265	ST0408	-1	319
216	1	0	-1.923779	0.302696	411.542088	9442.16724	1.451101	0.558296	612610.00	7174200.00	159.77	82.703	66.959	-700.379	ST0408	-1	319
217	1	0	-3.347579	0.416525	198.800509	2859.39526	1.262668	0.233386	606590.00	7173500.00	74.916	53.22	11.031	-751.284	MB	-2	380
218	1	0	-2.011357	0.074464	160.725342	1704.177	1.024611	0.093133	606640.00	7173300.00	59.622	40.125	46.44	-751.634	MB	-1	381
219	0	1	2.660502	0.050741	163.173798	1764.52222	1.913826	1.534044	606760.00	7173500.00	61.451	42.153	37.321	-745.038	MB	2	379
220	0	1	1.304994	0.085148	208.394646	1515.87988	1.649855	0.327148	606840.00	7173500.00	70.187	33.162	29.256	-745.747	MB	1	379
221	1	0	-4.223479	2.634911	287.822453	5079.62036	3.375169	2.93794	606790.00	7173500.00	100.24	72.919	41.938	-754.686	MB	-2	379
222	1	0	-2.730701	0.370015	306.164653	5054.19922	0.856872	0.151832	607610.00	7173000.00	102.92	71.258	20.523	-748.763	MB	-2	353
223	1	0	-2.876496	0.3742	596.787033	9872.12183	1.909616	0.99288	607840.00	7173600.00	173.79	85.818	72.392	-738.692	MB	-2	345
224	1	0	-2.476056	0.198834	528.383097	11343.7014	1.557781	0.645592	608220.00	7173300.00	147.71	113.42	129.15	-740.197	MB	-2	350
225	1	0	-3.245457	0.666033	500.672228	10761.2568	2.245351	2.131217	608400.00	7173500.00	188.41	83.257	82.245	-739.456	MB	-2	347
226	1	0	-0.962441	0.25211	699.411255	21100	1.505003	0.821068	608580.00	7173700.00	256.6	109.7	88.901	-731.602	ST0408	0	346
227	1	0	-0.909091	0.236491	576.984848	14250	0.961748	0.177888	608840.00	7173800.00	197.78	99.09	78.453	-729.161	ST0408	0	NA
228	1	0	-1.122951	0.402916	437.989899	12200	1.877743	1.052647	608740.00	7173400.00	149.11	111.81	6.4902	-736.929	ST0408	0	348
229	1	0	-1.938776	0.34319	261.421356	4900	1.970651	0.588937	608930.00	7173100.00	92.971	73.13	33.394	-734.012	ST0408	-1	354

230	1	0	-1.836066	0.202634	317.989899	6100	1.200375	0.236996	609000.00	7173500.00	111.3	74.602	85.966	-732.714	ST0408	-1	348
231	1	0	-3.178808	0.424981	480.416306	15150	1.417892	0.285723	609350.00	7172300.00	171.84	122.61	85.558	-745.068	ST0408	-2	360
232	1	0	-2.841501	0.475813	737.626298	26286.8081	1.851285	1.049341	609160.00	7173400.00	252.6	150.87	110.65	-734.273	MB	-2	352
233	1	0	-4.239804	1.542151	673.310129	28311.9692	3.218365	1.051063	609320.00	7173300.00	224.98	174.47	101.47	-740.378	MB	-2	352
234	1	0	-4.483185	3.581002	1233.96735	59156.2161	2.955253	2.948927	609160.00	7172900.00	446.15	187.76	71.346	-741.176	MB	-2	356
235	1	0	-1.892524	0.003887	304.68033	5615.33814	0.932615	0.452394	609460.00	7172500.00	116.93	67.85	81.07	-740.614	MB	-1	360
236	1	0	-1.819894	0.000729	143.126158	1292.81152	1.148002	0.023056	609580.00	7172600.00	48.826	37.71	32.825	-739.386	MB	-1	NA
237	1	0	-1.046834	0.000968	184.012921	1953.87695	0.595776	0.119853	609780.00	7172600.00	76.57	38.574	89.498	-736.357	MB	-1	358
238	1	0	-2.701128	0.470813	516.757748	11888.3738	2.385942	0.494837	609630.00	7173000.00	178.23	93.649	104.76	-736.936	MB	-2	357
239	1	0	-2.851905	0.128587	258.504116	4484.54932	2.377308	0.769103	609820.00	7172800.00	85.398	73.271	115.05	-737.066	MB	-2	358
240	1	0	-3.08311	0.375589	593.347784	16200.417	2.40728	1.510055	609510.00	7173500.00	211.21	115.95	97.93	-731.399	MB	-2	351
241	1	0	-1.714911	0.190399	1200.16511	25887.6836	1.343919	0.204718	609960.00	7173400.00	462.57	77.873	79.64	-726.904	ST0408	-1	326
242	1	0	-3.152765	0.556678	713.091543	20573.6858	2.36791	0.904352	609960.00	7173100.00	244.62	116.69	98.819	-732.887	MB	-2	332
243	1	0	-3.575583	1.343198	802.83363	24052.0215	2.174849	0.859676	610050.00	7172700.00	252.35	138.44	156	-735.27	MB	-2	336
244	1	0	-0.981965	0.00529	215.389114	2640.81201	0.602073	0.035851	610220.00	7173000.00	81.823	47.596	117.87	-729.085	ST0408	0	335
245	1	0	-1.6325	0.000562	200.219892	2459.64331	0.752448	0.042286	610210.00	7173200.00	69.429	50.673	92.566	-728.25	ST0408	-1	327
246	1	0	-1.667954	0.316431	293.42367	4552.49341	0.932827	0.307699	610320.00	7173400.00	110.48	60.452	53.945	-724.907	ST0409	-1	327
247	1	0	-0.970843	0.009378	178.771917	2224.25293	1.338008	0.041033	610460.00	7173500.00	69.587	46.027	40.016	-722.79	ST0410	0	328
248	1	0	-2.816434	0.170029	372.445089	6215.35156	1.527412	0.145015	610570.00	7173400.00	136.8	67.982	95.024	-725.901	MB	-2	328
249	1	0	-2.480207	0.000013	115.284031	928.558838	1.529361	0.134147	610620.00	7173200.00	43.904	31.264	73.779	-724.934	MB	-2	329
250	1	0	-2.956848	0.234238	240.561615	3718.948	1.158712	0.13034	610780.00	7173000.00	88.237	59.915	79.599	-725.541	ST0408	-2	333
251	1	0	-3.032054	0.252186	359.593521	7319.74976	2.853393	2.022779	610910.00	7172600.00	138.18	77.547	54.714	-727.119	MB	-2	338
252	1	0	-2.550578	0.000144	142.007196	1408.80908	0.891216	0.31953	611040.00	7172600.00	52.038	38.343	59.007	-726.051	MB	-2	338
253	1	0	-1.370225	0.052723	749.834739	18594.5024	1.052504	0.48103	611020.00	7172400.00	241.9	122.68	95.247	-725.901	MB	-1	341
254	1	0	-1.493473	0.000873	335.095862	5824.40625	1.236804	0.213221	611120.00	7172200.00	119.01	71.842	2.995	-726.913	MB	-1	341
255	1	0	-2.432923	0.000519	201.467141	2531.59546	0.926638	0.08935	610930.00	7172100.00	72.398	51.252	106.88	-730.657	MB	-2	344
256	1	0	-3.104978	0.76888	561.742976	16715.7136	2.432159	1.462683	611110.00	7173300.00	196.74	128.17	86.725	-721.75	MB	-2	330
257	1	0	-2.921006	0.275406	772.059673	23716.1858	2.236955	0.661175	610820.00	7173600.00	289.18	115.69	57.678	-722.099	MB	-2	324
258	1	0	-3.318459	0.654248	893.303795	42265.5801	2.331024	0.65427	611150.00	7173700.00	272.77	219.77	9.5894	-720.547	MB	-2	323
259	1	0	-2.838119	0.249352	322.171884	5407.44214	1.648997	0.712875	611410.00	7173300.00	132.03	57.648	82.034	-718.388	MB	-2	331
260	1	0	-2.614586	0.159795	541.392422	9324.41284	1.480651	0.655837	611490.00	7173000.00	203.86	68.216	104.96	-718.763	MB	-2	334
261	1	0	-2.135733	0.000772	70.155891	322.346436	0.811722	0.051502	611520.00	7173100.00	28.144	19.632	29.082	-716.735	MB	-2	334
262	1	0	-2.207831	0.001766	100.304882	678.125488	1.690762	0.162305	611620.00	7173300.00	40.284	26.406	78.471	-714.482	MB	-2	331
263	1	0	-2.743903	0.218656	244.326169	3127.1853	3.418022	1.820706	608610.00	7171500.00	79.688	55.272	169.4	-766.097	MB	-2	387

264	1	0	-1.318971	0.051288	162.687146	1169.99023	2.362455	0.144197	608700.00	7171500.00	49.942	34.927	57.737	-761.838	MB	-1	387
265	1	0	-1.152189	0.004305	501.865877	10317.0793	1.08692	0.159386	610610.00	7171600.00	195.09	76.88	167.99	-734.511	ST0408	-1	NA
266	1	0	-1.176802	0.001654	194.380406	2389.60303	1.245452	0.640662	611040.00	7171600.00	64.342	55.475	102.84	-729.835	ST0408	-1	NA
267	1	0	-1.175314	0.007456	349.006091	7132.16333	0.86668	0.072776	611310.00	7170200.00	136.55	75.748	49.134	-743.374	ST0408	-1	NA
268	1	0	-1.464712	0.00359	140.286706	1206.16699	1.229524	0.086388	611510.00	7170200.00	51.948	35.264	95.357	-741.264	ST0408	-1	NA
269	1	0	-2.91993	0.202019	381.128799	8301.98975	1.01667	0.219716	611540.00	7171600.00	138.3	83.551	105.89	-731.829	MB	-2	NA
270	1	0	-2.559101	0.070755	588.009927	9948.06055	1.805344	1.186569	611670.00	7171700.00	201.31	72.667	101.89	-726.843	MB	-2	NA
271	1	0	-2.147358	0.031102	212.604648	2925.65356	1.07183	0.244962	613220.00	7170100.00	74.968	58.34	30.273	-718.805	MB	-2	403
272	1	0	-2.804002	0.434258	474.124168	12520.9595	2.175329	0.630063	614430.00	7169900.00	179.46	99.537	22.333	-706.505	MB	-2	404
273	1	0	-3.695884	2.292024	579.617068	17459.7041	2.839949	3.050344	616620.00	7169500.00	206.84	121.11	125.3	-695.725	MB	-2	NA
274	1	0	-2.204504	0.040412	251.362764	3450.3457	0.594618	0.038692	614170.00	7180200.00	89.39	62.424	46.484	-647	MB	-2	NA
275	1	0	-1.447484	0.105254	387.387427	5265.41602	0.963166	0.263802	614350.00	7180200.00	144.78	58.676	24.702	-643.593	MB	-1	NA
276	1	0	-2.588743	0.027025	267.796726	4055.22266	1.582426	0.233967	614250.00	7180800.00	106.44	52.834	41.874	-644.439	MB	-2	NA
277	1	0	-2.564756	0.1374	209.074616	1717.38135	0.709161	0.058836	614470.00	7181100.00	69.096	36.976	78.939	-642.266	MB	-2	NA
278	1	0	-2.641224	0.090297	503.750458	10809.3213	1.721232	0.48224	614870.00	7180400.00	201.42	75.919	89.4	-640.632	MB	-2	NA
279	1	0	-2.118153	0.0042	217.246613	2021.37451	1.580395	0.431475	614860.00	7180300.00	94.99	32.523	129.93	-641.127	MB	-2	NA
280	0	1	2.905455	0.450543	282.882982	4942.51904	1.780154	1.156225	615220.00	7180800.00	99.573	74.69	43.934	-627.271	MB	2	NA
281	1	0	-1.871255	0.138023	574.640489	21631.873	1.343939	0.383802	613870.00	7188600.00	194.2	155.5	6.9512	-663.298	MB	-1	NA
282	1	0	-2.042774	0.072196	530.104749	15512.458	1.218466	0.536004	614120.00	7188600.00	189.3	117.21	76.052	-660.803	MB	-2	NA
283	1	0	-1.612312	0.339424	664.028046	15427.1699	1.332621	0.197615	610040.00	7183600.00	268.07	82.42	100.84	-688.03	MB	-1	60
284	1	0	-1.552228	0.00779	323.799302	6307.50879	0.833276	0.039961	610070.00	7183100.00	121.93	74.75	77.505	-688.803	MB	-1	NA
285	1	0	-2.514613	0.145823	336.262121	6809.92871	1.823376	1.179859	610300.00	7183000.00	114.54	86.768	155.85	-689.606	MB	-2	NA
286	1	0	-2.638896	0.200142	297.532811	5004.52832	1.416062	0.123946	610360.00	7183600.00	109.28	65.589	62.145	-689.125	MB	-2	59
287	1	0	-2	0	119.053782	1027.64136	1.974294	0.287426	610630.00	7183600.00	46.387	31.927	24.628	-684.273	ST0408	-1	59
288	1	0	-1.345507	0.003075	246.871233	3836.18164	0.793816	0.064102	609890.00	7182100.00	85.945	63.451	158.79	-691.539	MB	-1	NA
289	1	0	-1.354497	0.098755	434.098229	6993.75513	0.650057	0.076994	609380.00	7181800.00	164.16	67.822	84.895	-691.981	MB	-1	NA
290	1	0	-1.160193	0.003877	313.195903	4560.04077	0.607464	0.097187	610100.00	7182800.00	121.31	55.998	145.81	-689.135	MB	-1	NA
291	1	0	-1.253228	0.121524	324.175996	5950.73706	1.149373	0.343026	611420.00	7183200.00	114.65	84.474	141.28	-667.348	MB	-1	NA
292	1	0	-2.700239	0.122262	216.673663	2892.05615	0.907072	0.071759	610400.00	7183700.00	79.819	50.99	99.891	-690.275	MB	-2	59
293	1	0	-1.31442	0.126068	377.772731	8334.52466	0.991245	0.24223	612020.00	7182300.00	128.84	96.261	49.845	-660.507	MB	-1	NA
294	1	0	-1.841631	0.29358	361.638645	7151.4458	1.961881	0.804154	611100.00	7184200.00	137.72	73.37	22.548	-676.038	MB	-1	61
295	1	0	-2.689281	0.231366	294.102605	5724.32788	1.788299	0.064205	603250.00	7180000.00	97.192	85.323	77.137	-720.106	MB	-2	119
296	1	0	-1.787868	0.002816	228.92905	3283.19312	0.61895	0.150676	606250.00	7180100.00	84.459	54.403	155.22	-707.953	MB	-1	NA
297	1	0	-2.026751	0.158977	309.353245	6276.41357	1.336408	0.521575	598070.00	7179500.00	117.63	73.96	71.517	-744.285	ST0408	-1	67

298	1	0	-2.354092	0.543605	421.137772	11934.3005	0.782159	0.167419	599480.00	7179600.00	143.89	115.52	47.963	-737.262	ST0408	-1	85
299	0	1	1.400273	0.002617	298.426268	5808.88843	0.999212	0.167639	598080.00	7179600.00	111.56	73.266	30.669	-740.488	ST0408	1	67
300	1	0	-1.916537	0.082913	421.906281	7819.40918	1.528545	0.781365	608040.00	7178200.00	168.92	64.507	162.08	-707.05	MB	-1	218
301	1	0	-2.722716	0.516587	597.762139	12003.0374	1.409205	0.802853	608066.27	7172289.42	181.8	110.52	86.2816	-754.501	MB	-2	359
302	0	1	1.657628	0.242181	218.875901	2988.09497	2.895906	1.869173	608132.22	7172352.6	77.753	56.543	33.4376	-747.427	MB	1	359
303	1	0	-1.712977	0.008578	288.976621	4935.28296	1.712107	0.182561	599560.06	7181376.37	104.14	65.686	158.7	-727.819	MB	-1	30
304	1	0	-1.635773	0.007447	280.277752	3852.38745	1.120457	0.069136	599836.81	7181687.08	101.24	52.573	171.162	-724.993	MB	-1	35
305	1	0	-1.50339	0.004445	290.394378	4882.09473	1.204392	0.038274	600612.05	7181616.32	104.24	67.164	162.404	-721.893	MB	-1	32
306	1	0	-2.647999	0.155064	211.031883	2975.51343	0.797252	0.058822	600923.84	7180618.21	76.717	55.422	53.7218	-726.082	MB	-2	NA
307	1	0	-2.436645	0.00622	292.07102	5215.32617	1.750011	0.816013	612605.68	7185970.35	117.44	63.016	67.8414	-663.977	MB	-2	NA
308	1	0	-1.083239	0.001362	126.892538	944.163086	1.445875	0.055839	612984.57	7185786.66	55.075	27.278	60.5238	-655.221	MB	-1	NA
309	1	0	-1.639762	0.148955	321.302744	5621.65479	1.431115	0.796651	598468.59	7177957.89	125.2	65.873	48.7964	-757.255	MB	-1	73
310	1	0	-2.832478	0.332526	946.880316	29289.365	1.661783	1.291677	600052.92	7182783.09	273.42	171.01	56.4977	-726	MB	-2	44
311	0	1	2.105663	0.067539	613.742026	7363.0166	0.820051	0.187736	598494.69	7182684.94	178.81	100.83	170.089	-726	MB	2	45
312	1	0	-2.367646	0.206988	374.091223	8340.74829	1.732128	0.434394	597014.72	7178633.77	135.28	88.645	122.448	-761	ST0408	-2	71

J

Statistics of Acoustic chimneys

Notation:

Cnr = Chimney number
T = Top
B = Bottom
Pup = Pull up
Pdn = Push down

hor = horizon
Mpup = Maximum pull up
MPdn = Maximum push down
SA = Short axis length
LA = Long axis length

Orient = Orientation

Cnr	X-Coord	Y-Coord	T ms	B ms	T hor	B hor	Pup ms	Pdn ms	MPup hor	Sw hor	MPdn hor	SA	LA	Orient	Area
1	596998	7182680.67	-1029.83	-1420.19	2	11	14	0	6.5			124	300	31	29216.8117
2	597994.22	7182597.39	-1070.65	-1280.97	4	9	0.5	0	5			65	81	6	4135.12133
3	597262.82	7182338.65	-1075.53	-1217.82	4	7	8	0	6.5			63	196	124	9698.09652
4	598441.39	7182155.06	-981.21	-1377.56	1	11	13	0	6.5			165	358	163	46393.4695
5	597475.25	7182141.22	-1103.52	-1333.2	5	10	11	0	6.5			104	137	146	11190.353
6	596696.01	7182027.74	-998.31	-1406.84	1	11	15	0	7			209	227	36	37261.6451
7	596342.25	7182432.93	-1120.22	-1225.91	5	7	1	0	6.5			62	96	22	4674.68987
8	596825.72	7182325.73	-1112.52	-1225.98	5	7	3	0	6.5			60	142	59	6691.59235
9	597911.7	7182433.14	-984.07	-1208.84	1	7	3.6	0	4			74	448	164	26037.5199
10	597412.2	7181649.96	-990.18	-1570.81	1	14	18	0	7			234	453	16	83253.7761
11	597163.3	7180649.54	-999.6	-1403.75	1	11	9	0	7			142	769	12	85763.9086
12	598581.32	7181845.59	-1070.52	-1213.74	4	8	2	0	6.5			54	102	131	4325.97308
13	598153.3	7181580.27	-1113.86	-1378.97	5	11	11	0	7			146	329	35	37725.8154
14	598481.53	7181653.45	-1106.57	-1380.71	5	11	4.6	0	7			109	157	26	13440.5188
15	598604.22	7181468.34	-1106.89	-1272.86	5	9	3	0	7			109	143	129	12242.0012
16	598457.88	7181320.16	-1108.63	-1221.29	5	7	1.5	0	6.5			68	83	36	4432.78723
17	597798	7180868.84	-987.34	-1443.39	1	12	11	8.7	5	10	10	200	358	20	56234.5085
18	598095.14	7181013.6	-1078.02	-1217.45	5	7	2.8	0	6			90	143	3	10108.0744
19	598345.73	7180847.12	-1109.16	-1215.67	5	7	3	0	6.5			81	142	154	9033.64968
20	597610.02	7180536.99	-1119.61	-1303.57	5	9	3	0	6.5			70	368	19	20231.8567
21	599367.53	7180843.68	-1072.27	-1497.7	4	13	9.5	10	6.5	9	12	113	141	136	12513.7489
22	601064.2	7181141.53	-1029.88	-1299.44	3	10	8	0	6.5			143	199	126	22350.0755
23	600829.24	7181183.43	-1122.88	-1297.78	6	10	4	0	6.5			119	185	33	17290.5406

24	600627.76	7181204.83	-972.36	-1298.29	1	10	20	0	6.5			277	268	29	58304.8181
25	600153.36	7181161.11	-1008.58	-1199.34	2	7	9.5	0	5			90	185	13	13076.8794
26	599876.48	7181196.91	-981.6	-1404.25	1	12	17	0	7			133	191	17	19951.4695
27	599523	7181272.29	-975.02	-1300.92	1	10	10	0	6.5			134	280	13	29468.1391
28	599721.66	7181351.97	-975.97	-1300.89	1	10	8.5	0	6.5			143	285	16	32008.9021
29	600069.81	7181428.04	-982.57	-1407.16	1	12	45	0	8			228	362	17	64823.6228
30	599673.08	7181547.88	-974.38	-1300.31	1	10	10	0	7			181	359	17	51034.3873
31	600471.3	7181765.62	-1032.51	-1297.29	3	10	7.5	0	6.5			151	235	8	27869.8538
32	600718.28	7181852.33	-972.26	-1256.42	1	9	4.4	0	6.5			101	191	0	15151.116
33	599826.8	7181722.51	-1098.32	-1272.44	5	9	6	0	6.5			118	199	10	18442.7197
34	599068.13	7181764.25	-1096.8	-1315.76	5	10	10	0	6.5			191	289	161	43353.1932
35	599937.09	7181941.55	-975.2	-1294.02	1	10	2.5	0	6.5			80	283	8	17781.4144
36	600319.29	7182200.19	-974.56	-1535.07	1	14	17	0	6.5			313	416	171	102265.124
37	599975.43	7182175.49	-1056.51	-1420.54	4	12	12	9	6.5	10	12	160	215	173	27017.6968
38	599182.73	7182034.67	-1064.42	-1273.05	4	9	5	0	6.5			192	341	171	51421.5886
39	600769.71	7182265.79	-1057.32	-1192.21	4	8	2	0	6			94	122	176	9006.94614
40	601129.17	7182064.41	-970.97	-1293.21	1	10	7	0	6.5			107	332	166	27900.4844
41	601103.7	7182517.42	-1050.63	-1373.8	4	11	11	0	7			196	386	168	59420.0834
42	600115.94	7182373.57	-1034.19	-1293.23	3	10	7.5	0	7			91	184	0	13150.7068
43	599132.78	7182357.24	-975.17	-1300.26	1	10	1.5	0	6.5			101	225	168	17848.1733
44	600182.75	7182738.51	-972.16	-1611.65	1	15	15	13	5		12	227	335	174	59725.6033
45	598551.49	7182906.91	-980.35	-1418.01	1	12	10	0	10			332	498	24	129854.591
46	601921.25	7182687.22	-1016.5	-1400.56	3	12	8.5	3.8	6.5	10	11	140	179	8	19682.078
47	602720.77	7182499.19	-1076.86	-1277.4	5	10	2.5	0	6.5			111	422	141	36789.6208
48	601943.7	7182335.27	-956.05	-1479.83	1	13	18	0	10			198	423	2	65780.2378
49	601278.65	7181857.83	-1028.78	-1395.2	3	12	4.4	0	6.5			173	354	174	48099.3543
50	601710.28	7181793.83	-1050.85	-1281.95	4	10	5.8	0	6.5			163	181	51	23171.602
51	601509.26	7181637.69	-1086.01	-1285.65	5	10	15	0	6.5			172	301	51	40661.6337
52	602246.33	7181694.27	-1016.45	-1373.49	3	11	7.8	0	6.5			183	312	163	44843.0935
53	603045.32	7181658.4	-1048.22	-1481.99	4	13	10	4.4	6.5	10	11	182	204	7	29160.263
54	601732.96	7181188.18	-963.97	-1714.47	1	16	40	24	9	13	14	273	623	27	133579.734
55	603537.11	7181298.69	-1085.69	-1290.69	5	10	4	0	6.5			73	181	172	10377.4659
56	604598.46	7182112.95	-1046.22	-1276.84	4	10	7.8	0	6.5			130	336	98	34306.1918
57	603931.32	7181914.3	-1043.93	-1282.29	4	10	3	0	6.5			109	250	68	21402.1

L

58	604876.31	7181848.94	-1102.34	-1252.01	5	9	2.8	0	6.5			102	352	126	28198.9357
59	610533.64	7183992.23	-922.71	-1234.22	1	10	3	0	4			55	87	32	3758.13021
60	610251.91	7183925.83	-921.21	-1241.31	1	10	6	0	4			89	235	85	16426.6026
61	611255.71	7184554.1	-905.87	-1514.25	1	14	3	4	6	10	13	94	112	108	8268.67186
62	611630.41	7184583.3	-1358.03	-1610.16	12	15	0	4.7			14	68	93	22	4966.85799
63	611476.15	7184408.6	-1229.17	-1613.57	10	15	0	8.5			12	147	231	175	26669.7654
64	611034.31	7183456.2	-1237.72	-1685.41	10	16	0	9			14	132	340	146	35248.6696
65	612595.17	7182998.44	-1306.21	-1567.53	11	15	0	4			13	107	124	175	10420.6628
66	597862.07	7179914	-1088.74	-1337.86	4	10	6	0	6			94	107	0	7899.53473
67	598139.04	7179776.73	-996.48	-1635.66	1	15	27	11	5	10	11	240	335	8	63146.0123
68	597597.98	7179723.3	-1094.97	-1652.92	4	15	6	6	6.5	10	11	124	136	157	13244.9546
69	596492.38	7179536.91	-1012.64	-1356.81	1	10	26	0	6.5			289	472	17	107134.593
70	596960.87	7179199.17	-1016.2	-1353.99	1	10	9	0	4			100	272	0	21362.83
71	597188.21	7178826.31	-1021.63	-1543.2	1	13	9	0	6.5			176	438	32	60544.7736
72	597661.55	7178489.29	-1015.72	-1348.93	1	10	11	0	4			145	396	139	45097.5625
73	598554.76	7178162.65	-1015.24	-1648.18	1	10	13.5	0	6			160	541	8	67984.065
74	598769.55	7178168.56	-1136.27	-1335.96	5	10	4.8	0	6.5			88	283	7	19559.5559
75	597673.99	7177958.27	-1088.97	-1353.33	3	10	4	0	6.5			122	252	150	24146.2811
76	600814.09	7180876.75	-1097.83	-1304.77	5	10	9.5	0	6.5			85	168	130	11215.4858
77	600946.7	7180896.06	-1098.72	-1301.03	5	10	6.5	0	6.5			73	140	112	8026.76923
78	600553.05	7180661.11	-980.32	-1717.63	1	16	29	0	6.5			265	466	19	96988.8192
79	599173.32	7180409.44	-982.35	-1708.53	1	16	19	12	6	10	12	204	271	16	43419.9521
80	599804.86	7180501.41	-1103.47	-1307.27	5	10	3	0	6.5			96	133	19	10027.9638
81	600234.89	7180513.29	-976.02	-1302.06	1	10	8.5	0	7			109	167	2	14296.6028
82	600395.13	7180485.88	-1109.17	-1305.13	5	10	6.5	0	7			75	114	31	6715.1543
83	601060.37	7180658.89	-1134.67	-1305.45	6	10	3	0	6.5			52	150	54	6126.10567
84	599380.82	7180262.05	-985.39	-1311.42	1	10	3	0	7			87	707	167	48309.0556
85	599580.85	7179758.35	-987.31	-1499.44	1	13	2	9	4	7	10	76	166	176	9908.58323
86	599737	7179045.28	-1053.4	-1561.14	3	14	7	5	6.5	10	12	104	916	164	74820.1706
87	600270.98	7180061.83	-984.19	-1541.54	1	14	31	0	7			268	374	11	78722.0287
88	600732.45	7180154.41	-983.28	-1310.17	1	10	13	0	5			138	232	16	25145.3076
89	600099.3	7179732.35	-985.87	-1634.18	1	15	2	9.5	4	10	11	111	541	27	47163.9451
90	600743.86	7179775.48	-983.45	-1307.55	1	10	8	0	6			75	800	4	47123.8898
91	601471.47	7179602.35	-973.96	-1554.41	1	14	40	0	10			415	885	157	288457.11

92	599729.14	7179475.47	-1080.7	-1320.91	4	10	5.5	0	6.5			102	165	168	13218.2511
93	601032.42	7179183.18	-982.72	-1564.42	1	14	14.5	17.5	5	10	12	138	284	11	30781.3248
94	600963.1	7179426.82	-1078.16	-1312.93	4	10	7	0	7			94	245	118	18087.7197
95	600900.79	7179595.35	-1107.74	-1309.91	5	10	5	0	6			63	280	7	13854.4236
96	601109.85	7178915.36	-982.11	-1635.1	1	15	7	12	4	10	12	80	238	8	14953.981
97	601436.89	7178937.62	-1046.39	-1641.1	3	15	10	11	7	10	14	117	182	71	16724.2685
98	599344.59	7179673.19	-1081.03	-1291.08	4	9	2.5	0	6			58	288	168	13119.2909
99	599287.73	7179030.6	-990.19	-1323.16	1	10	8	0	4			121	515	153	48942.0866
100	600034.17	7178961.7	-1112.64	-1646.06	5	15	7	4	6.5	10	13	99	464	11	36078.05
101	599224.59	7178716.93	-998.14	-1642.85	1	15	10	7	4	10	12	120	197	167	18566.8126
102	599317.38	7178527.45	-1048.28	-1644.16	2	15	10	7	5	10	13	125	188	166	18456.8568
103	599823.22	7178550.38	-997.26	-1322.05	1	10	3.5	0	4			89	268	166	18733.317
104	600089.26	7178462.26	-992.73	-1314.85	1	10	18	0	7			170	322	118	42992.6955
105	599625.27	7178267.82	-1000.65	-1334.67	1	10	4	0	3			83	247	166	16101.4477
106	600371.71	7178351.16	-1034.73	-1653.74	2	15	11	10	6.5	10	13	137	193	1	20766.7128
107	602457.26	7181090.68	-1087.37	-1294.85	5	10	5	0	6.5			64	173	128	8695.92847
108	601414.74	7180888.11	-1063.12	-1292.52	4	10	4	0	6.5			72	112	50	6333.45079
109	602127.57	7180738.19	-965.55	-1478.81	1	13	2.5	6	5	10	11	93	414	135	30239.4001
110	601675.14	7180723.05	-1025.37	-1544.1	3	14	7.5	9	5	10	12	90	167	147	11804.5344
111	601855.74	7180749.35	-1128.09	-1296.6	6	10	5.5	0	7			75	231	176	13607.0232
112	603688.67	7181143.14	-953.75	-1754.35	1	16	6	11	5	10	11	99	186	9	14462.3218
113	603525.22	7180941.73	-951.26	-1297.53	1	10	11.5	0	6.5			116	240	88	21865.4849
114	604133.95	7180928.9	-952.34	-1293.87	1	10	8	0	6.5			98	107	133	8235.68514
115	603805.9	7180855.74	-1087.77	-1294.01	5	10	6	0	6.5			84	184	109	12139.114
116	601734.88	7180401.9	-1092.61	-1301.7	5	10	6.5	0	6.5			106	118	37	9823.76023
117	602453.96	7180405.14	-961.39	-1743.56	1	16	32	0	7			280	564	141	124030.078
118	602850.18	7180107.62	-960.23	-1272.2	1	9	4	0	5			74	78	15	4533.3182
119	603351.3	7180231.33	-959.5	-1306.95	1	10	8	0	6.5			119	160	148	14953.981
120	602653.7	7179977.51	-1066.33	-1551.53	4	14	7.5	9	7	10	11	139	176	151	19213.9807
121	603924.93	7179782.05	-1062.8	-1482.33	4	13	10	3	7	10	11	105	225	125	18555.0316
122	603462.33	7179689.31	-958.86	-1314.02	1	10	3	0	6			51	50	140	2002.76532
123	603619.23	7179661.41	-959.61	-1559.68	1	14	3	7.5	6.5	10	11	72	261	172	14759.2023
124	602780.28	7179716.84	-964.45	-1540.24	1	14		5.5		10	11	71	199	157	11096.8907
125	602019.97	7179453.87	-973.53	-1306.31	1	10	18	0	7			192	336	76	50667.6063

N

126	601649.77	7179349.22	-1074.28	-1549.04	4	14	11	6	6.5	10	11	135	317	168	33611.1144
127	602636.59	7179492.93	-962.92	-1481.83	1	13	3	5	6.5	10	11	95	149	138	11117.311
128	603091.5	7179432.32	-963.96	-1557.55	1	14	11	5.5	9	10	11	135	202	136	21417.8079
129	603901.64	7179550.3	-1063.07	-1486.9	4	13	5.7	5	6.5	10	11	72	120	16	6785.84013
130	603249.12	7179176.17	-966.04	-1787.55	1	16	3	3	4	10	11	79	235	172	14580.9169
131	603095.88	7179153.85	-963.01	-1485.32	1	13	3.8	3.4	4	10	11	55	150	148	6479.53485
132	602819.98	7178986.81	-964.27	-1372.25	1	11	12	0	7			69	176	142	9537.8753
133	602388.58	7178974.73	-971.54	-1659.19	1	15	5.7	5	9	10	12	75	222	16	13076.8794
134	603317.24	7179033.85	-964	-1666.81	1	15	0	7		10	11	101	178	142	14119.8882
135	602707.36	7178792.79	-969.13	-1310.88	1	10	4.4	0	3			60	251	2	11828.0963
136	602532.69	7178640.49	-970.43	-1665.03	1	15	3	8	4	10	13	59	135	144	6255.69637
137	605365.76	7181159.04	-945.79	-1648.57	1	15	8.5	10	6.5	7	12	109	110	125	9416.92398
138	603974.33	7180702.66	-1102.6	-1286.18	5	10	3	0	6.5			70	123	136	6762.27819
139	605174.12	7180420.68	-950.11	-1286.35	1	10	1	5	3			48	159	1	5994.15878
140	605165.06	7180114.89	-952.62	-1297.86	1	10	3	0	3			72	79	3	4467.34475
141	604491.53	7179712.32	-956.47	-1301.74	1	10	5	0	6.5			72	253	130	14306.8129
142	604810.18	7179327.4	-953.66	-1399.46	1	12	7	6	6.5	10	11	102	205	128	16422.6756
143	606157.27	7179574.32	-1087.71	-1275.29	5	15	6.6	0	6.5			68	157	140	8384.91079
144	604964.78	7178918.56	-966.66	-1475.08	1	13	30	0	10			262	482	143	99183.2217
145	606364	7179223.84	-1092.97	-1275.02	5	10	3	0	6.5			67	136	82	7156.54806
146	606584.93	7179205.27	-1094.22	-1271.73	5	10	2.5	0	6.5			55	153	157	6609.12554
147	605684.87	7179962.24	-947.05	-1531.27	1	14	0	5	0	10	12	96	244	153	18397.1666
148	606725.82	7181255.61	-1081.42	-1268.41	5	10	4.5	0	6.5			86	164	53	11077.2557
149	607320.04	7180301.86	-1051.33	-1258.01	4	10	2.5	0	6.5			66	106	7	5494.64555
150	607652.57	7180071.19	-1079.54	-1250.53	5	10	2.5	0	6.5			62	199	122	9690.24254
151	610870.51	7181504.01	-906.78	-1598.81	1	15	0	8	0	13	13	125	239	107	23463.7701
152	611323	7180732.6	-898.72	-1703.88	1	16	0	12.5	0	13	13	108	460	170	39018.5808
153	609183.64	7179634.48	-923.9	-1722.49	1	16	0	14	0	13	13	123	388	18	37482.3419
154	611830.42	7181187.09	-887.84	-1587.33	1	15	5.5	9	4	10	11	92	238	4	17197.0782
155	611704.6	7180610.56	-897.64	-1702.54	1	16	11	11	6	10	14	153	257	178	30882.6412
156	613157.38	7180746.02	-1315.25	-1574.09	12	15	0	4			13	86	92	42	6214.07027
157	612776.84	7180411.5	-880.51	-1689.3	1	16	0	4.7	0	13	13	120	241	6	22713.7149
158	598497.39	7177849.83	-1112.44	-1343.53	4	10	5.5		6.5			79	195	154	12099.0587
159	598604.56	7177865.44	-1081.62	-1344.23	3	10	6		6			78	189	168	11578.3397

O

160	597041.09	7177612.37	-1035.22	-1462.68	1	12	11.5		7			130	317	58	32366.2583
161	597651.38	7177346.04	-1126.93	-1358.91	4	10	4		6.5			79	150	5	9306.96824
162	597822.83	7177269.51	-1099.12	-1360.74	3	10	4		5			75	196	1	11545.353
163	598577.67	7176922.72	-1026.84	-1354.6	1	10	10.5		3			114	253	167	22652.4538
164	598371.6	7176765.85	-1035.14	-1352.04	1	10	2.7		3			66	185	168	9589.71158
165	598451.92	7176117.86	-1043.19	-1366.84	1	10	7.7		4			78	213	7	13048.6051
166	598492.84	7175844.72	-1045.21	-1361.75	1	10	14.5		7			97	291	160	22169.434
167	598722.58	7175979.66	-1045.45	-1359.91	1	10	4.5		4			89	209	166	14609.1912
168	597188.69	7175654.78	-1065.04	-1384.6	1	10	7		4			100	207	161	16257.742
169	599798.77	7177988.61	-998.54	-1566.96	1	14	4	7.5	4	10	12	66	218	5	11300.3088
170	599626.77	7177405.36	-1010.91	-1743.74	1	16	20	0	7			248	723	5	140825.032
171	600446.59	7178108.33	-999.58	-1570.55	1	14	6	4	5	10	11	77	153	10	9252.77576
172	600949.38	7178003.94	-994.59	-1328.46	1	10	8.5		4			139	192	119	20960.7062
173	600748.78	7178025.48	-995.2	-1499.86	1	13	5	11	4	10	11	78	138	5	8454.02583
174	601078.36	7177743.62	-997.57	-1502.13	1	13	7	7	6.5	10	11	76	184	161	10983.0079
175	601258.59	7177795.25	-1061.48	-1331.22	1	10	6		4			75	144	3	8482.30016
176	601493.65	7178159.33	-1118.35	-1316.85	5	10	5		7			83	244	126	15905.8836
177	601543.5	7177912.85	-1036.49	-1489.58	2	13	15	0	7			261	537	4	110079.05
178	601630.62	7177697.2	-989.2	-1323.92	1	10	10		5			81	145	0	9224.50143
179	600908.6	7177439.8	-1100.86	-1565.06	4	14	17		7			119	369	10	34487.6188
180	600925.23	7177264.61	-1202.01	-1327.72	6.5	10	6		7			81	171	124	10878.55
181	600052.89	7177137.57	-1205.16	-1435.64	6.5	12	8	4	8	10	12	70	85	33	4673.11907
182	600014.89	7177055.92	-1248.7	-1437.81	7	12	6	4	8	10	12	59	106	33	4911.88011
183	601357.69	7177200.73	-1199.4	-1327.32	6.5	10	3		7			35	87	30	2391.53741
184	601111.23	7176961.85	-1207.07	-1330.76	6.5	10	4		7			71	130	164	7249.22505
185	600164.81	7176773.27	-1015.22	-1213.11	1	6.5	2		4			68	88	168	4699.82261
186	598917.46	7177225.93	-1018.81	-1212.73	1	6.5	2		4			53	116	2	4828.62791
187	598954.39	7177485.04	-1018.15	-1212.64	1	6.5	1		4			67	92	11	4841.19428
188	600775.7	7176278.66	-1018.87	-1425.18	1	12	14	0	10			144	287	101	32458.9353
189	602636.98	7178376.58	-974.24	-1537.75	1	14	22	0	7			321	409	150	103114.139
190	601971.2	7178304.99	-975.91	-1313.07	1	10	3		4			63	174	170	8609.53467
191	601955.6	7178048.99	-980.38	-1314.31	1	10	5.5		4			77	204	165	12337.0344
192	601825.47	7177979.29	-982.52	-1318.84	1	10	2.5		4			65	89	8	4543.52838
193	603591.8	7178312.65	-1103.93	-1206.01	5	7	3		6.5			60	101	82	4759.51287

P

194	602840.28	7177822.61	-1018.93	-1400.83	2	12	7		7			131	266	163	27367.9844
195	603844.15	7177943.44	-971.58	-1209.33	1	7	2.5		4			72	229	138	12949.6449
196	604137.34	7177757.78	-1074.78	-1386.27	4	12	9.6		6.5			90	284	126	20074.7771
197	602383.27	7176969.5	-992.82	-1195.36	1	7	2.8		4			58	107	5	4874.181
198	602528.87	7176762.35	-1202.53	-1556.99	6.5	14	3.5	4	7		11	70	120	30	6597.34457
199	604203.51	7176574.89	-981.14	-1216.1	1	7	2		4			68	125	126	6675.88439
200	604186.6	7176369.44	-989.07	-1194.62	1	6.5	2		4			70	95	145	5222.89779
201	603334.86	7176220.03	-1096.19	-1323.5	4	10	2		4			75	141	150	8305.58558
202	606687.43	7178763.49	-953.55	-1271.95	1	10	8		7			78	182	167	11149.5123
203	605337.55	7178287.79	-1065.13	-1295.94	4	10	2		6.5			71	101	142	5632.09023
204	604324.37	7178013.38	-1033.46	-1557.56	3	14	6.5	6	6.5	10	11	99	107	159	8319.72274
205	606556.05	7177856.3	-1021.1	-1273.97	3	10	3		6			66	103	16	5339.13671
206	604620.35	7177346.05	-1077.06	-1300.73	4	10	1.5		6.5			69	99	75	5365.05485
207	605020.97	7177404.39	-1111.47	-1292.44	5	10	1.5		6.5			71	72		4014.95541
208	605833.07	7177345.03	-962.51	-1282.42	1	10	1.5		6.5			69	126	82	6828.25163
209	605957.01	7177286.98	-1070.28	-1281.91	4	10	4		5			130	169	82	17255.1976
210	606279.73	7177308.59	-959.53	-1271.13	1	10	1		6.5			63	104	4	5145.92877
211	606456.67	7177283.62	-962.11	-1194.94	1	8	7		5			71	143	131	7974.14755
212	604510.2	7176822.54	-976.32	-1303.03	1	10	4		6.5			73	132	21	7568.0967
213	604794.27	7176889.28	-971.62	-1302.77	1	10	4		2			61	139	152	6659.39103
214	605964.93	7176755.3	-981.2	-1478.33	1	13	7	0	5			222	447	76	77938.2013
215	608102.65	7179375.56	-932.36	-1165.32	1	8	1		6.5			42	78	123	2572.96438
216	607776.71	7179023.61	-938.82	-1176.12	1	8	0					53	139	143	5786.02827
217	607903.34	7178788.33	-937.82	-1170.67	1	8	0					75	221	145	13017.9746
218	608149.99	7178443.66	-938.44	-1160.16	1	8	3.5		4			65	259	145	13222.1781
219	608007.06	7178067.63	-1081.68	-1162.37	5	8	1.5		6.5			69	172	99	9321.1054
220	607254.85	7177932.69	-951.43	-1260.29	1	10	2		4			65	109	6	5564.54599
221	608823.16	7178059.6	-1041.58	-1516.07	4	14	19	0	8			351	467	57	128740.111
222	608514.18	7177811.63	-944.63	-1145.03	1	8	7.5		5			117	152	30	13967.5209
223	609080.72	7177944.88	-928.25	-1147.35	1	8	0					62	92	14	4479.91112
224	607519.9	7177539.96	-950.61	-1269.84	1	10	0					73	121	4	6937.42198
225	608386.49	7177387.07	-942.19	-1511.8	1	14	3.5	2	6.5	10	12	84	114	53	7520.97281
226	607796.61	7177326.53	-1057.43	-1157.79	4	8	4.5		6.5			67	97	82	5104.30266
227	609208.93	7177329.23	-935.67	-1170.27	1	8	0					51	101	50	4045.58594

Q

228	609438.54	7177362.66	-935.2	-1172.09	1	8	0					71	121	82	6747.35562
229	607485.63	7176951.39	-953.52	-1272.7	1	10	0					64	130	20	6534.51272
230	608164.11	7176999.46	-1053.5	-1258.29	4	10	6.5		6.5			66	196	135	10159.9106
231	607178.43	7176678.3	-963.51	-1276.68	1	10	0					89	195	82	13630.5851
232	608918.01	7176880.9	-940.47	-1171.34	1	8	0					55	123	12	5313.21858
233	608348.16	7176442.69	-948.97	-1271.76	1	10	5		6.5			57	113	40	5058.74957
234	607610.88	7176284.56	-959.08	-1278.84	1	10	4.5		5			73	134	15	7682.76483
235	607834.15	7176240.96	-960.06	-1273.32	1	10	12		9			169	241	50	31988.4818
236	608284.86	7176230.48	-953.31	-1264.45	1	10	10		6.5			139	209	45	22816.602
237	608567.99	7176297.1	-1055.05	-1272.07	4	10	4		5			60	139	11	6550.22068
238	608794.69	7176101.75	-950.55	-1058.57	1	4	0					64	129	122	6484.24724
239	609171.36	7176080.49	-947.09	-1286.65	1	10	16		6			104	235	70	19195.1311
240	607650.78	7175833.67	-963.67	-1286.89	1	10	6		5			89	225	75	15727.5982
241	608813.38	7175926.86	-959.48	-1506.03	1	10	8.5		12			115	182	8	16438.3836
242	608161.49	7175730.43	-964.11	-1295.48	1	10	7		6			72	155	121	8765.0435
243	607174.93	7175510.63	-973.59	-1290.22	1	10	2		5			56	114	58	5013.98188
244	608820.27	7175724.88	-953.11	-1315.18	1	10	3		6.5			84	141	3	9302.25585
245	608395.81	7175612.32	-961.41	-1114.83	1	6	3		4			58	122	46	5557.4774
246	608062.75	7175487.7	-960.66	-1304.19	1	10	26	0	7			169	431	38	57207.6168
247	608462.15	7175545.86	-959.85	-1207.58	1	8	1		5			70	90	26	4948.00843
248	607663.45	7175429.55	-1072.33	-1303.61	4	10	14	0	7			148	447	37	51958.8009
249	607152.52	7175355.14	-967.97	-1293.7	1	10	5.5		5			88	145	43	10021.6806
250	607731.02	7175261.77	-1067.98	-1203.46	4	8	3.5		5			97	297	45	22626.5357
251	609130.37	7175592.43	-1058.77	-1281.86	4	9	4.7		5			92	245	76	17702.8746
252	608677.7	7175323.52	-1067.29	-1284.49	4	9	5		5			60	91	47	4288.27397
253	609040.15	7175350.94	-963.49	-1291.29	1	9	5.5		5			90	173	56	12228.6494
254	608040.9	7175154.67	-958.22	-1321.62	1	10	29	0	6.5			303	534	39	127078.994
255	608399.1	7175206.83	-962.41	-1288.93	1	9	6.8		4			98	144	10	11083.5389
256	608561.8	7175205.15	-1068.91	-1336.51	4	10	2		5			49	88	128	3386.63688
257	609095.18	7175232.09	-956.21	-1297.41	1	9	6		6.5			61	520	63	24912.8297
258	608197.85	7175076.03	-969.77	-1069.03	1	4	1		3			70	84	27	4618.1412
259	607647.64	7174767.55	-975.98	-1280.47	1	9	4.7		5			100	325	30	25525.4403
260	607355.75	7174775.79	-973.31	-1321.81	1	10	20	0	4			251	446	33	87922.1828
261	607354.36	7174521.86	-983.99	-1331.03	1	10	13	0	4			176	530	107	73261.9407

R

262	607701.47	7174547.03	-1084.37	-1286.94	4	9	2.5		5			58	88	34	4008.67223
263	607921.25	7174604.41	-1080.71	-1296.51	4	9	2		5			58	104	156	4737.52172
264	607755.44	7174326.53	-984.4	-1299.2	1	9	4.7		5			118	230	122	21315.7062
265	610123.01	7179466.81	-1328.52	-1614.11	11	15	0	3.5			13	102	150	150	12016.5919
266	610651.19	7179264.63	-923.97	-1502.95	1	14		9		10	10	245	309	18	59458.568
267	610350.6	7179043.24	-924.15	-1138.13	1	8	1		4			65	86	37	4390.37573
268	611016.89	7179114.91	-921.62	-1216.36	1	10	2.5		5			40	125	45	3926.99082
269	611347.45	7179061.55	-914.1	-1584.28	1	15	8	10	6	12	13	102	223	31	17864.6666
270	611237.97	7178842.63	-921.47	-1235.53	1	10	7.6		4			117	255	6	23432.3542
271	611253.86	7178641.96	-919.77	-1478.53	1	14	7		5			78	249	1	15254.0031
272	610755.61	7178391.79	-926.12	-1151.83	1	8	4		5			78	124	128	7596.37104
273	610429.76	7178115.97	-1070.46	-1159.34	5	8	7.5		6.5			150	207	107	24386.613
274	611156.95	7178145.76	-921.58	-1249	1	10	6		5			108	165	40	13995.7953
275	611111.59	7177986.91	-925.06	-1254.87	1	10	5		4			87	144	14	9839.46819
276	610139.34	7177642.33	-934.75	-1732.36	1	14	44	14	6.5	15	15	382	657	51	197114.519
277	609670.19	7177523.26	-1038.27	-1249.38	1	10	15		6			199	343	82	53608.9224
278	610861.35	7177569.88	-924.37	-1262.4	1	10	35	0	5			244	596	81	114215.743
279	611474.65	7177836.81	-928.78	-1256.14	1	10	5		4			82	207	71	13331.3484
280	611712.43	7177541.59	-926.21	-1262.88	1	10	3		6			86	186	71	12563.229
281	609712.23	7177123.42	-938.1	-1265.31	1	10	3		4			104	169	58	13804.1581
282	610875.29	7177242.06	-931.37	-1272.69	1	10	1		4			76	181	94	10803.9371
283	611233.04	7177243.41	-928.06	-1241.99	1	9	8		5			83	441	68	28747.929
284	609946.28	7176929.15	-929.31	-1240.58	1	9	3.5		4			83	121	53	7887.75376
285	610224.96	7176918.99	-936.43	-1248.67	1	9	18		4			192	357	50	53834.3317
286	609941.06	7176725.41	-981.21	-1244.01	2	9	3		4			71	112	16	6245.4862
287	609575.08	7176545.25	-941.73	-1273.98	1	10	15		4			83	282	65	18383.0294
288	610306.64	7176575.67	-935.89	-1252.98	1	9	4		6			53	93	50	3871.22755
289	611902.29	7176731.94	-928.13	-1284.76	1	10	1		4			57	92	82	4118.62797
290	611560.03	7176656.71	-932.45	-1256.16	1	9	3		4			96	282	68	21262.2991
291	611255.99	7176510.95	-940.64	-1301.55	1	10	34	0	4			313	442	74	108656.694
292	610980.45	7176470.82	-936.68	-1261.52	1	9	3		4			61	564	70	27020.8384
293	611840.96	7176621.51	-929.36	-1262.08	1	9	7.5		4			96	181	73	13647.0785
294	609834.49	7176202.44	-942.14	-1259.02	1	9	27	0	4			311	836	76	204200.381
295	610753.78	7175981.09	-1044.7	-1305.91	4	10	2		5			58	856	67	38993.448

S

296	612034.51	7175685.53	-932.17	-1290.75	1	9	4.5		5			107	176	82	14790.6182
297	613290.08	7180080.28	-873.24	-1218.04	1	10	3		4			61	110	136	5270.02168
298	613068.83	7179794.33	-879.94	-1220.04	1	10	1		4			85	123	23	8211.3378
299	613062.31	7179615.78	-883.43	-1228.95	1	10	4		4			89	146	21	10205.4637
300	612778.83	7179244.64	-889.88	-1559.08	1	15	11	12	6		12	167	218	32	28593.2055
301	612215.4	7179390.93	-899.5	-1230.2	1	10	4		4			59	179	11	8294.59
302	612398.73	7179341.52	-885.7	-1231.69	1	10	6		3			130	191	37	19501.4364
303	611923.47	7179348.42	-896.5	-1578.95	1	15	6		3			104	154	98	12578.937
304	611780.21	7179327.56	-904.02	-1232.25	1	10	3		3			55	120	19	5183.62788
305	612093.02	7178941.78	-904.56	-1576.07	1	15	7	11	4	12	13	121	143	21	13589.7444
306	612000.09	7178623.77	-908.1	-1233.48	1	10	4.5		5			68	167	150	8918.98154
307	612896.46	7178830.42	-933.1	-1247.08	2	10	7.5		4			106	266	61	22145.0866
308	613121.9	7178837.88	-928.5	-1241.44	2	10	5.5		5			64	195	58	9801.76908
309	612341.24	7178470.46	-910.29	-1247.9	1	10	17		4			159	628	42	78423.5774
310	611863.56	7178451.65	-920.55	-1244.4	1	10	9		4			91	122	142	8719.49041
311	613090.62	7178351.25	-1019.52	-1556.54	4	15	5	9	5	10	13	178	512	17	71578.047
312	612817.29	7177575.63	-1270.61	-1562.54	10	15	0	15			13	125	177	35	17376.9344
313	612504.04	7177327.03	-1068.97	-1569.29	5	15	3.5	7.5	5	10	13	104	294	42	24014.3342
314	612265.79	7176962.49	-1280.19	-1571.01	10	15	0	9			13	126	246	35	24344.2015
315	612724.04	7176826.24	-909.45	-1704.28	1	15	14	14	4	10	13	182	561	82	80190.7233
316	612509.28	7176262.13	-921	-1298.52	1	10	20		4			193	315	75	47748.2813
317	612675.65	7176235.62	-1299.64	-1705.46	10	16	0	15			14	171	366	10	49154.9295
318	612587.54	7175766.07	-1042.66	-1287.51	4	9	12		5			133	355	73	37082.5743
319	612712.8	7174388.81	-930.34	-1318.09	1	9	4		4			78	198	70	12129.6892
320	612385.6	7174087.42	-936.85	-1317.58	1	9	3		4			84	141	82	9302.25585
321	612876.5	7172636.55	-944.74	-1228.89	1	8	4		4			128	182	140	18296.6356
322	612109.22	7174224.78	-939.37	-1199	1	8	9		5			109	220	107	18833.848
323	611214.67	7173942.27	-958.61	-1217.03	1	8	5		5			61	127	133	6084.47957
324	610912.19	7173796.73	-959.14	-1222.01	1	8	4		4			75	110	28	6479.53485
325	611591.39	7173895.64	-999.08	-1213.9	2	8	9.5		6.5			86	190	102	12833.406
326	610050.2	7173671.19	-964.91	-1327.45	1	9	9		6.5			112	521	78	45829.5536
327	610421	7173598.33	-963.85	-1223.48	1	8	6		5			78	153	65	9372.94168
328	610665.36	7173608.54	-967.79	-1329.51	1	9	4		4			99	161	78	12518.4613
329	610714.34	7173488.81	-963.36	-1326.6	1	9	8		5			79	218	110	13526.1272

T

330	611208.48	7173510.03	-961.59	-1324.1	1	9	6		5			123	594	80	57382.7606
331	611530.3	7173556.9	-955.31	-1318.54	1	9	5		5			110	273	93	23585.5068
332	610080.51	7173371.13	-967.47	-1234.36	1	8	6		3			113	339	89	30086.2474
333	610870.18	7173181.65	-965.11	-1421.19	1	10	3.5		6.5			75	104	75	6126.10567
334	611603.92	7173212.4	-955	-1317.03	1	9	9		6.5			104	209	95	17071.4145
335	610111.46	7173020.42	-976.47	-1228.95	1	8	2		3			50	88	82	3455.75192
336	610182.04	7172878.45	-979.88	-1795.34	1	16	16		15			115	316	33	28541.3693
337	610711.38	7172777.93	-1053.74	-1803.8	3	16	39	0	6.5			407	617	161	197228.401
338	611089.56	7172883.76	-962.64	-1315	1	9	17	0	6.5			272	440	88	93996.4522
339	612109.72	7173209.95	-1071.1	-1315.01	4	9	5		5			99	225	82	17494.7441
340	612070.41	7172925.12	-1074.89	-1314.83	4	9	5		6.5			117	385	71	35378.2603
341	611229.74	7172625.08	-962.64	-1316.05	1	9	4		6.5			55	99	128	4276.493
342	610644.26	7172438.31	-1141.71	-1589.87	5	14	2	21	6	9	10	143	256	9	28751.856
343	611588.92	7172575.89	-1086.49	-1318.5	4	9	4		5			84	156	42	10291.8575
344	611005.19	7172338.64	-968.98	-1316.53	1	9	2		6.5			63	95	19	4700.60801
345	607920.32	7173868.47	-984.34	-1309.67	1	9	3		3			121	327	82	31075.8491
346	608589.59	7173915.18	-977.2	-1314.38	1	9	1		5			89	189	90	13211.1825
347	608454.37	7173743.26	-988.92	-1420.82	1	12	7		4			99	219	88	17028.2176
348	608828.84	7173670.92	-978.63	-1418.56	1	10	5		4			60	112	28	5277.87566
349	608032.12	7173554.91	-997.27	-1307.35	1	9	8		4			152	295	88	35217.2536
350	608326.65	7173547.05	-988.03	-1313.33	1	9	3.5		4			90	208	110	14702.6536
351	609563.01	7173752.47	-972.37	-1329.87	1	9	3.5		4			95	284	103	21190.0424
352	609411.84	7173476.73	-982.3	-1313.91	1	9	9		4			125	284	111	27881.6348
353	607696.75	7173226.96	-999.22	-1304.81	1	9	4		3			84	147	45	9698.09652
354	609023.47	7173344.05	-980.42	-1313.78	1	9	1		4			59	83	53	3846.09481
355	608194.6	7173197.97	-988.97	-1422.7	1	10	1		4			61	121	6	5797.02384
356	609372.76	7173166.57	-993.21	-1311.4	1	9	14		6.5			119	424	103	39628.0497
357	609710.73	7173266.52	-979.67	-1313.84	1	9	6		4			108	207	104	17558.3613
358	609916.65	7173017.41	-980.52	-1310.36	1	9	6		4			81	148	107	9415.35318
359	608211.99	7172566.18	-996.87	-1325.76	1	9	10		4			148	194	114	22550.3521
360	609444.88	7172542.75	-992.93	-1445.48	1	10	3.5		5			106	132	137	10989.2911
361	609000.92	7171945.27	-1002.03	-1337.19	1	9	4		4			118	147	44	13623.5165
362	606729.91	7176511.49	-962.71	-1281.48	1	10	2.5		4			84	149	41	9830.04341
363	606326.71	7176376.66	-970.18	-1288.03	1	10	4.5		5			86	233	142	15737.8084

U

364	605510.78	7176308.56	-977	-1297.52	1	10	3.5		4			68	109	44	5821.37119
365	606431.7	7175909.86	-972.26	-1550.36	1	14	4	6	6.5	10	12	85	136	137	9079.20277
366	606490.91	7175740.87	-970.41	-1199.59	1	8	2		6.5			60	97	148	4571.01731
367	606305.98	7175637.82	-977.22	-1272.25	1	9	2		4			73	168	146	9632.12308
368	606925.43	7175017.59	-1052.7	-1296.91	3	10	1		6.5			77	122	9	7378.03035
369	606487.65	7174801.6	-988.95	-1321.49	1	10	5.5		4			99	211	110	16406.1822
370	606774.8	7174818.04	-983.85	-1306.35	1	10	5		6.5			71	113	31	6301.24946
371	606711.68	7174681.99	-988.03	-1305.56	1	10	4		4			66	102	35	5287.30044
372	606904.81	7174507.13	-983.97	-1319.85	1	10	16		4			164	480	34	61826.5434
373	606074.68	7174411.6	-992.67	-1294.41	1	9	7		3			99	188	38	14617.8306
374	606611.1	7174362.86	-988.98	-1286.55	1	9	5		4			92	143	22	10332.6982
375	606440.53	7174211.16	-995.88	-1313.38	1	9	3		4			87	97	14	6627.9751
376	607164.98	7174545.02	-984.28	-1282.57	1	9	10		5			80	160	115	10053.0965
377	607070.14	7174099.86	-986.51	-1294.32	1	9	9		4			94	234	39	17275.618
378	607121.22	7173777.46	-1048.12	-1287.64	1	9	8		6.5			101	329	10	26097.9956
379	606870.26	7173740.91	-989.96	-1338.78	1	10	14		6.5			136	288	10	30762.4753
380	606668.46	7173711.52	-1002.42	-1325.49	1	10	18		4			164	480	13	61826.5434
381	606696.65	7173487.28	-1003.72	-1329.29	1	10	7		4			89	124	5	8667.65413
382	606889.79	7173287.04	-1141.72	-1345.82	5	10	7		6.5			69	122	22	6611.48174
383	607143.68	7172512.08	-1088.12	-1319.55	3	9	9		6.5			98	454	53	34943.9351
384	606554.85	7172248.72	-1028.32	-1329.3	1	9	10		3			90	153	121	10814.9327
385	605959.42	7172060.52	-1036.82	-1360.54	1	10	6		3			118	144	47	13345.4856
386	607028.08	7171937.05	-1035.87	-1335.71	1	9	11		5			82	456	74	29367.6081
387	608702.78	7171749.6	-1014.91	-1455.64	1	10	9		6.5			87	162	8	11069.4017
388	609414.85	7171523.47	-1002.04	-1342.11	1	9	5		5			117	164	4	15070.22
389	607961.29	7171134.16	-1454.57	-1835.34	10	16	25		13			128	909	148	91382.6471
390	610380.46	7172196.91	-1135.29	-1320.02	5	9	3		6.5			98	145	32	11160.5079
391	610353.84	7172091.55	-1138.16	-1322.89	5	9	6		6.5			91	212	62	15151.9014
392	610282.6	7171497.6	-1428.51	-1591.5	10	14	8		13			165	387	11	50151.5997
393	610500.68	7171123.4	-1435.06	-1593.04	10	14	7		13			157	418	161	51542.5399
394	608224.6	7171476.98	-1361.34	-1619.29	9	14	11		10			148	246	145	28594.7763
395	607670.03	7171320.1	-1454.16	-1620.27	10	14	15		13			136	413	130	44114.244
396	608352.3	7171267.22	-1447.06	-1612.85	10	14	18		13			137	298	157	32064.6654
397	609049.44	7171444.88	-1351.61	-1588.05	9	14	14		10			112	281	11	24718.051

398	608760.02	7171275.85	-1460.32	-1595.54	10	14	14		13			181	311	82	44210.848
399	608058.29	7170843.81	-1374.56	-1835.46	9	16	15		13			176	331	170	45754.1554
400	608747.51	7170741.2	-1481.25	-1825.83	10	16	7		13			176	402	124	55568.4909
401	608246.8	7170516.04	-1388.11	-1846.75	9	16	10		13			140	335	4	36835.1739
402	609195.74	7170425.89	-1482.51	-1617.71	10	14	13		13			239	655	123	122950.155
403	613318.35	7170341.21	-952.59	-1339.8	1	9	2		4			40	76	5	2387.61042
404	614520.1	7170186.4	-936.69	-1322.85	1	9	6		4			120	196	14	18472.5648
405	607048.77	7170163.97	-1467.18	-1636.3	10	14	13		13			124	292	5	28437.6967
406	606677.79	7169424.87	-1482.56	-1862.89	10	16	12		13			214	544	10	91432.9126
407	597823.97	7175036.85	-1073.3	-1468.04	1	12	5		5			106	197	160	16400.6844
408	597616.45	7174651.42	-1082.48	-1455.83	1	11	7		5			115	224	29	20231.8567
409	597830.59	7174606.48	-1173.15	-1407.39	4	10	5		5			76	126	150	7520.97281
410	597562.55	7174237.6	-1318.7	-1416.6	7	10	5		9			63	112	15	5541.76944
411	599486.84	7174416.36	-1061.53	-1592.69	1	14	7.5	3.5	4	11	12	198	402	40	62514.5522
412	599325.97	7173986.96	-1072.78	-1470.12	1	12	12		9			213	291	10	48681.3344
413	597542.92	7173803.41	-1330.27	-1422.62	7	10	6		9			69	138	38	7478.56131
414	598678.54	7173740.43	-1316.97	-1478.33	7	12	5		9			90	148	43	10461.5035
415	598415	7173473.7	-1285.71	-1560.8	6.5	14	16		9			322	400	21	101159.283
416	597503.34	7173340.93	-1335.32	-1581.25	7	14	5		9			102	141	14	11295.5964
417	598301.15	7173076.52	-1333.65	-1494	7	12	4.5		9			68	137	22	7316.76929
418	598841.68	7173028.38	-1323.4	-1487.09	7	12	11		9			85	175	43	11682.7977
419	600805.46	7175750.17	-1224.79	-1433.56	6.5	12	5		9			89	128	130	8947.25588
420	600723.72	7175611.4	-1230.35	-1415.37	6.5	11	10		9			107	216	124	18152.1224
421	600960.87	7175595.19	-1224.88	-1436.45	6.5	12	7		9			75	207	127	12193.3065
422	600311.97	7175373.83	-1036.07	-1520.18	1	14	12		9			100	248	131	19477.8745
423	600460.76	7174989.53	-1041.28	-1520.57	1	14	7		6.5			73	243	169	13932.178
424	600410.43	7174753.84	-1048.14	-1449.65	1	12	5		5			91	139	170	9934.50137
425	600929.59	7174575.72	-1044.91	-1375.45	1	10	9		3			78	125	170	7657.63209
426	601171.28	7174509.43	-1176.45	-1372.81	5	10	3		6.5			69	166	175	8995.95056
427	600802.55	7173897.53	-1295.68	-1462.68	7	12	4.5		10			79	114	121	7073.29586
428	601093.55	7173939.9	-1290.62	-1461.2	7	12	4		9			73	133	75	7625.43077
429	603866.98	7175840.81	-994.12	-1321.51	1	10	3.5		6.5			69	216	166	11705.5742
430	603992.75	7175656.14	-997.96	-1317.77	1	10	7		4			125	206	155	20224.0027
431	603667.88	7175532.72	-998.54	-1325.9	1	10	4		4			102	163	109	13058.0299

W

432	604177.35	7175581.54	-997.16	-1317	1	10	2		4			77	152	6	9192.3001
433	604178.74	7175226.53	-1007.45	-1327.23	1	10	6		4			91	148	142	10577.7425
434	604573.46	7175284.01	-999.31	-1207.14	1	6.5	3.5		4			97	153	31	11656.0941
435	598695.12	7172601.06	-1339.15	-1497.6	7	12	5		9			84	179	37	11809.2468
436	598924.44	7172583.72	-1333.58	-1426.91	7	10	3.5		9			68	121	50	6462.25609
437	598749.44	7172203.01	-1348.16	-1502.73	7	12	5		9			93	104	79	7596.37104
438	597770.09	7171426.07	-1372.73	-1523.41	7	12	5		9			57	137	76	6133.17426
439	600460.21	7172858.13	-1315.7	-1480.96	7	12	4		9			87	148	39	10112.7868
440	614669.03	7169928.98	-934.5	-1326.1	1	9	4		4			65	119	11	6075.05479
441	615143.6	7168145.87	-962.82	-1333.9	1	9	7		4			123	186	97	17968.3392

X